Potential-driven surface phase transitions on iridium (hydr-)oxides and their relation to electrolytic water splitting

vorgelegt von
Master of Science
Lorenz Falling
geb. Frevel
ORCID: 0000-0002-2622-5166

an der Fakultät II – Mathematik und Naturwissenschaften
der Technischen Universität Berlin
zur Erlangung des akademischen Grades
Doktor der Naturwissenschaften
- Dr. rer. nat. -
genehmigte Dissertation

Promotionsausschuss:

Vorsitzender: Prof. Dr. Martin Lerch
Gutachter: Prof. Dr. Robert Schlögl
Gutachter: Prof. Dr. Peter Strasser
Gutachter: Prof. Dr. Mehtap Özaslan

Tag der wissenschaftlichen Aussprache: 16. November 2020

Berlin 2021

„No matter what you look at, if you look at it closely enough,
you are involved in the entire universe.“

Michael Faraday

Acknowledgements

I want to thank Axel Knop-Gericke and Robert Schlögl for their trust when they assigned the *iridium project* to me. This trust gave me the opportunity to follow my own ideas and execute them with full access to the infrastructure of the Anorganic Chemistry (AC) department at the Fritz-Haber-Institute of the Max-Planck-Society including the beamlines at BESSY II operated by the AC department and the Helmholtz Zentrum Berlin (HZB), namely the ISISS, BelChem PGM, and the CAT@EMIL beamline. I also used the infrastructure of the BESSY II facility and the EMIL project of the HZB. I want to take the opportunity to explicitly thank Robert Schlögl for his inspiring visions and the generous support of the project, in particular his support of a mini-conference about iridium which I could organize in the Alps. This extraordinary venture set the course for the development of the *iridium project* and pooled forces.

The experiments and experimental designs were supported or performed by many colleagues of the AC department who are named throughout this work but I want to particularly acknowledge Juan Velasco-Vélez, Rik Mom, and Detre Teschner for their critique, support, ideas, and advice whenever I needed it, Michael Hävecker for his resourceful advice and helpful support for everything related to synchrotron experiments, Woosun Jang for his dedication and efforts in computing theoretical contributions, and Eugen Stotz for realizing my drawings or ideas for technical instruments. A very special word of thanks is dedicated to Travis Jones. Not only did he guide me, but he has been a precious discussion-partner and friend. The countless scientific discussions over coffee had a great impact on this work and made it into what it is today. He also designed the theoretical approach in this work and executed computations. In addition, I would like to thank both Verena Streibel and Travis Jones who jump-started the *iridium project*. All I had to do was start running and jump onto this fast-moving project.

I also thank the group of Bettina Lotsch at the Max-Planck-Institute for Solid State Research and the group of Robert Schlögl at the Max-Planck-Institute For Chemical Energy Conversion for fruitful collaborations.

Furthermore, I am grateful to Peter Strasser, Bettina Lotsch, and especially Axel Knop-Gericke and Robert Schlögl, who readily shared their experience and knowledge in order to improve this work. My heartfelt thanks also to Robert Schlögl, Peter Strasser, and Mehtap Özaslan, who offered to invest their time to review my thesis. I also want to acknowledge Stanton Falling and Frances Falling for helping me with the subtleties of the English language.

Finally, I would like to mention my good friends, my dear family, and my loving wife. During my long and sometimes difficult journey, they have been the wind in my sails and the warming sun on my back. Thank you!

Abstract

The burning of fossil fuels and the resultant release of CO_2 into the atmosphere is the only tenable explanation for the rapid progression of climate change in recent decades. A sustainable energy economy is urgently needed to reduce the use of fossil fuels significantly. Hydrogen has been proposed to play a strategic role in this new energy economy and PEM electrolyzers are a promising way to produce hydrogen from water and renewable electricity. Improving the efficiency and longevity of these devices is challenged by the slow and eroding anodic reaction at which oxygen gas evolves, which is called the oxygen evolution reaction, or OER. Iridium (hydr-)oxides are stable and active catalysts for this reaction, but it is not fully understood which properties of their surface give them these qualities.

The present work contributes to this understanding by observing potential driven surface phase transitions with operando X-ray spectroscopy. We found that the surface of iridium (hydr-)oxide catalysts undergo several phase transitions before they reach their active state. These phase transitions are several 100 mV wide and occur via oxidative deprotonation of surface hydroxo groups. The electron holes created in this process reside on surface atoms and an oxidative charge is building up with larger anodic potentials. At the onset of the OER, this process is not yet complete and influences the rate of the OER. In fact, the complex current or rate response, e.g. a change in Tafel slope, can be fully explained when accounting for the phase transition. The catalytic rate is influenced in two ways: First, the availability of active sites changes, and, second, the oxidative charge on the surface, which changes the barrier of the rate determining step. The oxidative charge was found to increasingly reside on oxygen at potentials relevant to the OER. The key experimental findings of this work were only made possible by a novel approach to studying wet catalyst surfaces using surface sensitive X-ray photoelectron spectroscopy (XPS) and near-edge X-ray absorption fine structure (NEXAFS), which is also presented herein.

This thesis contributes to the fundamental understanding of OER catalyst surfaces by investigating a class of stable and active OER catalysts, namely iridium (hydr-)oxides. The experimental and computational approaches used herein, and especially their combination, provide a template for future studies furthering the knowledge about electrocatalysts and their technical development. Advances in these areas of research are urgently needed to successfully transition into a renewable energy economy.

Kurzzusammenfassung

Vermehrte CO_2 Emissionen, die durch die Nutzung fossiler Brennstoffe entstehen, sind die einzige, wissenschaftlich vertretbare Erklärung für den beschleunigten Klimawandel der letzten Jahrzehnte. Eine nachhaltige Energiewirtschaft wird dringend gebraucht, um die Nutzung fossiler Energieträger signifikant einschränken zu können. Wasserstoff wird im wissenschaftlichen Diskurs eine zentrale Rolle in dieser neuen Energiewirtschaft zugesprochen, und PEM-Elektrolysatoren sind eine vielversprechende Möglichkeit, den Strom aus erneuerbaren Energiequellen zu nutzen um aus dem Ausgangstoff Wasser Wasserstoffgas zu produzieren. Eine Verbesserung der Effizienz und Lebensdauer von PEM-Anlagen ist allerdings begrenzt durch die langsame und materialermüdende anodische Reaktion, bei welcher Sauerstoff entsteht. Die (Hydr-)oxide des Iridium sind stabile und reaktive Anodenmaterialien, die diese Reaktion katalysieren, aber es ist nicht vollständig geklärt, welchen Oberflächeneigenschaften sie ihre guten Eigenschaften verdanken.

Die vorliegende Arbeit trägt mit der Beobachtung von Phasenübergängen auf der Oberfläche des Katalysators zu einem besseren Verständnis dieser Beziehung bei. Wir haben beobachtet, dass die Oberfläche von Iridium (Hydr-)oxid Katalysatoren mit steigendem Potential mehrere Phasenübergänge durchläuft bevor sie ihre aktive Form erreicht. Diese Phasenübergänge erstrecken sich über eine Potentialspanne von einigen hundert Millivolt und veräußern sich auf atomarer Ebene in Form von oxidativer Deprotonierung der Oberflächenhydroxidgruppen. Die Elektronenlöcher, die in diesem Prozess entstehen, verorten sich auf Atomen nahe der Oberfläche, und eine oxidative Ladung baut sich auf. Bei dem Potential, an dem die Sauerstoffentwicklung beginnt, ist dieser Wandlungsprozess nicht abgeschlossen und beeinflusst die Reaktionsrate. Die komplexe Änderung dieser Reaktionsrate mit dem Potential, wie z.B. eine Änderung der Tafel-Steigung, kann unter Einbezug der Phasenübergänge allerdings vollständig erklärt werden. Die Reaktionsrate wird auf zwei Wegen beeinflusst: erstens, von der Verfügbarkeit der Reaktionszentren, und zweitens, von der oxidativen Ladung, die die Aktivierungsenergie der Reaktion herabsetzt. Die Dichteverteilung dieser oxidativen Ladung verschiebt sich mit steigendem Potential zunehmend von dem Metallzentrum auf Sauerstoff, welcher schließlich reagiert. Die Schlüsselexperimente dieser Arbeit wurden durch eine neuartige Technik zur Untersuchung von genässten Katalysatoren mit Oberflächen-empfindlicher Röntgenspektroskopie (XPS und NEXAFS) ermöglicht, die ebenfalls hier vorgestellt wird.

Diese Doktorarbeit trägt mit einer detaillierten Untersuchung von Iridium (Hydr-)oxiden in der Sauerstoffentwicklung zu dem fundamentalen Verständnis von elektrochemischen Katalysator-oberflächen bei. Die experimentelle Herangehensweise sowie die theoretische Behandlung und insbesondere die Kombination der beiden bietet eine Vorlage für zukünftige Studien an Elektro-Katalysatoren und deren technische Entwicklung. Fortschritte in diesen Forschungsbereichen werden dringend für eine erfolgreiche Energiewende benötigt.

Contents

List of Figures

List of Tables

Abbreviations

AEY	Auger Electron Yield
BE	Binding Energy
BSE	Bethe-Salpeter Equation
CE	Counter Electrode
BDD	Boron-Doped Diamond
BESSY	Berliner Elektronenspeicherring für Synchrotronstrahlung
BET	Brunauer-Emmett-Teller
BLG	Bilayer of Graphene
CUS	Coordinatively Unsaturated Site
CV	Cyclic Voltammogram
DFT	Density Functional Theory
DOS	Density of States
EC	Electrochemistry
EDX	Energy Dispersive X-ray Spectroscopy
ESEM	Environmental Scanning Electron Microscopy
EXAFS	Extended X-ray Absorption Fine Structure
FE	Fermi Energy
FWHM	Full Width Half Maximum
GC	Glassy Carbon
GGA	Generalized Gradient Approximation
HAADF	High Annular Dark Field
HER	Hydrogen Evolution Reaction
HOPG	Highly Oriented Pyrolytic Graphite
IMFP	Inelastic Mean Free Path
ISISS	Innovative Station for In Situ Spectroscopy
IWL	Intensity of the White Line

LDH	Layered Double Hydroxide
LSV	Linear Sweep Voltammetry
MD	Molecular Dynamics
ML	Monolayer
NAP	Near-Ambient Pressure
NEXAFS	Near-Edge Absorption Fine Structure
NHE	Normal Hydrogen Electrode
NP	Nanoparticle
OCP	Open Curcuit Potential
OER	Oxygen Evolution Reaction
PBE	Perdew-Burke-Ernzerhof
PDOS	Projected Density of States
PDF	Pair Distribution Function
PEEK	Polyether Ether Ketone
PEM	Proton Exchange Membrane
PES	Photoelectron Spectroscopy
PEY	Partial Electron Yield
PMMA	Poly(Methyl Methyl-Acrylate)
PXRD	Powder X-Ray Diffration
PZC	Potential of Zero Charge
RDS	Rate Determining Step
RE	Reference Electrode
RHE	Reversible Hydrogen Electrode
RXN	Reaction
SCF	Self-Consistent Field
SEM	Scanning Electron Microscopy
SI	Supporting Information

SOEC	Solid Oxide Fuel Cell
STEM	Scanning Transmission Electron Microscopy
SLG	Single Layer of Graphene
TBAOH	Tetrabutyl Ammonium Hydroxide
TEM	Transmission Electron Microscopy
TEY	Total Electron Yield
TPR	Temperature Programmed Reduction
UV-Vis	Ultraviolet-Visible
WE	Working Electrode
WL	White Line
XAS	X-ray Absorption Spectroscopy
XPS	X-ray Photoelectron Spectroscopy
XRD	X-Ray Diffraction
XS	X-ray Spectroscopy

1. Introduction

1.1 Climate change and the role of hydrogen in the energy market of the future

On November the 4th, 2016, the Paris Agreement [1] went into force. It is the most important international agreement to date that addresses global warming. In it, the ratifying governments agree to "[...] limit the temperature increase to 1.5°C above pre-industrial levels, recognizing that this would significantly reduce the risks and impacts of climate change". The parties thereby accept and take heed of a consensus which has been solidified in the scientific community at the beginning of the twenty-first century: the majority [2,3] of climate scientists concur, and accept as fact, that the rate at which the planet is warming is unusual and that greenhouse emissions caused by humans are the only reasonable explanation for this rapid rise of temperatures.[4–6]

The Paris agreement states that the reduction of greenhouse gas emissions is the main means of limiting global warming. The most prominent and influential greenhouse gas is CO_2, which is emitted in enormous quantities by the burning of fossil fuels for industrial processes, transportation, and electricity production. In the year 2018, 37.9 gigatons of fossil CO_2 [7] were emitted into the atmosphere but if emissions of today's magnitude would be sustained over the next decades, models predict a warming greater than 2 °C.[8] Reducing these emissions by replacing fossil energy sources is challenging, but a substantial expansion of renewable energy sources, such as solar, wind, and hydro power, has reduced their cost significantly in the last decade, and made them viable alternatives. Specifically, in recent years, a further decline in the cost has resulted in newly built plants (without the need of any subsidies) to produce renewable energy. One kilowatt hour from large scale photovoltaic installations in Germany, for example, dropped from 40 ct in 2005 to 9 ct in 2014.[9] Indeed, wind and solar energy sources have outpaced fossil fuels in terms of cost and are the cheapest source of energy currently available.[10] The low cost and independence from limited resources (e.g. biomass) makes renewable energy sources attractive and have led to a steep rise in its contribution to the global energy production. Germany, for example produced 46 % of its energy with renewable technologies in 2019, a year with above average amounts of wind and sunshine.[11]

These record levels of production are certainly a big win in terms of reducing CO_2 emissions, but electricity- and grid-providers are faced with the new challenge of balancing electricity production and consumption. Producing energy solely from renewable sources comes at the disadvantage of being contingent on complex weather phenomena, which cannot be regulated. The power consumption and production, thus, does not match up in space and time: Figure 1.1A-B shows the spatial mismatch in the form of two maps detailing information about solar irradiation density and power consumption. The temporal mismatch is illustrated in Figure 1.1C-D comparing the solar and fossil-based power production in Germany during week 35 of 2019. Electrical power produced from fossil fuels fills the gaps when solar power is not available.

How the existing gaps are closed best, depends on the time scale of storage. Short-term storage, such as capacitors, and medium-term storage, such as batteries or pumped-storage power plants, could close a large part of the temporal gap on a local level. These grid-stabilizing solutions, however, cannot offset seasonal differences and the availability of solar power on a global scale (see solar irradiation map in Figure 1.1A-B). A global shift from fossil to 100% renewable energy sources for all services and industrial processes can only be achieved if electrical energy can be transported and stored in similar quantities as fossil fuels.[12–14] This is especially true for technologies and facilities which are difficult to decarbonize, such as aviation or energy-hungry processes such as cement or steel production.[15] The challenge is immense: in 2018 alone 2.3 billion tons of crude oil and 943 billion cubic meters of gas [16] were transported in ships and pipelines around the world.

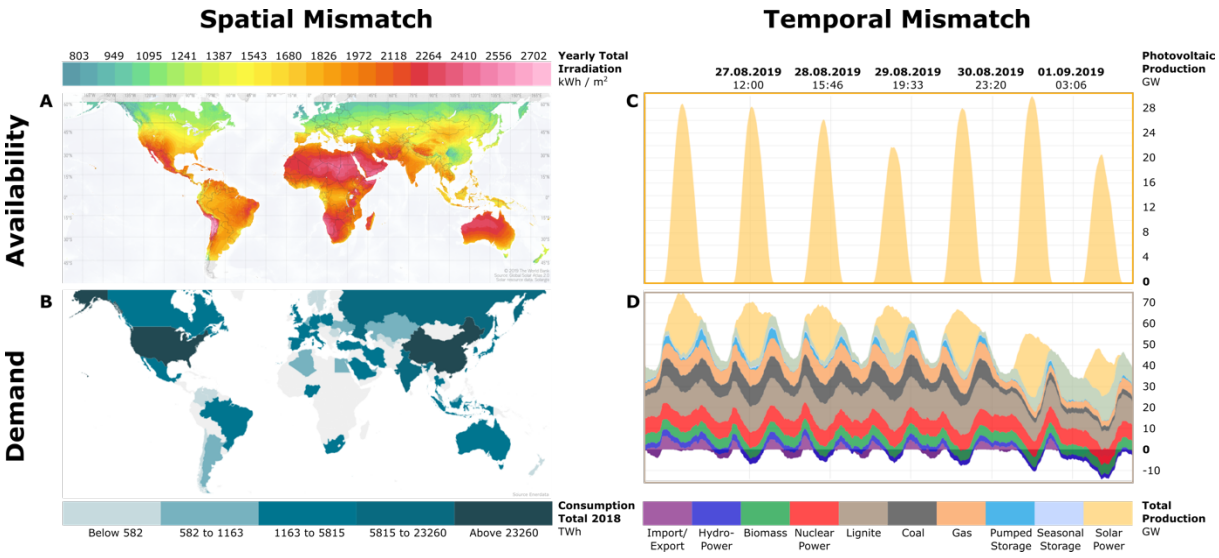

Figure 1.1: World maps of A) horizontal irradiation and B) total energy consumption per country; German energy charts in week 35, 2019, of C) the solar energy production and D) energy production by fossil fuels and trade; data and graphics were obtained from A) Solargis, B) Enerdata, C) and D) Fraunhofer ISE.

A renewable energy market needs to compete with these enormous trade volumes and close the temporal and spatial mismatch of production and consumption. This requires energy carriers which contain a large amount of energy per weight and volume and which can be transported over large distances with a negligible degradation or energy loss over time. Fulfilling these requirements narrows the field of possible solutions to chemical energy storage in form of molecules such as hydrogen, methanol, ammonia, or synthetic hydrocarbons.[12,13,15,17] These molecules need to be produced from ubiquitous sources, e.g. carbon dioxide, water, oxygen, nitrogen, or biomass, which should finally be integrated in a chemical cycle that is self-sustained. The conversion processes, however, consume energy, which needs to be provided by renewable power sources. Some future visions of possible conversion networks and cycles have been suggested,[13,15,18] but they all rely on a renewable source of hydrogen for transport, chemical infrastructure, or energy storage.

1.2 Green hydrogen production

Hydrogen is still largely produced from natural gas (48 %), liquid hydrocarbons (30 %), and coal (18 %).[17] For gaseous and volatile liquids, i.e. methane, three processes are used to produce hydrogen: steam reforming, partial oxidation, or autothermal reforming. In all these processes, hydrocarbons are converted into synthesis gas consisting of carbon monoxide and hydrogen, but at different ratios and pureness. This synthesis gas can be reacted with water in order to further increase the yield of hydrogen (this process is named water gas shift reaction). For solid feedstocks, e.g. coal or biomass, gasification or pyrolysis is used. Pyrolysis requires dry feedstocks and ideally only produces solid carbon and hydrogen, which makes it a promising type of reaction for a sustainable future energy system. Gasification on the other hand results in a gas mix called producer gas, which consists of nitrogen, carbon monoxide, carbon dioxide, methane, and hydrogen, which can further be used in the reactions mentioned above. Many of the above processes are well established at an industrial scale,[19] which makes them cost- and energy-efficient. However, almost all the processes require heat, which is currently supplied by fossil fuels, and all, except ideal pyrolysis, emit CO_2. If these developed technologies are to be used in a carbon-neutral energy system, carbon capture and storage is required.

Sustainable production of hydrogen is possible by the electrolysis of water using renewable power sources. This route is not yet as efficient as the conventional processes but will become competitive with falling costs of electrical power from renewable sources (see chapter 1.1) and a price on CO_2 emissions. In addition to electrolysis, other promising alternatives to produce green hydrogen exist (e.g. thermochemical, biochemical, and photolytical processes), but they are in early stages of development [20,21] and are beyond the scope of this work. Three types of electrolyzers are currently under consideration: alkaline, proton exchange membrane (PEM), and solid oxide electrolysis cells (SOEC). An overview of the techniques is given in Table 1.1.

Table 1.1: Comparison of existing water electrolyzer systems.[22]

	Alkaline	PEM	SOEC
Maturity	Commercial	Early commercial	Pilot
Electrolytic Charge Carrier	OH^-	H^+	O^{2-}
Operating Pressure	10-30 bar	20-50 bar	1-15 bar
Operating Temperature	60-90 °C	50-80 °C	700-900 °C
Current Densities	0.25-0.45 A/cm^2	1.0-2.0 A/cm^2	0.3-1.0 A/cm^2
Nominal System Efficiency*	51-60 %	46-60 %	76-81 %
Efficiency Degradation	0.25-5.0 %/a	0.5-2.5 %/a	3 -50 %/a
Investment Cost	800-1500 €/kW	1400-2100 €/kW	>2000 €/kW

*Including auxiliaries and heat supply; Data source: Buttler and Spliethoff (2018) [22]

SOECs differ significantly from the other processes, because they operate in the gaseous regime. The reaction enthalpy of water splitting in SOECs is therefore fundamentally lower than in PEM and alkaline electrolyzer, due to a lower entropy cost (for more thermodynamic considerations, see Section 1.3.1).

Faradaic efficiencies close to 100 % can be achieved and they remain higher than for electrolysis of liquids when accounted for heating.[22] Another benefit of SOECs is their operational flexibility: SOECs can be operated in reverse as a fuel cell and they could produce synthesis gas from a co-feed of water and carbon dioxide. The operation at high temperatures, however, leads to a quick degradation of seals and the oxide membranes delaying technical use of SOECs on a larger scale. [23,24]

The most mature technique is the alkaline electrolysis and it can be implemented routinely at the MW scale.[25] Stacks can be made from available materials at comparatively low cost and a long lifetime.[21,22,25,26] However, alkaline electrolyzers have startup times of 1-2 h (cold) or 1-5 min (warm), which is too long to react to the fluctuations of intermittent sources like solar or wind power. In addition, the hydrogen gas needs cleaning from the alkaline electrolytes NaOH or KOH and oxygen from cross permeation. PEM electrolyzers offer solutions to that. They can be operated with water as their only feedstock, they have negligible cross permeation of oxygen, they tolerate large current densities, they can be operated dynamically, and they can produce hydrogen gas at high pressures (up to 350 bar).[22,25,26] These benefits allow for compact and more flexible systems which can be easily integrated and produce clean hydrogen at large pressures. These benefits are reflected in a sharp increase of the PEMs share of total electrolyzer conversion power: in 2010-2014, 4.6 MW of the total 41.6 MW were produced by PEM electrolyzers; in 2015-2019 that number rose to 82.9 MW of a total 95.3 MW.[25] This sharp rise can be taken as a sign of how attractive this technology appears to investors.

Although technically promising, electrochemical water splitting with PEM based electrolyzers might be limited by the availability and lifetime of catalyst materials – the reason being a corrosive environment in PEM electrolyzers. They use water as their feedstock, which is supplied at the anode. In the oxygen evolution reaction (OER)

$$Anode\colon\ 6\,H_2O(l) \rightarrow\ O_2 + 4\,H_3O^+ + 4\,e^- \qquad \text{(Reaction 1)}$$

the feedwater is split into oxygen and solvated protons, i.e. hydroxonium ions. The latter ions are transported via the proton exchange membrane to the cathode at which the hydrogen evolution reaction (HER)

$$Cathode\colon\ 2\,H_3O^+ + 2\,e^- \rightarrow H_2 + 2\,H_2O(l) \qquad \text{(Reaction 2)}$$

occurs. Reaction 2 is formally correct in liquids. Proton transport in PEMs is, however, a complex issue [27] and it might occur faster than the transport of water. The stoichiometry of Reaction 2 might, thus, not hold in a PEM electrolyzer in which water on the side of the cathode solely originates from diffusion through the PEM. The protons produced in the OER decrease the local pH and create an acidic environment. If paired with radical intermediates of the OER at the anode, this environment is strongly corrosive. Most catalyst materials dissolve under acidic conditions and anodic potentials [28] and the range of possible catalyst materials narrows to mostly noble metals oxides, which still dissolve, but are more robust.[29,30] Unfortunately, the abundance of these elements in the earths crust is small and the production volumes are tied to other metals, e.g. nickel.[31] The supply of the noble metal catalyst might

be insufficient to cover future demand for water electrolysis.[32] This catalyst shortage and degradation contributes to higher costs at a shorter lifetime of PEM electrolyzers.

Besides the stability, also the electrode kinetics influence how efficiently hydrogen can be produced. At the cathode, platinum is widely employed as the active component. Platinum is an almost ideal catalyst for the HER, because it is, together with palladium, unmatched in the rate of hydrogen production.[26,33] Alternatives are nevertheless needed due to the high cost and scarcity of platinum or palladium. While the kinetics at the cathode are rapid, the anodic OER needs to supply the protons for the hydrogen production and can limit the overall production rate of hydrogen. And it does: the OER is often termed a "sluggish" reaction because of its slow kinetics.[33–35] In order to solve that problem, much of the recent research activity, including the present work, is concerned with understanding or improving the oxygen evolution reaction under acidic conditions. A popular material system for catalyzing the OER are iridium (hydr-)oxides, meaning hydrated iridium oxides with the general formula $Ir(H_2O)_x(OH)_yO_z$. This material class appears unique, because it is both active and stable [36–38] – two properties thought to be antagonistic.[29,39,40] The concerns expressed above about the quick deterioration and the sluggish kinetics do not apply to iridium (hydr-)oxides as strongly. This rather unique property makes iridium (hydr-)oxides an intriguing object of scientific studies. Succeeding in these studies will be key to rationalize and perhaps improve the catalysis of electrochemical water splitting under acidic conditions.

The following chapters will lay the groundwork to interpret the findings of the present work and introduce the scientific question this work revolves around.

1.3 The oxygen evolution reaction on iridium oxo-hydroxides

This chapter aims to provide a fundamental basis for water splitting on iridium oxo-hydroxides. It starts out with a general thermodynamic description of water splitting and discusses the influences of pressure, temperature, and pH on the thermodynamic requirements of the overall reaction. It is then discussed how the energetics will be influenced if the total reaction is split into elementary reaction steps on an electrode surface. The properties of the latter are described in two sections, one about the bulk properties of iridium (hydr-)oxide electrodes and another about their surface properties. Finally, a comment is made on a proper description of the reaction rate.

1.3.1 Thermodynamic considerations

For simplicity, the water electrolysis in PEM electrolyzers will be treated as a reaction in liquid evolving gaseous products, which follow the behavior of ideal gases. The overall reaction is obtained by adding reaction 2 to reaction 1 twice:

$$Watter\ splitting:\ \ 2\,H_2O(l) \rightarrow 2H_2 + O_2 \qquad \text{(Reaction 3)}$$

In an ideal electrolyzer with no ohmic losses, no heat losses, no mass transport limitations, and no overpotentials caused by the non-ideal catalyst materials, the minimal free energy required to drive this reaction is obtained from the chemical potentials of its components:

$$\Delta G_{T,p} = \mu_{H_2O} - \mu_{H_2} - 0.5\,\mu_{O_2} \qquad \text{(Equation 1)}$$

With the assumption of ideal gas behavior and gaseous and liquid water being at equilibrium with its gas phase, the relations $\mu_i = \tilde{G}_i^0 + RT \ln p_i$ (where $\tilde{G}_i^0$ is the molar free energy of an ideal gas) and $p_{H_2} = p_{O_2} = p - p_{H_2O(g)}$ can be used to rewrite equation 1 into

$$\Delta G_{T,p} = \left[\tilde{G}^0_{H_2O(g)} - \tilde{G}^0_{H_2} - 0.5\,\tilde{G}^0_{O_2}\right]_T + RT \ln\left(\frac{p_{H_2O(g)}}{\left(p - p_{H_2O(g)}\right)^{1.5}}\right) \qquad \text{(Equation 2)}$$

It can further be shown [41] that the first term on the right equals the free energy of formation of liquid water $\Delta G_f^0[H_2O(l)]_T$ if a correction of $RT \ln p^*_{H_2O(g)}$ is subtracted (where $p^*_{H_2O(g)}$ is the water vapor pressure at equilibrium), so that

$$\Delta G_{T,p} = \Delta G_f^0[H_2O(l)]_T + RT \ln\left(\frac{p_{H_2O(g)}}{\left(p - p_{H_2O(g)}\right)^{1.5} p^*_{H_2O(g)}}\right) \qquad \text{(Equation 3)}$$

The free energy can also be expressed in terms of a reversible voltage with $\Delta G = -nFV_{rev}$, while the standard potential of the reaction is given by $-\Delta G_f^0[H_2O(l)]_{25°C} = 237.18\,\frac{kJ}{mol} = 2FV^0_{rev}$ [42] leading to a reversible standard potential of $V^0_{rev} = 1.229\,V$ at standard conditions ($T = 25°C; p = 1atm$). This potential is the theoretical lower limit of oxygen evolution.

The practical lower limit is larger. As is evident from Reaction 1-3, the gas evolution takes place in liquid, which is consumed in the reaction. This leads to additional energy costs: first, gas evolution from the liquid phase comes at an entropic cost making the enthalpy more positive than the free energy; second, water needs to evaporate in order to equilibrate with the gas phase and third, depending on temperature and pressure, the water feed needs to be heated and compressed. In the following passage these necessary additions and their dependence on temperature and pressure will be discussed.

The formal expression for the enthalpy of electrochemical water splitting for ideal gases and ideal gas mixtures can be expressed as the thermoneutral voltage [41]

$$\begin{aligned} nFV_{tn} = {} & \left[\widetilde{H}_{H_2} + 0.5\,\widetilde{H}_{O_2} - \widetilde{H}_{H_2O(l)}\right]_{t,p-p_{H_2O(g)}} && \text{Term I - Reverse enthalpy of formation } \Delta\widetilde{H}_f[H_2O(l)] \\ & - \left[\widetilde{H}_p - \widetilde{H}_{p-p_{H_2O(g)}}\right]_{H_2O(l),t} && \text{Term II - Isothermal compression of } H_2O(l) \\ & + \phi\left[\widetilde{H}_{H_2O(g),p_{H_2O(g)}} - \widetilde{H}_{H_2O(l),p}\right]_t && \text{Term III - Vaporization of } H_2O(l) \\ & + [1+\phi]\left[\widetilde{H}_{t,p} - \widetilde{H}^0_{25°C}\right]_{H_2O(l)} && \text{Term IV - Heating and compression of feedwater} \end{aligned}$$

where $\phi = 1.5\,p_{H_2O(g)}/(p - p_{H_2O(g)})$ is the amount of water per mole hydrogen (and half a mole oxygen), which will be evaporated into the gas phase reaching equilibrium. In a first approximation, the

case of $p/p_{H_2O(g)} \rightarrow \infty$ will be treated in which ϕ becomes negligible. Term II will be dropped because it is small. This leads to a simplified expression in which Term I and the second part of Term IV are left.

$$nFV_{HHV} = \left[\tilde{H}_{H_2} + 0.5\,\tilde{H}_{O_2} - \tilde{H}_{H_2O(l)}\right]_{t,p-p_{H_2O(g)}} + \left[\tilde{H}_{t,p} - \tilde{H}^0_{25°C}\right]_{H_2O(l)}$$
$$= nFV^0_{t,p} + \left[\tilde{H}_{t,p} - \tilde{H}^0_{25°C}\right]_{H_2O(l)} \qquad \text{(Equation 5)}$$

with the voltage of the higher heating value V_{HHV} and the enthalpic voltage $V^0_{t,p}$. The latter is the minimum requirement excluding heating of the feedwater and results in $V^0_{25°C,1bar} = 1.481\,V$ at standard conditions. This additional cost originates from rising entropy upon conversion from liquid to product gases and cannot be avoided. The enthalpic voltage is thereby the practical lower limit of oxygen evolution under steady state conditions. The temperature dependence of this quantity is given in Figure 1.2A (data for the calculations was obtained from JANAF [43] tables, and the IAPWS [44,45] formulation). The enthalpic voltage drops with increasing potential. However, as soon as heating of the feedwater is included, the voltage (of the higher heating value) increases with temperature. This trend is enhanced by taking vaporization into account, due to the strong dependence of vapor pressure on temperature and the respective changes in ϕ. This can be seen in the reciprocal behavior of the thermoneutral voltage with temperature (Figure 1.2A). Also due to changes in ϕ, V_{tn} drops with increasing pressure, while V_{tn} and $V^0_{t,p}$ hardly depend on pressure, due to ideality of the gases (Figure 1.2B).

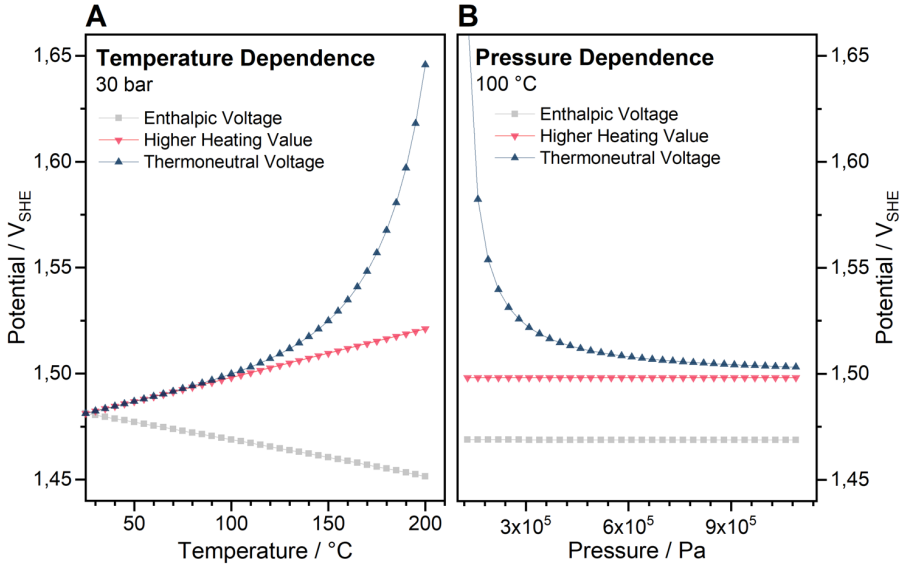

Figure 1.2: A) Temperature and B) pressure dependence of the enthalpic voltage, the voltage of the higher heating value and the thermoneutral voltage at 30 bar and 100 °C, respectively.

The reversible potential, the enthalpic voltage, the voltage of the higher heating value, and the thermoneutral voltage add useful fundamental insights on how much energy is needed at a given temperature and pressure to split water, but there are remaining energy contributions that have not been discussed here. First, a real electrolyzer system would lose heat via radiation or convection and additional compression of hydrogen might be needed for practical purposes, which will change the

overall efficiency of the system. Second, fundamental corrections might be needed, due to the electrolyzer design: as mentioned above, the local pH and the amount of water passing through the polymer membranes is unknown. The former will influence the reversible potential by $V_{rev} = V_{rev}^{0} - 0.059 \cdot pH$ and the latter will determine how wet the hydrogen gas is and thereby influence the higher heating voltage and the thermoneutral voltage.

Independently of the upper estimate of the energy cost for electrochemical water splitting, the energy was assumed to have been solely supplied by electrical power. Indeed, current PEM electrolyzer systems are operated at potentials higher than the thermoneutral voltage.[17] The ohmic losses over the (solid) electrolytes and the rest of the electrolyzer stack architecture provides sufficient heat and no additional heat source is required. However, this need not be the case. External heating from, for example, solar thermal power, combined with smart electrolyzer design could lower the voltages and improve the electrical efficiency. The lower limit to splitting water electrochemically remains the reversible potential. However, this lower limit can only be reached if the reaction occurs essentially barrier-less and the reaction is connected to an endless bath of water and heat. In other words, only an ideal catalyst at the anode and cathode could realize water electrolysis at the reversible potential (involving external heating). Real anode materials catalyzing the oxygen evolution reaction are not ideal, though, and require an overpotential to catalyze the reaction, which is independent of the amount of supplied heat. The next section will focus on this issue and discuss the influence of the mechanism on the overpotential of the reaction. The influence of the hydrogen evolution, which is very fast compared to the oxygen evolution, and limiting mass transport on the overpotential of the total reaction will be omitted in the following.

1.3.2 Mechanistic aspects

The anodic oxygen evolution reaction (Reaction 1) involves two water molecules and the transfer of four electrons for one oxygen molecule. Due to this complexity, it is nearly impossible that these events occur in one concerted step. To the contrary, the OER is a multi-step process with several intermediates. A relatively simple scheme, in which water is oxidized by one electron at a time is shown in Figure 1.3. It is an indirect pathway through hydrogen peroxide via the radical intermediates •OH and H•O_2. Such radical intermediates, however, are not stable in water and H_2O_2, or the corresponding ionized species HO_2^-, have not been detected during OER.[46] The experimental case for a stepwise process in solution is, therefore, weak and also thermodynamic arguments are unfavorable: each intermediate of the indirect pathway have a higher free energy than the direct connection of the total reactions and the first oxidation of water.

Adsorption of intermediates offers a way out. By interacting with adsorbed species, the electrode surface alters their energetics. In the multi-step OER, however, several intermediates are expected, and the adsorption energies of all intermediates influence the overall energetics of the reaction. This requirement makes the OER strongly dependent on the electrode material and the mechanism. The former has been observed experimentally.[33] Much of the OER research in the 20th century thus tried

to describe which properties of the surface make for a suitable electrode and which mechanism explains the electrochemical experiments. The remaining section will discuss the development of mechanistic schemes and sections 1.3.3 and 1.3.4 will discuss what role the framework of the active site has.

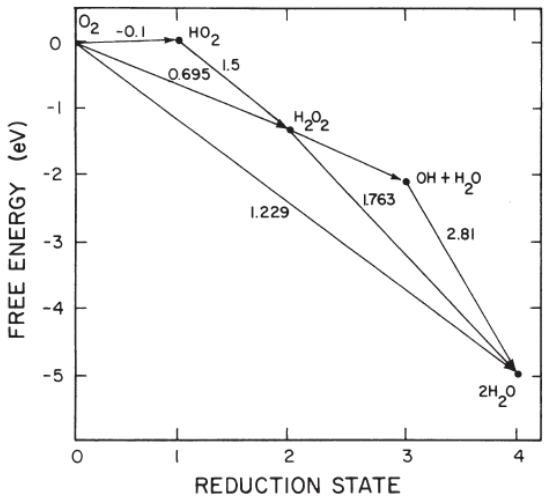

Figure 1.3: Free energy relationships for stepwise reduction/oxidation of water or molecular oxygen; obtained from reference [46].

Mechanistic studies have, for the most part, been a *Gedankenexperiment*. The reason is scarce experimental evidence. The intermediates exist for a short time and just on the surface of the catalyst. Any technique attempting to detect them is therefore limited by the lifetime of an intermediate and the small share of surface species relative to all species in the probed volume. Because of these hurdles, the mechanism was long deduced from production rates of oxygen in relation to the applied potential. However, not knowing the rate determining step, the adsorption energies of each intermediate and transition state, the state of the surface, and the electron transfer rate leads to a large uncertainty. Because of this uncertainty many different mechanisms have been proposed and discussed for iridium-based electrodes. The ones most discussed in the literature [35,46–48] are compiled in Figure 1.4 using the letter S as a general adsorption site. In this graphical representation it becomes clear that the adsorbed hydroxide S-OH and oxygen S-O appear in every mechanism except the hydrogen peroxide path of Bockris.[49] How these adsorbed species oxidize further to O_2, seems to be under discussion: it either occurs by direct combination of two S-O or via a peroxide intermediate. Also open to discussion is the question whether a given step proceeds in a concerted electrochemical step, a non-concerted electrochemical step, or a purely chemical step. While all authors agree that the first adsorption of water proceeds in a concerted electrochemical step, the pathways beyond S-OH are not clearly of one type or the other and are often mixed. This is, again, due to the uncertainty caused by limited knowledge on electron transfer rates, state of the surface, and adsorption energies of intermediates and transition states.

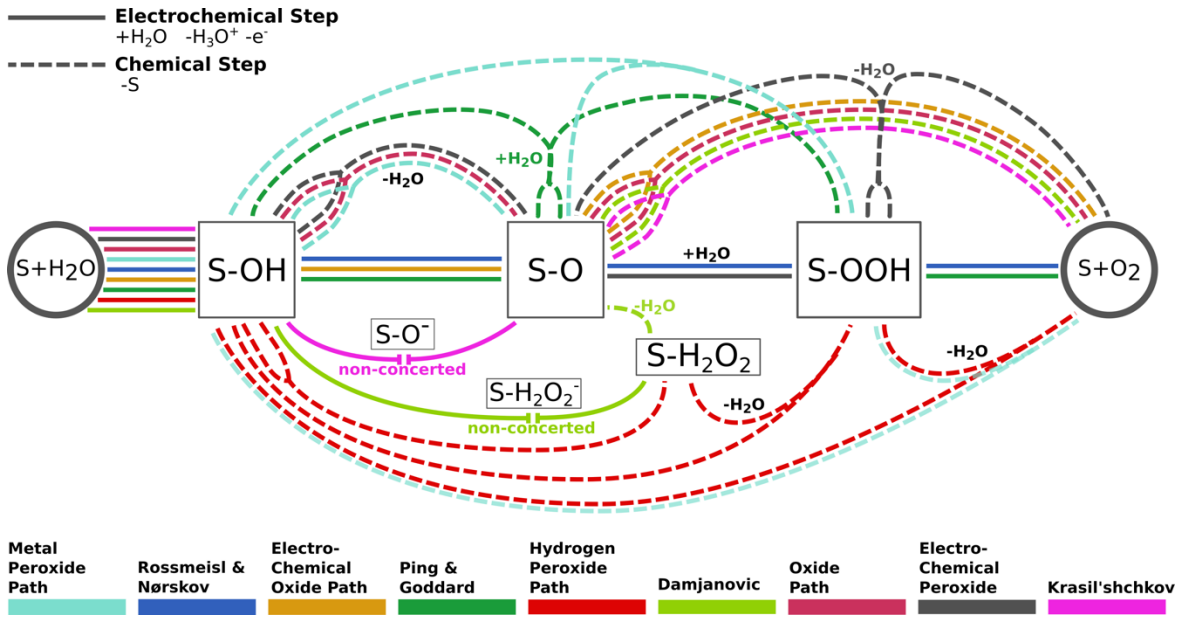

Figure 1.4: Compilation of mechanistic pathways in the oxygen evolution reaction; solid lines indicate electrochemical steps including an electron transfer, while dashed lines indicate chemical steps.

The advent of efficient ab initio methods, such as density functional theory (DFT), and a rapid increase in computational power in recent decades has made it possible to calculate the adsorption energy of intermediates and barriers for any given surface and transition state. The choice of surface, intermediates, and transition states still leaves some room for uncertainty, but using ab initio techniques for the mechanistic *Gedankenexperiment* can rationalize the choice of reaction pathways with thermodynamic insight. Nørskov, Rossmeisl, and Gauthier,[50–52] as well as Ping and Goddard[53] pioneered DFT studies on the rutile IrO_2(110) surface (except for [50]), which is the most stable surface of the most stable iridium oxide. Rossmeisl and Nørskov concluded that a large barrier is expected from direct combination of S-O. Ping and Goddard confirmed this and quantified: direct combination of S-O is either completely unstable or thermodynamically less favorable (the free energy cost at 1.53 V_{NHE} is 0.63 eV) than electrochemical peroxide formation. This finds experimental support by a study on iridium electrodes using ^{18}O isotope labelling.[54] All studies, therefore, used peroxide pathways. Their calculated overpotentials were in fairly good agreement with experiments. However, there were some slight differences in the reaction pathways. On the one hand, Nørskov, Rossmeisl, and Gauthier used concerted transfers of one electron and proton for each step (see Figure 1.4). The released protons were only considered from an energetic point of view and not in the calculated structure. On the other hand, Ping and Goddard simulated the actual reaction. They found that the proton in the step of the O-O bond formation between S-O and H_2O was transferred to a neighboring S-O site (see Figure 1.4), which makes the O-O bond formation a chemical step. Another interesting result from treating the proton explicitly was that the deprotonation of S-OOH was found barrierless and the authors suggested the O_2 release could be a non-concerted proton electron transfer step. No indications for stable S-O^- or S-(H_2O_2) intermediates were found. It can be summarized that DFT studies

on IrO_2(110) were able to simplify the scheme of possible intermediates and it appears quite likely that the reaction proceeds via a peroxide intermediate and not direct coupling of adsorbed oxygen.

Although the calculation of reaction pathways is undoubtedly a big step forward, some issues with current calculations are still causing uncertainty. First, charged intermediates or ions are largely avoided, because of their overly strong effect in small, periodically repeated structures. However, it cannot be excluded that they play a role in the mechanism of the OER. Second, the method used to apply the electrochemical potential limits the scope of the conclusions. The simplest and most efficient way is to calculate charge neutral systems before and after the process of interest and apply the potential via the energy of the electron at the computational counter electrode; a method that Norskov and Rossmeisl introduced.[51,55] This method can be used to identify a potential determining step, but cannot be used for kinetic arguments. Ping and Goddard performed the reactions ab initio using either constant charge, or constant potential calculation. In the former, the total charge of a given system is fixed and in the latter electric charge can be exchanged with a reservoir, i.e. a computational electrode, which ultimately defines the potential. They found that these two methods led to two different rate determining steps underlining the importance of the method for a proper interpretation. Third, a water overlayer and electrochemical double layer could interact with intermediates or transition states. The OER is a electrocatalytic process, so the interaction of the surface with the adsorbate will dominate the picture. This is true, but Gauthier indicates that a layer of water on the surface has a small effect on the adsorption energetics of adsorbed oxygen. However, they found a sizeable variation in free energy of S-OH (up to 0.3 eV) and S-OOH (~0.4 eV) by adding several bilayers of water.[52] Also Ping and Goddard found an influence of the solvent on the absolute energy (barriers barely changed) of the transition state in O-O bond formation by as much as 0.5-0.7 eV. The double layer could affect the energetics in two ways: by changing the energetics of transition states, as the solvent water does, and by adsorbing on the surface, which leads to the next issue. Fourth, the adsorption energy of intermediates depends strongly on other adsorbates, i.e. ions from the electrolyte, and the state of the surface.[56] Most DFT calculations, however, use simple, ordered, and fixed surfaces in order to limit complexity and computational cost of the calculations. The state of a catalytical surface and the coverage with adsorbed species, however, is likely to depend on the applied bias, which would lead to convoluted effects of "*adsorption of the reacting species, an electron-transfer step, a preceding chemical reaction, [and] coadsorption of a catalyst*" onto the overall rate.[56] This underlines the importance of the electrode and surface. The next three sections will give an impression of what is known about iridium (hydr-)oxide electrodes as well as its surfaces in the acidic OER and then shortly comment on the rate of the oxygen evolution on these surfaces.

1.3.3 Iridium (hydr-)oxide electrodes

Much of the discussion above focused on iridium (hydr-)oxides as catalysts in the OER. This is, because iridium metal is oxidized at potentials well below 1.23 V_{RHE}, the thermodynamic minimum of oxygen evolution. In extensive studies on metallic iridium electrodes, Buckley,[57] Gottesfeld,[58] Mozota, and Conway[59,60] were able to show with electrochemical methods that a surface oxide is formed irreversibly

at about 1.0 V_{RHE} and increases in thickness with potential cycling. Gottesfeld aptly phrased that "*even in the case of the noble-metal electrodes the 'science' of the OER is a 'science' of the oxides and their properties.*" Such anodic oxides were found to be of a low average density by McIntyre [61] (2.0 g/cm^3 instead of the 11.68 g/cm^3 expected for IrO_2 in the rutile structure), but with a large surface area caused by a high density of macro- and micro-pores. Conway added the observation that cracking occurs with increasing thickness of the anodic oxide. The large surface area and low density are in good agreement with the large capacitance values of anodic oxide films found in electrochemical studies.[57–60] In one of these studies, Conway suspected that pseudocapacity, which is capacitative behavior of an electrode caused by electrochemical surface reactions, can explain a major part of this effect.[60] X-ray photoelectron spectroscopy (XPS) of anodic films by Augustynski [62] and Hall [63] indeed observed hydroxides and water in thin and thick anodic films and thereby confirmed the hydrous nature of the anodic (hydr-)oxides. With further electrochemical oxidation by further cycling the films condense and become more oxidic.[62] This observation by Augustynski explained previous results of Buckley, who reported decreasing capacity with further oxidation of the electrode.[57] The condensation of the hydrous oxides to higher oxides (i.e. IrO_2) with further oxidation has been confirmed in a more recent study by Li,[64] in which the authors could reconstruct a three-dimensional surface structure of an oxidized metal electrode from atom probe tomography. Another study using XPS and inductively coupled plasma mass spectrometry comes to similar conclusions.[65] This means, anodic oxides range from hydrous structures with a low density to compact oxides. A schematic overview of this process is provided in Figure 1.5A.

A similar variety of oxide density is observed for thermally prepared electrodes. In early studies, Trasatti[66] and Ardizzone[67] describe thermochemical oxides prepared from a metal precursor, which were calcined in air at a range of temperatures. The calcination temperature in their study influenced the surface area, the charge storage capacity, electrocatalytic activity, and the acidity of the surface. It was later shown by X-ray diffraction (XRD) and electron diffraction that the crystallinity of comparable oxides correlated with calcination temperature.[68,69] At calcination temperatures >500 °C or long-term electrochemistry, a crystalline oxide forms, which is known to adapt the structure of the most common oxide of iridium, a rutile type IrO_2 structure. In fact, lower and higher oxides are often metastable and the superior stability of Ir^{IV} is thought to originate from relativistic effects, i.e. contraction of the 6s orbital,[70] which cannot be circumvented. However, involving hydrogen in the form of protons or water opens a wider stability window for (hydr-)oxides. A good illustration is provided by the Ir^{III} oxide: Ir_2O_3 has not been crystallized yet, but the layered $Ir^{III}OOH$ has been made.[71] The large variety of anodic and thermal iridium compounds mentioned above owe their stability to hydrogen.

But not only the stability and variety, also the chemical flexibility of these oxides and the variation in their electronic structure are brought about by hydrogen. By the exchange of hydrogen with the solution, the oxidation state of the oxide can be changed. An example is the hypothetical reaction

$$Ir^{III}(OH)_3 + n\,H_2O \rightleftharpoons Ir^{III+n}O_n(OH)_{3-n} + n\,H_3O^+ + n\,e^- \qquad \text{(Reaction 4)}$$

in which the oxidation state of Ir is changed by (de-)protonation. (Formally correct is (de-)hydrogenation, but (de-)protonation will be used instead for easier readability.) Reaction 4 is an electrochemical reaction transferring an electron and can therefore be accessed by electrochemical potentials. For a hydrous bulk material, such as the hypothetical $Ir(OH)_3$, this means that the electronic structure of the (hydr-)oxide depends on the applied potential. That this is indeed the case, can be shown by taking the example of the conductivity of hydrous anodic oxides. Gottesfeld calculated that the anodic layer oxidizes from an Ir^{III} to an Ir^{IV} (hydr-)oxide, while the conductivity of the layer improved with increasing oxidation state.[58] The latter was directly measured with the response of similar films to alternating currents [72,73] (see for example Figure 1.5B) and by in situ conductivity measurements.[74] Conway noticed the consequence of this change in conductivity as "*Due to the potential-dependent change in conductivity, the oxide can be 'turned on' or 'turned off' in the electrochemical sense, i.e. redox processes can take place in, or at the hyper-extended surface of the oxide film*". As a result, the cyclic voltammetry appears narrow at low potentials and the full capacity of the electrode leads to a wider cyclic voltammogram (CV) at high potentials. An example CV is given in Figure 1.5B, next to a Mott-Schottky plot, which indicates a gapped system in the narrow part of the cyclic voltammogram. This "switch" occurs reversibly at a potential of about 1 V_{RHE} and is accompanied by a coloring and bleaching of the anodic film.

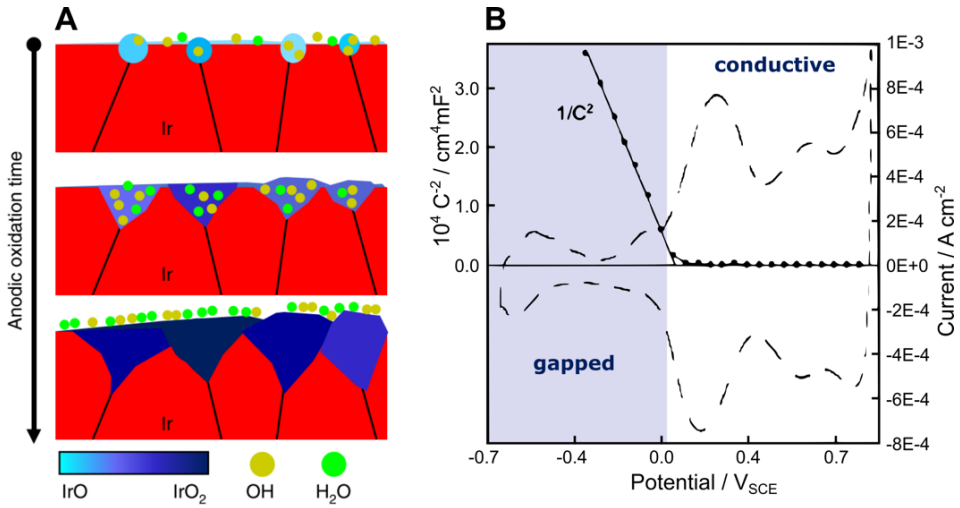

Figure 1.5: A) Schematic oxidation of metallic iridium films over short, long, and very long anodic polarization, obtained from reference 64; B) cyclic voltammogram and Mott-Schottky plot of an anodic film on iridium in a neutral phosphate buffer solution, adapted from reference 73; the potential is given in V against the saturated calomel electrode (SCE), which can be converted to V_{RHE} by adding ~0.7 V in the given solution.

A band-structure model can connect the change in conductivity to a changing oxidation state. Ir^{III} is expected to have a $[Xe]6s^05d^6$ configuration. This leaves the Fermi energy in a gap between the fully filled t_{2g} and empty e_g states in an octahedral coordination environment, which is quite common for iridium (hydr-)oxide (see next section). Oxidation to Ir^{IV} in the $[Xe]6s^05d^5$ configuration creates empty states in the t_{2g} conduction band. The hypothetic Reaction 4 with $n = 1$ would then formally describe a switch between a gapped Ir^{III} and conductive Ir^{IV} (hydr-)oxide by means of an electrochemical reaction

transferring a proton and electron. For each part of this example, experimental evidence could be found: first, Kötz showed the existence of a gap by ex situ valence band spectroscopy of polarized anodic films and found that the iridium band contributed virtually nothing at the Fermi level at 0.25 V_{RHE} (in the bleached state). On the contrary, the iridium band had more states at the Fermi level in the same film polarized at 1.5 V_{RHE} (in the colored state). Second, they also found fewer hydroxides on the surface of the oxidized film indicating a deprotonation reaction. Later, Lezna confirmed with in situ infrared spectroscopy that the coloration of anodic films is in fact accompanied by a deprotonation reaction.[75] Finally, it could be shown with the help of combined optical and coulometric measurements,[61] and by in situ X-ray absorption studies of the Ir L-edges [76,77] that the redox transition at about 1.0 V_{RHE} is related to oxidation the of Ir^{III} to Ir^{IV}. In summary, electrodes made of iridium (hydr-)oxide range from compact oxides to porous and hydrous types and their properties, i.e. electronic structure, chemistry, or catalytic properties, will depend on their initial state, their history of treatments, and on the applied potential. The influence of a support material was not discussed.

1.3.4 Active sites and their framework

In the previous section, the bulk properties of iridium (hydr-)oxide electrodes have been discussed, but most relevant for catalysis is the state of their surface. The adsorption energetics of intermediates and transition states on these surfaces determine the overall thermodynamics and kinetics of the reaction, respectively (see section 1.3.2.). The state of the surface is thus of paramount importance to the catalysis of the OER. The discussion begins with acid-base properties of iridium hydroxides, which is by definition a property of the surface (or interface) and is influenced by adsorbed impurities, the oxidative state of the surface, and degree of hydration.[78] Trasatti recognized the importance of acid base chemistry for oxygen evolution catalysts arguing that "*the acid-base properties of the surface of oxides are extremely sensitive to any change in the nature of surface coordination complexes. Their investigation can give evidence to small changes in the structure of the surface active sites*".[66] In a later review, Ardizzone and Trasatti summarized the findings of many studies and came to the conclusion that preparation method, e.g. calcination temperature, and the polarizing potential both influence the point of zero charge (pzc) of iridium (hydr-)oxides.[67] (The point of zero charge is the pH at which the surface is charge neutral.) In the case of thermal oxides the pzc was around 3, which relates to an acidic surface. If samples of comparable crystallinity were pre-treated at low potentials (i.e. 0.5 V), the surface became, with a pzc of 6.5 more charge neutral.[79] The process could be reversed by polarization to higher anodic potentials and reverted asymptotically to a pzc of 3. This means, within the donor-acceptor approach, that surface iridium in the oxidation state close to Ir^{IV} is quite electronegative compared to O^{-II} and the difference becomes much smaller for Ir^{III} and O^{-II} - a fact that takes on importance for the discussion of active sites below. These distinct acid-base properties also entail another crucial aspect of iridium (hydr-)oxide surfaces, namely that they are oxygen- hydroxide-, or water- terminated. This is widely accepted and has been corroborated by ab initio calculations.[51,53] This means that metal sites do not lie bare in solution, except for the short time of oxygen release during the catalytic cycle of OER. Ping and Goddard found that water adsorption on an empty site is essentially barrierless.[53] In turn, this

means that surface oxygen takes part in the first cycle of oxygen evolution reaction. A study by Fierro using differential electrochemical mass spectrometry and ^{18}O labelling showed that surface oxygen is involved in the oxygen evolution reaction.[54]

Measuring the point of zero charge offers information about the (Brønstedt) acid-base properties and maybe bond polarizations but does not allow for exchange of charge, which is the key element of electrochemical reactions. It has already been discussed above that bulk irdium (hydr-)oxides can be (oxidized) reduced by electrochemical potentials and that this process probably occurs via (de-)protonation. The same is true for surfaces and the hypothetical Reaction 4 can be formulated for the surface by using a general surface metal site S.

$$S^{+n}\text{–}OH + H_2O \rightleftharpoons S^{n+1}\text{–}O + H_3O^+ + e^- \qquad \text{(Reaction 5)}$$

Because of the kinetics involved, Reaction 5 is arguably more likely to occur than the hypothetical Reaction 4, because the barrier to reconstruct a bulk (hydr-)oxide is expected to be very large compared to the barrier for surface deprotonation, which is known to have small barriers.[53] The free energy of Reaction 5 depends on the chemical potential of the proton in solution (H_3O^+ on the right hand side). Consequently, the pH of the interfacial electrolyte is expected to alter the standard potential of Reaction 5. At equilibrium, the pH will thus also act on the potential against a reference electrode, such as a hydrogen electrode. By this property, it follows that the pH-dependent equilibrium potential can indicate whether Reaction 5 is relevant for real surfaces of iridium (hydr-)oxides. It is relevant: the experimental pH dependence of the open circuit (equilibrium) potential is 59 mV per unit pH for crystalline samples.[80,81] It thereby follows the so-called Nernstian behavior. For anodic [81,82] or electrodeposited films [83] a super-Nernstian behavior with values up to 80 mV per unit pH were reported. Reasons for the super-Nernstian behavior are still under discussion. A similar dependence on pH is observed in the reversed process, in which the pH shifts the center potential of oxidation features in cyclic voltagrams.[60,83,84] This approach is interesting, because the potential control allows the separation of different surface processes.[84,85] On the downside, the transient nature of cyclic voltammetry introduces the possibility of mass transport limitations and an applied potential leads to a double layer changing the interfacial structure and therefore local chemical potential of protons. In addition, anion insertion could play a role when forced by a potential. Anions were indeed found by electrochemical studies,[60,67,86] with the help of quartz crystal microbalance,[87] and by X-ray spectroscopy.[63]

It appears that iridium (hydr-)oxides have a versatile acid base chemistry, which is closely connected to the oxidation state of the surface and is thereby accessible by electrochemical potentials. The active sites are integrated into this oxygen-, hydroxide-, or water-terminated surface, but it is not yet clear what their local coordination environment is and what chemical properties they have. A broadly accepted fact is that the local coordination of iridium is octahedral, which is consistent with Raman spectroscopy on anodic iridium (hydr-)oxides,[88] Ir L-edge absorption of various stoichiometric iridium oxides,[89] and in situ investigations using extended X-ray absorption fine structure (EXAFS) of Ir L-edges

on anodic,[76] sputtered,[77] electrodeposited,[90] or thermochemical [91] iridium (hydr-) oxide electrodes. Slight distortion of the octahedra is not unusual and it even occurs in stable crystalline oxides, such as rutile type IrO_2.[90–92] Under applied potential, the average Ir-O bond length in the octahedra varies by about 0.05 Å per formal oxidation state of iridium.[76,77,90,91,93] The values ranged from 0.05 Å above and below the average bond length in cyrstalline rutile IrO_2 of 1.986 Å (given in [89]). However, these bond lengths should be understood in its context; the analysis of Ir L-edges for bond lengths averages over all iridium atoms, including bulk species. These different species vary in their Ir-O bond lengths, as Abbott showed by analyzing comparable iridium (hydr-)oxides with varying surface to bulk ratio and hydration.[91] Along similar lines, ab initio calculations by Ping and Goddard show Ir-O bond length variation of ~0.2 Å.[53] This bond length variation opens the possibility that the shift of the average could be caused by surface species only. However, the octahedral coordination is largely untouched by the applied potential.

Depending on how the octahedra are connected, the coordination of oxygen is either one-, two-, or three-fold. Which of those are active sites has not yet been determined, but ab initio calculations give a first insight. On an oxygen-terminated IrO_2(110) surface, Rossmeisl [51] and Ping [53] found with ab initio techniques that only terminal oxygen, with one bond to iridium, is a feasible active site for the direct coupling with water. Surface or bulk oxygen with a larger coordination number were not considered for the same reason. The large reactivity of terminal oxygen was explained by its radical character.[53] If the radical character is interpreted more broadly as an electron deficiency, also experimental evidence for a reactive electron deficient oxygen species on iridium was found: Pfeifer and Jones investigated the hole character on oxygen in iridium (hydr-)oxides by using experimental and computational O K-edge absorption from powders and ab initio model calculations, respectively. They found that oxidizing the IrO_2 model structure by iridium vacancies created electron-deficient oxygen species with a distinct absorption feature.[94,95] A commercial IrO_x powder exhibiting the predicted absorption feature was able to oxidize CO at room temperature.[96] The electron deficient species was consumed in this process. In a following study, they found in situ that anodic polarization of metallic iridium could create the same absorption feature.[97] Other computational findings support the importance of electron deficient oxygen for the OER.[53,85,98] The studies conclude that the chemistry of oxygen plays an important role in the catalysis of the OER.

While the evidence is consistent that hole character on oxygen is likely to be connected to the function of the active site, the scientific arguments for the oxidation state of the adjacent iridium site are more scattered. The in situ L-edge absorption studies mentioned above partly attributed bond lengths shorter than in the reference $Ir^{IV}O_2$ to an oxidation state larger than Ir^{IV},[76,90] but others reported a maximum oxidation state of Ir^{IV}.[77] A fourth study took a closer look at the width of the absorption white line and came to the conclusion that it originates from a mixed oxidation state of Ir^{III} and Ir^{V}.[99,100] Another explanation for the variation in width was given by Hillman et al.: the authors suggested that a wider distribution of Ir-O bond lengths causes the broadening, which is in better agreement with the different types of oxygen species (see above). More evidence for oxidation states higher than Ir^{IV} comes

from combined optical and coulometric measurements, which point towards a maximum change in oxidation state of more than one per iridium atom in the film, which would formally lead to a formal oxidation greater than Ir^{IV}.[61] Finally, the IrO_2(110) surface, which was calculated to be mostly deprotonated under potential relevant to oxygen evolution,[51,53] has two iridium sites being formally oxidized to +4 2/3 and +5 1/3. The descrepancy between formal and measured oxidation states could be explained by the strong hybridization between the electronic states of oxygen and iridium, which is well known for iridium oxides.[70,92,101] The resulting covalency leads to shared hole character on iridium and oxygen.[102,103] The strength of this effect is determined by the relative position of the O 2p and Ir 5d bands to the Fermi energy. By using iridium vacancies in IrO_2 structures [102] or high-energy surfaces of IrO_2,[103] it was found that oxidizing iridium beyond Ir^{IV} resulted in increasingly strong hole character on oxygen. In other words, iridium oxides enter a negative charge transfer regime for oxidation states above Ir^{IV}, because Ir 5d states are lower in energy than the O 2p band. This is in good agreement with the quite acidic surface of oxidized iridium (hydr-)oxide electrodes indicating that Ir^{IV} is quite electronegative compared to O^{-II}. The seemingly conflicting evidence about the oxidation state of Ir is resolved if oxygen is not strictly O^{-II} but is considered as actively involved in the redox processes of iridium (hydr-)oxides.

1.3.5 Description of the rate

Being able to predict the activity and rate of an electrode material is one of the most relevant goals of electrocatalysis, since it deals with the evolution of the desired product. For that reason, a number of different descriptors have been suggested. Their superordinate idea is the interaction of iridium with oxygen. This choice is well made, because the energy of intermediates and transition states on the catalysts surface will all depend on the interaction between iridium and oxygen (see section 1.3.2). A screening across the periodic table has indeed been predicted by several descriptors: First, Trasatti picked the activation energy for homomolecular isotopic O_2 exchange on the oxide surface as a measure for oxygen interaction and found fairly good scaling with their activity in the OER.[66] Second, in the same publication Trasatti also used the enthalpy of the lower to higher oxide transition as a descriptor for the activity in the OER and it resulted in a volcano-shaped behavior. To explain this shape, the Sabatier principle was used: the lower to higher oxide transition was interpreted as the adsorption of oxygen on an oxide. If the adsorbed oxygen is bound too strongly, the product will not be formed or will remain on the surface, and if it is bound too weakly, the intermediate might desorb before the reaction occurs. Third, for 3d metal oxide catalysts, the number of outer d-electrons was found to describe the activity in the OER.[104,105] Fourth, the adsorption energies of O, OH, and OOH computed with DFT and linear combinations of the same can be used to describe the trends in the activity of oxygen evolution catalysts.[51,52,106–108] It is currently the most common method and roughly captures trends in the periodic table. Fifth, it has been suggested that the more complex parameters of the charge transfer, which can also be calculated ab initio, describe the activity of 3d metal oxides more accurately than the previous method.[109,110] The latter approach would agree with the apparent importance of (negative) charge transfer for the active site discussed in section 1.3.4.

The descriptors of metal-oxygen interaction above are useful to provide a rough idea of what energetics to expect for a given mechanism and active site. The actual description of the rate, i.e. the current-potential characteristic, is more challenging. Schmickler goes as far to state in his book: "*There is no general law for the current-potential characteristics of inner-sphere reactions.*"[56] The reason for the difficulty of arriving at such a law, is that inner-sphere reactions, which occur on the surface of the catalyst, are sensitive to a multitude of effects ranging from the state of the surface (i.e. coverage with intermediates, adsorbed ions, and coadsorption of a catalyst), interaction between adsorbates, over the influence of the solvent or electrical double layer, to the rate of the electron transfers. All of these influences are expected to depend on the potential and complicate the description of the rate. For one of these influences in the enumeration above, namely the state of the surface, tentative computational studies evaluate its influence on the rate. In one study on mixed ruthenates, Halck and Rossmeisl found that involving a neighboring site as a proton acceptor can positively influence the energetics of the reaction on the active site.[111] Similarly, in another study by Ping and Goddard on IrO_2(110) it was reported that one proton was transferred to a neighboring oxygen site during the dynamic simulation of O-O bond formation.[53] They also found that the degree of protonation on the surface influenced the energy of the transition state for O_2 release. The protonation dynamics on the surface, hence, matter for the rate. These studies are a hopeful beginning in estimating the influence of adsorbed species on the current-potential characteristic. However, many factors influencing the rate are still unknown and computational as well as experimental evidence needs to follow. This work is an attempt to contribute to this open field with a combination of surface-sensitive operando spectroscopy and molecular dynamic calculations on iridium (hydr-)oxide surfaces.

1.4 Scientific objective

This work aims to answer these questions:

How do iridium (hydr-)oxide surfaces change under applied potential and in which way do these changes affect the oxidation of water to molecular oxygen?

As laid out in the previous sections, iridium (hydr-)oxide surfaces have a complex acid-base chemistry and the actual transfer of protons is coupled to oxidation and reduction reactions on the surface (see Section 1.3.4). The degree of surface protonation is thus potential dependent. Computational results, in turn, point out that surface protonation influences the energies of intermediates and transition states in the oxygen evolution reaction (see Section 1.3.5). This situation leads to convoluted effects of the electrochemical potential on the reaction rate. The objective of the present study is to learn more about the active surface and separate out its effect on the oxygen evolution reaction. The task consists of four parts answering the questions

Q1 Which species occur on the surface?

Q2 How can they be detected?

Q3 How does their coverage change with potential?

Q4 In which way do they influence the rate of the reaction?

Finding answers to these questions is a staggering challenge. The catalytic reaction occurs at the picosecond time scale and at the nanometer length scale, but in a very complex environment including an electrochemical double layer, adsorbates, liquid solvent, the electrode mesostructured, and so on. The rate of the oxygen evolution will depend on these factors, since energy changes of the transition state in the order of milli-electronvolt will influence the overall rate. In order to fully understand the OER, the reaction needs to be described at this level of precision regarding space, time, energy, and complexity. Capturing all the criteria with just one technique is near impossible. Combining techniques covering a part of this field, however, creates uncertainty if their correlative overlap is too small. The scheme in Figure 1.6 is an attempt to visualize the criteria, how they are matched by a technique, and how large the correlative overlap between the techniques is. It contains one axis for each criterion, while the outer end serves as a good description of the OER. A technique is represented as a colored area being the measurable output of the respective technique. On the basis of this picture, the remaining part of the passage will discuss the scientific approach of the present work. The discussion does not attempt to be exhaustive or generally applicable but will give an overview of the benefits and limits of the scientific approach.

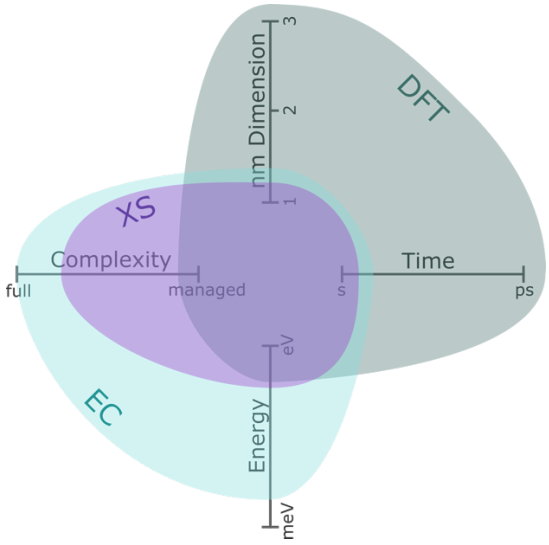

Figure 1.6: Criteria for atomistic investigations of the OER, the coverage of density functional theory (DFT), electrochemistry (EC), and soft X-ray spectroscopy (XS), and their correlative overlap; "nm Dimensions", for example, refers to the number of dimensions the technique can investigate on a nanometer length scale.

In the present work, the above questions shall be addressed with a combination of operando X-ray spectroscopy and density functional theory (DFT). The latter is an ab initio method, which allows full

control of the atomic surface structure and it can be performed dynamically at the picosecond time scale. The power of DFT is to predict the energy of the designed system at many levels, ranging from electronic states to total energy of the periodic system. This allows to compute spectra, surface stability, the energy of a transition state, and many more properties that are otherwise difficult to access on an atomic scale. The limit of DFT calculations lies in the complexity of the system. Incorporating a counter electrode, a liquid solvent layer, anion adsorption, or calculating large systems, are challenging to implement or realize.

X-ray spectroscopy is an experimental method and captures the complexity of a catalyst surface. It is, therefore, well suited to test hypotheses. The correlative overlap of the ab initio with the experimental technique is the length scale and the energy precision: First, using soft X-rays reduces the probing depth to only a few nanometers beyond the surface, resulting in a nm-range sensitivity in one dimension. Laterally, X-ray spectroscopy usually probes several hundred micrometers of the sample and the complexity of the system is captured in average. Second, the energy precision in X-ray spectroscopy is in the order of a tenth of an electronvolt (eV), which is roughly similar to what ab initio methods can provide.

The accompanying information of in situ spectroscopy on electrocatalysts is the potential control and the current response of the measured system. Since electrochemical reactions occur at or near the catalyst surface, the current response is very surface sensitive. However, remote properties of the system including resistances, the counter electrode performance, or mass transport play a role for the current response, too, making it a complex measure. On top of that, the current response, or rate of reaction, is sensitive to meV-changes in the energy of the transition state(s). Electrochemistry, thus, is a surface sensitive measurement with sensitivity to minute energy changes, but convoluted influences complicate the interpretation.

In summary, combining ab initio techniques with surface-sensitive operando X-ray spectroscopy fulfills the criteria necessary for a meaningful investigation of the OER at an atomic scale and their correlative overlap should allow for coherent studies. Informed by this overview, the next two sections will discuss how Q1-Q4 can be addressed with DFT (Section 1.5) and X-ray spectroscopy (Section 1.6). It should be noted, though, that parts of the answers to Q1-Q4 are already discussed and partly answered in the literature: see Section 1.3.4 for Q1, or Section 1.3.5 for Q4.

1.5 Density functional theory (DFT)

Since the postulate of the Schrödinger equation for the electronic structure of any system of N electrons and fixed nuclei, i.e. the Born-Oppenheimer approximation, much effort was focused on finding ways to approximate the ground state energy of many-electron systems ab initio. Analytical or correct solutions are not feasible. One approach stands out as the most successful for ab initio calculations of solid state properties and it has made its way into calculation of molecular systems and

reactions: density functional theory, or DFT. The following description of the ab initio methods were guided by references [112] and [113].

The fundament for DFT was laid by Hohenberg and Kohn,[114] who demonstrated that the density uniquely defines the wave-function, and the Hamiltonian and thereby the ground state energy of any N electron system. Further, they showed that any density different from the correct density has a higher ground state energy, opening the possibility of calculating the correct energy by variation of the density. A remaining question was in which way the kinetic energy or the electron-electron interaction, i.e. exchange and correlation, depend on the density. One important step in this direction was the approach by Kohn and Sham,[115] in which a system of N non-interacting electrons in N natural spin orbitals was used to calculate the largest part of the kinetic energy exactly. The difference to the true kinetic energy in an interacting system and the contribution from exchange and correlation of electrons, which are small and unknown, were pooled in the so-called exchange-correlation potential. This treatment breaks down the problem of solving the total equation to sets of one-electron problems in an effective potential created by all electrons. In a self-consistent reduction of the energy by variation of the density these approximations make it possible to calculate the ground state energy with good accuracy, since only the exchange-correlation potential needs to be approximated.

Optimizing the functional for the exchange correlation term is an ongoing discussion and the effectiveness of the functional depends on the material properties under consideration. The discussion of the exchange correlation functional will therefore be restricted to what is already shown to work well for iridium (hydr-)oxides. The most studied case is rutile type IrO_2, because it is the only stable iridium oxide. The most extensive comparison of functionals was performed by Ping, Galli, and Goddard.[92] They compared the Perdew-Burke-Ernzerhof (PBE) functional [116] with a Hubbard-U corrected version and the two hybrid functionals PBE0 and B3PW91, and they found that PBE gave the best agreement between the calculated density of states (DOS) and the experimental valence band spectra of IrO_2. Their conclusion finds support from more publications in the field comparing results using the PBE functional to experimental lattice constants,[70,117,118] the work function,[117] or X-ray absorption spectroscopy.[94,95] The very similar functional PBEsol, which is PBE adjusted for solids, gave a DOS in excellent agreement with valence band spectroscopy.[101] For this, it can safely be assumed that the generalized gradient functional by Perdew, Burke, and Ernzerhof adequately captures the electronic properties of IrO_2. This conclusion is expected, since the metallicity of IrO_2 is dominated by extended d-orbitals with great overlap.[92] As a consequence, the density of valence electrons is delocalized and slowly-varying. The generalized gradient approximation (GGA) and, more specifically, PBE is known to work for such systems.[116,119] The delocalization error, which is a common problem for DFT,[120] should therefore be small in IrO_2, but it is under discussion if the compensation of the same should be included by a Hubbard-U correction or hybrid functionals.[92,121]

The choice of a basis set and core potentials for the construction of the wavefunction is also consistent. All of the above studies used plane wave basis sets and ultrasoft pseudopotentials, respectively.[70,92,94,95,121] Ultrasoft pseudopotentials are beneficial, because they, first, limit the number

of electrons actively involved in the calculation by static treatment of core electrons, and, second, they limit the number of plane waves which are needed to represent the core potential (by smoothening the otherwise sharp core potential).[122] In addition, the plane-wave approach greatly improves calculation efficiency of periodic systems by utilizing fast Fourier transformation.[123] The above studies indicate that including scalar relativistic effects is advisable but a fully relativistic description by including explicit spin-orbit coupling changes the energies only slightly.[70,92,101]

Having outlined a proper combination of methods to calculate ground state energies of conductive iridium oxides ab initio, the focus of the remaining passage deals with how the calculation results can help answer question Q1-Q4. The discussion will start out with the calculation of core hole spectroscopy. The latter is the main tool in this work and comparing experimental results to ab initio calculations helps to de-convolute and interpret them, addressing the question of how surface species can be detected (Q2). The discussion will then move on to computational electrodes, which establish a link between the electrochemical potential in the experiments and the potential of the calculated system. This link is useful to the aim of understanding how the coverage with surface species changes with potential (Q3). Finally, a short description will be provided on how ab initio calculations can yield the energy of a transition state and thereby the barrier to a reaction. The barrier height is essential to approach the question of how the state of the surface influences the rate of the OER (Q4).

1.5.1 Ab initio spectroscopy

Core level spectroscopy is the excitation of core electrons into unoccupied states (X-ray absorption spectroscopy, or XAS) or the continuum (X-ray photoelectron spectroscopy, or XPS) with X-rays. This process brings the electron configuration from its initial ground state to a final excited state with a core hole. Describing excited states within the Kohn Sham framework can be done exactly,[124] but the full description is not always necessary. It has been shown that differences between Kohn Sham eigenvalues of the ground state and of the excited state have a physical meaning in that they are a zeroth order approximation to the electron-electron interaction.[124] This approach is known as the ΔSCF method, referring to the difference in two self-consistent field (SCF) calculations. ΔSCF gives single-point excitation energies for any given atom including final state effects. The comparison to (absolute) experimental values can be done by proper referencing. It has been shown that ΔSCF works well for molecules and extended solids,[125,126] and that it is able to reproduce experimental XP spectra.[127]

XAS is the resonant excitation of core electrons into unoccupied states resulting in a strongly interacting electron-hole pair. Calculation of XAS thus requires the potential energy surface of the unoccupied states and a proper treatment of the electron-hole interaction of the final state. Two methods to calculate the final state will be used in this work. First, the full set of Kohn-Sham wavefunctions and eigenvalues are calculated for the ground- and the excited state. The probability for the transition of an electron from a core level at the ground state into an unoccupied state of the excited system then gives the absorption spectrum. This method works well for materials with weak electron-electron interaction and, more generally, for delocalized final states, and has been shown to

be in good agreement with experiments for K-edge absorption.[128,129] Second, the solution of the Bethe-Salpeter equation [130] can be used to account for the electron hole interaction and to calculate the final state.[131,132] The benefits of this approach are that only the ground state wavefunctions are needed to solve for any given excitation. The energy alignment of both methods is done using ΔSCF and referencing with experimental spectra.

Calculating X-ray spectroscopy can help to interpret and deconvolute experimental spectra from active surfaces. Particularly useful for the present work is the O K-edge absorption of surface oxygen species on iridium (hydr-)oxides, because they exhibit well separated and relatively intense pre-edge features [97] (see also Section 1.6).

1.5.2 Computational electrodes

Another useful interface between experimental results and ab initio calculations is the electrochemical potential. As described above, the electrochemical potential influences the electronic structure of iridium (hydr-)oxide electrodes (Section 1.3.3), the coverage of adsorbates (Section 1.3.4), and the rate of the OER. It is thus of central importance in answering questions Q3 and Q4. The simplest way to recover the potential of a surface reaction is by the chemical potential of hydrogen. This procedure introduced by Nørskov and Rossmeisl [55] is applicable to any reaction involving a coupled transfer of an electron and a proton, and directly relates the potential to the standard hydrogen electrode (SHE), which is convenient since the SHE is a widespread reference in electrochemical measurements. The calculation is purely thermodynamic in that it requires only the full ground state energy before and after the reaction, which can be obtained routinely by DFT. The actual reaction including the charge transfer using solvated protons and electrons is not treated explicitly. The potential is calculated after the fact. This simple and pragmatic approach has a low computational cost and has been shown to be effective in predicting the experimental activity trends of oxides in the OER.[51]

If the aim is to describe the thermodynamically limiting step and its potential, the above method is useful, but explicit treatment of the potential is needed to describe biased interfaces and the actual charge transfer. The latter two are of particular importance in the search for transition states and the rate of the reaction (Q4). A computationally efficient method was proposed by Otani and Sugino.[133] They introduced an effective screening medium as a counter electrode, which balances the charge of the biased working electrode, i.e. the material of interest. The potential is applied by either fixing the (counter) charge, or by allowing the exchange of electrons with a reservoir at a defined potential.[133,134] The latter is a relative entity but can be linked to the standard hydrogen electrode by the previous method of Nørskov and Rossmeisl.

1.5.3 Molecular dynamics and transition states using DFT

Approaching the kinetics of the OER (Q4) requires the energy of a transition state. This task can be done routinely if all atomic positions of the transition state were precisely known. If they are not, the reaction pathway needs to be computed. The solution of this problem involves a time- and temperature-dependent calculation of the total energy and of atomic forces. Since this is a complicated

endeavor, it will only be outlined here. Temperature will be implemented with stochastic (non-local) coupling to an external bath,[135] molecular motion will be implemented by small steps in time and electronic ground states (Born-Oppenheimer molecular dynamics), and the energy surface of the reaction will be determined by the climbing image nudged elastic band method.[136]

All theoretical calculations in this work were performed by either Travis E. Jones or Woosun Jang.

1.6 X-ray spectroscopy

X-ray spectroscopy is the main tool in this work to investigate the catalyst surface under applied potential. The technique is particularly useful to answer questions Q1-Q3 because it can be

X1 element specific,

X2 surface sensitive,

X3 sensitive to the oxidation state or hole density, and

X4 informative concerning the electronic structure of the material or surface.

While properties X1 and X2 help to identify surface species (Q1 and Q2), X3 and X4 give insight on how these species oxidize with potential (Q3) and what the active state of the surface is. However, X1-X3 can only be accomplished if certain prerequisites are fulfilled, such as using soft X-rays and detecting electrons. The remaining part of this section seeks to identify these prerequisites and the fundamental origins of X1-X4. The section about X-ray spectroscopy is based on and guided by the references 137, 138, 139, and 140.

At the essence of X-ray spectroscopy is the interaction of X-rays with matter. X-rays are elastically and inelastically scattered, which is weakly dependent on the atomic number and the energy of the X-rays. While these processes are valuable for X-ray diffraction, for example, scattering mostly influences X-ray spectroscopy in that it contributes to the background of energy-dependent X-ray absorption. The absorption of X-rays is the second important process and it describes the complete absorption of a photon by any electron in matter bound by an energy smaller than or equal to the photon energy. The electron is then excited into an unoccupied state. This state can be, first, a local state, such as atomic orbitals, molecular orbitals, Rydberg states, or the atomic contribution to the valence band in a solid, and, second, a state in a continuum, such as the Fermi sea of the conduction band in a metal, or vacuum (see Figure 1.7A for a scheme). Also, multi-electron excitations are possible, during which the main excitation is accompanied by small excitations from occupied into unoccupied states close to the Fermi energy, as in a conduction band of metals.

Any of the above excitations creates one electron hole or more, as is the case with multi-electron excitations, which leaves the atom in a state of high energy. The energy is lowered via charge compensation, referred to as screening of the electron hole. This screening charge originates from the remaining electrons of the absorbing atom which can spatially contract in order to screen the electron

hole. Additional charge can be donated by a conduction band (metallic screening) or by neighboring atoms (charge transfer). The energy cost of these screening processes differs with each process and material. And since the final state of the excitation is reached after the screening has occurred, X-ray spectroscopy is inherently sensitive to the electronic structure of the material (X3). Metals, for instance, can make use of the efficient metallic screening while insulators can only screen atomically or by charge transfer.

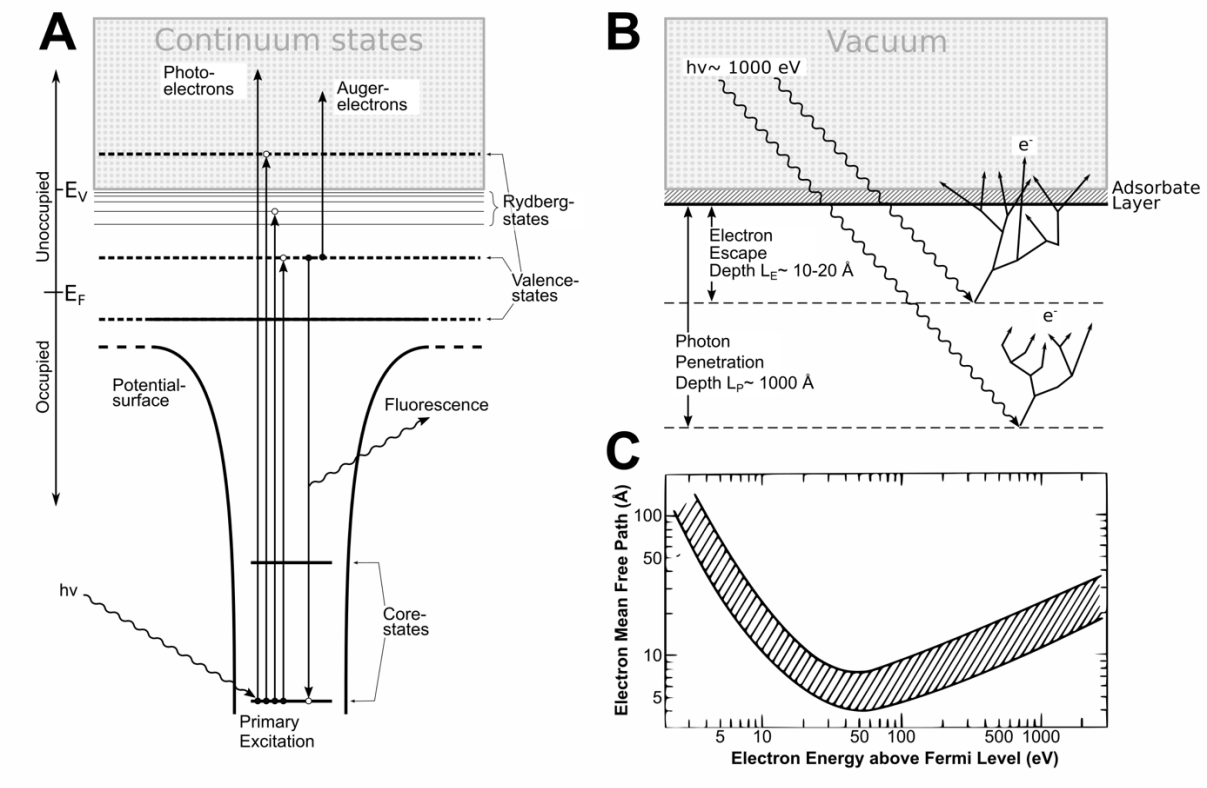

Figure 1.7: A) schematic photon absorption of a core electron and its excitation into unoccupied continuum-, Rydberg-, and valence-states; Secondary processes in form of Auger- and fluorescent relaxation are also given; B) schematic of the electron escape depth for excitations with 1000 eV; the deeper photon penetration depth and the shallower electrons escape depth are illustrated by electron cascades from secondary processes; C) electron mean free path in solids as a function of the kinetic energy. Figures drawn in style of reference 137.

The probability of exciting an electron from its initial state into a final state is given by Fermi's golden rule, which is

$$P_{if} = \frac{2\pi}{\hbar} \left|\langle \psi_f | \bar{V} | \psi_i \rangle\right|^2 \varrho_f(E) \qquad \text{(Equation 7)}$$

In this formulation, the operator $\bar{V}$ is a perturbation to the wave function of the initial state ψ_i. The overlap integral of the perturbed state with the final state wave function ψ_f multiplied with the energy density of the final state $\varrho_f(E)$ then gives the probability for the excitation. The total cross section for the absorption of X-rays is given by P_{if} divided by the energy flux of the radiation. Equation 7 shows that the interaction of X-rays with the initial state, its overlap with the final state, and the energy density of the final state contribute to the probability of absorption.

The decay of the excited state occurs after a limited lifetime, which in turn gives rise to uncertainty in their energy by Heisenberg's uncertainty principle. There are two decay processes. In both of them, the hole is filled by an electron from an occupied state with higher energy. The energy gain of this electron is then emitted either as a photon or as another electron (see Figure 1.7A). These relaxations are called fluorescence or Auger decay, respectively. Which of the two relaxation channels statistically occurs, depends on the atomic number of the observed element: While light elements tend to emit electrons, heavier ones have a tendency to emit photons when relaxing. These secondary photons and electrons cause an avalanche (Figure 1.7B) if they are absorbed or inelastically scattered, respectively. As a result, more electrons or photons are emitted than have been initially excited or absorbed.

Since the method in this work aims to be surface sensitive, it is of interest to discuss the probing depth of these emission processes. For energies larger than 50 eV, X-rays have larger mean free paths than electrons. At the energy of 1000 eV, for example, the mean free path of photons is about 1000 Å in most materials, while it is 10-20 Å for electrons (see Figure 1.7B). The dependence of the electron's mean free path against its kinetic energy is provided in Figure 1.7C. The mean free path increases towards large kinetic energies. At small kinetic energies this trend is reversed by electron tunneling and a minimum occurs at about 50 eV with a mean free path of about 4-9 Å. The detection of primary electrons and the use of soft X-rays (100-1000 eV) can thus provide surface sensitive information (X2). However, the avalanche triggered by the excitation carries information from deeper than the primary electron (see Figure 1.7B), which can extend up to 65 Å in the case of metallic aluminum. Hence, the electron signal varies in information depth. For this reason, the probing depth of the techniques used herein, namely XPS and NEXAFS, will be discussed separately later in the text.

Another benefit of X-ray spectroscopy is that it can probe core-levels, which are discrete and narrow states with low energy or high binding energy. The energy of these states is characteristic for a given element, which makes core-hole spectroscopy element specific (X1). This is also true for Auger-electrons, for which two element-specific states determine the energy of the outgoing electron or photon (see Figure 1.7A).

In summary, X-ray spectroscopy is, first, inherently sensitive to the electronic structure of the material (X4), because final state effects are involved, second, surface sensitive (X2), if soft X-rays and electron-detection are used, and third, element specific (X1), if core levels are probed. The following two subsections discuss the way in which the above processes (e.g. primary electrons, secondary electrons, the transition probability, or screening) contribute to the signal of the actual measurements and what information they carry. Two types of spectroscopy were used in this work and will therefore be discussed: X-ray photoelectron spectroscopy (XPS) and near-edge X-ray absorption fine structure (NEXAFS).

1.6.1 X-ray photoelectron spectroscopy (XPS)

When an electron is excited into the continuum of vacuum, it is called a photoelectron. It is a primary electron with a kinetic energy of

$$E_{kin} = h\nu - \{E(N-1) - E(N)\} - \Phi \qquad \text{(Equation 8)}$$

while $h\nu$ is the energy of the photon, $E(N)$ and $E(N-1)$ are the energies of the initial and final states relative to the Fermi energy, and Φ is the work function. The difference between the final and initial energy is called the binding energy of an electron. The kinetic energy of Equation 8 and, at a given binding energy and work function, the photon energy determine the probing depth of XPS. A synchrotron X-ray source with a tunable excitation energy thus allows for variable probing depth. The sensitivity of the technique is proportional to the number of species in a given probing volume. In the present work these properties have been used to measure surface sensitive core level XPS (X1 and X2).

The oxidation state of the probed atom (X3) enters Equation 8 via $E(N)$ and is hence measurable. This is so because the initial state $E(N)$ of any given core level changes with the electron density in the valence shell: analogous to atomic screening of a final state, all electrons compensate the change in electron density and contract or expand in order to lower the total energy. Removing charge from the valence shell, for example, would cause the core electrons to contract and lower their energy. An oxidation would, thus, lead to a larger binding energy. This initial state effect is called the chemical shift and it can be a useful measure of the oxidation state (X3) – a property which contributes to the popularity of XPS. However, final state effects can enhance, weaken, or even reverse the trend set by the chemical shift.

Screening processes of the final state enter Equation 8 via $E(N-1)$ and thus also influence the measured binding energy. Atomic screening always occurs; the metallic and charge transfer screening act on top of it. Metallic screening, in which the Fermi sea screens the core hole, is most efficient, since reorganization of charge within the valence band has a low energy cost. The energy of the final state $E(N-1)$ is comparatively low and the binding energy, which is the difference between $E(N)$ and $E(N-1)$, becomes smaller. Less efficient is the screening via charge transfer from nearest neighbors because the donated electrons are bound more strongly than in a Fermi sea. Charge transfer is, nevertheless, advantageous over mere atomic screening. These three different screening mechanisms would appear at three different binding energies, thereby leading to three possible contributions within a spectrum. All three contributions are possible in metals, while only charge transfer and atomic screening are available to semiconductors and insulators. This difference in behavior, depending on the electronic structure of the material, is reflected in XPS, making it a valuable tool for investigating the electronic structure (X4).

So far, XPS spectra have been viewed as delta-functions with a defined binding energy. Measured spectra have an energy dependent intensity distribution. Universal contributions to their width are the lifetime broadening of the final state, giving rise to a Lorentzian distribution, and instrumental broadening in form of a Gaussian distribution. In addition, secondary and inelastically scattered electrons create a tail towards smaller kinetic or larger binding energies, which results in an increase of the background signal with binding energy (see Figure 1.8). The shape of this background is not

known precisely, necessitating the use of approximations. In metallic systems, electron scattering is particularly pronounced, since the delocalized electrons scatter excited electrons with a large probability. As a result, small excitations from occupied into unoccupied states close to the Fermi energy are triggered and lead to a line shape which is asymmetrically broadened towards larger binding energies. If the DOS around the Fermi energy is flat, the asymmetry is smooth and can be described by the so-called Doniach-Šunjic function.[141] In case the DOS around the Fermi energy is structured, the line shape becomes more complex.[142,143] The line shape thus carries information about the electronic structure near the Fermi energy (X4).

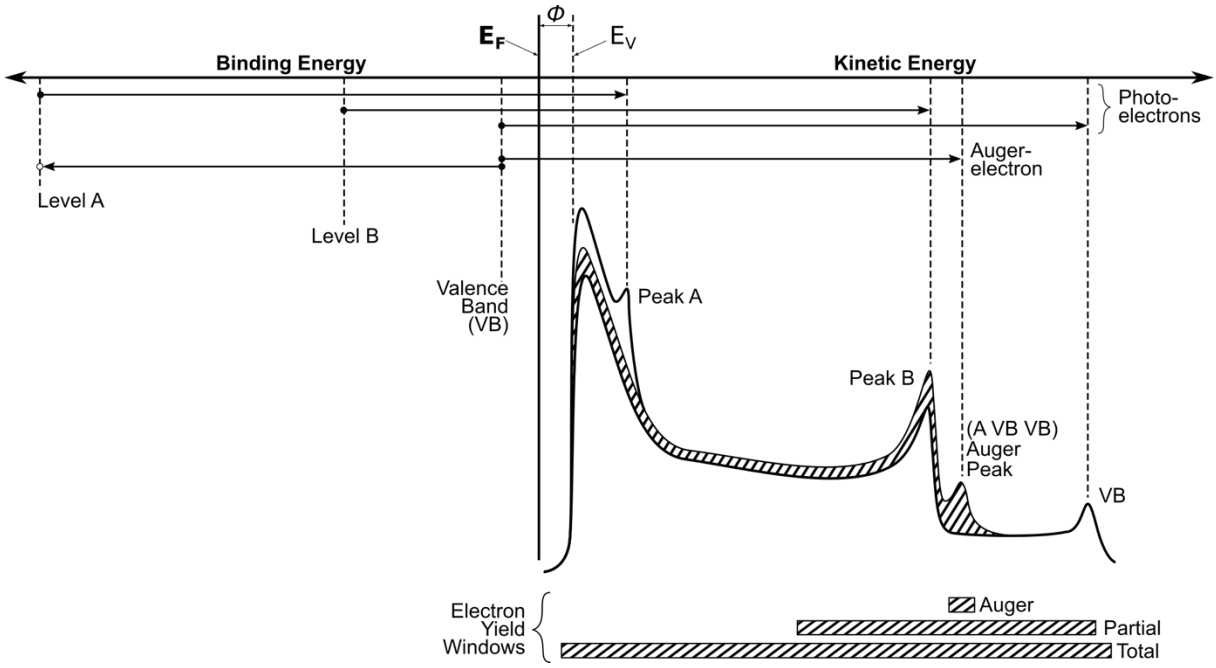

Figure 1.8: Scheme of a typical XPS spectrum and background on an energy scale relative to the Fermi energy E_F; electron excitations occur from core levels A and B or the valence band on the left into the continuum on the right above the vacuum level E_V; the energy difference between E_F and E_V is marked as the work function ϕ; regions of signal integration for absorption spectroscopy are given below as Auger-, partial-, and total electron yield; the figure was drawn in the style of reference 137.

Additional contributions to the energy shift and the line shape of XPS peaks may also appear but are not essential for the model used in this work.

In short, XPS can be element specific (X1) and surface sensitive (X2) if the excitation of a core electron is chosen in such a way that the electrons are slow and have a small probing depth. The line shape and position of XPS features give some indication of the oxidation state (X3) and the electronic structure (X4) near the Fermi energy of the material. However, the large number of contributions and overlapping effects can be difficult to disentangle, which limits the accessibility of the information. Ab initio techniques (see Section 1.5) can help the deconvolution. Further clarity can be achieved by examining the X-ray absorption as a complementary technique to XPS.

1.6.2 Near-edge X-ray absorption fine structure (NEXAFS)

X-ray absorption is the excitation of an electron from an occupied state into a state that is unoccupied but still bound. The probability of such a transition (see Equation 7) varies with excitation energy and the related total cross section (see Section 1.6) leads to an absorption spectrum. If the occupied state is a core level, the technique is element specific (X1). In such a case, a core electron is excited into either a discrete state or a continuum state.

Examples for discrete states are atomic states, atomic contributions to a band or molecular orbital, or Rydberg states (Figure 1.7A). Excitations into such states are resonant and are expressed as distinct features. Similar to the broadening of XP spectra, the line shape is broadened by the life time of the final state and by the instrument with a Lorentzian and Gaussian distribution, respectively. Also, multi-electron excitations are possible, during which the dominant excitation is accompanied by small excitations between states close to the Fermi energy. Regardless of its shape, the resonant excitation into discrete states follows the so-called sum rule, according to which the integrated intensity is proportional to the number of holes.[144,145] The approach works for 2p to 3d transitions in 3d metals [146] and holds for iridium-compounds in the case of 2p to 5d transitions,[89] but is expected to hold for transitions from 1s orbitals, too. This phenomenon is valuable for the study of surfaces catalyzing the OER because the OER is an oxidative process and the oxygen intermediates on the surface are thus expected to have a more intense absorption feature. As a result, the sensitivity towards these intermediates is greatly improved and the oxidation of oxygen can be tracked (X3).

The excitation into a continuum, such as the conduction band of a metal or vacuum, results in step-like functions, which lead to the so-called edge jump far away from the absorption onset. The height of the edge jump is proportional to the number of absorbing atoms at a given probing depth (see below for a discussion on probing depth).

More generally, the discrete and continuum states can be summarized as the DOS of the absorber, or projected DOS. The fine structure of the absorption can therefore resemble the projected DOS of the absorber in the presence of a core hole. This is true for absorption spectra of the small and centro-symmetric 1s orbitals, or K-edge absorption, as it has been shown for silicon or oxygen K-edges.[129] NEXAFS of K-edges can thereby act as a measure of the unoccupied and projected DOS (X4).

Additional resonances occur from scattering processes of the X-rays or the excited electrons with the local environment of the absorber, from which structural information can be obtained. Scattering contributions will not be mentioned further, since they are not essential to the discussion in the present work.

It remains to discuss the probing depth of the technique, which will be based on the conclusions of Section 1.6. Several detection methods are available to X-ray absorption. First and foremost, the direct absorption, which is the ratio of the beam intensity before and after the sample. This method measures the true absorption, but surface sensitivity is mostly determined by the sample morphology. Second, fluorescent photons (see Figure 1.7A) can be detected. They originate from secondary processes but

are proportional to the primary absorption. This method allows for more flexibility in the choice of sample, but the technique has a probing depth comparable to the penetration depth of the initial beam, making it mostly sensitive to the bulk. Third, the detection of secondary electrons can be used, which is more surface sensitive (X2), due to the smaller escape depth of electrons compared to photons (Figure 1.7B).

Three modes of electron detections are available; all of them are proportional to the true absorption: the total electron yield (TEY), the partial electron yield (PEY), and the Auger electron yield (AEY). The TEY collects all available primary and secondary electrons (see Figure 1.8), which provides a good signal to noise ratio at an intermediate probing depth of about 50-150 Å for soft X-rays (see Section 1.6). The surface sensitivity can be improved by PEY, collecting electrons from a smaller energy range and cutting off the largest part of the secondary electrons at low kinetic energies (Figure 1.8). This choice trades in a smaller overall signal for an enhanced signal to background ratio. The most surface sensitive mode of electron detection is the AEY, which collects Auger electrons from the absorbing species in a narrow energy window matching the fixed kinetic energy of Auger electrons (Figure 1.8). AEY can achieve a probing depth below 10 Å for Auger electrons of low kinetic energy (~50 eV), but photoelectrons may contribute unwanted signal intensity to the AEY absorption signal.

In short, X-ray absorption can be element specific (X1) if core levels are probed and can be surface sensitive if electrons are detected (X2). Integrated intensities of resonant absorption features are proportional to the hole density, which provides information about the oxidation state (X3). The shape of K-edge absorption spectra resembles the projected DOS in the presence of a core hole, which allows direct insight into the unoccupied states of the probed species (X4).

In conclusion, the properties X1-X4 can be fulfilled by XPS and NEXAFS if core electrons are excited with soft X-rays of variable energy and if electrons with a low kinetic energy are measured. These prerequisites can only be fulfilled at sufficient sensitivity if synchrotron radiation is used in combination with a detection system capable of measuring slow electrons efficiently (see Section 1.8). In addition, such a detection system needs to be adapted to measure an electrochemical interface, since questions Q3 and Q4, which pertain to the potential dependence and the influence of the surface coverage on the reaction rate, can only be explored using joint electrochemistry and spectroscopy. A brief description of the electrochemical part of this couple follows in the next section. The technical challenge presented by this adaption will form the central focus of the next chapter.

1.7 Electrochemistry (EC)

Question Q1 asked which species occur on the surface of an electrocatalyst. Although EC does not contain information about spectator species, every surface species created or removed by a reaction including an electron transfer, such as oxidation or reduction reactions, can be detected by measuring the charge transfer to or from the electrode. This electric current can be measured precisely and with ease. The rate of a catalytic reaction, such as the OER, is proportional to the current (Q4). The

integrated current equals the charge, which is in turn proportional to the amount of the resulting product. If the surface area of the electrocatalyst is known, the charge can be used to calculate the coverage of an adsorbate, addressing Q3. The currents from different reactions, however, are not distinguishable from one another and do not help surface speciation.

Electrochemical processes can, however, be identified by their characteristic potential. As every other reaction, electrochemical surface reactions have a defined free energy. The electrostatic potential enters the free energy by changing the energy of the electrons inside the electrode. The potential can thereby control whether the reaction occurs in the forward or backward direction. The equilibrium potential at which the rate of both directions are equal is thus related to the free energy of the reaction, which can help speciation of surface processes (Q1 and Q2). A common and simple method is cyclic voltammetry or linear sweep voltammetry, in which the potential is varied at a constant rate and the current response is measured. The rate of a catalytic reaction, however, is best observed under steady state conditions and constant potential, so that currents related to chemical changes in the electrode become negligible (Q4). The description in this section is based on references 56 and 147.

1.8 Instrumentation

Since most key findings in this work are supported by in situ and operando spectroscopy using soft X-rays, the infrastructure of the experiment deserves special attention. While a detailed description of the in situ cells and the sample assemblies is provided in the next chapter, the experimental framework and the X-ray source are only briefly mentioned. These missing pieces of information are provided in this section of the text.

The X-ray source of the main experimental setups were the ISISS and BelChem PGM beamlines at the BESSY II synchrotron, all of which are specialized in the soft X-ray regime. BESSY II is a third-generation synchrotron, which uses compact combinations of dipole, quadrupole, and sextupole magnets to bend, focus, and fine-tune the electron bunches in the storage ring, respectively. A higher-order-mode (HOM) superconducting radio-frequency (SRF) cavity controls the kinetic energy of the electron bunches at about 1.7 GeV. The current in the storage ring is about 300 mA in normal operation. Insertion devices such as undulators are used. The UE56-2 is such an undulator and was used as the light source for the BelChem PGM (former UE56-2 PGM2) beamline. It is an elliptical undulator providing horizontal, vertical, or circular polarization. The beamline is a plane-grating monochromator beamline with exchangeable 400 (high flux) and 1200 (high resolution) lines per millimeter gratings. The beamline's flux (up to $1 \cdot 10^{12}$ photons per 100mA storage ring current and per second) is optimized for soft X-rays between 100 eV and 500 eV but the intensity can be altered by de-tuning the undulator. The ISISS beamline is complementary and is optimized for photon energies between 400 eV and 1500 eV at a flux of up to $1 \cdot 10^{11}$ photons per 100mA storage ring current and per second. The X-ray beam intensity can be varied by filters. The radiation source is a bending magnet.

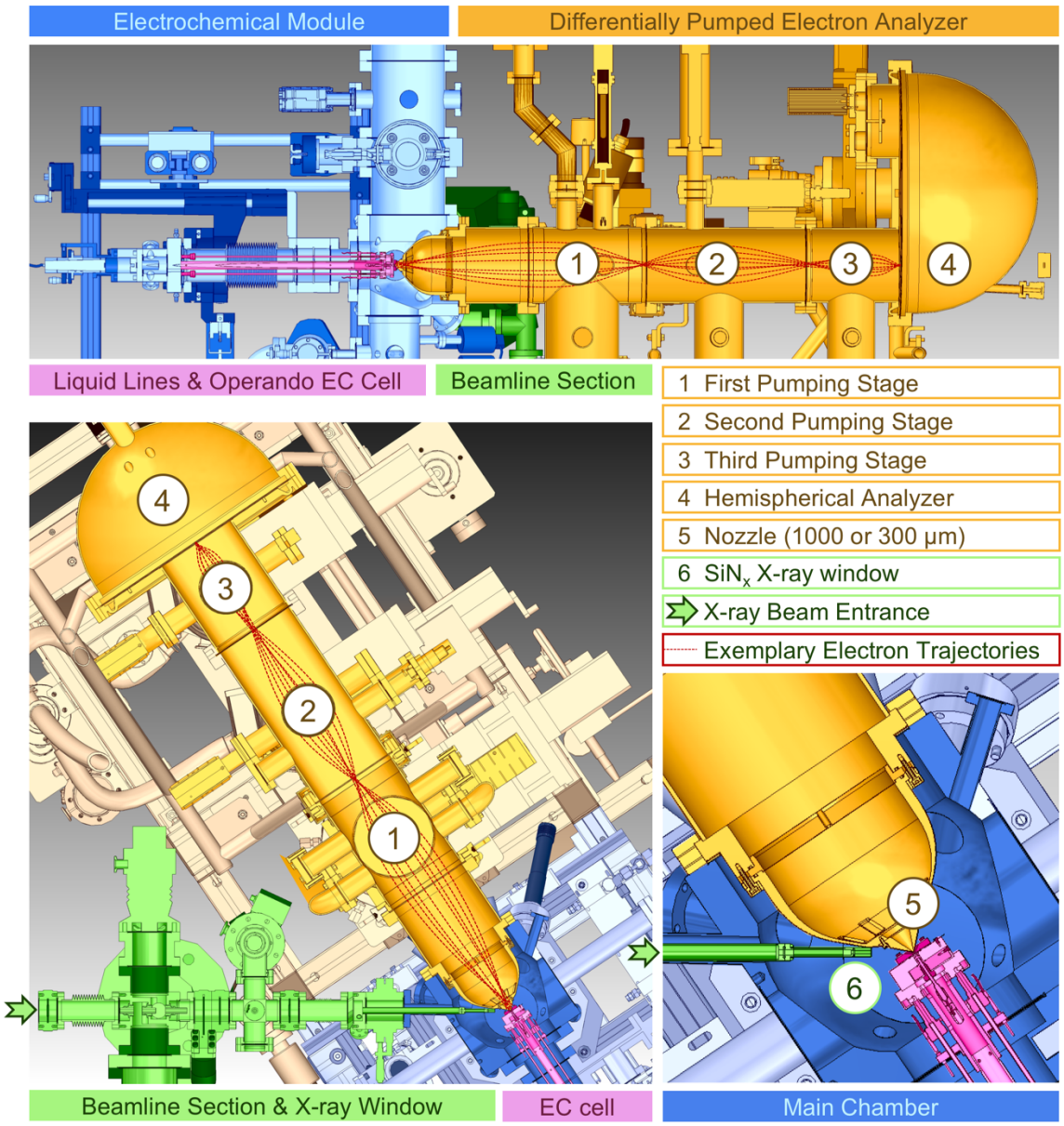

Figure 1.9: Rendered overview of the setup for electrochemical operando spectroscopy; side view (top) with a cut along the center of the cylindrical pumping stages, and top view (bottom) of the setup with a cut on the height of the X-ray beam.

Attached to both beamlines is a near-ambient pressure (NAP) electron analyzer, which has been developed through a cooperation between the Fritz-Haber-Institute and Berkeley Labs [148] and adapted by SPECS, the company manufacturing the devices today. It makes use of an X-ray membrane close to the sample, differential pumping in the analyzer, and electrostatic lenses, in order to minimize losses of electrons and photons and to maximize detection efficiency of electrons (see Figure 1.9).[148] The endstation consists of the analyzer and a measurement chamber which is easily exchangeable and specialized. One chamber, or module, is dedicated to electrochemical in situ spectroscopy and is shown in Figure 1.9. It is equipped to flow liquid electrolyte to and from the in situ cell, which is done via a peristaltic pump. The electrolyte supply system can carry a wide range of electrolytes due to the exclusive use of inert plastics such as PEEK. Electrical contacts can be made to the reference, counter,

and working electrode. These electrodes, the in situ cell body, and the electrolyte are electrically decoupled from the setup. Potential control can be realized by a commercial potentiostat.

1.9 Bibliography

(1) Paris Agreement https://unfccc.int/files/essential_background/convention/application/pdf/english_paris_agreement.pdf.

(2) Oreskes, N. The Scientific Consensus on Climate Change. *Science* 2004, *306* (5702), 1686–1686.

(3) Cook, J.; Nuccitelli, D.; Green, S. A.; Richardson, M.; Winkler, B.; Painting, R.; Way, R.; Jacobs, P.; Skuce, A. Quantifying the Consensus on Anthropogenic Global Warming in the Scientific Literature. *Environ. Res. Lett.* 2013, *8* (2), 024024.

(4) IPCC, 2001. *Climate Change 2001: Synthesis Report. Contrib. Working Grs I, II and III, 3rd Assessment Rep. of the Intergovernmental Panel on Climate Change.*; 2001.

(5) Core-Writing-Team; Pachauri, R. .; Reisinger, A. *IPCC, 2007: Climate Change 2007: Synthesis Report. Contribution of Working Groups I, II and III to the Fourth Assessment Report of the Intergovernmental Panel on Climate Change*; Geneva, 2007.

(6) Rahmstorf, S. Anthropogenic Climate Change: Revisiting the Facts. In *Global warming: Looking beyond Kyoto*; Zedillo, E., Ed.; Brookings Institutions Press: Yale, 2008; pp 34–53.

(7) Crippa, M.; Oreggioni, G.; D, G.; Muntean, M.; Schaaf, E.; Lo Vullo, E.; Solazzo, E.; Monforti-Ferrario, F.; Olivier, J. G. .; Vignati, E. *Fossil CO2 and GHG Emissions of All World Countries - 2019 Report*; Luxembourg, 2019.

(8) Core-Writing-Team; Pachauri, R. K.; Meyer, L. A. *IPCC 2014: Climate Change 2014: Synthesis Report. Contribution of Working Groups I, II, and III to the Fifth Assessment Report of the Intergovernmental Panel on Climate Change*; Geneva, Switzerland, 2014.

(9) Mayer, J. N.; Phillips, D. S.; Hussein, N. S.; Schlegl, D. T.; Senkpiel, C. *Current and Future Cost of Photovoltaics: Long-Term Scenarios for Market Development.*; 2015.

(10) Lazard. *Lazard's Levelized Cost of Energy - Version 12*; 2018.

(11) Burger, B. *Öffentliche Nettostromerzeugung in Deutschland Im Jahr 2019*; Freiburg, 2020.

(12) Gruss, P.; Schüth, F. *Die Zukunft Der Energie*; Verlag C. H. Beck: Munich, 2008.

(13) Schlögl, R. Sustainable Energy Systems: The Strategic Role of Chemical Energy Conversion. *Top. Catal.* 2016, *59* (8–9), 772–786.

(14) Henning, H. *100 % Erneuerbare Energien Für Strom Und Wärme in Deutschland*; 2013.

(15) Davis, S. J.; Lewis, N. S.; Shaner, M.; Aggarwal, S.; Arent, D.; Azevedo, I. L.; Benson, S. M.; Bradley, T.; Brouwer, J.; Chiang, Y. M.; et al. Net-Zero Emissions Energy Systems. *Science* 2018, *360* (6396).

(16) Spencer, D. *BP Statistical Review of World Energy Statistical Review of World*; 2019.

(17) Sterner, M.; Stadler, I. *Energiespeicher - Bedarf, Technologien, Integration*; Sterner, M., Stadler, I., Eds.; Springer Berlin Heidelberg: Berlin, Heidelberg, 2017; Vol. 53.

(18) Sartbaeva, A.; Kuznetsov, V. L.; Wells, S. A.; Edwards, P. P. Hydrogen Nexus in a Sustainable Energy Future. *Energy Environ. Sci.* 2008, *1*, 79–85.

(19) Holladay, J. D.; Hu, J.; King, D. L.; Wang, Y. An Overview of Hydrogen Production Technologies. *Catal. Today* 2009, *139* (4), 244–260.

(20) Turner, J.; Sverdrup, G.; Mann, M. K.; Maness, P.-C.; Kroposki, B.; Ghirardi, M.; Evans, R. J.; Blake,

D. Renewable Hydrogen Production. *Int. J. Energy Res.* 2008, *32* (5), 379–407.

(21) Hosseini, S. E.; Wahid, M. A. Hydrogen from Solar Energy, a Clean Energy Carrier from a Sustainable Source of Energy. *Int. J. Energy Res.* 2019, No. September, 1–22.

(22) Buttler, A.; Spliethoff, H. Current Status of Water Electrolysis for Energy Storage, Grid Balancing and Sector Coupling via Power-to-Gas and Power-to-Liquids: A Review. *Renew. Sustain. Energy Rev.* 2018, *82*, 2440–2454.

(23) Laguna-Bercero, M. A. Recent Advances in High Temperature Electrolysis Using Solid Oxide Fuel Cells: A Review. *J. Power Sources* 2012, *203*, 4–16.

(24) Wang, Y.; Li, W.; Ma, L.; Li, W.; Liu, X. Degradation of Solid Oxide Electrolysis Cells: Phenomena, Mechanisms, and Emerging Mitigation Strategies—A Review. *J. Mater. Sci. Technol.* 2019.

(25) IEA. *The Future of Hydrogen for G20*; 2019.

(26) Carmo, M.; Fritz, D. L.; Mergel, J.; Stolten, D. A Comprehensive Review on PEM Water Electrolysis. *Int. J. Hydrog. Energy* 2013, *38*, 4901–4934.

(27) Mauritz, K. A.; Moore, R. B. State of Understanding of Nafion. *Chem. Rev.* 2004, *104* (10), 4535–4585.

(28) Pourbaix, M. *Atlas of Electrochemical Equilibria in Aqueous Solutions*, Second Eng.; National Association of Corrosion Engineers: Houston, 1974; Vol. 2.

(29) Danilovic, N.; Subbaraman, R.; Chang, K. C.; Chang, S. H.; Kang, Y. J.; Snyder, J.; Paulikas, A. P.; Strmcnik, D.; Kim, Y. T.; Myers, D.; et al. Activity-Stability Trends for the Oxygen Evolution Reaction on Monometallic Oxides in Acidic Environments. *J. Phys. Chem. Lett.* 2014, *5* (14), 2474–2478.

(30) Cherevko, S. Electrochemical Dissolution of Noble Metals Native Oxides. *J. Electroanal. Chem.* 2017, *787*, 11–13.

(31) Holleman, A. F.; Wiberg, E. *Lehrbuch Der Anorganischen Chemie*, 101st ed.; de Gruyter: Berlin, New York, 1995.

(32) Bernt, M.; Siebel, A.; Gasteiger, H. A. Analysis of Voltage Losses in PEM Water Electrolyzers with Low Platinum Group Metal Loadings. *J. Electrochem. Soc.* 2018, *165* (5), F305–F314.

(33) Miles, M. H.; Thomason, M. A. Periodic Variations of Overvoltages for Water Electrolysis in Acid Solutions from Cyclic Voltammetric Studies. *J. Electrochem. Soc.* 1976, *123*, 1459–1461.

(34) Burke, L. D.; McCarthy, F.; O´Meara, T. O. The Oxygen Electrode - Part 3. -- Inhibition of the Oxygen Evolution Reaction. *J. Chem. Soc. Faraday Trans. 1* 1972, *68*, 1086–1092.

(35) Dau, H.; Limberg, C.; Reier, T.; Risch, M.; Roggan, S.; Strasser, P. The Mechanism of Water Oxidation: From Electrolysis via Homogeneous to Biological Catalysis. *ChemCatChem* 2010, *2* (7), 724–761.

(36) Cherevko, S.; Reier, T.; Zeradjanin, A. R.; Pawolek, Z.; Strasser, P.; Mayrhofer, K. J. J. Stability of Nanostructured Iridium Oxide Electrocatalysts during Oxygen Evolution Reaction in Acidic Environment. *Electrochem. commun.* 2014, *48*, 81–85.

(37) Geiger, S.; Kasian, O.; Shrestha, B. R.; Mingers, A. M.; Mayrhofer, K. J. J.; Cherevko, S. Activity and Stability of Electrochemically and Thermally Treated Iridium for the Oxygen Evolution Reaction. *J. Electrochem. Soc.* 2016, *163* (11), F3132–F3138.

(38) Jovanovič, P.; Hodnik, N.; Ruiz-Zepeda, F.; Arčon, I.; Jozinović, B.; Zorko, M.; Bele, M.; Šala, M.;

Šelih, V. S.; Hočevar, S.; et al. Electrochemical Dissolution of Iridium and Iridium Oxide Particles in Acidic Media: Transmission Electron Microscopy, Electrochemical Flow Cell Coupled to Inductively Coupled Plasma Mass Spectrometry, and X-ray Absorption Spectroscopy Study. *J. Am. Chem. Soc.* 2017, *139* (36), 12837–12846.

(39) Cherevko, S.; Geiger, S.; Kasian, O.; Kulyk, N.; Grote, J. P.; Savan, A.; Shrestha, B. R.; Merzlikin, S.; Breitbach, B.; Ludwig, A.; et al. Oxygen and Hydrogen Evolution Reactions on Ru, RuO2, Ir, and IrO2 Thin Film Electrodes in Acidic and Alkaline Electrolytes: A Comparative Study on Activity and Stability. *Catal. Today* 2016, *262*, 170–180.

(40) Kasian, O.; Grote, J.-P.; Geiger, S.; Cherevko, S.; Mayrhofer, K. J. J. The Common Intermediates of Oxygen Evolution and Dissolution Reactions during Water Electrolysis on Iridium. *Angew. Chemie Int. Ed.* 2018, *57* (9), 2488–2491.

(41) LeRoy, R. L.; Bowen, C. T.; LeRoy, D. J. The Thermodynamics of Aqueous Water Electrolysis. *J. Electrochem. Soc.* 1980, *127* (9), 1954–1962.

(42) Wagman, D. D.; Evans, W. H.; Halow, I.; Parker, V. B.; Bailey, S. M.; Schumm, R. H. *Selected Values of Chemical Thermodynamic Properties Part 1. Tables for the First Twenty-Three Elements in the Standard Order of Arrangement*; Washington, 1965.

(43) Chase, M. W.; Davies, C. A.; Downey, J. R.; Frurip, D. J.; McDonald, R. A.; Syverud, A. N. *NIST-JANAF Thermochemical Tables*; Gaithersburg, 1985.

(44) Wagner, W.; Pruß, A. The IAPWS Formulation 1995 for the Thermodynamic Properties of Ordinary Water Substance for General and Scientific Use. *J. Phys. Chem. Ref. Data* 2002, *31* (2), 387–535.

(45) IAPWS. *Revised Release on the IAPWS Industrial Formulation 1997 for the Thermodynamic Properties of Water and Steam*; Lucerne, 2007.

(46) Tarasevich, M. R.; Sadkowski, A.; Yeager, E. B. Oxygen Electrochemistry. In *Comprehensive Treatise of Electrochemistry, Vol. 7*; Conway, B. E., Bockris, J. O., Yeager, E. B., Eds.; Eds. Plenum Press: New York, 1983; pp 301–398.

(47) Matsumoto, Y.; Sato, E. Electrocatalytic Properties of Transition Metal Oxides for Oxygen Evolution Reaction. *Mater. Chem. Phys.* 1986, *14* (5), 397–426.

(48) Duca, M.; Koper, M. T. M. Fundamental Aspects of Electrocatalysis. In *Surface and Interface Science, Volume 8: Interfacial Electrochemistry*; Wandelt, K., Ed.; Wiley VCH: Weinheim, 2020; pp 773–890.

(49) Bockris, J. O. Kinetics of Activation Controlled Consecutive Electrochemical Reactions: Anodic Evolution of Oxygen. *J. Chem. Phys.* 1956, *24* (1956), 817.

(50) Nørskov, J. K.; Bligaard, T.; Logadottir, A.; Bahn, S.; Hansen, L. B.; Bollinger, M.; Bengaard, H.; Hammer, B.; Sljivancanin, Z.; Mavrikakis, M.; et al. Universality in Heterogeneous Catalysis. *J. Catal.* 2002, *209* (2), 275–278.

(51) Rossmeisl, J.; Qu, Z.-W.; Zhu, H.; Kroes, G.-J.; Nørskov, J. K. Electrolysis of Water on Oxide Surfaces. *J. Electroanal. Chem.* 2007, *607* (1–2), 83–89.

(52) Gauthier, J. A.; Dickens, C. F.; Chen, L. D.; Doyle, A. D.; Nørskov, J. K. Solvation Effects for Oxygen Evolution Reaction Catalysis on IrO2(110). *J. Phys. Chem. C* 2017, *121*, 11455–11463.

(53) Ping, Y.; Nielsen, R. J.; Goddard, W. A. The Reaction Mechanism with Free Energy Barriers at Constant Potentials for the Oxygen Evolution Reaction at the IrO 2 (110) Surface. *J. Am. Chem.*

Soc. 2017, *139* (1), 149–155.

(54) Fierro, S.; Nagel, T.; Baltruschat, H.; Comninellis, C. Investigation of the Oxygen Evolution Reaction on Ti/IrO2 Electrodes Using Isotope Labelling and on-Line Mass Spectrometry. *Electrochem. commun.* 2007, *9* (8), 1969–1974.

(55) Nørskov, J. K.; Rossmeisl, J.; Logadottir, A.; Lindqvist, L.; Kitchin, J. R.; Bligaard, T.; Jónsson, H. Origin of the Overpotential for Oxygen Reduction at a Fuel-Cell Cathode. *J. Phys. Chem. B* 2004, *108* (46), 17886–17892.

(56) Schmickler, W.; Santos, E. *Interfacial Electrochemistry*, 2nd ed.; Springer Berlin Heidelberg: Berlin, Heidelberg, 2010.

(57) Buckley, D. N.; Burke, L. D. The Oxygen Electrode - Part 5. - Enhancement of Charge Capacity of an Iridium Surface in the Anodic Region. *J. Chem. Soc., Faraday Trans. 1* 1975, *71*, 1447–1459.

(58) Gottesfeld, S.; Srinivasan, S. Electrochemical and Optical Studies of Thick Oxide Layers on Iridium and Their Electrocatalytic Activities for the Oxygen Evolution Reaction. *J. Electroanal. Chem.* 1978, *86*, 89–104.

(59) Mozota, J.; Conway, B. E. Surface and Bulk Processes at Oxidized Iridium Electrodes-I. Monolayer Stage and Transition to Reversible Multilayer Oxide Film Behaviour. *Electrochim. Acta* 1983, *28* (1), 1–8.

(60) Conway, B. E.; Mozota, J. Surface and Bulk Processes at Oxidized Iridium Electrodes-II. Conductivity-Switched Behaviour of Thick Oxide Films. *Electrochim. Acta* 1983, *28*, 9–16.

(61) Mcintyre, J. D. E.; Peck, W. F.; Nakahara, S. Oxidation-State Changes and Structure of Electrochromic Iridium Oxide-Films. *J. Electrochem. Soc.* 1980, *127* (6), 1264–1268.

(62) Augustynski, J.; Koudelka, M.; Sanchez, J.; Conway, B. E. ESCA Study of the State of Iridium and Oxygen in Electrochemically and Thermally Formed Iridium Oxide Films. *J. Electroanal. Chem. Interfacial Electrochem.* 1984, *160* (1–2), 233–248.

(63) Hall, H. Y.; Sherwood, P. M. A. X-Ray Photoelectron Spectroscopic Studies of the Iridium Electrode System. *J. Chem. Soc., Faraday Trans. 1* 1984, *80*, 135–152.

(64) Li, T.; Kasian, O.; Cherevko, S.; Zhang, S.; Geiger, S.; Scheu, C.; Felfer, P.; Raabe, D.; Gault, B.; Mayrhofer, K. J. J. Atomic-Scale Insights into Surface Species of Electrocatalysts in Three Dimensions. *Nat. Catal.* 2018, *1* (4), 300–305.

(65) Scohy, M.; Abbou, S.; Martin, V.; Gilles, B.; Sibert, E.; Dubau, L.; Maillard, F. Probing Surface Oxide Formation and Dissolution on/of Ir Single Crystals via X-Ray Photoelectron Spectroscopy and Inductively Coupled Plasma Mass Spectrometry. *ACS Catal.* 2019, *9* (11), 9859–9869.

(66) Trasatti, S. Electrocatalysis in the Anodic Evolution of Oxygen and Chlorine. *Electrochim. Acta* 1984, *29* (11), 1503–1512.

(67) Ardizzone, S.; Trasatti, S. Interfacial Properties of Oxides with Technological Impact in Electrochemistry. *Adv. Colloid Interface Sci.* 1996, *64*, 173–251.

(68) Reier, T.; Weidinger, I.; Hildebrandt, P.; Kraehnert, R.; Strasser, P. Electrocatalytic Oxygen Evolution Reaction on Iridium Oxide Model Film Catalysts: Influence of Oxide Type and Catalyst Substrate Interactions. *ECS Trans.* 2013, *58* (2), 39–51.

(69) Bernicke, M.; Ortel, E.; Reier, T.; Bergmann, A.; Ferreira De Araujo, J.; Strasser, P.; Kraehnert, R. Iridium Oxide Coatings with Templated Porosity as Highly Active Oxygen Evolution Catalysts: Structure-Activity Relationships. *ChemSusChem* 2015, *8* (11), 1908–1915.

(70) Miao, M.-S.; Seshadri, R. Rh2O3 versus IrO2: Relativistic Effects and the Stability of Ir4+. *J. Phys. Condens. Matter* **2012**, *24* (21), 215503.

(71) Weber, D.; Schoop, L. M.; Wurmbrand, D.; Nuss, J.; Seibel, E. M.; Tafti, F. F.; Ji, H.; Cava, R. J.; Dinnebier, R. E.; Lotsch, B. V. Trivalent Iridium Oxides: Layered Triangular Lattice Iridate K0.75 Na0.25 IrO2 and Oxyhydroxide IrOOH. *Chem. Mater.* **2017**, *29*, 8338–8345.

(72) Glarum, S. H.; Marshall, J. H. The A-C Response of Iridium Oxide Films. *J. Electrochem. Soc.* **1980**, *127*, 1467–1474.

(73) Silva, T. M.; Simões, A. M. P.; Ferreira, M. G. S.; Walls, M.; Da Cunha Belo, M. Electronic Structure of Iridium Oxide Films Formed in Neutral Phosphate Buffer Solution. *J. Electroanal. Chem.* **1998**, *441*, 5–12.

(74) Ilyukhina, L.; Sunde, S.; Haverkamp, R. G. Electronic Structure and Growth of Electrochemically Formed Iridium Oxide Films. *J. Electrochem. Soc.* **2017**, *164* (14), F1662–F1670.

(75) Lezna, R. O.; Kunimatsu, K.; Ohtsuka, T.; Sato, N. In Situ Infrared Spectroscopy of Iridium Oxide. *J. Electrochem. Soc.* **1987**, *134* (12), 3090–3094.

(76) Hüppauff, M.; Lengeler, B. Valency and Structure of Iridium in Anodic Iridium Oxide Films. *J. Electrochem. Chem.* **1993**, *140*, 598–602.

(77) Pauporté, T.; Aberdam, D.; Hazemann, J.-L.; Faure, R.; Durand, R. X-Ray Absorption in Relation to Valency of Iridium in Sputtered Iridium Oxide Film. *J. Electroanal. Chem.* **1999**, *465*, 88–95.

(78) Parks, G. A. The Isoelectric Points of Solid Oxides, Solid Hydroxides, and Aqueous Hydroxo Complex Systems. *Chem. Rev.* **1965**, *65* (2), 177–198.

(79) Petrii, O. A.; Vitins, A. Adsorption Properties of an Iridium Oxide Electrode: A Thermodynamic Approach. *Elektrokhimiya* **1991**, *27*, 461.

(80) Ardizzone, S.; Carugati, A.; Trasatti, S. Properties of Thermally Prepared Iridium Dioxide Electrodes. *J. Electroanal. Chem.* **1981**, *126*, 287–292.

(81) Yao, S.; Wang, M.; Madou, M. A PH Electrode Based on Melt-Oxidized Iridium Oxide. *J. Electrochem. Soc.* **2001**, *148* (4), H29.

(82) Burke, L. D.; Mulcahy, J. K.; Whelan, D. P. Preparation of an Oxidized Iridium Electrode and the Variation of Its Potential with PH. *J. Electroanal. Chem. Interfacial Electrochem.* **1984**, *163*, 117–128.

(83) Steegstra, P.; Ahlberg, E. Influence of Oxidation State on the PH Dependence of Hydrous Iridium Oxide Films. *Electrochim. Acta* **2012**, *76*, 26–33.

(84) Kuo, D. Y.; Kawasaki, J. K.; Nelson, J. N.; Kloppenburg, J.; Hautier, G.; Shen, K. M.; Schlom, D. G.; Suntivich, J. Influence of Surface Adsorption on the Oxygen Evolution Reaction on IrO 2 (110). *J. Am. Chem. Soc.* **2017**, *139* (9), 3473–3479.

(85) Steegstra, P.; Busch, M.; Panas, I.; Ahlberg, E. Revisiting the Redox Properties of Hydrous Iridium Oxide Films in the Context of Oxygen Evolution. *J. Phys. Chem. C* **2013**, *117* (40), 20975–20981.

(86) Fonseca, I. T. E.; Lopes, M. I.; Portela, M. T. C. A Comparative Voltammetric Study of the Ir|H2SO4 and Ir|HClO4 Aqueous Interfaces. *J. Electroanal. Chem.* **1996**, *415* (1–2), 89–96.

(87) Birss, V. I.; Elzanowska, H.; Gottesfeld, S. Quartz Crystal Microbalance Measurements During Oxidation Reduction of Hydrous Ir Oxide Electrodes. *J. Electroanal. Chem.* **1991**, *318* (1–2), 327–333.

(88) Pavlovic, Z.; Ranjan, C.; Gao, Q.; van Gastel, M.; Schlögl, R. Probing the Structure of a Water-Oxidizing Anodic Iridium Oxide Catalyst Using Raman Spectroscopy. *ACS Catal.* **2016**, *6* (12), 8098–8105.

(89) Clancy, J. P.; Chen, N.; Kim, C. Y.; Chen, W. F.; Plumb, K. W.; Jeon, B. C.; Noh, T. W.; Kim, Y. J. Spin-Orbit Coupling in Iridium-Based 5d Compounds Probed by x-Ray Absorption Spectroscopy. *Phys. Rev. B - Condens. Matter Mater. Phys.* **2012**, *86* (19), 1–8.

(90) Mo, Y.; Stefan, I. C.; Cai, W.-B.; Dong, J.; Carey, P.; Scherson, D. A. In Situ Iridium L III-Edge X-Ray Absorption and Surface Enhanced Raman Spectroscopy of Electrodeposited Iridium Oxide Films in Aqueous Electrolytes. *J. Phys. Chem. B* **2002**, *106* (14), 3681–3686.

(91) Abbott, D. F.; Lebedev, D.; Waltar, K.; Povia, M.; Nachtegaal, M.; Fabbri, E.; Copéret, C.; Schmidt, T. J. Iridium Oxide for the Oxygen Evolution Reaction: Correlation between Particle Size, Morphology, and the Surface Hydroxo Layer from Operando XAS. *Chem. Mater.* **2016**, *28*, 6591–6604.

(92) Ping, Y.; Galli, G.; Goddard, W. A. Electronic Structure of IrO2: The Role of the Metal d-Orbitals. *J. Phys. Chem. C* **2015**, *119*, 11570–11577.

(93) Hillman, A. R.; Skopek, M. A.; Gurman, S. J. X-Ray Spectroscopy of Electrochemically Deposited Iridium Oxide Films: Detection of Multiple Sites through Structural Disorder. *Phys. Chem. Chem. Phys.* **2011**, *13* (12), 5252–5263.

(94) Pfeifer, V.; Jones, T. E.; Velasco Vélez, J. J.; Massué, C.; Arrigo, R.; Teschner, D.; Girgsdies, F.; Scherzer, M.; Greiner, M. T.; Allan, J.; et al. The Electronic Structure of Iridium and Its Oxides. *Surf. Interface Anal.* **2016**, *48* (5), 261–273.

(95) Pfeifer, V.; Jones, T. E.; Velasco Vélez, J. J.; Massué, C.; Greiner, M. T.; Arrigo, R.; Teschner, D.; Girgsdies, F.; Scherzer, M.; Allan, J.; et al. The Electronic Structure of Iridium Oxide Electrodes Active in Water Splitting. *Phys. Chem. Chem. Phys* **2016**, *18*, 2292–2296.

(96) Pfeifer, V.; Jones, T. E.; Wrabetz, S.; Massué, C.; Velasco Vélez, J. J.; Arrigo, R.; Scherzer, M.; Piccinin, S.; Hävecker, M.; Knop-Gericke, A.; et al. Reactive Oxygen Species in Iridium-Based OER Catalysts. *Chem. Sci.* **2016**, *7*, 6791–6795.

(97) Pfeifer, V.; Jones, T. E.; Velasco Vélez, J. J.; Arrigo, R.; Piccinin, S.; Hävecker, M.; Knop-Gericke, A.; Schlögl, R. In Situ Observation of Reactive Oxygen Species Forming on Oxygen-Evolving Iridium Surfaces. *Chem. Sci.* **2017**, *8*, 2143–2149.

(98) Grimaud, A.; Demortière, A.; Saubanère, M.; Dachraoui, W.; Duchamp, M.; Doublet, M.-L.; Tarascon, J.-M. Activation of Surface Oxygen Sites on an Iridium-Based Model Catalyst for the Oxygen Evolution Reaction. *Nat. Energy* **2017**, *2* (1), 16189.

(99) Minguzzi, A.; Lugaresi, O.; Achilli, E.; Locatelli, C.; Vertova, A.; Ghigna, P.; Rondinini, S. Observing the Oxidation State Turnover in Heterogeneous Iridium-Based Water Oxidation Catalysts. *Chem. Sci.* **2014**, *5* (9), 3591–3597.

(100) Minguzzi, A.; Locatelli, C.; Lugaresi, O.; Achilli, E.; Cappelletti, G.; Scavini, M.; Coduri, M.; Masala, P.; Sacchi, B.; Vertova, A.; et al. Easy Accommodation of Different Oxidation States in Iridium Oxide Nanoparticles with Different Hydration Degree as Water Oxidation Electrocatalysts. *ACS Catal.* **2015**, *5*, 5104–5115.

(101) Kahk, J. M.; Poll, C. G.; Oropeza, F. E.; Ablett, J. M.; C??olin, D.; Rueff, J. P.; Agrestini, S.; Utsumi, Y.; Tsuei, K. D.; Liao, Y. F.; et al. Understanding the Electronic Structure of IrO2 Using Hard-X-Ray Photoelectron Spectroscopy and Density-Functional Theory. *Phys. Rev. Lett.* **2014**, *112* (11), 1–6.

(102) Nong, H. N.; Reier, T.; Oh, H.-S.; Gliech, M.; Paciok, P.; Vu, T. H. T.; Teschner, D.; Heggen, M.; Petkov, V.; Schlögl, R.; et al. A Unique Oxygen Ligand Environment Facilitates Water Oxidation in Hole-Doped IrNiOx Core–Shell Electrocatalysts. *Nat. Catal.* 2018, *1* (11), 841–851.

(103) Velasco-Vélez, J. J.; Jones, T. E.; Streibel, V.; Hävecker, M.; Chuang, C.-H.; Frevel, L.; Plodinec, M.; Centeno, A.; Zurutuza, A.; Wang, R.; et al. Electrochemically Active Ir NPs on Graphene for OER in Acidic Aqueous Electrolyte Investigated by in Situ and Ex Situ Spectroscopies. *Surf. Sci.* 2019, *681*, 1–8.

(104) Suntivich, J.; May, K. J.; Gasteiger, H. A.; Goodenough, J. B.; Shao-horn, Y.; Calle-vallejo, F.; Oscar, A. D.; Kolb, M. J.; Koper, M. T. M.; Suntivich, J.; et al. A Perovskite Oxide Optimized for Molecular Orbital Principles. *Science* 2011, *334* (6061), 2010–2012.

(105) Calle-Vallejo, F.; Inoglu, N. G.; Su, H.-Y.; Martínez, J. I.; Man, I. C.; Koper, M. T. M.; Kitchin, J. R.; Rossmeisl, J. Number of Outer Electrons as Descriptor for Adsorption Processes on Transition Metals and Their Oxides. *Chem. Sci.* 2013, *4* (3), 1245.

(106) Man, I. C.; Su, H. Y.; Calle-Vallejo, F.; Hansen, H. A.; Martínez, J. I.; Inoglu, N. G.; Kitchin, J.; Jaramillo, T. F.; Nørskov, J. K.; Rossmeisl, J. Universality in Oxygen Evolution Electrocatalysis on Oxide Surfaces. *ChemCatChem* 2011, *3* (7), 1159–1165.

(107) Subbaraman, R.; Tripkovic, D.; Chang, K. C.; Strmcnik, D.; Paulikas, A. P.; Hirunsit, P.; Chan, M.; Greeley, J.; Stamenkovic, V.; Markovic, N. M. Trends in Activity for the Water Electrolyser Reactions on 3d M(Ni,Co,Fe,Mn) Hydr(Oxy)Oxide Catalysts. *Nat. Mater.* 2012, *11* (6), 550–557.

(108) Seitz, L. C.; Dickens, C. F.; Nishio, K.; Hikita, Y.; Montoya, J.; Doyle, A.; Kirk, C.; Vojvodic, A.; Hwang, H. Y.; Norskov, J. K.; et al. A Highly Active and Stable IrOx/SrIrO3 Catalyst for the Oxygen Evolution Reaction. *Science* 2016, *353* (6303), 1011–1014.

(109) Hong, W. T.; Stoerzinger, K. A.; Lee, Y. L.; Giordano, L.; Grimaud, A.; Johnson, A. M.; Hwang, J.; Crumlin, E. J.; Yang, W.; Shao-Horn, Y. Charge-Transfer-Energy-Dependent Oxygen Evolution Reaction Mechanisms for Perovskite Oxides. *Energy Environ. Sci.* 2017, *10* (10), 2190–2200.

(110) Yamada, I.; Takamatsu, A.; Asai, K.; Shirakawa, T.; Ohzuku, H.; Seno, A.; Uchimura, T.; Fujii, H.; Kawaguchi, S.; Wada, K.; et al. Systematic Study of Descriptors for Oxygen Evolution Reaction Catalysis in Perovskite Oxides. *J. Phys. Chem. C* 2018, *122* (49), 27885–27892.

(111) Halck, N. B.; Petrykin, V.; Krtil, P.; Rossmeisl, J. Beyond the Volcano Limitations in Electrocatalysis-Oxygen Evolution Reaction. *Phys. Chem. Chem. Phys.* 2014, *16* (27), 13682–13688.

(112) Parr, R. G.; Yang, W. *Density-Functional Theory of Atoms and Molecules*, First edit.; Breslow, R., Goodenough, J. B., Halpern, J., Rowlinson, J. S., Eds.; Oxford University Press: New York, 1989.

(113) Kantorovich, L. *Quantum Theory of the Solid State: An Introduction*, First edit.; Van der Merwe, A., Ed.; Springer Netherlands: Dordrecht, 2004.

(114) Hohenberg, P.; Kohn, W. Inhomogeneous Electron Gas. *Phys. Rev.* 1964, *136* (3B), B864–B871.

(115) Kohn, W.; Sham, L. J. Self-Consistent Equations Including Exchange and Correlation Effects. *Phys. Rev.* 1965, *140* (4A), A1133–A1138.

(116) Perdew, J. P.; Burke, K.; Ernzerhof, M. Generalized Gradient Approximation Made Simple. *Phys. Rev. Lett.* 1996, *77*, 3865–3868.

(117) Zhang, H.; Soon, A.; Delley, B.; Stampfl, C. Stability, Structure, and Electronic Properties of Chemisorbed Oxygen and Thin Surface Oxides on Ir(111). *Phys. Rev. B - Condens. Matter Mater. Phys.* 2008, *78* (4), 1–12.

(118) García-Melchor, M.; Vilella, L.; López, N.; Vojvodic, A. Computationally Probing the Performance of Hybrid, Heterogeneous, and Homogeneous Iridium-Based Catalysts for Water Oxidation. *ChemCatChem* **2016**, *8* (10), 1792–1798.

(119) Perdew, J. P.; Schmidt, K. Jacob's Ladder of Density Functional Approximations for the Exchange-Correlation Energy. In *AIP Conference Proceedings*; AIP, 2001; Vol. 577, pp 1–20.

(120) Cohen, A. J.; Mori-Sánchez, P.; Yang, W. Insights into Current Limitations of Density Functional Theory. *Science* **2008**, *321* (5890), 792–794.

(121) Xu, Z.; Rossmeisl, J.; Kitchin, J. R. A Linear Response DFT+U Study of Trends in the Oxygen Evolution Activity of Transition Metal Rutile Dioxides. *J. Phys. Chem. C* **2015**, *119* (9), 4827–4833.

(122) Vanderbilt, D. Soft Self-Consistent Pseudopotentials in a Generalized Eigenvalue Formalism. *Phys. Rev. B* **1990**, *41* (11), 7892–7895.

(123) Kresse, G.; Furthmüller, J. Efficiency of Ab-Initio Total Energy Calculations for Metals and Semiconductors Using a Plane-Wave Basis Set. *Comput. Mater. Sci.* **1996**, *6* (1), 15–50.

(124) Görling, A. Density-Functional Theory for Excited States. *Phys. Rev. A* **1996**, *54* (5), 3912–3915.

(125) Hellman, A.; Razaznejad, B.; Lundqvist, B. I. Potential-Energy Surfaces for Excited States in Extended Systems. *J. Chem. Phys.* **2004**, *120* (10), 4593–4602.

(126) Maurer, R. J.; Reuter, K. Excited-State Potential-Energy Surfaces of Metal-Adsorbed Organic Molecules from Linear Expansion A-Self-Consistent Field Density-Functional Theory (ASCF-DFT). *J. Chem. Phys.* **2013**, *139* (1).

(127) Pehlke, E.; Scheffler, M. Evidence for Site-Sensitive Screening of Core Holes at the Si and Ge (001) Surface. *Phys. Rev. B.* **1993**, *71*, 2338–2341.

(128) Taillefumier, M.; Cabaret, D.; Flank, A. M.; Mauri, F. X-Ray Absorption near-Edge Structure Calculations with the Pseudopotentials: Application to the K Edge in Diamond and (Formula Presented)-Quartz. *Phys. Rev. B - Condens. Matter Mater. Phys.* **2002**, *66* (19), 1–8.

(129) Gougoussis, C.; Calandra, M.; Seitsonen, A. P.; Mauri, F. First-Principles Calculations of x-Ray Absorption in a Scheme Based on Ultrasoft Pseudopotentials: From α -Quartz to High- Tc Compounds. *Phys. Rev. B - Condens. Matter Mater. Phys.* **2009**, *80* (7), 1–8.

(130) Salpeter, E. E.; Bethe, H. A. A Relativistic Equation for Bound-State Problems. *Phys. Rev.* **1951**, *84* (6), 1232–1242.

(131) Shirley, E. L. Ab Initio Inclusion of Electron-Hole Attraction: Application to X-Ray Absorption and Resonant Inelastic X-Ray Scattering. *Phys. Rev. Lett.* **1998**, *80* (4), 794–797.

(132) Soininen, J. A.; Shirley, E. L. Scheme to Calculate Core Hole–Electron Interactions in Solids. *Phys. Rev. B* **2001**, *64* (16), 165112.

(133) Otani, M.; Sugino, O. First-Principles Calculations of Charged Surfaces and Interfaces: A Plane-Wave Nonrepeated Slab Approach. *Phys. Rev. B* **2006**, *73* (11), 115407.

(134) Bonnet, N.; Morishita, T.; Sugino, O.; Otani, M. First-Principles Molecular Dynamics at a Constant Electrode Potential. *Phys. Rev. Lett.* **2012**, *109* (26), 266101.

(135) Berendsen, H. J. C.; Postma, J. P. M.; Van Gunsteren, W. F.; DiNola, A.; Haak, J. R. Molecular Dynamics with Coupling to an External Bath. *J. Chem. Phys.* **1984**, *81*, 3684–3690.

(136) Henkelman, G.; Uberuaga, B. P.; Jónsson, H. A Climbing Image Nudged Elastic Band Method for

Finding Saddle Points and Minimum Energy Paths. *J. Chem. Phys.* 2000, *113* (22), 9901–9904.

(137) Stöhr, J. *NEXAFS Spectroscopy*, First Edit.; Ertl, G., Gomer, R., Mills, D. L., Eds.; Springer Berlin Heidelberg: Berlin, Heidelberg, 1992.

(138) Behrens, P. XANES, EXAFS and Related Techniques. In *Molecular Sieves - Science and Technology, Vol. 4*; Karge, H. G., Weitkamp, J., Eds.; Springer Berlin Heidelberg: Berlin, Heidelberg, 2004; pp 427–466.

(139) Hüfner, S. *Photoelectron Spectroscopy: Principles and Applications*, First Edit.; Lotsch, H. K. V., Cardona, M., Fulde, P., von Klitzing, K., Queisser, H.-J., Eds.; Springer-Verlag Berlin Heidelberg: Berlin, Heidelberg, 1995.

(140) Hillebrecht, F. U.; Kisker, E. Oberflächenphysik. In *Lehrbuch der Experimentalphysik, Band 6, Festkörper*; Raith, W., Ed.; Walter de Gruyter: Berlin, New York, 1992.

(141) Doniach, S.; Sunjic, M. Many-Electron Singularity in X-Ray Photoemission and X-Ray Line Spectra from Metals. *J. Phys. C Solid State Phys.* 1970, *3* (2), 285–291.

(142) Wertheim, G. K.; Walker, L. R. Many-Body Effects in Transition Metals: Role of the Density of States. *J. Phys. F Met. Phys.* 1976, *6* (12), 2297–2306.

(143) Wertheim, G. K.; Guggenheim, H. J. Conduction-Electron Screening in Metallic Oxides: IrO2. *Phys. Rev. B* 1980, *22* (10), 4680–4683.

(144) Thole, B. T.; Carra, P.; Sette, F.; van der Laan, G. X-Ray Circular Dichroism as a Probe of Orbital Magnetization. *Phys. Rev. Lett.* 1992, *68* (12), 1943–1946.

(145) Stöhr, J.; König, H. Determination of Spin- and Orbital-Moment Anisotropies in Transition Metals by Angle-Dependent X-Ray Magnetic Circular Dichroism. *Phys. Rev. Lett.* 1995, *75* (20), 3748–3751.

(146) Stöhr, J. X-Ray Magnetic Circular Dichroism Spectroscopy of Transition Metal Thin Films. *J. Electron Spectros. Relat. Phenomena* 1995, *75*, 253–272.

(147) Abrahams, I.; Bebelis, S.; Bouwmester, H.; Bruce, P.; Burggraaf, A.; de Wit, H.; Fabry, P.; Fransen, T.; Gellings, P.; Gerischer, H.; et al. *The CRC Handbook of Solid State Electrochemistry*, 1st ed.; Gellings, P., Bouwmester, H., Eds.; CRC Press Inc.: Boca Raton, New York, London, Tokyo, 1997.

(148) Salmeron, M. B.; Schlögl, R. Ambient Pressure Photoelectron Spectroscopy: A New Tool for Surface Science and Nanotechnology. *Surf. Sci. Rep.* 2008, *63* (4), 169–199.

2. Graphene-capped liquid thin films for electrochemical operando X-ray spectroscopy and scanning electron microscopy

2.1 Preliminary Remarks

The second chapter sets forth to characterize a novel approach to study solid liquid interfaces with in situ and operando X-ray spectroscopy as well as scanning electron microscopy. This first characterization is vital to the results in the present work because it allows judgement on how similar the liquid thin film of the in situ sample assembly is to bulk electrolyte. The wetting of the catalyst in the sample assembly and the mass transport to and from the solid liquid interface determine the relevance of the in situ and operando results, influencing Q2-Q4.

The approach is built on previous developments in the electronic structure group led by Axel Knop-Gericke in the department of anorganic chemistry under the direction of Robert Schlögl. The development of an in situ cell was initiated by Rosa Arrigo and contained two metallic films on both sides of the permeable membrane Nafion wetted from the backside with a flow of liquid electrolyte.[1] This cell was further developed by Verena Streibel (née Pfeifer into a chemically inert three electrode cell.[2] Eugen Stotz was and is the engineer of all developments connected to the in situ cells. Michael Hävecker oversaw the developments and helped with the practical implementation. Another approach to electrochemical in situ spectroscopy utilizing free-standing graphene was brought into the group by Juan-Jesús Velasco-Vélez.[3] He also suggested to combine permeable membranes with a graphene window in order to use separated nanoparticles while retaining conductivity between them. This chapter presents the findings that resulted from following this suggestion.

Rik Mom furthered the development of the idea by contributing new types of polymer membranes which made the approach more versatile and by investigating some important properties of the sample assembly (see Figure 2.6b, Figure 2.17-19. The approach was adapted to the scanning electron microscope together with Luis Sandoval Diaz, Juan-Jesús Velasco-Vélez, and Rik Mom in the group of electron microscopy led by Thomas Lunkenbein. This team conducted the experiments at the scanning electron microscope (Figure 2.2, Figure 2.7 and Figure 2.9-10. The characterization of the sample assembly was supported by Danail Ivanov. Siamak Nakhaie played a major role in characterizing the graphene transfer with Raman spectroscopy.

2.2 Abstract

Electrochemistry is a promising building block for the global transition to a sustainable energy market. Particularly the electroreduction of CO_2 and the electrolysis of water might be strategic elements for chemical energy conversion. The reactions of interest are inner-sphere reactions, which occur on the surface of the electrode, and the biased interface between the electrode surface and the electrolyte is of central importance to the reactivity of an electrode. However, a potential-dependent observation of this buried interface is challenging, which slows the development of catalyst materials. Here we describe a sample architecture using a graphene blanket that allows surface sensitive studies of biased electrochemical interfaces. At the examples of near ambient pressure X-ray photoelectron spectroscopy (NAP-XPS) and environmental scanning electron microscopy (ESEM) we show that the combination of a graphene blanket and a permeable membrane leads to the formation of a liquid thin film between them. This liquid thin film is stable against a water partial pressure below 1 mbar. These properties of the sample assembly extend the study of solid-liquid interfaces to highly surface sensitive techniques, such as electron spectroscopy/microscopy. In fact, photoelectrons with an effective attenuation length of only 10 Å can be detected, which is close to the absolute minimum possible in aqueous solutions. The in situ cells and the sample preparation necessary to employ our method are comparatively simple. Transferring this approach to other surface sensitive measurement techniques should therefore be straightforward. We see our approach as a starting point for more studies on electrochemical interfaces and surface processes under applied potential. Such studies would be of high value for the rational design of electrocatalysts.

2.3 Introduction

The solid-liquid interface plays an important role in technical processes like electroplating, etching, or electrocatalysis, as well as biological and environmental processes, such as corrosion, ice formation, or transport phenomena across lipid membranes. In all of them, the interaction between a solid surface and the covering layer of solvated species is crucial. Visualizing this interface with spectroscopy or imaging methods is very desirable but poses a fundamental challenge. Either the probe penetrates bulk layers of liquid and a small part of the signal is obtained from the interface, like it is the case for hard X-rays and infrared light, or the probe is surface-sensitive and even thin layers of liquid prevent the probe or the measurand from reaching the interface, as is the case for soft X-rays or electron microscopy. Finding technical solutions is challenging.

Attempts to overcome these limitations took different avenues. The first is to enhance the signal from the interface, like in surface enhanced Raman spectroscopy [4] or sum frequency generation.[5] This approach is elegant but features of vibrational spectroscopy are not element specific and the non-trivial signal enhancement inside plasmonic cavities impedes quantification. The second approach is to reduce the thickness of the liquid layer and to use core-level spectroscopy. The dip-and-pull method in combination with tender X-rays [6] is a good example of that (for comparison see Table 2.1). The third

approach is to reduce the thickness of the solid. Graphene-capped micro-channels [7,8] or an electrochemical in situ cell with graphene windows [3,9,10] used exactly that strategy to enable soft X-ray spectroscopy of a solid-liquid interface. In the latter case, it is assured that the liquid phase has bulk properties, but the fragile, atomically thin windows pose a high risk to the experimental setup (see Table 2.1). The fourth approach is the nanofabrication of chips for liquid phase electron microscopy,[11] which tries to diminish the thickness of both the solid and the liquid with success. A more detailed overview of the techniques used in the field of near ambient pressure X-ray photoelectron spectroscopy (NAP-XPS) and environmental electron microscopy can be found in the publications [9,12] and, [13–15] respectively. A summary of approaches comparable to ours are given in Table 2.1.

Table 2.1: Benefits and drawbacks of existing approaches in comparison.

	Benefits	Drawbacks
Dip and pull	⊕⊕ Real electrolyte ⊕ Buried interfaces accessible	⊖ Limited mass transport ⊖ Intermediate probing depth ⊖ Liquid open to vacuum
Graphene covered, holey SiN_x membrane	⊕⊕ Real electrolyte ⊕ Surface sensitive	⊖ Fragile window and limited graphene stability ⊖ Challenging sample preparation ⊖ Small area
PEM without graphene	⊕ Safe in vacuum ⊕ Simple preparation ⊕ Surface sensitive	⊖ Beam sensitive polymer ⊖ Limited mass transport ⊖ No liquid
PEM with graphene (this work)	⊕ Safe in vacuum ⊕ Simple preparation ⊕ Confined liquid comparable to bulk ⊕ Surface sensitive	⊖ Beam sensitive polymer ⊖ Ion transport depends on membrane ⊖ Homogeneity required

Herein, we describe a method that uses a thin graphene window and confined electrolyte. It is safe and simple to use and allows for investigations of the solid-liquid interface. At the heart of our approach is a sample preparation that can be done in any chemical lab (Figure 2.1): we use solid polymer electrolytes for the transport of ions and water, as others have done before,[1,2,16,17] but we cover the polymer membrane or the topping layer of material with graphene (compare Figure 2.1). The graphene blanket then serves as an evaporation barrier (as shown elsewhere)[3,7,18] and leads to a higher partial pressure of water below it. In previous uses of polymer membranes for similar purposes,[1,2,16,17] the catalyst layer faced vacuum and the electrolyte could evaporate. As we will demonstrate in the present manuscript, the graphene barrier helps to retain a thin film of liquid behind graphene at water partial pressures as low well below a millibar. At the same time, graphene provides electrical conductivity [19,20] and is mostly transparent to a wide range of wavelengths [21–23] and slow electrons.[24–26] These benefits allow studies under wet conditions using surface sensitive spectroscopy [27–29] or electron microscopy with the same type of sample.

The material of interest, e.g. an electrocatalyst, is sandwiched between the membrane and the graphene blanket (see Figure 2.1). The thin film of liquid behind graphene is retained. Electrical contact to the material is provided by the graphene cover and ultimately the lid which holds the membrane assembly in place during the measurement. We use a niobium lid coated with boron-doped diamond.

It is chemically inert and stable over a wide range of potentials.[30] Ion transport to the deposited material is realized via a polymer electrolyte membrane (PEM), which functions as a solid electrolyte connecting the working electrode with the counter and reference electrode, which are immersed in the bulk liquid (see Figure 2.1 and experimental section).

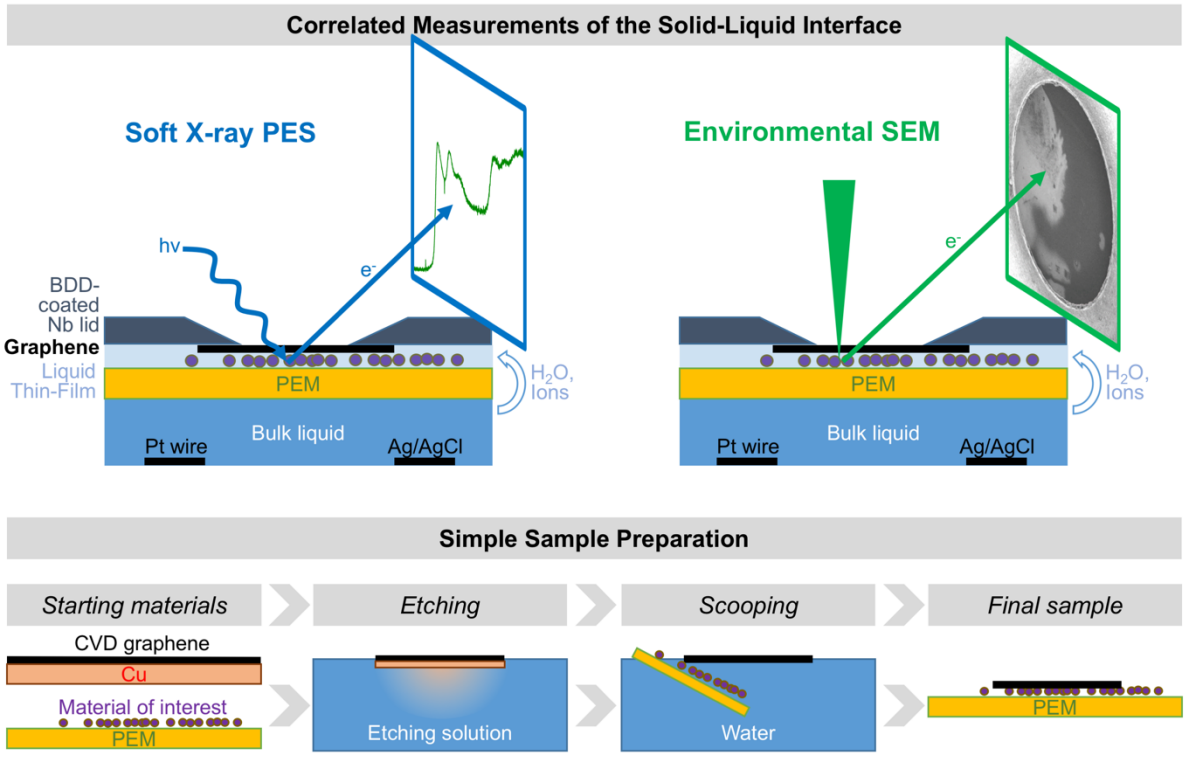

Figure 2.1: Surface-sensitive investigation of a solid-liquid interface; illustration of the sample architecture and measurement approach (top) as wells as an outline of the sample preparation (bottom).

In the following we will characterize the sample assembly we advocate. We will start with the homogeneity of the samples and the graphene properties, then proceed to a study on how external parameters influence the wetting, discuss the ion transport under vacuum, and we will make some remarks about the influence of the beam and about product analysis. In the end, we discuss two scientific showcases to demonstrate the scope of our technique. The first showcase concerns the dissolution of ruthenium under high potentials, and the second visualizes electrodeposition of copper on graphene.

For a convenient recognition of the sample architecture, we will use the short form (0.1 M H_2SO_4)/FAD/IrNPs/SLG to refer to a polymer membrane FAD that is wetted from the back with 0.1 M H_2SO_4 and supports iridium nanoparticles (IrNPs) covered by a single layer of graphene (SLG).

2.4 Results and discussion

2.4.1 Sample morphology

The sample assemblies consist of a polymer membrane and a graphene cover. The polymer membranes are usually smooth on the micrometer scale. Nafion 117, for example, has a root mean square variation in height of 2.2-3.9 nm, depending on humidity (it becomes smoother when properly hydrated).[31] In this publication we will use Nafion 117 supplied by Ion Power as well as FAD and FKD membranes by Fumatech. The choice of membrane is important in the approach, since it determines the ionic conductivity and can introduce contaminants. For more details on the membrane properties, their pre-treatments, and on their chemical structure can be found in the Experimental Section. CVD graphene from Graphenea is transferred as a single layer of graphene (SLG), a bilayer of graphene (BLG), or as a single layer supported by PMMA (SLGp) in a wet chemical process (see Experimental Section). A representative example of the morphology after transfer is given in Figure 2.2a-b. These micrographs stem from an environmental scanning electron microscope (ESEM) and show BLG on an FKD membrane. After the mechanical transfer graphene can exhibit tears, but the film is otherwise uninterrupted over hundreds of micrometer (Figure 2.2a). Sample screening with an optical microscope can, hence, be used to avoid tears in the graphene cover. At larger magnification, wrinkles are evident (Figure 2.2b) but, due to their low density, they will only have a slight impact on the electrical conductivity, the function as a molecular barrier, and a window for radiation and electrons.

In most cases an additional layer, i.e. an electrocatalyst, is sandwiched between the polymer membrane and graphene. The homogeneity of this layer will depend on the preparation method. We will show results from sputter-deposited films (see Experimental Section for more details), since they are homogeneous and well defined, but other techniques like spin coating, dropcasting, electrodeposition, reductive deposition, or electrophoretic deposition could be applied as well. Figure 2.2c-d provides SEM micrographs of a sputtered ruthenium film on FAD covered with BLG. The film is homogeneous on a millimeter length scale. However, the films are cracked, as the larger magnification shows (Figure 2.2d). These cracks likely originate from a mismatch between the metallic layer and the polymer membrane, which swells with increasing humidity.

We can conclude that the present samples are homogeneous on the millimeter length scale. This is important for the following characterization, in which we will make use of Raman and synchrotron-based X-ray spectroscopy to characterize the samples. The spot sizes of these measurements are in the range of a few and one hundred micrometers, respectively (see Experimental Section). Homogeneity beyond the length scale of the measurement is advisable. It was taken care in this work that the sample assemblies did provide the necessary homogeneity.

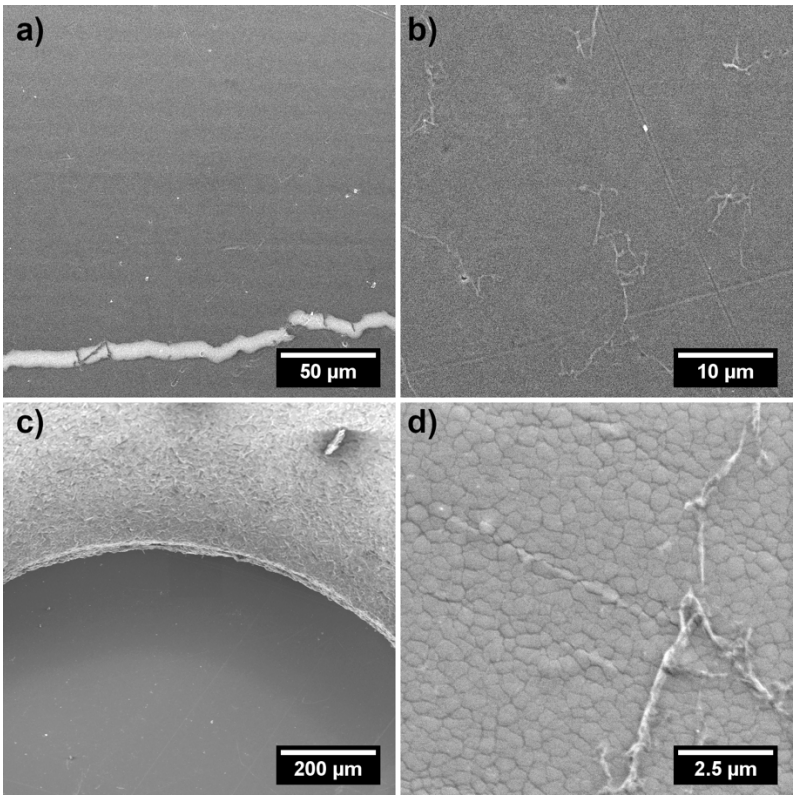

Figure 2.2: SEM micrographs of a)-b) FKD/BLG and c)-d) FAD/Ru(~4nm thick)/BLG under ~2 mbar of water; the backsides of the polymer membranes are in contact with aqueous solutions of 50 mM Cu_5O_4 or 0.1 M H_2SO_4, respectively; c) shows the circular opening of the boron-doped diamond coated niobium lid.

2.4.2 Properties of graphene

Since graphene transfer involves a chemical etching step, the structural and chemical properties of graphene after the transfer need to be assessed. To that end, we provide Raman spectra of SLG and BLG after being transferred with the same method on an oxidized silicon wafer (see Figure 2.3a). Three typical Raman features of graphene will be used for the characterization: first, a defect-induced peak of zone-boundary phonons (D) at ~1350 cm^{-1}, second, the vibrational excitation of a doubly degenerate zone center E_{2g} mode (G) at ~1580 cm^{-1}, and third, a peak related to the second order of zone-boundary phonons (2D).[32] The intensity ratio of D to G (I_D/I_G) has been used to evaluate the degree of disorder in graphene.[32,33] The SLG and BLG both show an I_D/I_G ratio ~0.1 after transfer. Together with a sharp G peak (the full width half maximum is about 20 cm^{-1}) this ratio is indicative of a good structural integrity. The wet transfer method, hence, provides graphene cover layers. A more detailed analysis of the Raman spectroscopy and a comparison to PMMA-assisted graphene transfer process is provided in the Supporting Information.

Since the morphological and structural integrity of the graphene layer after transfer is now shown, we will discuss how this graphene layer assists the goal of measuring a biased solid-liquid interface. It fulfills three functions. First, it is used as a current collector and support, second, it serves as a window for radiation and electrons, and, third, it acts as an evaporation barrier for water.

To fulfill its first function, graphene needs to be in good contact to the lid (see Figure 2.1) and provide conductivity over the range of the circular front plate opening, which is 1.5 mm in diameter. This property is demonstrated by X-ray photoelectron spectroscopy of the C 1s spectrum at several potentials and measurement positions (see Figure 2.3b). The main peak of the C1s spectrum is originating from graphene, as the black reference spectrum of SLG on gold at the bottom of Figure 2.3b indicates. Graphene's peak position is expected to be constant with potential if the working electrode, i.e. graphene, is conductive and grounded to the electron analyzer, which is why it was used as standard configuration, except in Figure 2.3b (see Experimental Sectionfor more detail). Figure 2.3b shows the C1s spectrum at different potentials and measurement positions (each measurement is ~0.2 mm apart). The variation of the peak position in Figure 2.3b is < ±0.2 eV and is probably composed of an uncertainty in the excitation energy, which is ±0.1 eV (see Experimental Sectionthe work function of the sample, and incomplete screening of the surface potential of graphene.[34] The latter is caused by quantum capacity effects.

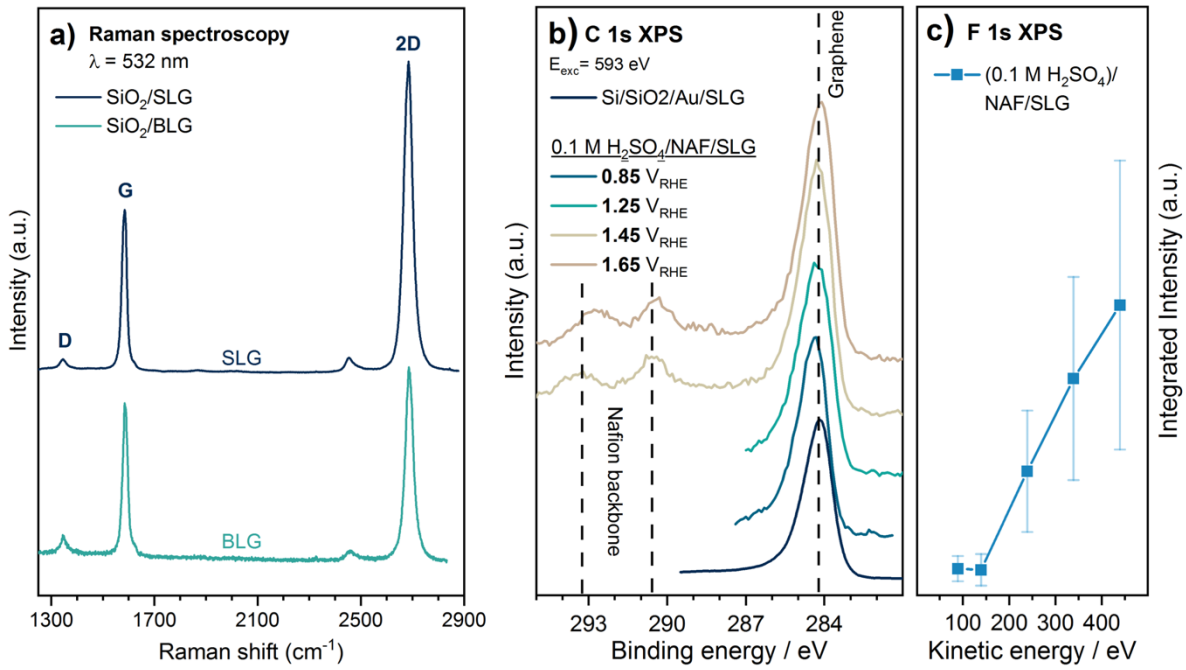

Figure 2.3: a) Raman scattering of Si/SiO_2/SLG and Si/SiO_2/BLG at an excitation wavelength of 532 nm; b) C 1s photoelectron spectra of (0.1 M H_2SO_4)/NAF/SLG at various potentials and of a Si/SiO_2/Au/SLG reference; c) integrated F 1s intensity of (0.1 M H_2SO_4)/NAF/SLG at different kinetic energies.

The second function of graphene is to be a window for incoming and outgoing radiation and slow electrons. It has indeed been shown earlier that graphene is transparent for most radiation [21–23] and slow electrons.[25,26,35] Especially the latter is crucial for surface sensitive photoelectron spectroscopy used in this work. We determined the minimal kinetic energy of photoelectrons required to pass graphene by depth profiling of the F 1s photoelectron spectrum in (0.1 M H_2SO_4)/Nafion/SLG. The F 1s photoelectron signal originates from the tetrafluoroethylene-backbone of the Nafion membrane below graphene, so the photoelectrons originating from Nafion have to (at least) pass SLG. Figure 2.3c shows

the integrated F 1s intensities for kinetic energies of the electrons ranging from 90 to 440 eV. The corrected intensity of the F 1s (see Experimental Section) signal is constant below 150 eV and continuously increases above that value. This means that electrons with a kinetic energy of higher than ~200 eV are already fast enough to escape from the (hydrated) polymer membrane through SLG. This is well in line with the result obtained from free standing BLG, in which the kinetic energy must be higher than 400 eV.[36] The probing depth expected for electrons with a kinetic energy of 200 eV is approximately 1 nm. In fact, such a kinetic energy is close to the minimum effective attenuation length in water,[37] making our technique well suited for extremely surface sensitive measurements of the solid-liquid interface.

2.4.3 Wetting

It has now been shown that the covering graphene layer can serve as a current collector and as a window for radiation and electrons faster than 200 eV, but we have not yet shown that there is a liquid layer between the membrane and graphene. In the following, we will provide evidence from O K-edge absorption that there is a layer of confined water which is similar to bulk water. We also systematically studied whether the partial pressure of water in the gas phase, the number of graphene layers, and the contact of the polymer to bulk water influences the wetting.

We start the evaluation of wetting with the comparison of two O K-edge absorption spectra (Figure 2.4a). Both spectra show an FAD membrane with a BLG cover at 1 mbar H_2O, but only one of the samples is wetted with bulk water from the backside. The two spectra are normalized to the integrated pre-edge intensity at ~532 eV, which originates from the polymer membrane and carbonaceous species, and subtracted from each other (see Experimental Section for more details and reasoning). The difference spectrum presented in red shows a clear fingerprint of liquid water. This becomes especially apparent when comparing to a reference spectrum of liquid water measured in transmission (shown as a dotted line; used with permission from Schreck and Wernet et al. [38]). This thin film of liquid is trapped between the polymer membrane and graphene. These boundaries are expected to disturb the local hydrogen bonding and hence lead to an enhancement of single-donor hydrogen bonding. As a consequence, the pre- and main-edge feature at 535 eV and 537.5 eV originating from single-donor hydrogen bonding should be enhanced relative to the post-edge, which can be assigned to water in a double-donor hydrogen bonding network.[39,40] Strongly confined liquid indeed show a strong enhancement of the main-edge contribution.[41] However, we cannot detect a significant difference from bulk liquid water with our method. This means that the liquid is thick enough to not show altered hydrogen bonding. According to Cicero et al.[42], water confined by graphene adapts bulk properties within 5 Å from the interface. This suggests that the liquid thin film using this method needs to exceed 10 Å. This is sensible considering that the height variation of polymer membranes is in the order of a few nanometer.[31] These voids are covered by graphene and could be filled with liquid as long as graphene seals.

The XPS signal of the O 1s level (see Figure 2.4b) also provides evidence for a phase similar to bulk water. In order to extract the changes in the O 1s spectra that are related to an improved wetting, we

scaled the integrated intensity of the XPS spectrum by the edge jump of the respective O K-edge (Figure 2.4a). This procedure is correct if the integrated intensity of XPS and the edge jump of XAS are proportional to the number of species in the probed volume. The latter is expected to be larger for the partial electron yield of the XAS measurement, leading to an underestimation of the liquid contribution in the XPS difference spectrum. The scaled O 1s XP spectra in the dry and the wet state and their difference are given in Figure 2.4b. A feature at ~538 eV appears in the difference, indicating bulk water.[37] The main peak also shows slight deviations between the dry and the wet state, but they could be caused by a different peak width or a different distribution of carbonaceous species.

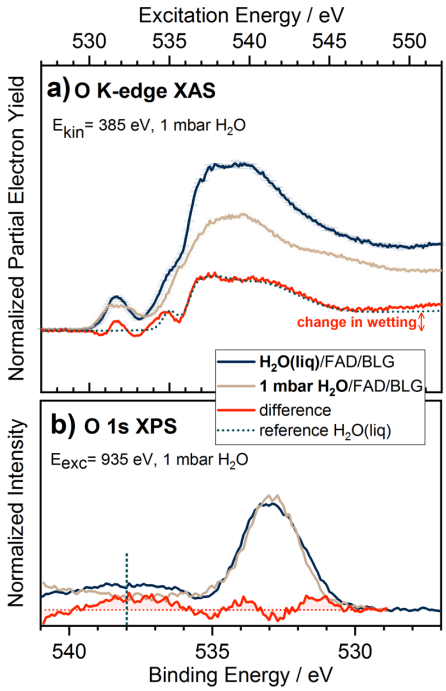

Figure 2.4: a) O K-edge absorption and b) O 1s PES of (1 mbar H_2O)/FAD/BLG and H_2O(liq)/FAD/BLG in 1 mbar H_2O, their difference, and a comparison to a liquid water reference are shown; the reference absorption spectrum of liquid water was provided by Schreck et al. .[38]

In order to describe how the water backpressure, the number of graphene layers, and bulk water behind the PEM membrane influence the liquid thin-film, we varied these parameters systemically. By comparing two different conditions at a time (as in Figure 2.4a), we found that bulk water behind the polymer membrane had the largest impact on the level of wetting. Water backpressure had a weak effect on wetting, unless the samples were in contact with liquid water from the back. Samples covered with SLG and BLG behaved similarly. For the complete discussion, we refer to the Supporting Information.

The study on wetting showed that a liquid thin-film is formed between graphene and a polymer membrane. A close contact between graphene and the polymer membrane is, however, not strictly necessary to create wet conditions. It can also form if a layer of catalyst is sandwiched between the two (compare Figure 2.17), suggesting that graphene's role as an evaporation barrier is mostly determining the wetting, not the interaction between graphene and the material below it.

2.4.4 Ion transport

After verifying the wet conditions below the graphene layer, we turn to the ion transport necessary for most processes of interest at the liquid solid interface. Crucial for the ion transport is the polymer membrane, which serves as a solid electrolyte. An appealing side effect of using solid electrolytes is that the choice of membrane can selectively allow some ions to pass and block others. Among the membranes we used in our studies, there is Nafion (NAF) conducting water and protons, the FAD membrane conducting anions in addition, and the FKD membrane, which conducts water and cations. The FAD membrane is therefore suited for aqueous acidic electrolytes, the FKD can be used for solvated metal ions, and Nafion can be used to study a given electrolyte without the counter ions and only protons.

As a summarizing example of ion transport in our approach we chose the diffusion of the electrolyte H_2SO_4 across an FAD membrane. The experiment is equivalent to the wetting experiment in Figure 2.4a-b but the sample is wetted with 0.1 M H_2SO_4 instead of pure water. The potential is controlled at 0.25 V_{RHE}. The resulting difference-spectra of the O K-edge absorption (Figure 2.5a) and O 1s XP spectra (Figure 2.5b) change drastically. A liquid layer is still present, as the differences of the O K-edge absorption exhibit the features of liquid water, but the O K-edge absorption intensities at about 537 eV and 547 eV increased, while the intensity around 541 eV decreased when compared to pure water (Figure 2.4a-b). This behavior is in good agreement with the study of Niskanen et al.[43], in which the authors report very similar changes in the O K-edge absorption of sulfuric acid at different concentrations measured by inelastic X-ray scattering. The XP difference spectrum has a feature slightly above 532 eV, in addition to the one at about 538 eV. The latter originates from water, while the former fits well to the reported O 1s binding energy of sulfuric acid at low temperatures (532.3 eV).[44] The S 2p contribution at 169 eV shows that sulfate ions can indeed pass (inset of Figure 2.5b). It is also noticeable that the contribution at ~538 eV is not symmetric, due to an increase at ~536 eV.

The observed changes in the O K-edge difference spectra between 0.1 M H_2SO_4 sulfuric acid and pure water in the present study are comparable to the changes observed by Niskanen et al. [43] for 4-8 M H_2SO_4 and pure water, despite the much lower concentration in the present experiment. The reason can be found in the probing depth. In the present study we used the kinetic energy of roughly 400 eV, which just exceeds the energy needed to pass the two layers of graphene. In contrast, X-ray scattering used in the study of Niskanen is a bulk sensitive method. That means, the solid-liquid interface between sulfuric acid and graphene is, in comparison to bulk sulfuric acid, enriched with sulfate ions. The dependency of this effect on the applied potential was not investigated in the present publication.

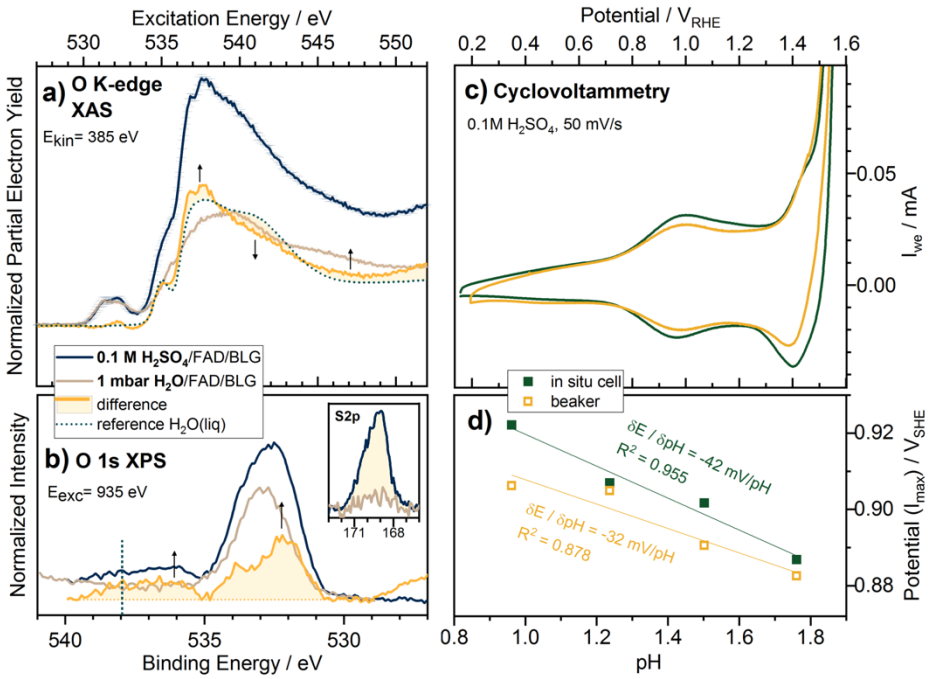

Figure 2.5: a) and b) are analogues to Figure 2.4a) and b) but recorded on (0.1 M H_2SO_4)/FAD/BLG at 0.25V_{RHE}; c) cyclovoltammogram at 50 mV/s and d) the potential shift of the oxidation wave at ~1 V_{RHE} with varying pH of (0.1 M H_2SO_4)/FAD/IrNPs/SLG and HOPG/IrNPs/(0.1 H_2SO_4).

An alternative explanation is that this local pH effect is enhanced in the liquid thin film when compared to bulk electrolyte. We thus compared to an experiment in bulk electrolyte by depositing Ir nanoparticles on highly oriented pyrolytic graphene (HOPG) and recording cyclovoltagramms (CVs) in bulk electrolyte and in the in situ setup at varying concentrations of H_2SO_4. Two exemplifying CVs using 0.1 M H_2SO_4 are given in Figure 2.5c. Their features and general shape match and differ only slightly. The most prominent oxidation feature at ~1 V_{RHE}, which is characteristic for iridium (hydr-)oxides and known to shift with pH,[45,46] was then used to track the pH shift. The results are shown in Figure 2.5d. Both the beaker experiment and the in situ cell behave similarly, though there are differences in the slope of the linear fits. We, therefore, cannot exclude that the local pH at the graphene-electrolyte interface in our sample assembly is different from what it would have been in bulk electrolyte. However, the difference is much smaller than 1 pH unit, based on the potential shift between the curves.

We have seen that the sample architecture we suggest can provide a thin-film of sulfuric acid containing water, protons, and sulfate ions between a polymer membrane and graphene. In two further examples, we can show that a proper transport of ions in this approach is not limited to the example of sulfuric acid but can indeed be extended to other solutions. First, Figure 2.18 shows that the addition of chloride ions to 0.1 M H_2SO_4 leads to a strong increase in Cl 2p signal on the side of graphene. Second, we demonstrate that a copper sulfate solution behind the membrane allows copper deposition on graphene or its dissolution in a reversible fashion (compare “Showcase 2”).

2.4.5 Interaction with an X-ray beam

Soft X-rays or fast electrons interact with the polymer membrane, which then suffers from radiation damage. Examples are given in Figure 2.6. Part a) shows the image of a Nafion membrane after ~20 minutes of beam exposure at the ISISS beamline, which equates to a beam dose of about 0.3 Gy assuming the beam is completely absorbed (see Experimental Section). The damage is obvious in the elongated rectangles, which roughly resemble the shape of the beam spot at the ISISS beamline at 111 µm slit size. Although the exact route of damage is unknown, the bubbles in Figure 2.6a point towards radiolysis of the liquid and the polymer.

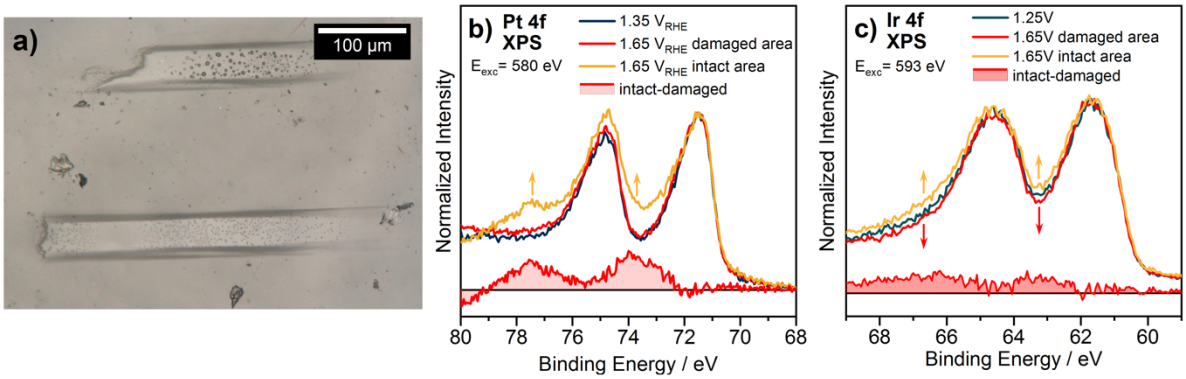

Figure 2.6: Interaction with a soft X-ray beam; a) image obtained from an optical microscope of Nafion/Ir NPs/SLG after intensive beam exposure; b) operando Pt 4f XP spectra of 0.1 M H_2SO_4/Nafion/Pt/SLG and c) operando Ir 4f XP spectra of 0.1 M H_2SO_4/Nafion/Ir NPs/SLG recorded at intact and damaged measurement positions; their difference is shown in red.

The induced damage leads to a limited charge transport through the membrane. The evidence is provided in Figure 2.6b and c. Both show XP spectra of a metal core level in 0.1 M H_2SO_4 before and after an oxidation step. The oxidized state was recorded in two areas – an area damaged by the beam and a fresh, intact area. In the case of platinum (Figure 2.6b), the intact area, which was only irradiated during data collection for ~80 s, shows the expected oxidation to Pt^{4+} leading to a doublet at ~73.5 eV and ~77.5 eV.[17,28] However, the area irradiated for about 20 min shows almost no change after the oxidation step. A similar effect can be seen with oxidized iridium nanoparticles on Nafion (Figure 2.6c). By increasing the potential from 1.25 V_{RHE} to 1.65 V_{RHE}, it is expected that the spectrum broadens towards high binding energies.[10,27] This is not the case for the measurement on the same spot, after 15 minutes of beam exposure, but is true for the fresh spot, which was only irradiated during the data acquisition of 150 s. Consequently, the change caused by the applied bias is slow or hindered when the area is damaged by the beam. This is likely to be caused by a limited mass transport after damage. A loss of electrical conductivity is unlikely, since the binding energy of the metal is stable with potential, even after damage. We recommend not to exceed a beam dose of ~0.1 Gy for a reliable result (see Experimental Section).

2.4.6 Interaction with an electron beam

In the case of electron microscopy, the beam dose can be regulated by acceleration voltage, emission current, and magnification, but radiolysis of liquids caused by an electron beam is a known phenomenon for SEM[47,48] and TEM.[14,15,49] We optimized the acceleration voltage and the magnification for the operando experiments in the environmental scanning electron microscope. In order to demonstrate the damage caused by an electron beam, copper deposition in 50 mM $CuSO_4$/FKD/BLG is chosen as an example

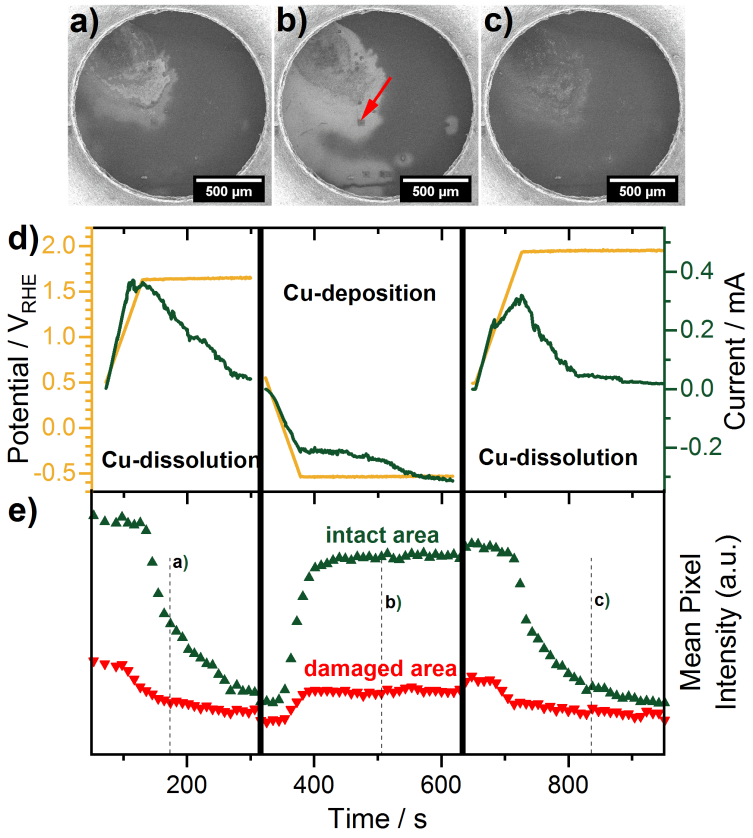

Figure 2.7: Operando SEM micrographs of (50 mM Cu_SO_4)/FKD/BLG at a) 1,65 V_{RHE}, b) -0,55 V_{RHE}, and c) 1.95 V_{RHE} with d) the respective potential and current and e) the mean pixel intensity of a damaged area (dark rectangle indicated in part b) by a red arrow) and of a pixel array with the same size slightly above the damaged area.

. The upper micrographs (Figure 2.7a-c) show snapshots of copper dissolution and deposition at small magnification. The respective potentials and electrochemical currents are given in Figure 2.7d. The pixel arrays of a damaged area (indicated in Figure 2.7b) and an intact region slightly above it were analyzed for the average pixel intensity, which is given in Figure 2.7e. Respective snapshots (Figure 2.7a-c) are indicated in Figure 2.7e. It becomes evident that a change in the mean brightness is initiated by electrochemical currents. Anodic potentials and positive currents lead to dissolution and a decrease in the mean brightness while cathodic potentials and negative currents increase the mean brightness. This effect is, however, much more pronounced in the intact region compared to the damaged region, pointing towards a strongly limited mass transport after intense exposure to the electron beam.

As hinted in the section about the morphology of the sample, it becomes more evident now, why it is important to provide homogeneity on the length scale of the respective measurement. After investigation of one spot at a given condition, the mass transport on that position will be affected. It is therefore needed to change the position for the next measurement at a new condition. In such an experiment, homogeneity is the prerequisite for a reliable comparison of the findings at different experimental conditions.

2.4.7 Product analysis

For operando investigations of electrocatalysts, product analysis is crucial. In the in situ technique suggested here, it is possible to detect gaseous products, evolving at the working electrode. In our setup for in situ X-ray spectroscopy, for example, a mass spectrometer behind a leak valve was used for the analysis of the gas atmosphere. With this method, an oxygen evolution of 2 nmol/s is well above the detection limit (see Figure 2.19).

2.4.8 Two showcases of in situ electrochemistry

We chose two showcases to illustrate the properties and scope of the in situ setup described above. First, we show the dissolution of ruthenium at anodic potentials with in situ electron microscopy and X-ray spectroscopy. Second, the same two techniques are used to track copper deposition on the graphene cover. In addition to the showcases in the present publication, recently published articles show the electrochemical oxidation of iridium[27] or platinum nanoparticles[28] under acidic conditions.

Showcase 1

The first showcase is the dissolution of ruthenium under anodic potentials. The sample assembly is an FAD membrane covered with a thin layer of sputtered ruthenium metal and SLG. It was activated with 20 cycles between 0 V_{RHE} and 1.15 V_{RHE} at 50 mV/s. The O K-edge absorption of the activated layer shows few signs of oxidation (Figure 2.8a), except for a feature slightly above 531 eV, which could be related to ruthenium hydroxides. Applying an oxidative potential (e.g. 1.25 V_{RHE}) instantly leads to an absorption white line at 529 eV (see Figure 2.8a), which is known for oxidized ruthenium. A further increase of the potential from 1.25 V_{RHE} to 1.45 V_{RHE} leads to a more intense white line. This effect, however, does not sustain for long. The signal from oxidized ruthenium is strongly diminished in a consecutive spectrum about two minutes later (Figure 2.8b). The current of the working electrode is quickly degrading (Figure 2.8c).

An explanation for this behavior is well illustrated by an analogue study in the environmental SEM. We used the same type of sample as in the previous experiment (0.1 M H_2SO_4/FAD/Ru/SLG), but partially covered with SLG. We activated this assembly by 50 voltammetric cycles between 0.05 V_{RHE} and 1.25 V_{RHE} at a rate of 50 mV/s. The micrograph recorded after this treatment shows a layer of ruthenium traversed by cracks. The Ru layer is homogeneously distributed and partially covered with graphene (Figure 2.9a). After polarization of this layer to 1.45 V_{RHE} for 25 minutes and 1.55 V_{RHE} for 4 min, another micrograph was recorded (Figure 2.9b). The bright contrast of the ruthenium layer disappeared in the areas covered with graphene. However, in the areas without a graphene cover, the

ruthenium layer appears unchanged by the treatment. This demonstrates the importance of graphene in this arrangement. By providing conductivity and a wetted environment, electrochemical processes and significant mass transport can occur at pressures below 1 mbar (darker areas in Figure 2.9). Without graphene, these processes are hindered and sluggish (bright areas in Figure 2.9).

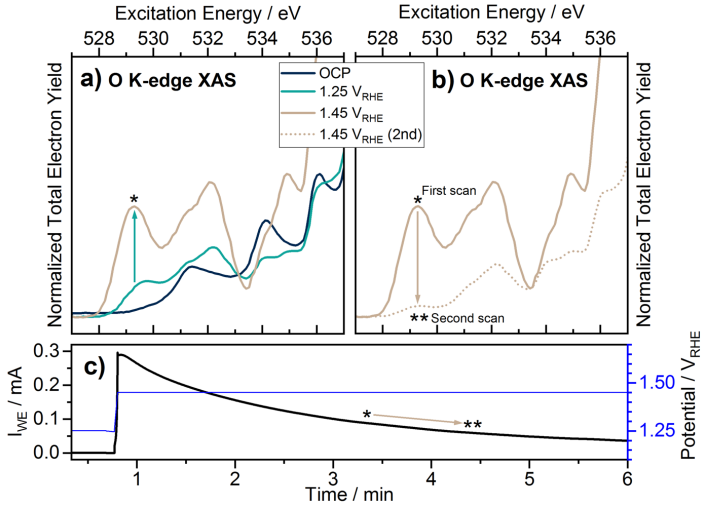

Figure 2.8: Oxidation of (0.1 M H_2SO_4)/FAD/Ru(4 nm thick)/SLG; a) operando O K-edge absorption at three potentials and b) two consecutive spectra at 1.45 V_{RHE}; c) the respective potential and currents during spectroscopy.

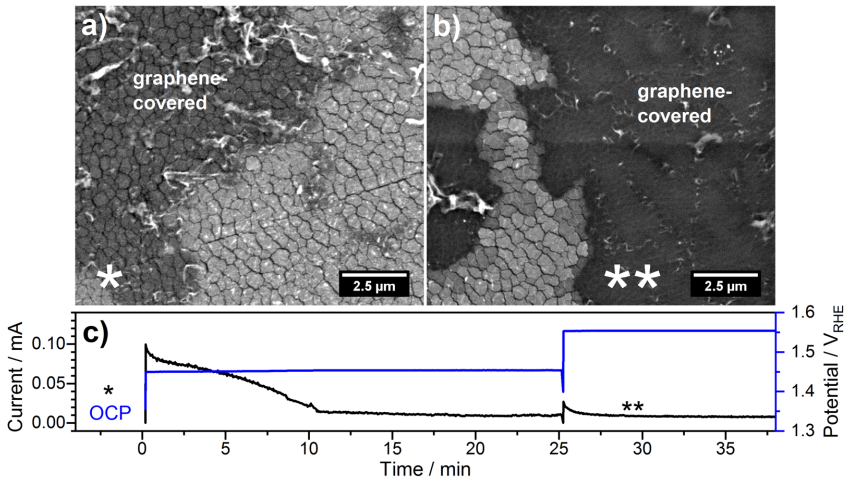

Figure 2.9: Oxidation of (0.1 M H_2SO_4)/FAD/Ru(4 nm thick)/SLG; operando SEM micrographs of a) before and b) after Ru dissolution in the graphene-covered areas; c) the respective potential and current during the experiment.

Showcase 2

The second showcase is the electrodeposition of copper. To enable the transport of Cu cations, we used the FKD membrane and covered it with a bilayer of graphene (BLG). We introduced an aqueous solution of $CuSO_4$ (50 mM) and deposited copper particles at potentials below -1.3 V_{RHE}. The result obtained in the environmental SEM can be seen in Figure 2.10a. The copper particles appear bright and they are stable at potentials < 1 V_{RHE} (see also Figure 2.7). The particles are some tens of nanometers wide. If the potential was increased to 1.8 V_{RHE} the particles dissolve again (see Figure

2.10b). The re-deposition of Cu at -1.3 V_{RHE} (from Figure 2.10c-d) in the same area results in the growth of bright, but fewer particles. This hysteresis is likely caused by the damage of the membrane with the electron beam slowing down the mass transport significantly (see also section about beam interaction).

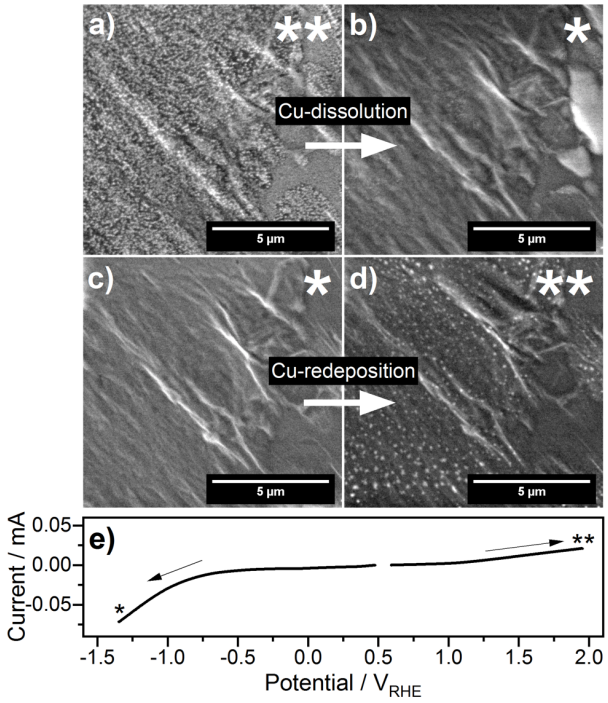

Figure 2.10: Dissolution and re-deposition of Cu; operando SEM micrographs of (50 mM Cu_5O_4)/FKD/BLG at a) d) -1.35 V_{RHE} and b) c) 1.95 V_{RHE}; e) the respective linear sweep voltammetries.

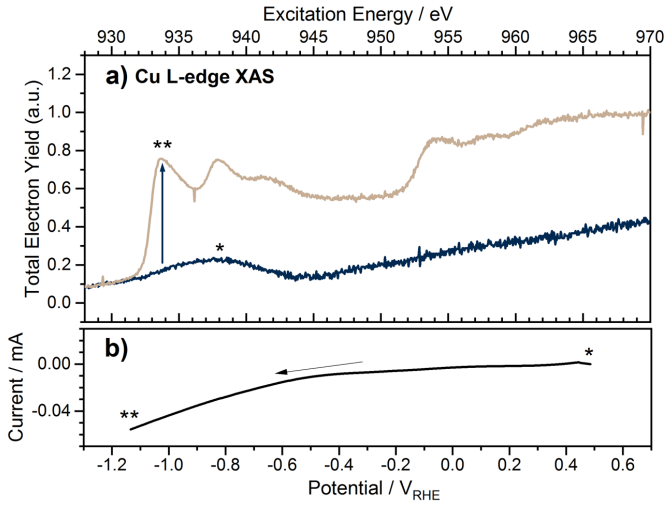

Figure 2.11: Deposition of Cu; a) operando Cu L-edges of (50 mM $CuSO_4$)/FKD/BLG before (dark blue) and after (beige) Cu deposition at -1.15 V_{RHE}; b) the respective linear sweep voltammetry.

The same process can be observed with operando X-ray spectroscopy (Figure 2.11). Again, an aqueous solution of $CuSO_4$ is provided behind an FKD membrane. Figure 2.11a shows the Cu L-edge spectrum

before deposition. A broad background-feature between 935 eV and 940 eV is observed. As soon as copper is deposited at -1.15 V_{RHE}, characteristic absorption resonances of metallic copper [50] appear at 933.7 eV, 937.9 eV, and 941.7 eV.

2.5 Conclusion

We demonstrated a way to investigate the solid-liquid interface by using a sample preparation method that can be done in any chemical lab. The key to our approach is the sample assembly, in which an electrocatalyst is sandwiched between a (bi-)layer of graphene and a permeable membrane in contact with bulk electrolyte. Water and ions pass from the bulk electrolyte through the membrane and form a liquid thin film beneath the graphene blanket. This liquid film is stable at pressures in the mbar range and was found to be similar to bulk liquid. Furthermore, photoelectrons with kinetic energies down to 200 eV can be detected through the liquid thin film and the graphene window, which allows for extremely interface sensitive measurements of solid-liquid interfaces. We show this ability with X-ray photoelectron spectroscopy and scanning electron microscopy – two powerful techniques which are still rarely used for the study of the solid-liquid interface or electrochemical processes, due to technical hurdles. In two showcases, we performed operando X-ray spectroscopy and operando SEM on the same sample types and could follow electrochemical dissolution of ruthenium and the electrodeposition of metallic copper under wet conditions.

2.6 Experimental Section

2.6.1 Sample preparation

We used the following polymer membranes: FAD55 (FAD) and FKD provided by Fumatech; Nafion 117 (Nafion) provided by Sigma Aldrich. Nafion is an ionomer produced by the copolymerization of perfluorinated vinyl ether and tetrafluoroethylene.[51] Both membranes by Fumatech are functionalized polyarylenes, while the FAD membrane is a quaternized polyphenyloxide and the FKD membrane is a sulfonated polyetherketone. All of them were cut to circular disks of 11 mm in diameter but activated and stored them in different ways. FAD disks were soaked for at least three days in 0.5 M Na_2SO_4 solution. The solution was exchanged several times during that treatment. This procedure exchanges bromide ions contained in the membrane with sulfate ions. Samples including FAD membranes were stored in the soaking solution until use. FKD membranes were not activated and stored dry. Nafion disks were purified for 2 h at 80 °C in 3 % H_2O_2 solution and another 2h at the same temperature in 0.5 M H_2SO_4. Samples prepared from Nafion were stored in a dry state until used.

We used the following polymer membranes: FAD55 (FAD) and FKD provided by Fumatech, and Nafion 117 (Nafion) provided by Sigma Aldrich (see Table 2.2 for their basic properties). Nafion is an ionomer produced by the copolymerization of perfluorinated vinyl ether and tetrafluoroethylene.[51] Both membranes by Fumatech are functionalized polyarylenes, while the FAD membrane is a quaternized polyphenyloxide and the FKD membrane is a sulfonated polyetherketone. All of them were cut to

circular disks of 11 mm in diameter but activated and stored them in different ways. FAD disks were soaked for at least three days in 0.5 M Na_2SO_4 solution in order to exchange bromide counter ions for sulfate ions. The solution was exchanged several times during treatment. Residual bromide remains.[27,28] Samples including FAD membranes were stored in the soaking solution until use. FKD membranes were not activated and stored dry. Contamination originating from the FKD membrane was not detected. Nafion disks were rid of carbonaceous contamination for 2 h at 80 °C in 3 % H_2O_2 solution and another 2 h at the same temperature in 0.5 M H_2SO_4. Samples prepared from Nafion were stored in a dry state until used.

Table 2.2: Properties of polymer membranes as specified by the supplier.

	Nafion N117	FAD	FKD
Thickness / µm	183	50-60	68-77
pH range	-	1-9	1-14
Type of exchange	H^+	Anion / H^+	Cation / OH^-
Selectivity / %	-	85[a]	> 95[a]
H^+ / OH^- conductivity or transfer rate	> 0.1[b] S cm^{-1}	8000-10000[c] µmol min^{-1} cm^{-2}	< 250[c] µmol min^{-1} cm^{-2}

[a] measured in concentration cell with 0.1 / 0.5 mol kg-1 KCL at T = 25 °C
[b] conditioned at 100 °C, measured by impedance at 25 °C 52
[c] from pH potential measurement in concentration cell with 0.1 M HCl / 0.1 M NaCl at T = 25 °C

The material of interest was deposited by the DC magnetron sputter coater 208HR by Cressington (Watford, UK). The sputtering process was always carried out at 0.1 mbar argon atmosphere and with a sputtering current of 40 mA. The thickness was controlled by sputtering time. The iridium sputter target was provided by Elektronen-Optik Service GmbH (Dortmund, Germany) and the ruthenium target by ChemPur (Karlsruhe, Germany).

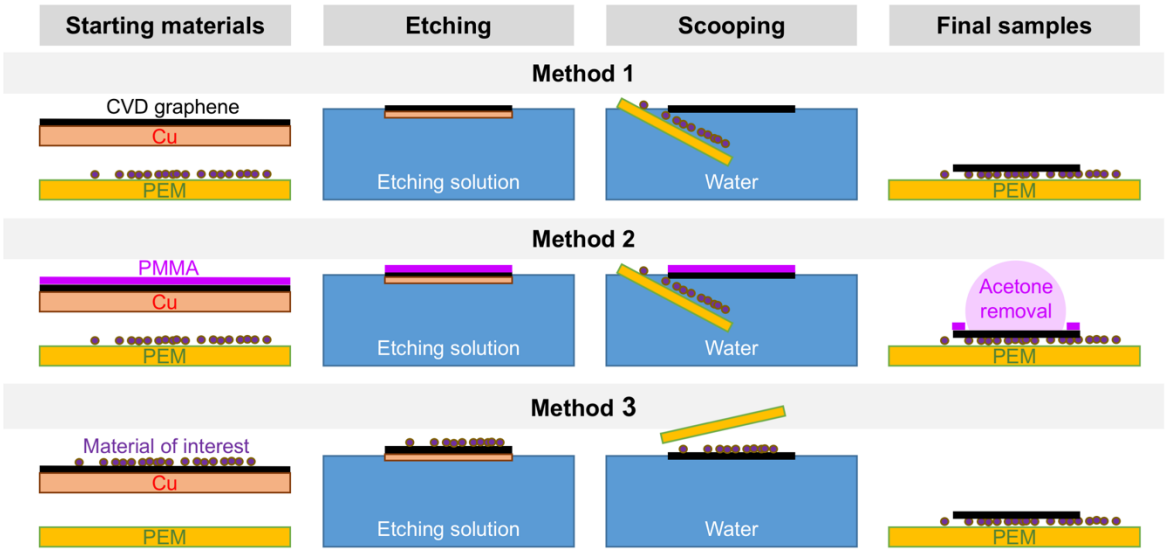

Figure 2.12: Schematics of three sample preparation methods; wet chemical transfer from below (method 1), PMMA-assisted transfer from below (method 2), and a transfer from above (method 3).

The material of interest was deposited by the DC magnetron sputter coater 208HR by Cressington (Watford, UK). The sputtering process was always carried out at 0.1 mbar argon atmosphere and with a sputtering current of 40 mA. The thickness was controlled by sputtering time. The iridium sputter target was provided by Elektronen-Optik Service GmbH (Dortmund, Germany) and the ruthenium target by ChemPur (Karlsruhe, Germany).

Graphene was transferred in a wet chemical method. Graphene on copper foil was purchased from Graphenea in form of a single layer, a PMMA-coated single layer, or a double layer. They were stored as shipped or in the glovebox after being opened. Graphene on copper was cut into rectangular pieces of about 4 mm using scissors and the supporting copper foil was etched in an aqueous solution of 40 g/L $(NH_4)_2S_2O_8$ overnight. After exchanging the solution to pure water, the floating graphene layer, which is visible against a white background, was transferred from below onto the polymer membrane disks (see Figure 2.12). Alternatively, the layer can be picked up from the top, as illustrated in Figure 2.12 (Method 3). Residues of PMMA after transfer were removed dropwise with acetone (Method 2). The samples were dried on air at room temperature after transfer. We assured proper placement of graphene by visual inspection. The quality of graphene was examined with SEM. If the relative placement of graphene on the polymer membrane is relevant, the assembly can be cut after transfer.

2.6.2 Raman spectroscopy

Raman spectra collected using a confocal Raman microscope (TriVista TR557 spectrometer - S&I GmbH) equipped with a 532 nm excitation laser (EL = 2.33 eV) which was focused on the samples using a 50x objective on the samples. The measurement areas were chosen randomly in the relevant sample area. Special care has been taken to avoid laser-induced change or damage. Raman scattering was collected using laser powers between 0.1 and 10 mW for 20 to 1200 s. No significant change of the spectral features was observed over these times.

2.6.3 In situ X-ray spectroscopy

All experiments were performed at the ISISS beamline at BESSY II in Berlin. An exception is the study of relative wetting, which was performed at the UE56-2 PGM1 beamline, also at BESSY II. Both use differentially pumped analyzers designed for pressures in the millibar range. The same measurement chamber was used at the two beamlines. The chamber, including the manipulator, was designed for the purpose of electrochemical in situ studies and has been shown earlier.[36] The cell design used in this publication is shown in Figure 2.13a. The main body made of PEEK houses the tip of the reference electrode and the counter electrode in form of a curled platinum wire (see Figure 2.13a and c). Both are in a stream of liquid provided through PEEK tubing. The polymer membrane is mounted on the front, supported by a grid and sealed by an o-ring. The pressure from the top is provided by a lid made of glassy carbon or niobium with a boron-doped diamond coating. A photograph of a mounted cell is given in Figure 2.13b, a technical drawing of the cross section in Figure 2.13c.

During the experiments, potentials were referenced to the Ag/AgCl electrode DRIREF-2SH, which was stored in saturated KCl solution between experiments. The working electrode including graphene and the cover lid was grounded to the hemispherical analyzer. An exception is data of Figure 2.3b, in which

the electrolyte was grounded, and the recorded signal was shifted by the applied potential. The latter procedure therefore includes changes in the work function of the sample. All potentials were corrected for pH and iR, but we neglected possible deviations caused by incomplete screening of the surface charge,[34] whose magnitude was not measured. For reasons of the latter, the significant figures of the calculated potentials against the reversible hydrogen electrode (RHE) might not be adequate. During the experiment the pressure ranged from $5.0 \cdot 10^{-2}$ to $1.5 \cdot 10^{-1}$ mbar. In the case of pressure control, additional water vapor was added to the chamber via a low pressure-difference mass flow controller by Bronkhorst (Ruurlo, Netherlands), and a PID-controlled, pressure-regulating valve by Pfeiffer Vacuum GmbH (Asslar, Germany) was used to keep the pressure in the chamber constant.

The dose of the beam was calculated by dividing the total energy per time by the mass of the membrane in the area of the beam at a given thickness.[53] We assumed full absorption of the beam. For the example of a Nafion 117 membrane (183 µm thick) irradiated at the ISISS beamline with an excitation energy of 800 eV (flux(800eV) ≈ $1 \cdot 10^{11}$ photons/s) and a beam size of 150x100 µm we obtain:

$$dose/sec = \frac{energy/sec}{mass} = \frac{1 \cdot 10^{11} photons/s \cdot 800 eV/photon}{2 \mu g/\mu m^3 \cdot 1.5 \cdot 10^4\ \mu m^2 \cdot 183\ \mu m} \qquad \text{(Equation 1)}$$

$$dose/sec \approx 1.5 \cdot 10^9 \frac{MeV}{s \cdot kg} = 0.24\, mGy/s$$

where we assumed monochromized radiation and neglected higher-order contributions to the beam. A measurement of 3 minutes would under the stated assumptions result in ~0.04 Gy. We recommend avoiding beam doses of above > 0.1 Gy for reliable results. This recommendation is based on experience at the ISISS beamline investigating OER catalysts under acidic and basic conditions, as well as copper deposition. After about 7 mins of measurements at the ISISS beamline, the measurement spot was notably affected by radiation damage.

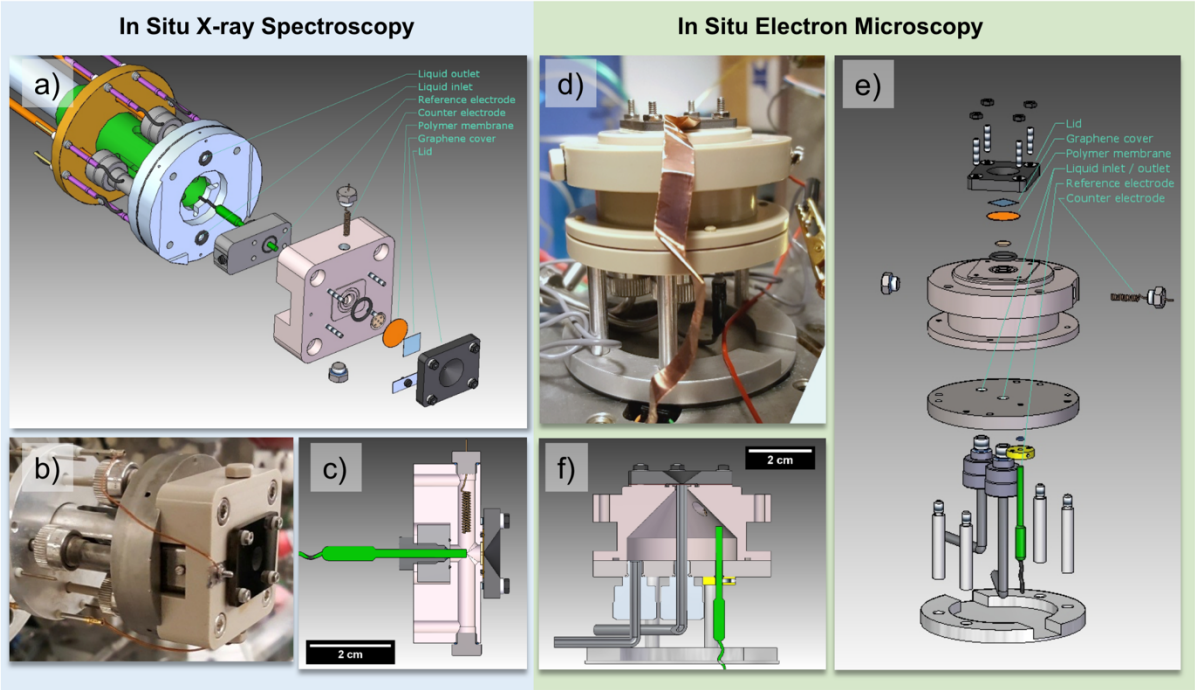

Figure 2.13: Cell for in situ spectroscopy with a) exploded view, b) photograph of a mounted cell, and c) cross section; cell for in situ electron microscopy with d) a photograph of the mounted cell, e) the exploded view, and f) the cross section.

2.6.4 In situ electron microscopy

Environmental electron microscopy was carried out on a modified scanning electron microscope (SEM) FEI Quanta 200 FEG. All measurements were carried out at an acceleration voltage of 5 kV. The gas mixture was composed of Ar, dosed with 1 mL/min, and H_2O leaking from the in situ cell. The operating pressure during experiments was around 0.2 mbar. A photograph of the home-built in situ cell is shown in Figure 2.13d, an exploded view in Figure 2.13e. The cell provides the same sample surrounding as the in situ cell for X-ray spectroscopy described above. The counter and reference electrode are chosen as described above. However, the reference and counter electrode are placed differently, and the electrolyte exchange is realized in another way: the cell is filled from below, while the outlet is a tube reaching just below the membrane. Reference and counter electrode are immersed in the liquid but have different spacing to the working electrode. A cross section is provided in Figure 2.13f.

2.6.5 Data analysis

The O K-edge absorption was calibrated to the 3p-Rydberg state of gas phase water at 537.25 eV[40]. The excitation energy in the case of X-ray photoelectron spectroscopy was calibrated with tables created by using the Fermi edge of a gold foil during the same week. The uncertainty using this method is ~0.1 eV for the beamlines we used.

A self-made Python-based script was used to process the O K-edge absorption spectra. It accounts for energy calibration, the ring current of the synchrotron, and the flux of the beamline. It also normalizes

to zero and one at given excitation energies. Furthermore, it compensates for gas phase attenuation of the X-rays as in reference [54]. The flux reference was recorded on a gold foil free of oxygen.

Integrated intensities of F 1s (Figure 2.3c) were obtained by subtracting a Shirley background and integrating the total area. The results were corrected for cross section and an averaged asymmetry parameter, obtained from the tables of Yeh and Lindau,[55] and the flux of the beamline. The depth profiling was performed on four positions and averaged. The average deviation from the mean is given as an error.

The wetting of a sample (compare Figure 2.4) was obtained by normalizing the O K-edge absorption spectra to their integrated intensities up to 533.5 eV. Since this pre-edge cannot belong to the contribution of liquid water, this normalization should scale the contributions of carbon-oxygen species also in the region above 534 eV, in which liquid water contributes. This procedure assumes that the carbonaceous species are similar in the compared samples. A reference of liquid water obtained by Schreck and Wernet [38] was fitted to the difference of two absorption spectra that should be compared by using a least-square algorithm. The edge jump of the reference spectrum at 550 eV was used to determine the change in wetting.

2.7 Supporting Information

2.7.1 Raman and graphene quality

Lorentzian functions were used for fitting the graphene-characteristic peaks between 1200 – 2800 cm^{-1}, namely D, G, and 2D. However, the D' peak had always zero contribution in peak deconvolutions. In Figure 2.14 spectral parameters (average of at least 5 measurements at random positions) collected from i) SLG or ii) BLG transferred onto SiO_2/Si using a PMMA-free transfer method, iii) SLG transferred onto SiO_2/Si using a PMMA-assisted transfer method. Reference measurements of the width and position were measured on HOPG and are given as horizontal lines in Figure 2.14. The reference spectra showed no D peak; the measured position of G was found to be 1578 cm^{-1} with a FWHM of ~14 cm^{-1}, which are values consistent with previous reports.[56] By these measures, all SLG and BLG samples exhibited values close to HOPG. In addition, they demonstrated an average I_D/I_G of ca. 0.1 (integrated intensity ratio) showing good structural quality of the graphene. Observation of a sharp and symmetric 2D peak, which is well fitted with a single Lorentzian, and an I_{2D}/I_G of ca. 4 for SLG samples confirm their monolayer character.[32] Although quite small, the measured standard deviations of the spectral parameters (also between samples) can be related to the strain and doping introduced during the transfer,[57,58] as well as electronic coupling and grain rotation effects in the case of BLG.[59] Among these samples, the spectral parameters measured for SLG transferred with PMMA are closest to unstrained and undoped SLG[57,60] as well as the HOPG reference.[56] The second best quality was obtained with PMMA-free transfer of BLG, most likely due to its enhanced macroscopic mechanical strength (for transfer), than SLG. Engineering growth parameters to enhance mechanical strength of SLG [61,62] might help improving structural quality of SLG after wet transfer without PMMA.

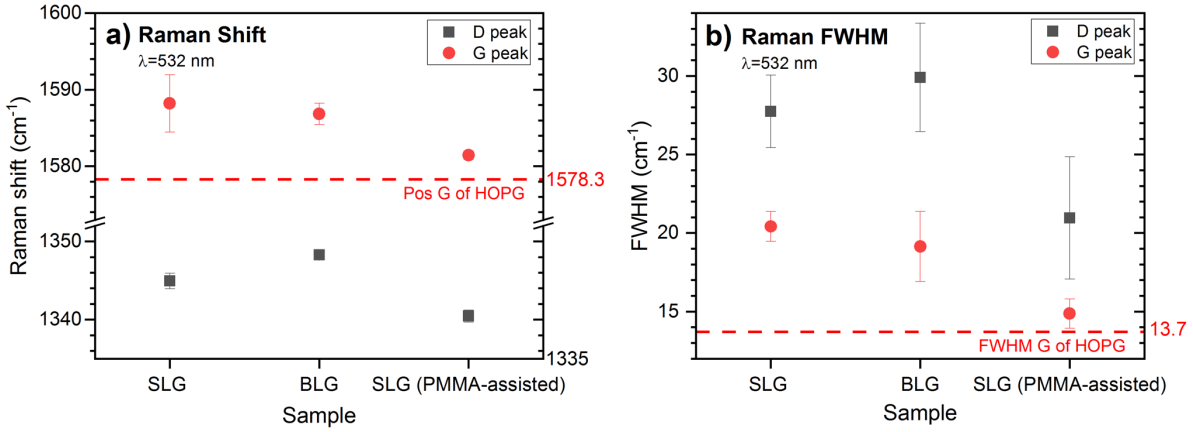

Figure 2.14: The average a) Raman shift and b) FWHM of the Lorentzian functions fitted to the Raman spectra of SLG or BLG on Si/SiO2; SLG and BLG were transferred with the PMMA-free method, unless otherwise noted; dotted lines indicate values from reference measurements on HOPG.

2.7.2 Wetting

In the wetting experiments, the O K-edge absorption spectra are compared by scaling them to the integrated pre-edge intensity at around 532 eV and subtracting them from each other. In this way the carbonaceous contributions are grossly eliminated. The remaining oxygen species are seen in the

difference and were found to belong mostly to the liquid thin film. If the measurements at 0.1 and 1 mbar are scaled to their pre-edge, the reference spectrum of liquid water fits well to their difference (see Figure 2.15b). However, increasing the pressure from 1 mbar to 5 mbar leads to a considerable change in line shape (see Figure 2.15a), which causes a mismatch of their difference and the reference spectrum (see Figure 2.15c). The measurements are not comparable and cannot be used for evaluation of the change in wetness.

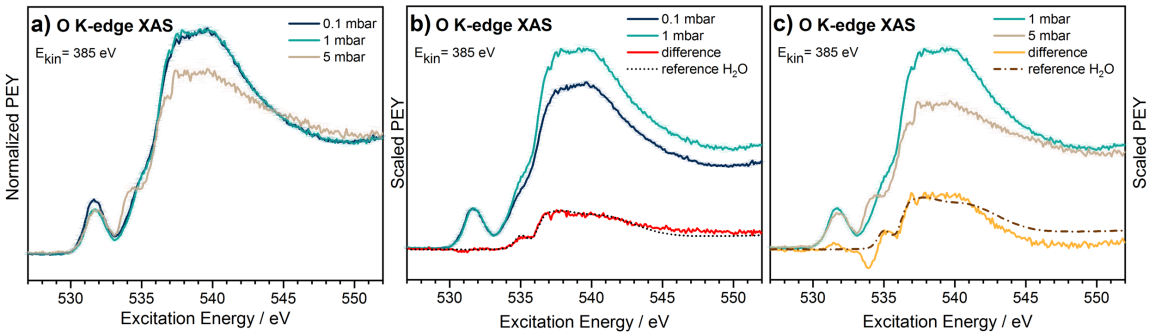

Figure 2.15: O K-edge absorption of H_2O(liq.)/FAD/BLG at 0.1, 1, and 5 mbar; a) normalized to the edge jump at 552 eV and b)-c) scaled to the pre-edge absorption feature; a reference spectrum of liquid water was obtained from Schreck et al. [38] and fitted to the differences.

In order to describe how the water backpressure, the number of graphene layers, and the effect of bulk liquid water behind the PEM influence the liquid thin-film, we will discuss the relative change in wetting when one of the parameters is varied. The change in wetting (CIW) is defined as the relative contribution of liquid water to the O K-edge absorption at 550 eV comparing the initial and final condition:

$$CIW = \frac{I_{550eV}(H_2O\ ref)}{I_{550eV}(initial)} \approx \frac{I_{550eV}(final) - I_{550eV}(initial)}{I_{550eV}(initial)} \qquad \text{(Equation 2)}$$

with the O K-edge absorption intensity at 550 eV of the final and initial condition (see also Figure 2.16a). The absorption spectra used for this analysis were normalized to their integrated pre-edge intensity, as described in the Experimental Section of the main text. The CIW is thereby defined as the relative contribution of liquid water to the O K-edge absorption edge-jump when the measurements of the final and the initial condition are compared (exemplified in Figure 2.16a). This means, CIW is a relative measure of how much liquid can be found in the probed volume. Since we have chosen to detect secondary electrons in a narrow window of kinetic energy (centered at 385 eV) as a partial electron yield signal of the absorption, we expect a probing depth of a few nanometer. We varied three parameters influencing the wetting: first, the partial pressure of gas phase water, which was controlled at 0.1, 1.0, or 5.0 mbar; second, the supply of bulk liquid water from the backside of the polymer membrane, and third, the number of graphene layers deposited on the membrane, namely single and double layers. The result is shown in Figure 2.16b.

A weak effect on liquid within the probing depth is observed when increasing the backpressure of water from 0.1 to 1 mbar (top, Figure 2.16b), unless the membrane is already wetted from the back.

The increase from 1 to 5 mbar could not be evaluated (see Figure 2.15). Wetting the membrane from the backside leads to larger CIW (center of Figure 2.16b, gas → liq.). The gain is most pronounced for 1 mbar but is already significant at 0.1 mbar, which further supports that increased backpressure can aid the wetting if the sample is wetted from the backside with liquid water. Why the CIW is smaller in a denser gas atmosphere (5 mbar) is less clear. The reason could be that wetting from the back is less important at this pressure, or interactions with the dense gas phase, i.e. photoelectrons interacting with space charges, alter the probing depth. In addition, the analysis is complicated by changes in the spectral shape at 5 mbar (see supporting information). The number of graphene layers (bottom Figure 2.16b) affects the CIW marginally if the samples are not wetted from the back. The CIW is negative when the liquid thin film has formed, i.e. using wetting from the back. The most likely explanation is that BLG has a larger contribution to the O K pre-edge in, which leads to an apparent reduction in our analysis (the spectra are normalized to the pre-edge, see Experimental Section of the main text for more details). Unfortunately, a direct comparison to the blank polymer membrane could not be made, due to charging of the samples.

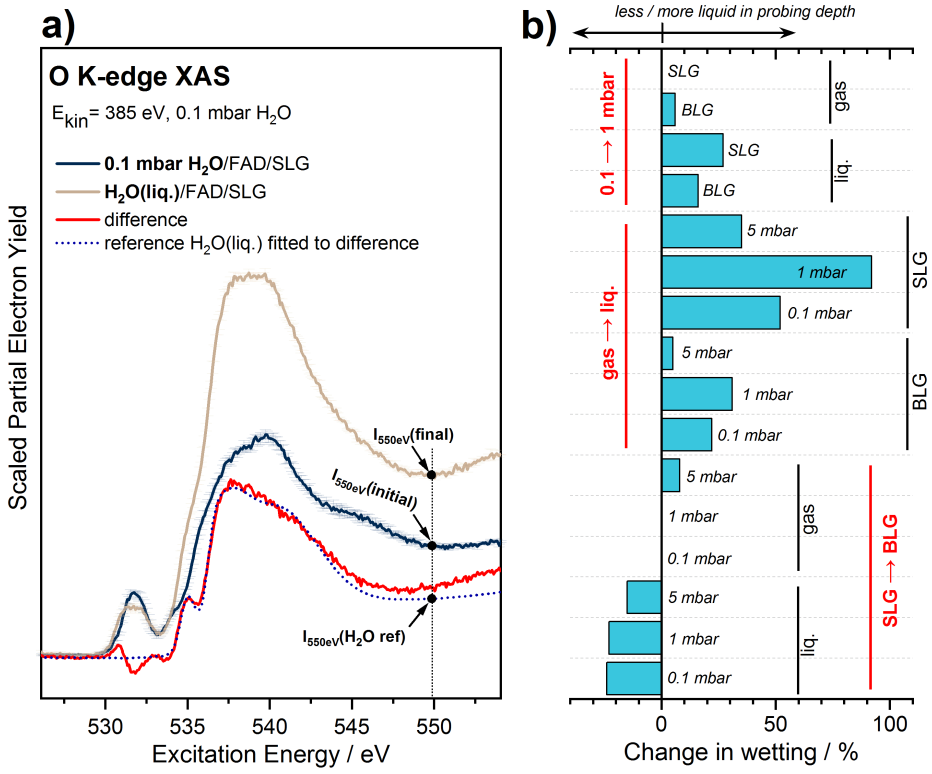

Figure 2.16: a) Pre-edge scaled O K-edge absorption of (0.1 mbar H_2O)/FAD/SLG and H_2O(liq.)/FAD/BLG in 0.1 mbar H_2O, their difference, and a comparison to a liquid water reference are shown; the reference absorption spectrum of liquid water was provided by Schreck et al.[38]; intensities referenced in Equation 2 are marked by black dots; b) Change in wetting (CIW, see Equation 1) of FAD/graphene when a parameter (bold, red font in the figure) is changed; more details can be found in the Experimental Section of the main text; the parameter change "gas → liq." stands for the introduction of liquid water at the backside of the membrane; constant parameters are given in a black font; an example: the seventh bar from the top shows that the sample H_2O(liq.)/FAD/SLG in 0.1 mbar H_2O, relative to the sample

FAD/SLG in 0.1 mbar H_2O, has a 50 % higher contribution of H_2O(liq.) to the total number of oxygen species within the probing depth (see also part a) of the figure and Equation 2).

That proper wetting is also possible with a layer of material between the polymer membrane and the graphene sheet, is shown in the following. Figure 2.17 contains two O K-edges in a wet state. A layer of gold (mass equivalent to a layer of 2 nm, forms 10 nm wide nanoparticles on carbon) is the first example (Figure 2.17a), the second is a layer of platinum with a thickness between 4 and 6 nm. Both show an absorption feature at 535 eV, which is characteristic for bulk liquid water (reference in the main text). Also, the main- and post-edge features at ~537 eV and 541 eV are visible without further analysis.

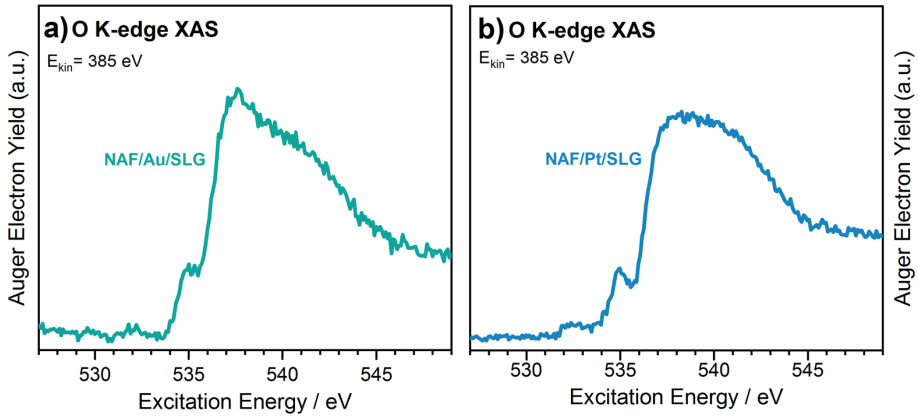

Figure 2.17: O K-edge absorption of a) H_2SO_4/NAF/Au/SLG at 0.75 V_{RHE} and b) H_2SO_4/NAF/Pt/SLG at open circuit potential.

2.7.3 Conduction of ions

Figure 2.18 shows the comparison of Cl 2p XP spectra before and after introduction of KCl in 0.06 M H_2SO_4. The chloride anion passed the FAD membrane without applied potential.

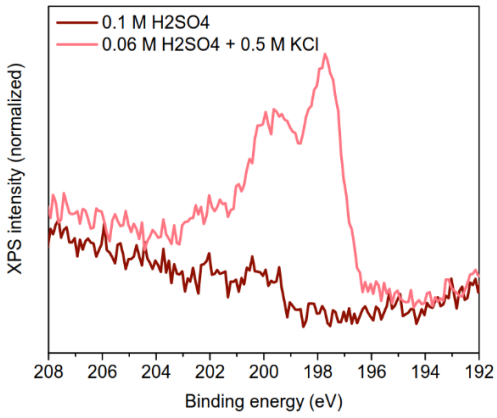

Figure 2.18: Cl 2p XP spectra before and after introduction of KCl in H_2SO_4/NAF/SLG.

2.7.4 Gas detection

Gaseous products during oxygen evolution of an iridium oxide catalyst were recorded (Figure 2.19). A potential of 1.4 V_{RHE} was held for about 12 minutes. The current falls from a peak to 0.8 mA over that period. Assuming the complete current is converted into oxygen, the given current would correspond

2 nmol/s oxygen. This amount is clearly detected in the mass spectrum. It takes, however, about 5 minutes to equilibrate, which limits the time resolution of product detection.

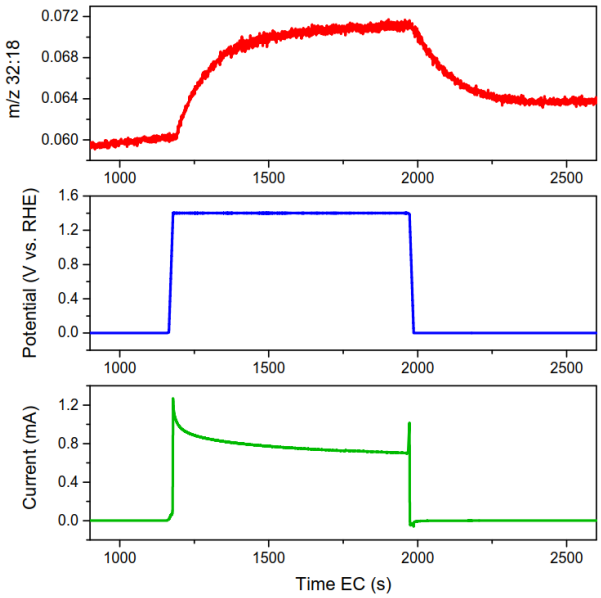

Figure 2.19: Trace of O_2 (m/z=32) relative to water (m/z=18) (top); potential (middle), and current (bottom) of 0.1 M H_2SO_4/Nafion/IrOx/SLG versus the elapsed time of the experiment.

2.8 Bibliography

(1) Arrigo, R.; Hävecker, M.; Schuster, M. E.; Ranjan, C.; Stotz, E.; Knop-Gericke, A.; Schlögl, R. In Situ Study of the Gas-Phase Electrolysis of Water on Platinum by NAP-XPS. *Angew. Chemie - Int. Ed.* 2013, *52* (44), 11660–11664.

(2) Pfeifer, V.; Jones, T. E.; Velasco Vélez, J. J.; Arrigo, R.; Piccinin, S.; Hävecker, M.; Knop-Gericke, A.; Schlögl, R. In Situ Observation of Reactive Oxygen Species Forming on Oxygen-Evolving Iridium Surfaces. *Chem. Sci.* 2017, *8*, 2143–2149.

(3) Velasco-Velez, J. J.; Pfeifer, V.; Hävecker, M.; Weatherup, R. S.; Arrigo, R.; Chuang, C.-H.; Stotz, E.; Weinberg, G.; Salmeron, M.; Schlögl, R.; et al. Photoelectron Spectroscopy at the Graphene-Liquid Interface Reveals the Electronic Structure of an Electrodeposited Cobalt/Graphene Electrocatalyst. *Angew. Chemie Int. Ed.* 2015, *54* (48), 14554–14558.

(4) Ataka, K. I.; Yotsuyanagi, T.; Osawa, M. Potential-Dependent Reorientation of Water Molecules at an Electrode/Electrolyte Interface Studied by Surface-Enhanced Infrared Absorption Spectroscopy. *J. Phys. Chem.* 1996, *100* (25), 10664–10672.

(5) Hunt, J. H.; Guyot-Sionnest, P.; Shen, Y. R. Observation of C-H Stretch Vibrations of Monolayers of Molecules Optical Sum-Frequency Generation. *Chem. Phys. Lett.* 1987, *133* (3), 189–192.

(6) Axnanda, S.; Crumlin, E. J.; Mao, B.; Rani, S.; Chang, R.; Karlsson, P. G.; Edwards, M. O. M.; Lundqvist, M.; Moberg, R.; Ross, P.; et al. Using "Tender" X-Ray Ambient Pressure X-Ray Photoelectron Spectroscopy as A Direct Probe of Solid-Liquid Interface. *Sci. Rep.* 2015, *5*, 9788.

(7) Guo, H.; Strelcov, E.; Yulaev, A.; Wang, J.; Appathurai, N.; Urquhart, S.; Vinson, J.; Sahu, S.; Zwolak, M.; Kolmakov, A. Enabling Photoemission Electron Microscopy in Liquids via Graphene-Capped Microchannel Arrays. *Nano Lett.* 2017, *17*, 1034–1041.

(8) Nemšák, S.; Strelcov, E.; Duchoň, T.; Guo, H.; Hackl, J.; Yulaev, A.; Vlassiouk, I.; Mueller, D. N.; Schneider, C. M.; Kolmakov, A. Interfacial Electrochemistry in Liquids Probed with Photoemission Electron Microscopy. *J. Am. Chem. Soc.* 2017, *139* (50), 18138–18141.

(9) Knop-Gericke, A.; Pfeifer, V.; Velasco-Velez, J.-J.; Jones, T.; Arrigo, R.; Hävecker, M.; Schlögl, R. In Situ X-Ray Photoelectron Spectroscopy of Electrochemically Active Solid-Gas and Solid-Liquid Interfaces. *J. Electron Spectrosc. Relat. Phenom.* 2017, *221*, 10–17.

(10) Velasco-Vélez, J. J.; Jones, T. E.; Streibel, V.; Hävecker, M.; Chuang, C.-H.; Frevel, L.; Plodinec, M.; Centeno, A.; Zurutuza, A.; Wang, R.; et al. Electrochemically Active Ir NPs on Graphene for OER in Acidic Aqueous Electrolyte Investigated by in Situ and Ex Situ Spectroscopies. *Surf. Sci.* 2019, *681*, 1–8.

(11) Williamson, M. J.; Tromp, R. M.; Vereecken, P. M.; Hull, R.; Ross, F. M. Dynamic Microscopy of Nanoscale Cluster Growth at the Solid–Liquid Interface. *Nat. Mater.* 2003, *2* (8), 532–536.

(12) Carbonio, E. A.; Velasco-Velez, J.-J.; Schlögl, R.; Knop-Gericke, A. Perspective—Outlook on Operando Photoelectron and Absorption Spectroscopy to Probe Catalysts at the Solid-Liquid Electrochemical Interface. *J. Electrochem. Soc.* 2020, *167* (5), 054509.

(13) De Jonge, N.; Ross, F. M. Electron Microscopy of Specimens in Liquid. *Nat. Nanotechnol.* 2011, *6* (11), 695–704.

(14) Ross, F. M. Opportunities and Challenges in Liquid Cell Electron Microscopy. *Science* 2015, *350* (6267).

(15) Hodnik, N.; Dehm, G.; Mayrhofer, K. J. J. Importance and Challenges of Electrochemical in Situ

Liquid Cell Electron Microscopy for Energy Conversion Research. *Acc. Chem. Res.* 2016, *49* (9), 2015–2022.

(16) Sanchez Casalongue, H. G.; Ng, M. L.; Kaya, S.; Friebel, D.; Ogasawara, H.; Nilsson, A. In Situ Observation of Surface Species on Iridium Oxide Nanoparticles during the Oxygen Evolution Reaction. *Angew. Chem., Int. Ed.* 2014, *53*, 7169–7172.

(17) Saveleva, V. A.; Papaefthimiou, V.; Daletou, M. K.; Doh, W. H.; Ulhaq-Bouillet, C.; Diebold, M.; Zafeiratos, S.; Savinova, E. R. Operando Near Ambient Pressure XPS (NAP-XPS) Study of the Pt Electrochemical Oxidation in H2O and H2O/O2 Ambients. *J. Phys. Chem. C* 2016, *120* (29), 15930–15940.

(18) Nappini, S.; Matruglio, A.; Naumenko, D.; Dal Zilio, S.; Bondino, F.; Lazzarino, M.; Magnano, E. Graphene Nanobubbles on TiO2 for In-Operando Electron Spectroscopy of Liquid-Phase Chemistry. *Nanoscale* 2017, *9*, 4456–4466.

(19) Morozov, S. V.; Novoselov, K. S.; Katsnelson, M. I.; Schedin, F.; Elias, D. C.; Jaszczak, J. A.; Geim, A. K. Giant Intrinsic Carrier Mobilities in Graphene and Its Bilayer. *Phys. Rev. Lett.* 2008, *100* (1), 11–14.

(20) Bolotin, K. I.; Sikes, K. J.; Hone, J.; Stormer, H. L.; Kim, P. Temperature-Dependent Transport in Suspended Graphene. *Phys. Rev. Lett.* 2008, *101* (9), 1–4.

(21) Salvat, F.; Jabloski, A.; Powell, C. J. NIST Standard Reference Database (SRD) 64. National Institute of Standards and Technology, USA: Gaithersburg 2002.

(22) Nair, R. R.; Blake, P.; Grigorenko, A. N.; Novoselov, K. S.; Booth, T. J.; Stauber, T.; Peres, N. M. R.; Geim, A. K. Fine Structure Constant Defines Visual Transparency of Graphene. *Science* 2008, *320* (5881), 1308.

(23) Basov, D. N.; Fogler, M. M.; Lanzara, A.; Wang, F.; Zhang, Y. Colloquium: Graphene Spectroscopy. *Rev. Mod. Phys.* 2014, *86* (3), 959–994.

(24) Mutus, J. Y.; Livadaru, L.; Robinson, J. T.; Urban, R.; Salomons, M. H.; Cloutier, M.; Wolkow, R. A. Low-Energy Electron Point Projection Microscopy of Suspended Graphene, the Ultimate 'Microscope Slide.' *New J. Phys.* 2011, *13* (6), 063011.

(25) Longchamp, J.-N.; Latychevskaia, T.; Escher, C.; Fink, H.-W. Low-Energy Electron Transmission Imaging of Clusters on Free-Standing Graphene. *Appl. Phys. Lett.* 2012, *101* (11), 113117.

(26) Miyauchi, H.; Ueda, Y.; Suzuki, Y.; Watanabe, K. Electron Transmission through Bilayer Graphene: A Time-Dependent First-Principles Study. *Phys. Rev. B* 2017, *95* (12), 1–3.

(27) Frevel, L. J.; Mom, R.; Velasco-Vélez, J.-J.; Plodinec, M.; Knop-Gericke, A.; Schlögl, R.; Jones, T. E. In Situ X-Ray Spectroscopy of the Electrochemical Development of Iridium Nanoparticles in Confined Electrolyte. *J. Phys. Chem. C* 2019, *123* (14), 9146–9152.

(28) Mom, R.; Frevel, L.; Velasco-Vélez, J.-J.; Plodinec, M.; Knop-Gericke, A.; Schlögl, R. The Oxidation of Platinum under Wet Conditions Observed by Electrochemical X-Ray Photoelectron Spectroscopy. *J. Am. Chem. Soc.* 2019, *141* (16), 6537–6544.

(29) Velasco-Velez, J.-J.; Mom, R. V.; Sandoval-Diaz, L.-E.; Falling, L. J.; Chuang, C.-H.; Gao, D.; Jones, T. E.; Zhu, Q.; Arrigo, R.; Roldan Cuenya, B.; et al. Revealing the Active Phase of Copper during the Electroreduction of CO 2 in Aqueous Electrolyte by Correlating In Situ X-Ray Spectroscopy and In Situ Electron Microscopy . *ACS Energy Lett.* 2020, *5* (6), 2106–2111.

(30) Martin, H. B.; Argoitia, A.; Landau, U.; Anderson, A. B.; Angus, J. C. Hydrogen and Oxygen

Evolution on Boron-Doped Diamond Electrodes. *J. Electrochem. Soc.* 1996, *143* (6), L133-136.

(31) Lehmani, A.; Durand-Vidal, S.; Turq, P. Surface Morphology of Nafion 117 Membrane by Tapping Mode Atomic Force Microscope. *J. Appl. Polym. Sci.* 1998, *68* (3), 503–508.

(32) Ferrari, A. C.; Meyer, J. C.; Scardaci, V.; Casiraghi, C.; Lazzeri, M.; Mauri, F.; Piscanec, S.; Jiang, D.; Novoselov, K. S.; Roth, S.; et al. Raman Spectrum of Graphene and Graphene Layers. *Phys. Rev. Lett.* 2006, *97* (18), 1–4.

(33) Cançado, L. G.; Jorio, A.; Ferreira, E. H. M.; Stavale, F.; Achete, C. A.; Capaz, R. B.; Moutinho, M. V. O.; Lombardo, A.; Kulmala, T. S.; Ferrari, A. C. Quantifying Defects in Graphene via Raman Spectroscopy at Different Excitation Energies. *Nano Lett.* 2011, *11* (8), 3190–3196.

(34) Strelcov, E.; Arble, C.; Guo, H.; Hoskins, B. D.; Yulaev, A.; Vlassiouk, I. V.; Zhitenev, N. B.; Tselev, A.; Kolmakov, A. Nanoscale Mapping of the Double Layer Potential at the Graphene-Electrolyte Interface. *Nano Lett.* 2020, *20* (2), 1336–1344.

(35) Kraus, J.; Reichelt, R.; Günther, S.; Gregoratti, L.; Amati, M.; Kiskinova, M.; Yulaev, A.; Vlassiouk, I.; Kolmakov, A. Photoelectron Spectroscopy of Wet and Gaseous Samples through Graphene Membranes. *Nanoscale* 2014, *6* (23), 14394–14403.

(36) Velasco-Vélez, J. J.; Pfeifer, V.; Hävecker, M.; Wang, R.; Centeno, A.; Zurutuza, A.; Algara-Siller, G.; Stotz, E.; Skorupska, K.; Teschner, D.; et al. Atmospheric Ppressure X-Ray Photoelectron Spectroscopy Apparatus: Bridging the Pressure Gap. *Rev. Sci. Instrum.* 2016, *87*, 053121.

(37) Ottosson, N.; Faubel, M.; Bradforth, S. E.; Jungwirth, P.; Winter, B. Photoelectron Spectroscopy of Liquid Water and Aqueous Solution: Electron Effective Attenuation Lengths and Emission-Angle Anisotropy. *J. Electron Spectros. Relat. Phenomena* 2010, *177*, 60–70.

(38) Schreck, S.; Wernet, P. Isotope Effects in Liquid Water Probed by Transmission Mode X-Ray Absorption Spectroscopy at the Oxygen K-Edge. *J. Chem. Phys.* 2016, *145*, 104502.

(39) Wernet, P.; Nordlund, D.; Bergmann, U.; Cavalleri, M.; Odelius, N.; Ogasawara, H.; Näslund, L. Å.; Hirsch, T. K.; Ojamäe, L.; Glatzel, P.; et al. The Structure of the First Coordination Shell in Liquid Water. *Science* 2004, *304* (5673), 995–999.

(40) Nilsson, A.; Nordlund, D.; Waluyo, I.; Huang, N.; Ogasawara, H.; Kaya, S.; Bergmann, U.; Näslund, L. Å.; Öström, H.; Wernet, P.; et al. X-Ray Absorption Spectroscopy and X-Ray Raman Scattering of Water and Ice; an Experimental View. *J. Electron Spectrosc. Relat. Phenom.* 2010, *177*, 99–129.

(41) Yamazoe, K.; Higaki, Y.; Inutsuka, Y.; Miyawaki, J.; Cui, Y. T.; Takahara, A.; Harada, Y. Enhancement of the Hydrogen-Bonding Network of Water Confined in a Polyelectrolyte Brush. *Langmuir* 2017, *33* (16), 3954–3959.

(42) Cicero, G.; Grossman, J. C.; Schwegler, E.; Gygi, F.; Galli, G. Water Confined in Nanotubes and between Graphene Sheets: A First Principle Study. *J. Am. Chem. Soc.* 2008, *130*, 1871–1878.

(43) Niskanen, J.; Sahle, C. J.; Juurinen, I.; Koskelo, J.; Lehtola, S.; Verbeni, R.; Müller, H.; Hakala, M.; Huotari, S. Protonation Dynamics and Hydrogen Bonding in Aqueous Sulfuric Acid. *J. Phys. Chem. B* 2015, *119* (35), 11732–11739.

(44) Wren, A. G.; Phillips, R. W.; Tolentino, L. U. Surface Reactions of Chlorine Molecules and Atoms with Water and Sulfuric Acid at Low Temperatures. *J. Colloid Interface Sci.* 1979, *70* (3), 544–557.

(45) Conway, B. E.; Mozota, J. Surface and Bulk Processes at Oxidized Iridium Electrodes-II. Conductivity-Switched Behaviour of Thick Oxide Films. *Electrochim. Acta* 1983, *28*, 9–16.

(46) Kuo, D. Y.; Kawasaki, J. K.; Nelson, J. N.; Kloppenburg, J.; Hautier, G.; Shen, K. M.; Schlom, D. G.;

Suntivich, J. Influence of Surface Adsorption on the Oxygen Evolution Reaction on IrO 2 (110). *J. Am. Chem. Soc.* 2017, *139* (9), 3473–3479.

(47) Jensen, E.; Købler, C.; Jensen, P. S.; Mølhave, K. In-Situ SEM Microchip Setup for Electrochemical Experiments with Water Based Solutions. *Ultramicroscopy* 2013, *129*, 63–69.

(48) Møller-Nilsen, R. In-Situ SEM Electrochemistry and Radiolysis, Technical University of Denmark (DTU), 2016.

(49) Schneider, N. M.; Norton, M. M.; Mendel, B. J.; Grogan, J. M.; Ross, F. M.; Bau, H. H. Electron-Water Interactions and Implications for Liquid Cell Electron Microscopy. *J. Phys. Chem. C* 2014, *118* (38), 22373–22382.

(50) Velasco-Vélez, J. J.; Jones, T.; Gao, D.; Carbonio, E.; Arrigo, R.; Hsu, C. J.; Huang, Y. C.; Dong, C. L.; Chen, J. M.; Lee, J. F.; et al. The Role of the Copper Oxidation State in the Electrocatalytic Reduction of CO 2 into Valuable Hydrocarbons. *ACS Sustain. Chem. Eng.* 2019, *7* (1), 1485–1492.

(51) Mauritz, K. A.; Moore, R. B. State of Understanding of Nafion. *Chem. Rev.* 2004, *104* (10), 4535–4585.

(52) Zawodzinski, T. A.; Neeman, M.; Sillerud, L. O.; Gottesfeld, S. Determination of Water Diffusion Coefficients in Perfluorosulfonate Ionomeric Membranes. *J. Phys. Chem.* 1991, *95* (15), 6040–6044.

(53) L'Annunziata, M. F. Radiation Physics and Radionuclide Decay. In *Handbook of Radioactivity Analysis*; L'Annunziata, M. F., Ed.; Elsevier: Amsterdam, 2012; pp 1–162.

(54) Hävecker, M.; Cavalleri, M.; Herbert, R.; Follath, R.; Knop-Gericke, A.; Hess, C.; Hermann, K.; Schlögl, R. Methodology for the Structural Characterisation of V x O y Species Supported on Silica under Reaction Conditions by Means of in Situ O K-Edge X-Ray Absorption Spectroscopy. *Phys. status solidi* 2009, *246* (7), 1459–1469.

(55) Yeh, J. J.; Lindau, I. Atomic Subshell Photoionization Cross Sections and Asymmetry Parameters: 1 < Z < 103. *At. Data Nucl. Data Tables* 1985, *32* (1), 1–155.

(56) Ferrari, A. C. Raman Spectroscopy of Graphene and Graphite: Disorder, Electron–Phonon Coupling, Doping and Nonadiabatic Effects. *Solid State Commun.* 2007, *143* (1–2), 47–57.

(57) Mueller, N. S.; Heeg, S.; Alvarez, M. P.; Kusch, P.; Wasserroth, S.; Clark, N.; Schedin, F.; Parthenios, J.; Papagelis, K.; Galiotis, C.; et al. Evaluating Arbitrary Strain Configurations and Doping in Graphene with Raman Spectroscopy. *2D Mater.* 2017, *5* (1), 015016.

(58) Lee, J. E.; Ahn, G.; Shim, J.; Lee, Y. S.; Ryu, S. Optical Separation of Mechanical Strain from Charge Doping in Graphene. *Nat. Commun.* 2012, *3* (1), 1024.

(59) Kim, K.; Coh, S.; Tan, L. Z.; Regan, W.; Yuk, J. M.; Chatterjee, E.; Crommie, M. F.; Cohen, M. L.; Louie, S. G.; Zettl, A. Raman Spectroscopy Study of Rotated Double-Layer Graphene: Misorientation-Angle Dependence of Electronic Structure. *Phys. Rev. Lett.* 2012, *108* (24), 246103.

(60) Das, A.; Pisana, S.; Chakraborty, B.; Piscanec, S.; Saha, S. K.; Waghmare, U. V.; Novoselov, K. S.; Krishnamurthy, H. R.; Geim, A. K.; Ferrari, A. C.; et al. Monitoring Dopants by Raman Scattering in an Electrochemically Top-Gated Graphene Transistor. *Nat. Nanotechnol.* 2008, *3* (4), 210–215.

(61) Robertson, A. W.; Bachmatiuk, A.; Wu, Y. A.; Schäffel, F.; Rellinghaus, B.; Büchner, B.; Rümmeli, M. H.; Warner, J. H. Atomic Structure of Interconnected Few-Layer Graphene Domains. *ACS Nano* 2011, *5* (8), 6610–6618.

(62) Bayer, B. C.; Caneva, S.; Pennycook, T. J.; Kotakoski, J.; Mangler, C.; Hofmann, S.; Meyer, J. C.

Introducing Overlapping Grain Boundaries in Chemical Vapor Deposited Hexagonal Boron Nitride Monolayer Films. *ACS Nano* 2017, *11* (5), 4521–4527.

3. In Situ X-ray Spectroscopy on the Electrochemical Development of Iridium Nanoparticles in Confined Electrolyte

3.1 Preliminary Remark

The previous chapter described an approach to study surfaces of electrocatalysts under wet conditions with soft X-ray spectroscopy. In this chapter, the approach is applied to iridium nanoparticles. The work is pioneering in three ways. First, it probes the surface of an anodic iridium (hydr-oxide film under wet conditions at a good signal to noise ratio (addressing Q2. Second, it uses molecular dynamics on a wet rutile-type IrO_2 (110 surface to predict spectroscopic features and the thermodynamic stability of surface phases (addressing Q1. Third, it introduces potentiodynamic X-ray absorption, which can directly connect oxidation currents to electrochemical oxidation of surface species, addressing Q3. The combination of these experimental and ab initio results can identify surface phase transitions and how wide they are against potential change.

The way to these advances has been paved by earlier work of Verena Streibel (née Pfeifer and Travis Jones. They already predicted the spectroscopic fingerprints of surface oxygens of various rutile type IrO_2 surfaces and found first indication of deprotonated surface species in situ.[1] The study in this chapter was developed in close exchange with Travis Jones, who has performed all calculations. Technical development was supported by Rik Mom, Juan-Jesús Velasco-Vélez and the Electronic Structure group of Axel Knop-Gericke in the department of Anorganic Chemistry at the Fritz-Haber-Institute directed by Robert Schlögl. Milivoj Plodinec characterized the distribution and size of iridium nanoparticles with a transmission electron microscope.

3.2 Abstract

Iridium oxide based catalysts are uniquely active and stable in the oxygen evolution reaction. Theoretical work attributes their activity to oxyl, or μ_1-O, species. Verifying this intermediate experimentally has, however, been challenging. In the present study, these challenges were overcome by combining theory with new experimental strategies. Ab initio molecular dynamics of the solid liquid interface were used to predict spectroscopic features, while a sample architecture, developed for surface sensitive X-ray spectroscopy of electrocatalysts in confined liquid, was used to search for these species under realistic conditions. Through this approach, we have identified μ_1-O species during oxygen evolution. Potentiodynamic X-ray absorption additionally shows that these μ_1-O species are created by electrochemical oxidation currents in a deprotonation reaction.

3.3 Introduction

The energy sector currently lacks an affordable infrastructure to transit from fossil fuels to zero-emission technologies. One promising building block is hydrogen.[2,3] Hydrogen can be integrated into the existing gas grid by insertion, converted into electricity via fuel cells, and used to synthesize fuels; methanol and ammonia, for example. The insufficient green production of hydrogen, however, is a bottleneck in the development of a sustainable hydrogen network.

Electrolytic water splitting in acidic electrolytes addresses this problem by making use of the intermittent nature of renewable energies to produce hydrogen at high pressures. The limiting process is the anodic oxygen evolution reaction (OER), which is plagued by high overpotentials and electrode degradation.[4] A prevalent anode material is iridium oxide, which has long been known to provide a good balance between two antagonists of an OER catalyst: activity and stability.[5,6] However, iridium is scarce and expensive, which limits its use. Large scale production of hydrogen at affordable costs requires new catalyst materials or reduced iridium loadings.

In order to avoid black-box improvement strategies and enable rational design of OER catalysts, a deeper understanding of the catalysts' electronic structure during operation is necessary. Herein, we contribute to this understanding by presenting an in situ study on the chemical state of anodized iridium nanoparticles. In this study, we use predictions from ab initio molecular dynamic calculations to connect two main oxidation waves, which are well known from electrochemical studies on bulk iridium electrodes,[7] with the formation of electron deficient oxygen species on the catalysts surface.

In an effort to be sensitive to the active surface and the atom type, we turned to soft X-ray spectroscopy. Using low-energy photons as a probe, however, requires innovative design of the ambient pressure XPS setup and the in situ measurement cell,[8–10] as well as the sample architecture. Previous in situ studies of this sort were carried out on proton exchange membranes (PEMs).[1,11,12] In one study, $Ir^{IV}O_2$ nanoparticles (NPs) were oxidized electrochemically and the authors found an Ir 4f feature with a binding energy (BE) above the one of the initial material.[11] The authors of another study

were able to find an oxygen absorption pre-edge resonance at 529 eV via electrochemical oxidation of metallic Ir NPs.[1] They assigned this spectroscopic feature to an electron deficient oxygen species, which is also active in CO oxidation.[13,14] In a third study, the authors oxidized metallic iridium nanoparticles in situ and found a conversion of Ir^{III} to Ir^{IV} with increasing anodic potentials.[12]

The three in situ studies mentioned above used thin layers of NPs on a PEM open to vacuum. In such a setup, water diffuses through the permeable membrane and subsequently evaporates or forms ice, which then sublimes into the vacuum. Under these conditions a steady liquid layer is unlikely to form, which limits proton transport and, thus, slows down electrochemical reactions significantly.

3.4 Results and discussion

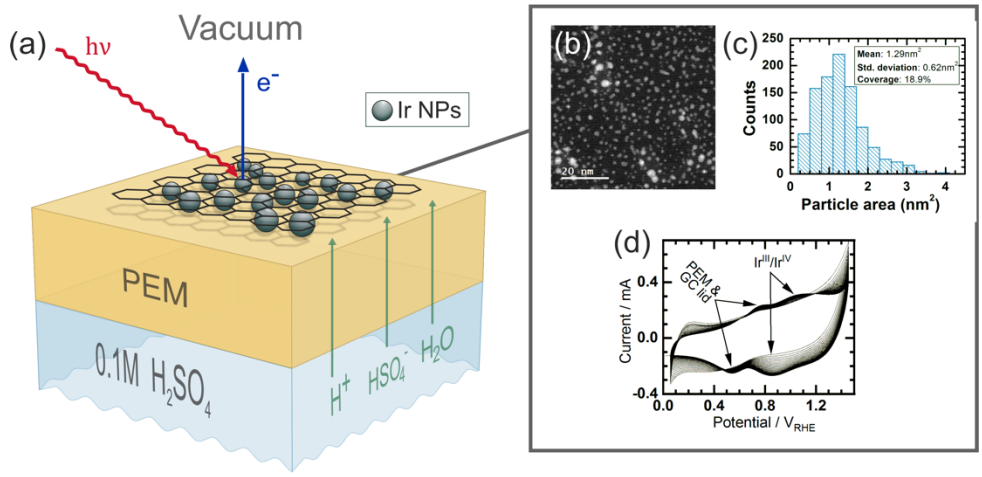

Figure 3.1: Experimental setup and properties: a) Scheme of the sample architecture: a proton exchange membrane (PEM), wetted with electrolyte from the bottom, covered with nanoparticles and sealed with graphene on the top side; b) high angle annular dark field micrograph of the iridium nanoparticles on a TEM grid; c) histogram of their size distribution; d) the activation step – oxidative cycles (no. 2 – 50) at 500 mV/s.

To assure proper wetting, we improved the concept of the in situ cell in reference [1] by changing the sample architecture. The membrane (or solid electrolyte) we used is permeable for all molecules essential to an electrolyte: water, anions, and protons. The catalyst nanoparticles are in direct contact with this solid electrolyte, assuring the best possible ion transport. On top of that, graphene covers the assembly of the membrane and the particle (Figure 3.1a). Graphene fulfills three functions: First, it is an evaporation barrier. In that function, it promotes condensation between the membrane and graphene. As soon as liquid forms, graphene is an effective barrier between liquid and a vacuum.[15–17] Second, the graphene cover serves as an electrical contact for the catalyst particles, even if they are separated from each other. Third, graphene is almost transparent to photoelectrons. With such a sample preparation, the catalyst nanoparticles are in proximity to the solid electrolyte, surrounded by confined liquid, and can be accessed with soft X-ray photoelectron spectroscopy, presenting an ideal situation for in situ studies on the electronic structure of electrocatalysts.

An assembly identical to the one shown in Figure 3.1a but without nanoparticles was used to demonstrate condensation between the membrane and graphene. Figure 3.2 shows oxygen K-edges of the membrane in the dry state and in a state in which it has been wetted from the backside with 0.1 M H_2SO_4. A difference between the two spectra shows the characteristic shape of liquid water with a pre-edge feature at 535 eV, a main-edge resonance shortly above 537 eV, and a post-edge feature at 541 eV.[17–19] Such a fingerprint is a good indicator for a densely hydrogen bonded system, similar to liquid water. The relatively small deviation of the O K-edge spectrum for confined and bulk liquid was predicted by DFT simulations of confined water between graphene sheets, where confined water was shown to adopt the electronic properties of bulk water already 0.5 nm beyond the interface to graphene.[20]

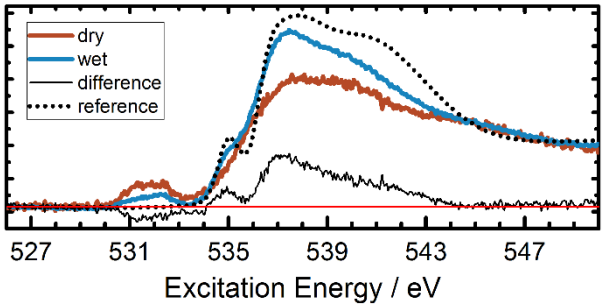

Figure 3.2: Wetting experiment: Graphene on a proton exchange membrane (FAD55) facing vacuum; oxygen K-edge spectra, normalized at 550 eV of a dry sample (red) and a sample, which was wetted from the backside with 0.1 M H_2SO_4 (blue); the difference of both (black) and the reference spectrum (dotted) of liquid water (data from reference 18) are compared.

For the in situ investigation, sputtered Ir NPs were embedded in the confined electrolyte described above (Figure 3.1a, also see Experimental and Computational Methods and Supporting Information, for more details on sample preparation). High resolution transmission electron microscopy of the NPs on a TEM grid (Figure 3.1b) reveals that the NPs have a mean area of 1.29 nm^2 and cover roughly a fifth of the total area (Figure 3.1c).

The electrode assembly was initially activated with cyclic voltammetry performed at 500 mV/s between 0.05 V with respect to the reversible hydrogen electrode (V_{RHE}) and 1.45 V_{RHE} (Figure 3.1d). Two oxidation waves persisted throughout the cycling: a feature at ~0.75 V_{RHE}, originating from the membrane and the glassy carbon lid (compare Figure 3.11), and another at ~1.1 V_{RHE}, which is characteristic for iridium oxides and is usually assigned to the Ir^{III}-Ir^{IV} transition.[21–24] In the following we refer to the transition at ~1.1 V_{RHE} as the first oxidation wave. After 20 cycles, the shape of the cyclovoltagramm below 0.4 V_{RHE} narrowed and remained unchanged upon further cycling. Similar behavior has been seen before and it has been attributed to capacitive effects on a metal-electrolyte interface below the insulating surface oxide.[7] It can be concluded that the system responds rapidly to the changing potential without signs of transport problems and the working electrode appears to form

an anodic film quickly. This film is likely to be hydrated and possibly contains oxide-, oxohydroxide-, and hydroxide structures. For simplicity we will refer to such oxidized iridium structures as iridium (hydr-)oxides.

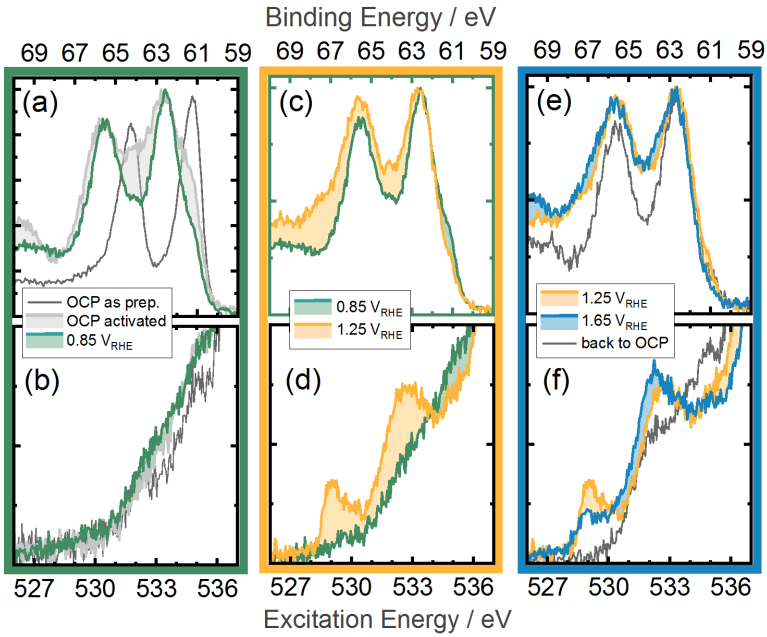

Figure 3.3: Potential steps: Ir 4f (top row, Eexc=598 eV) and O K-edge spectra in partial electron yield (bottom row, Ekin=385 eV) of iridium nanoparticles between a permeable membrane (FAD55) and graphene, equilibrated at different potential steps.

X-ray photoelectron (XP) spectroscopy confirms the hypothesis of an oxidized and hydrated shell around the iridium particles. The normalized Ir 4f XP spectrum (Figure 3.3a) of the fresh sample at open circuit potential (OCP) shows a main (Ir 4f 7/2) BE close to the reference BE of metallic iridium. We refer to the Supporting Information for details on energy calibration. After the cyclovoltammetric activation (as described above), the intensity of the metallic peak in the Ir 4f spectrum decreases markedly, though some intensity persists. The main components in the spectrum are located above 62 eV, indicating a surface layer containing oxidized iridium. Similar BE shifts have previously been found ex situ on activated iridium electrodes [23,25] and in situ on iridium nanoparticles.[12] The spectroscopic feature at a BE of 69 eV belongs to Br 3d 5/2, since Br is part of the permeable membrane. The respective O K-edge spectra after activation exhibit a slight increase between 532 eV and 534 eV (Figure 3.3b). More importantly, however, is the absence of white lines below 531 eV, which typically appear in weakly- or non-hydrated iridium oxides.[13] These missing oxide absorption features and the decreasing metal contribution in the Ir 4f spectrum point towards a core shell structure with metal in the core and a well hydrated iridium hydroxide shell after activation. This concurs with the interpretation of previous studies on anodic films of bulk metal electrodes.[7,22–26]

Equilibration at 0.85 V_{RHE} further decreases the metal contribution in the Ir 4f spectrum, which leads to a sharper and relatively symmetric peak shape (Figure 3.3a). The Ir 4f main-peak BE and the O K-

edge spectra (Figure 3.3b) remain unchanged, which allows the conclusion that the hydrated iridium hydroxide formed during activation is still stable at 0.74 V_{RHE}. Binding energy shifts caused by the applied potential are excluded by grounding the working electrode to the electron analyzer. The small changes in electronic structure at 0.85 V_{RHE}, compared to the OCP, can be explained by the low conductance of anodic films on iridium below 0.85 V_{RHE}, which was demonstrated for anodic films on bulk iridium electrodes.[26] These observations fit our spectroscopic findings well, since the shape of the Ir 4f spectrum after activation (Figure 3.3a) is relatively symmetric in comparison to the initial state indicating poor conductivity or a lack of metallic screening. The dominant oxidation state of iridium before the first oxidation wave, is generally believed to be +III.[7,21–24,26] The Ir^{III} 4f 7/2 contribution of such gapped iridium (hydr-)oxides is expected to appear above 62 eV, as measurements on IrOOH have shown.[27] The Ir 4f BE found herein (Figure 3.3a) matches the one reported for IrOOH [27] and an Ir^{III} contribution obtained from deconvolution of in situ results.[12]

The step to 1.25 V_{RHE} passes the first oxidation wave around 1.1 V_{RHE}, which is generally assigned to the Ir^{III}-Ir^{IV} transition. Indeed, the electronic structure changes drastically. On the side of XPS, the Ir 4f peak position (Figure 3.3c) changes only marginally towards higher BEs, but a distinct feature, roughly 2 eV above the main line, appears. Such a strong high-BE feature has not been resolved by the previous in situ studies mentioned above and points towards improved electrochemical conditions. The large shift would be consistent with a higher oxidation state of iridium. However, final state effects are known to play a large role for iridates [27,28] and make it challenging to extract the oxidation state from Ir 4f spectra alone.

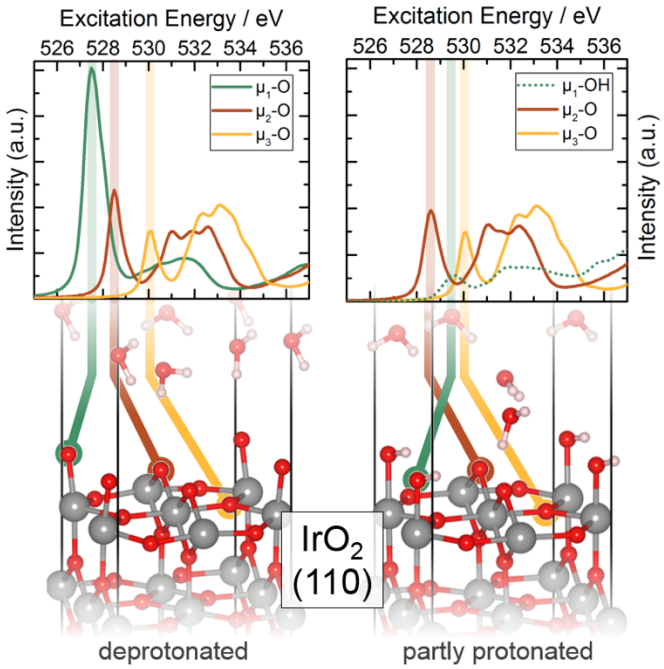

Figure 3.4: Molecular dynamic snapshots: Exemplary snapshots of the IrO_2 (110) surface covered with water in a deprotonated and partially protonated version from ab initio molecular dynamics; the spectra above are averaged over four snapshots each and all equivalent oxygen species in the given cell.

Fortunately, valence states of iridium and oxygen are strongly hybridized,[29–31] which allows the study of the electronic structure in iridium (hydr-)oxides via oxygen states. The O K-edge spectrum has proven to be particularly informative for iridium oxides, because of its distinct pre-edge features.[1,13] Three general types of oxygen are expected on iridium (hydr-)oxide surfaces: the μ_1, μ_2, and μ_3 oxygen species, which are bound to one (μ_1), two (μ_2), or three (μ_3) iridium atoms. The (110) surface of rutile type IrO_2 contains all three types and was used herein to calculate the absorption characteristics of each individual species (Figure 3.4). To account for influences of hydrogen bonding in a wetted environment, we performed molecular dynamics at the DFT level. In these calculations the IrO_2 (110) surfaces are covered with water and equilibrated at 300K. Snapshots of the molecular dynamics simulations were then used to compute absorption spectra of each oxygen species in that snapshot. The spectra generated for each snapshot were then averaged by type to obtain a realistic picture of their contribution to the measured spectra (details of the computational procedure are provided below and in the Supporting Information in greater detail). The results are shown in Figure 3.4. The absorption of all three types of oxygen, namely μ_1, μ_2, and μ_3, exhibit similar characteristics: a pre-edge feature, due to transitions from O 1s to O 2p hybridized with Ir π*-like states, and a broader band ~3 eV above the pre-edge feature, due to transitions from O 1s to O 2p hybridized with Ir σ*-like states. The energy shift of the pre-edge feature calibrated to the white line of bulk IrO_2, however, is distinct for the three types of oxygen species: the pre-edge of the μ_1-O species appears at ~528 eV, the one of μ_2-O at ~529 eV, and the one of μ_3-O at ~530 eV, where the magnitude of the resonance's red-shift is proportional to the electron deficiency of the oxygen, with the μ_1-O species showing significant radical character (see also Supporting Information). A blue shift of the spectroscopic features was found for the protonated forms, as the spectrum for μ_1-OH with a pre-edge above 529 eV demonstrates. The magnitude of this shift, however, is influenced by hydrogen bonding (see Figure 3.14 and the corresponding discussion in the Supporting Information). With these trends identified, it becomes possible to understand the absorption experiments.

Figure 3.3d shows the O K-edge spectra before and after the first oxidation wave, at 0.85 V_{RHE} and 1.25 V_{RHE}, respectively. The change is drastic: absorption features at 529 eV, 530 eV and around 533 eV appear. Based on the calculations discussed above, the pre-edge feature at 529 eV would be caused by μ_1-OH or μ_2-O type oxygen and the one at 530 eV by μ_3-O. The μ_1 and μ_2 types are, however, of special interest, because their deprotonated forms have been reported to be electron deficient and prone to form the oxygen-oxygen bond in a peroxo-mechanism.[1,32] Interestingly, the relatively strong feature at 529 eV in Figure 3.3d appears after the first oxidation wave, well below the onset of the OER. Oxygen species absorbing at 529 eV can therefore be created in the first oxidation wave and appear to be stable at 1.25 V_{RHE}.

In the step from 1.25 V_{RHE} to 1.65 V_{RHE}, the second oxidation wave is crossed. The assignment of this oxidation wave to a certain transition, is still under discussion. The (further) oxidation of iridium from +IV to +V [23,24,33] and the oxidation of oxygen from -II to -I [1] have been suggested. The two explanations differ in their predictions where additional holes tend to localize in a zero order approximation

(covalent bonding between oxygen and iridium leads to a sharing of hole character).[30,31] The recorded Ir 4f spectrum in the OER, at 1.65 V_{RHE}, (Figure 3.3e) is slightly broadened on the high-BE side and shows a reduced metal contribution, suggesting that the sample is indeed oxidized further. The O K-edge absorption spectrum (Figure 3.3f) shows a reduced pre-edge feature at 529 eV and a shift of the absorption at 533 eV to lower excitation energies by almost one electron volt. The latter is likely caused by oxygen species in graphene or the membrane (compare Figure 3.12). Of greater interest here is the loss of intensity at 529 eV, since it is caused by the μ_1-OH and μ_2-O species. The intensity loss could be caused by multiple processes: deprotonation of μ_1-OH species, consumption of the μ_2-O species, or condensation of the material via dehydration, which would increase the average coordination towards μ_3-O with a white line at 530 eV (compare Figure 3.4). However, the intensity loss could also be caused by normalization: the O K-edge spectra in Figure 3.3 are normalized to the edge jump at 550 eV and, thus, show the intensity relative to all oxygen species, including the ones originating from graphene, the membrane, the electrolyte, and so on. Consequently, if the total number of all oxygen species changes, the relative intensity at 529 eV will also change.

In order to obtain more detailed information about how the iridium-related oxygen species develop with applied potential, we used potentiodynamic X-ray absorption spectroscopy. In this experiment, we track an absorption feature in an electrochemical cycle between 0.15 V_{RHE} and 1.65 V_{RHE}. Potentiodynamic X-ray absorption has several advantages over the steady state experiment described above. First, the absorption intensity is relative to the intensity of the starting point at 0.04 V_{RHE} and the pre-edge region is therefore independent of the total amount of oxygen. Secondly, the development of the spectroscopic features can be directly related to electrochemical currents, since both are recorded simultaneously and are related to charge.

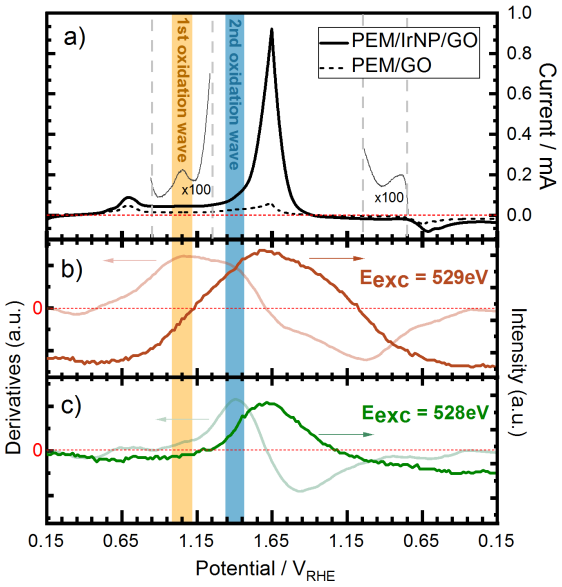

Figure 3.5: Potentiodynamic X-ray absorption: a) current of the working electrode, consisting of a PEM with iridium nanoparticles and covered with graphene, over the turn of an electrochemical cycle between 0.15 V_{RHE} and 1.65 V_{RHE} at 25 mV/s; the current of a comparable sample without catalyst is shown as a dotted line; b) and c) show the total electron

yield (red and green) at excitation energies of 529 eV and 528 eV, respectively; the smoothened time derivatives are shown in light-red and light-green.

The spectroscopic results for voltammetric cycles at 25 mV/s are summarized in Figure 3.5 and a reference measurement without iridium nanoparticles is given for comparison in the Supporting Information, Figure 3.13. The currents of the working electrode are given in Figure 3.5a for the sample and the blank as a solid or dotted line, respectively. The normalized absorption (normalization procedure in Section 3.7.8) at 529 eV has its onset at roughly 0.85 V_{RHE} (Figure 3.5b), which aligns well with the onset of the first oxidation wave. In the time derivative of the same absorption signal (see Supporting Information), it appears even clearer: the maximal increase of the absorption at 529 eV coincides with the current maximum of the first oxidation wave. Hence, the formation of the μ_1-OH and μ_2-O oxygen species, which absorb at 529 eV, is coupled with an electron transfer, giving rise to the first oxidation wave. After that, the absorption signal continues to increase and falls with decreasing potentials. A consumption process of the oxygen species absorbing at 529 eV is not directly evident from the intensity in the potentiodynamic absorption experiment. However, the time derivative of the tracked intensity gives the first indication for consumption: growth of the absorption at 529 eV slows down after passing the first oxidation wave and decelerates swiftly while passing the second oxidation wave. It stands to reason that a deprotonation of the μ_1-OH species (scheme 1) causes this swift change.

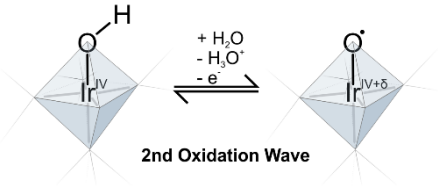

Figure 3.6: Structural drawing: deprotonation and oxidation of a μ_1-O species, suggested to be linked to the second oxidation wave at ~1.4 V_{RHE}.

We tested the μ_1 deprotonation hypothesis by tracking the absorption of the intense pre-edge feature predicted for μ_1-O (Figure 3.4) over time and changing potentials. Positively, absorption at 528 eV starts with the onset of the second oxidation wave, reaches its maximum, and quickly decays on the reverse scan (Figure 3.5c). The respective derivative also shows clearly that the maximum gain in the absorption signal at 528 eV slows down the growth of the absorption intensity at 529 eV. These findings support the deprotonation hypothesis suggested above. It appears that μ_1-OH, with a small contribution to the absorption at 529 eV, is transformed into μ_1-O with a sharp pre-edge absorption at ~528 eV during the second oxidation wave. Consistently, the white lines of O K-edges at constant potential broaden towards low excitation energies (Figure 3.8).

Further support for the deprotonation hypothesis comes from the theoretical calculation of the deprotonation potential. The deprotonation step from μ_1-OH to μ_1-O was calculated to be ~1.5 V_{NHE} (see Supporting Information for more details), which is in fair agreement with the experimental value.

Creation of a μ_1-O species at the onset of the OER also explains the shortening of the Ir-O bond length at high potentials observed in many EXAFS studies:[24,30,33–36] the average equilibrium bond length of μ_1-O(H) in our ab initio molecular dynamics calculations decreases from 1.98 Å to 1.81 Å when deprotonating μ_1-OH to μ_1-O.

As we have seen, many pieces of evidence suggest that a μ_1-O species is created by deprotonation at the onset of the OER, where a second oxidation wave is expected.[1,7,22] The electron deficient nature of the μ_1-O species makes them susceptible to the attack by water in the O-O bond formation step. In fact, DFT calculations performed at constant potential suggest that such μ_1-O species with unpaired spins are the active sites for O-O bond formation during OER.[37]

On a final note, the absorption features below 530 eV (Figure 3.3f) and the high-BE shoulder 2 eV above the Ir 4f main line (Figure 3.3e) almost completely disappear after a few minutes at OCP. This demonstrates general reversibility and proper electrochemical response of the investigated system and underlines that the spectroscopic features discussed herein are relevant to the electrochemical cycle of iridium (hydr-)oxides in the oxygen evolution reaction.

3.5 Conclusion

We suggest a sample architecture allowing for surface sensitive X-ray spectroscopy under confined liquid and we studied the electrochemical oxidation of iridium nanoparticles using this technique. We found experimental evidence of a connection between the first two oxidation waves (around 1.1 V_{RHE} and 1.4 V_{RHE}) and two absorption features. We assigned these features to two classes of oxygen species (μ_2-O and μ_1-O, respectively) based on ab initio molecular dynamics calculations coupled with the solution of the Bethe-Salpeter equation for the O K-edges. Both oxygen species appear to be electron deficient in the calculations and are possible candidates for the oxygen-oxygen bond formation. However, μ_1-O was predicted to be the more active of these two oxygen species.[37] Potentiodynamic X-ray absorption provides evidence that μ_1-O is created at the onset of the OER via a deprotonation mechanism.

3.6 Experimental and Computational Methods

As a proton exchange membrane, we used fumatech's FAD55 membrane, which is permeable for water, protons, and anions. Iridium nanoparticles were sputtered deposited onto a disk of the same membrane in an argon atmosphere. The graphene blanket swimming on a liquid solution was captured with the membrane assembly from below and dried afterwards. The samples were stored in sodium sulfate solution until their use in the in situ cell setup.

The sample assemblies described above were mounted onto an in situ cell described earlier[11] and used in a near-ambient pressure X-ray spectroscopy setup connected to the ISISS beamline at the BESSY II synchrotron facility. In the rear of the sample, in the bulk electrolyte, we used an Ag/AgCl (KCl

saturated) reference electrode and a platinum wire as counter electrode in constant flow of 0.1 M H_2SO_4. The working electrode contact was fixed with a glassy carbon lid and grounded to the electron analyzer. The water backpressure in the experiment chamber ranged from 0.05 mbar to 0.15 mbar.

DFT calculations were performed using the Quantum ESPRESSO package [38] and the Perdew, Burke, and Ernzerhof (PBE) [39] exchange and correlation potential. For calculations of the absorption spectra, we treated the electron hole problem with the Bethe-Salpeter equation (BSE) [40] within many body perturbation theory. All calculations were performed non-spin polarized with the inclusion of scalar relativistic effects.

A more detailed description of the experimental and computational procedure can be found in the Supporting Information.

3.7 Supporting Information

3.7.1 Sample preparation

Fumatech's (Bietigheim-Bissingen, Germany) FAD55 membrane was used as a proton exchange membrane (PEM). Disks with a diameter of 11 mm were stamped out from a larger sheet. The iridium nanoparticles were deposited for 5 s with a plasma sputter coater, the Cressington (Watford, UK) 208HR, in 0.1 mbar argon atmosphere and a sputter current of 40 mA. The iridium target by the Elektronen-Optik Service GmbH (Dortmund, Germany) was cleaned from carbon in Ar plasma for 5 s beforehand. The (sputtered) membranes were then soaked in 0.5 M sodium sulfate solution for at least two days at room temperature to exchange bromide from the membrane and to wet it. Graphenea (San Sebastian, Spain) supplied single layers of graphene on copper. Those were placed on an etching solution with 10 g of $(NH_4)_2SO_4$ in 250 mL MilliQ water (Merck, Darmstadt, Germany) for 12 hours. The swimming graphene sheets were then transferred onto the membrane by hand. After drying for 20 minutes in air, the samples were stored in sodium sulfate solution until they were used. For the transmission electron microscopy, a TEM gold grid R1.2/1.3 coated with holey carbon from QUANTIFOIL was used to sputter iridium nanoparticles in the same manner as above.

3.7.2 Transmission electron microscopy

High-angle annular dark-field scanning transmission electron microscopy (HAADF STEM investigations for the particle size distributions and coverages were carried out using a cold FEG, double Cs-corrected scanning transmission electron microscope, JEOL JEM-ARM200CF microscope operated at 200 kV. The particle size distribution was obtained by automated image analysis in the ImageJ software and counted with a bin size of 0.1 nm^2. The resulting histogram was the basis for the statistical analysis. Figure 3.7 shows a larger magnification than Figure 3.1b in the main text and demonstrates the crystallinity of the sample as prepared.

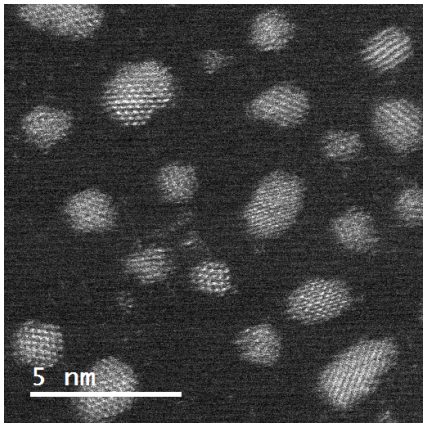

Figure 3.7: High angle annular dark field (HAADF) micrograph of the Ir nanoparticles on a TEM grid.

3.7.3 In situ setup

All spectroscopic and electrochemical measurements presented were performed at the ISISS beamline with the attached NAP-XPS end station and a module dedicated to electrochemistry. The in-situ cell

design is described in reference [1]. The equilibrium pressure in the chamber was a balance between the evaporation from the in situ cell and the pumping speed via the 1 mm nozzle to the analyzer of the NAP-XPS endstation and ranged from 5.0e-2 mbar to 1.5e-1 mbar.

3.7.4 In situ electrochemistry

World Precision Instruments (Sarasota, USA) provided the Ag/AgCl reference electrodes of the type DRIREF-2SH, which was stored in saturated KCl solution, and a platinum wire was used as a counter electrode. The membrane was pressed onto the cell body with a glassy carbon lid. The lid had a circular opening with a diameter of roughly 1 mm. The electrolyte was prepared by diluting 9.8 g concentrated sulfuric acid (Sigma Aldrich, St. Louis, USA) in 1 L of MilliQ water. A flow of 0.5 mL per minute assured a constant supply of electrolyte to the rear of the membrane during all experiments involving electrochemistry.

The counter, reference, and working electrode were connected to the SP-300 potentiostat (Bio-Logic, Seyssinet-Pariset, France). The working electrode was grounded to the electron analyzer of the end station. The channels of the potentiostat were operated in floating mode. A noise filtering for 50 kHz was applied in the EC-Lab software (Bio-Logic) controlling the potentiostat. For potential conversion from the Ag/AgCl/KCl(sat.) to the reversible hydrogen electrode (RHE), the Nernstian equation (below) was used. A pH value of 0.96 was estimated for 0.1 M H_2SO_4 assuming full deprotonation to HSO_4^- and partial deprotonation to SO_4^{2-}. The standard potential $E^0_{Ag/AgCl}$ = 0.197 V [41] for the Ag/AgCl/KCl(sat.) redox system was used for conversion.

$$E_{RHE} = E^{00} + \frac{RT}{F}\left(\ln(\mathrm{a}[H_3O^+]) - \frac{1}{2}\ln(p[H_2])\right)$$

$$= E_{Ag/AgCl} + E^0_{Ag/AgCl} + 0.059 \cdot pH$$

$$\approx E_{\frac{Ag}{AgCl}} + 0.254V \quad for \quad E^0_{\frac{Ag}{AgCl}} = 0.197V_{NHE}\ and\ pH = 0.96)$$

3.7.5 Spectroscopy

Near-Edge X-ray Absorption Fine Structure (NEXAFS) was recorded via two channels simultaneously, the total (TEY) and partial electron yield (PEY). The first uses a bias voltage of 90 V on the nozzle against the analyzer and working electrode to collect as many electrons from the sample as possible. The latter is a partial electron yield selecting only electrons with a kinetic energy of 385 eV; the pass energy was 50 eV. The choice of this kinetic energy and the applied bias on the nozzle efficiently eliminates contributions from oxygen-containing species in the gas phase.[42] For the O K-edge spectra, the step size was 0.05 eV and the dwell time 0.2 s. A self-written script was used to process all O K-edge spectra. It calibrates the energy axis, normalizes to the ring current, then normalizes to the flux, subtracts the minimum value of the curve, and normalizes to a given value. It proceeds in the stated order. For energy calibration, the 3p-Rydberg state was set to the reference value of 537.25 eV.[18] The reference spectrum for the flux reference was an O K-edge of an oxygen-free iridium (111) single crystal at 823 K. All O K-edge spectra were normalized to the edge jump, in this case 550 eV.

X-ray Photoelectron Spectroscopy (XPS) was recorded with the same bias voltage of 90 V against the nozzle. This broadens and therefore eliminates contributions from the gas phase efficiently.[42] The excitation energy for the given Ir 4f spectra was set to 593 eV. Since Ir 4f measurements always succeeded O K-edge spectra and the excitation energy offset had been found to be smaller than 0.1eV for energies less than 100 eV apart, the energy calibration of the preceding O K-edge spectra was used for Ir 4f. The working electrode was in direct contact with the electron analyzer, which avoids shifts caused by applied potentials. All Ir 4f spectra were normalized to their Ir 4f 7/2 peak intensity.

3.7.6 Wetting experiment

A completely dry sample was mounted and three O K-edge spectra from different positions on the sample were averaged after processing them as described above. The same was done for a second sample of that type, which was wetted from the backside with 0.1 M H_2SO_4. On this sample, the spectra of five different positions were averaged. A simple difference of the averaged O K-edge spectra of the wet and the dry sample was compared to the O K-edge spectrum of liquid water. Many thanks to Schreck and Wernet for the permission to use the O K-edge absorption spectrum of liquid water measured in transmission.[19]

3.7.7 In situ steady state experiment

The state "as prepared" refers to the sample at stable open circuit potential and stable chamber pressure. Afterwards, electrochemical activation was performed with 50 cycles between 0.15 V_{RHE} and 1.65 V_{RHE} at a scanning rate of 500 mV/s. In the steady state experiment, the potential was always changed by linear sweep voltammetry with a rate of 100 mV/s and then held in a chronoamperometric step until the spectroscopic measurements were finished. Both, NEXAFS and XPS were recorded on two separate spots on the sample for each potential. Before and after the potential step spectra were recorded on the same spot. This procedure captures the change on one spot and double-checks the change on a fresh spot, which is not damaged by the beam. In this work, the spectra of the fresh spots were chosen for the presented plot (Figure 3.3), since those spots are not damaged by the beam. The trends between two fresh spots and potentials were carefully compared to the trends on one spot. On each potential step, the sample equilibrated for at least six minutes. A spectroscopic set on one spot took about eight minutes.

A support for an absorption feature well below 529 eV is not only found in the potentiodynamic experiment (Figure 3.5c), but also in the steady state experiment. When normalized to 529 eV, the O K-edges shows a clear broadening towards lower excitation energies in both, the total electron and partial electron yield (Figure 3.8).

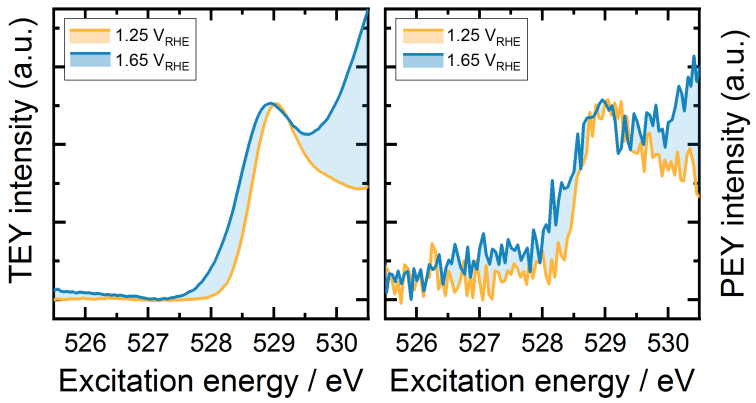

Figure 3.8: O K-edge measurements as presented in the main text, Figure 3.3f, but normalized to an excitation energy of 529 eV; on the left, the total electron yield (TEY) is shown; on the right, the partial electron yield at Ekin = 385 eV (PEY) is shown.

3.7.8 Potentiodynamic X-ray absorption

The sample was activated in the same manner as in the steady state experiment. After initial characterization, the working electrode was kept at 0.15 V_{RHE} for one minute, followed by two cycles between 0.15 V_{RHE} and 1.65 V_{RHE} at a scanning rate of 25 mV/s. The beamshutter was opened shortly before the two cycles and immediately closed afterwards. Only the second cycle is shown in Figure 3.5 in the main text. This procedure was repeated for each absorption energy. The PEY and TEY for the excitation energies of 528 eV and 529 eV were both normalized for the ring current. A background absorption signal was recorded and processed at an excitation energy of 526 eV, which is shown with the respective current (Figure 3.9a) and the derivative in Figure 3.9b. The background shows a gradual monotonic increase with increasing potential in contrast to strong structured changes for the features at 528 eV and 529 eV (see Figure 3.5). The background intensity at 526 eV was subtracted from the absorption signal recorded at the excitation energies 528 eV and 529 eV. The remaining absorption intensity at the excitation energies 528 eV and 529 eV is shown in Figure 3.5. The current given in the same figure was picked from the tracking of the absorption at 528 eV but can be viewed as representative for all. For comparison, the currents of a comparable sample without catalyst nanoparticles are also shown in Figure 3.5 but are unrelated to the spectroscopic measurements shown in the same figure.

The derivatives with respect to time were performed in OriginPro 2016 using a Savitzky-Golay smoothing function with a second order polynomial and a window including 20 points. The vertical axes of the absorption intensity and the derivatives are equivalent for both excitation energies and are therefore directly comparable.

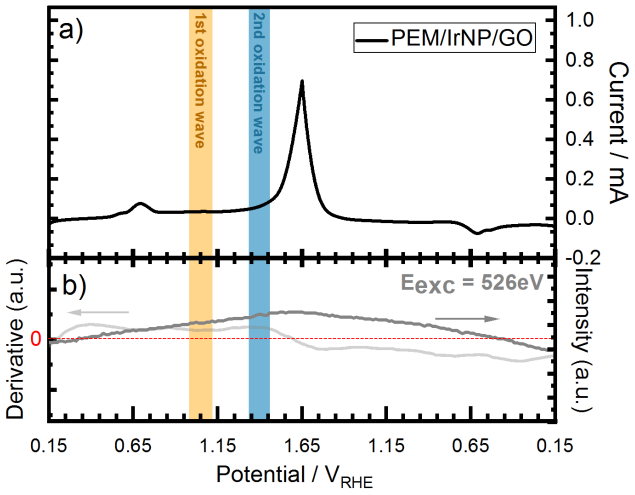

Figure 3.9: a) The current between the counter and the working electrode during potentiodynamic X-ray absorption; b) background absorption signal at 526 eV; the range of the intensity axis is directly comparable to Figure 3.5 in the main text.

3.7.9 Quickstep experiment

The sample for this experiment was prepared as described above, except for the sputtering, which was carried out for 10 s at 40 mA with a Cressington 108HR sputter coater, and the etching of the copper foils supporting graphene, which was carried out for 15 hours instead of 12 hours. Moreover, a niobium lid with a boron doped diamond coating was used instead of the glassy carbon lid.

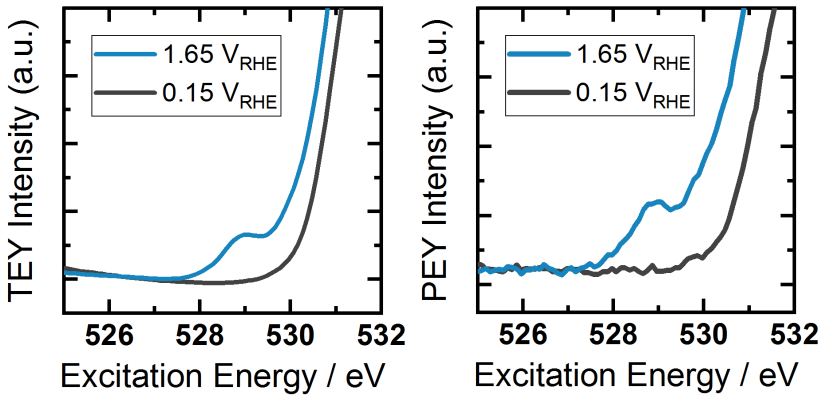

Figure 3.10: Pre-edge O K-edge absorption spectra at 0.15 V_{RHE} and shortly after ramping up to 1.65 V_{RHE} with a rate of 25 mV/s; the total electron yield (TEY) is shown on the left, the partial electron yield (at Ekin= 385 eV) on the right hand side; spectra of several spots on the sample were averaged.

In the quickstep experiment, the potential was held at 0.15 V_{RHE} for several minutes, then ramped up to 1.65 V_{RHE} with a rate of 25 mV/s and held at that potential. O K-edge spectra were recorded at 0.15 V_{RHE} and shortly after reaching 1.65 V_{RHE}. The procedure was repeated on multiple spots and the spectra recorded at the same potential were averaged. The resulting spectra are shown in Figure 3.10. An absorption signal at 528 eV is clearly visible from the spectra obtained via the total and the partial electron yield. It is possible that the feature at 528 eV is a tail of the larger absorption pre-edge at 529

eV, but the absorption edge rise is usually sharper (compare Figure 3.3d). The distinct development of the absorption at 528 eV with potential (compare Figure 3.5c) also indicates a separate species. The background below 528 eV in Figure 3.10 barely changes for the two potentials.

3.7.10 In situ blank experiments

For reference purposes, the measurements presented in the main text and above were also repeated without nanoparticles. The preparation procedure was as described above, except for the sputtering step, which was left out. The samples were wetted from the back with 0.1 M H_2SO_4 and were activated in the same manner as described above. An example for the initial oxidative cycling with 500 mV/s is shown in Figure 3.11. A clear feature develops at ~0.6 V_{RHE}. It can be attributed to the glassy carbon (GC) lid and the PEM membrane FAD55. The increase above 1.3 V_{RHE} can be attributed to corrosion and weak OER on the GC lid.[43]

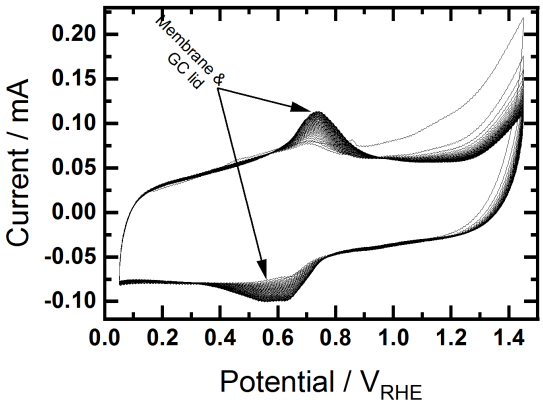

Figure 3.11: Initial cyclovoltammetry of graphene on the polymer membrane FAD55, wetted from the backside with 0.1 M H_2SO_4 and held down with a glassy carbon lid; 50 consecutive cycles with a scanning rate of 500 mV/s are shown.

3.7.11 Blank in situ steady state experiment

Potential stepping was performed as described above. The O K-edge spectra, which are normalized to the edge jump at 550 eV, are shown in Figure 3.12. They can directly be compared to Figure 3.3, because the intensity and excitation energy scales of the normalized O K-edge spectra are the same. The activated graphene electrode does not undergo oxidations visible in the O K-edge spectra below 1.25 V_{RHE}. Above, at 1.65 V_{RHE}, an increase of absorption between 530 eV and 533 eV is observed.

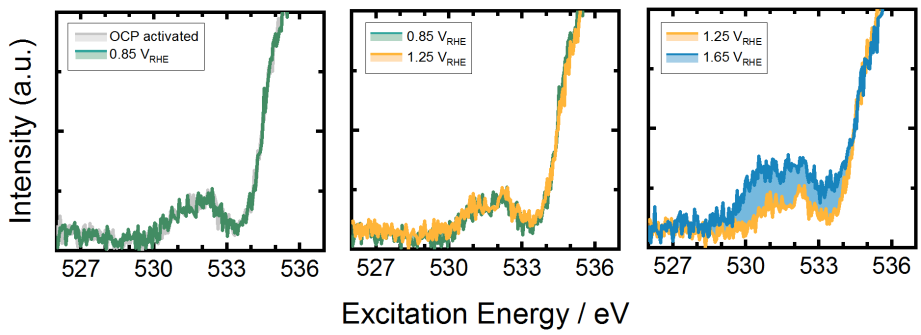

Figure 3.12: O K-edge spectra of graphene (oxide) on the PEM FAD55, wetted from the backside with 0.1 M H_2SO_4 at four potentials: OCP, 0.85 V_{RHE}, 1.25 V_{RHE}, and 1.65 V_{RHE}.

3.7.12 Blank potentiodynamic X-ray absorption

Also, the potentiodynamic X-ray absorption was repeated without iridium nanoparticles. The scanning speed was, again, 25 mV/s and spectroscopy and electrochemistry were recorded simultaneously. The partial and total electron yield for two excitation energies, 529 eV and 528 eV, are shown in Figure 3.13.

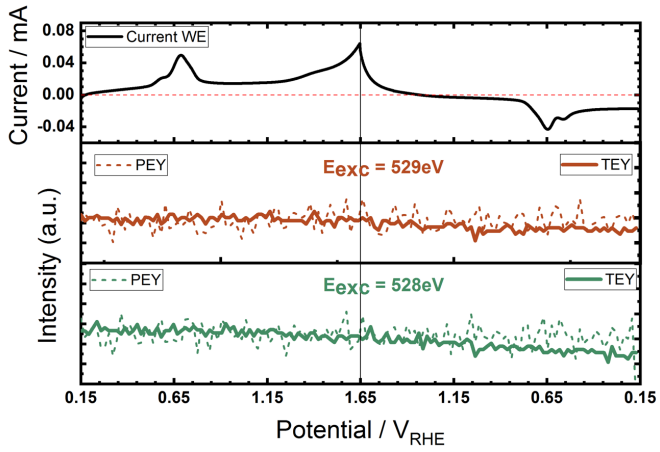

Figure 3.13: Graphene (oxide) on FAD55 membrane, wetted from the backside with 0.1 M H_2SO_4; on the top, the current of one cyclovoltammetric cycle at 25 mV/s is shown, below, the absorption at the excitation energies 528 eV and 529 eV (background signal recorded at 526 eV was subtracted) are shown over the turn of one electrochemical cycle.

The respective background signal at an excitation energy of 526 eV was subtracted from all absorption measurements shown in Figure 3.13. They exhibit no remarkable features. An exemplary current to the working electrode is given in the top part of Figure 3.13. Contributions to the currents are described above.

3.7.13 Computational details

DFT calculations were performed using the Quantum ESPRESSO package [38] using the Perdew, Burke, and Ernzerhof (PBE) exchange and correlation potential.[39] All calculations were performed non-spin polarized with the inclusion of scalar relativistic effects, unless stated otherwise.

To account for the possible role of hydrogen bonding in the O K-edge spectra, we performed Born Oppenheimer molecular dynamics simulations of two (110) IrO_2 slabs in water. The two types of slabs used in the MD simulations are shown in Figure 3.4. In one case the surface is terminated with μ_1-OH and μ_2-O, while in the other case the surface is fully oxidized; it is terminated with μ_1-O and μ_2-O. The molecular dynamics simulations were performed ultrasoft pseudopotentials with a kinetic energy (charge density) cutoff 30 Ry (300 Ry) and (4x4x1) **k**-point mesh for a (2x2) surface unit cell of a (110) IrO_2 slab with 5 metal layers and 12 D_2O molecules in the 0.15 nm separating periodic images. During each simulation the bottom two layers of the slab were held fixed. Simulations were run for 2 ps, 1 fs step size, using a Berendsen thermostat to efficiently equilibrate the system to 300 K.[44] Four snapshots of each surface were taken and used to generate the average O K-edge spectra of this surfaces in the presence of a water layer at 300 K. The different environments sampled by the snapshots recover the changes in O K-edge spectra with changes in local hydrogen bonding.

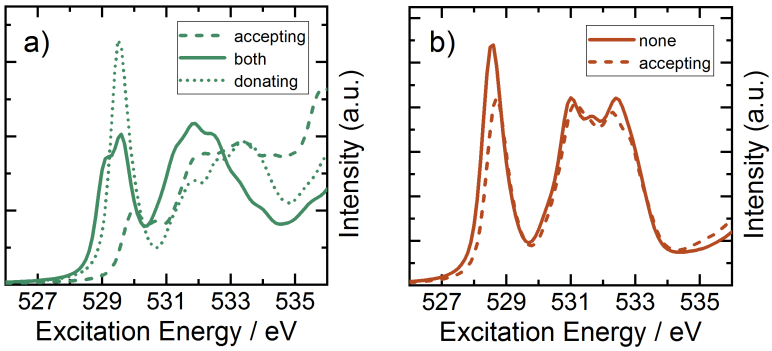

Figure 3.14: Influence of hydrogen bonding on the O K-edge spectrum, obtained from molecular dynamic snapshots of a) μ_1-OH and b) μ_2-O.

The O K-edge spectra of the oxygen on the IrO_2 slabs were computed using a Bethe-Salpeter Equation (BSE) approach to faithfully recover the screened core-hole potential and electron-hole dynamics. For this purpose we employed the ground state Kohn Sham wavefunctions computed with Quantum ESPRESSO together with the NIST core-level BSE solver [45,46] by way of the OCEAN package.[40,47] (Note, however, that we used normconserving pseudopotentials with a kinetic energy (charge density) cutoff of 100 Ry (400 Ry) for the spectroscopic calculations.) The relative core level shifts of the O K-edge spectra of individual absorber atoms in the slabs were computed by way of the ΔSCF method [48] using the (2x2) cell. The absolute alignment was accomplished using bulk IrO_2 by assuming an O 1s binding energy of 530.1 eV.

The calculated O K-edge spectra shown in Figure 3.4 are averaged over the snapshot. In Figure 3.14 the influence of hydrogen bonding on the edge structure of the μ_1-OH and μ_2-O species is also shown in the form of O K-edge spectra averaged over the nature of the hydrogen bonding associated with each absorber. That is, the contribution of the μ_1-OH involved in hydrogen bond donation is separated from the fraction involved in hydrogen bond accepting. For the case that the surface oxygen/hydroxide is a hydrogen bond acceptor, the pre-edge feature appears blue-shifted. When the surface μ_1-OH is

hydrogen bonding the spectra are red-shifted and the white line intensity increases, in-line with the fact the O K-edge is a measure of the projected density of unoccupied O 2*p* states. From this it is clear the maximum in white line intensity of μ_1-OH species will be sensitive to the local hydrogen bonding environment though generally falling between roughly 529-530 eV.

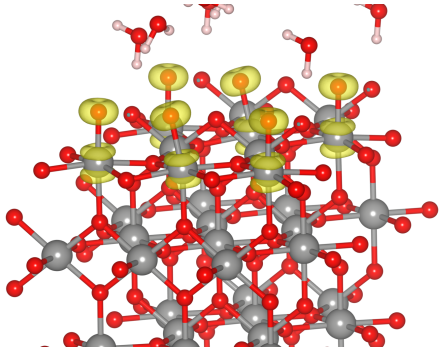

Figure 3.15: Spin density isosurface of the rutile type IrO_2 (110) surface covered with water.

The spin density isosurface in Figure 3.15 computed for an IrO_2 (110) surface shows only the μ_1-O species have significant radical character. All other oxygen atoms have paired spins.

We further calculated the surface energies based on the model of Rossmeisl et al. [32] using slabs in vacuum as solvation effects play a minor role on the relative stability of the species considered here.[49] We thereby created a surface phase diagram as a function of applied potential against a computational hydrogen electrode, given in V_{NHE}. We found that the surface is fully protonated below ~1.3 V_{NHE}. Bridging hydroxide, or μ_2-OH, is deprotonated at ~1.3 V_{NHE}, and CUS hydroxide (μ_1-OH) is deprotonated at ~1.5 V_{NHE}.

3.8 Bibliography

(1) Pfeifer, V.; Jones, T. E.; Velasco Vélez, J. J.; Arrigo, R.; Piccinin, S.; Hävecker, M.; Knop-Gericke, A.; Schlögl, R. In Situ Observation of Reactive Oxygen Species Forming on Oxygen-Evolving Iridium Surfaces. *Chem. Sci.* 2017, *8*, 2143–2149.

(2) Schlögl, R. Sustainable Energy Systems: The Strategic Role of Chemical Energy Conversion. *Top. Catal.* 2016, *59* (8–9), 772–786.

(3) Sartbaeva, A.; Kuznetsov, V. L.; Wells, S. A.; Edwards, P. P. Hydrogen Nexus in a Sustainable Energy Future. *Energy Environ. Sci.* 2008, *1*, 79–85.

(4) Carmo, M.; Fritz, D. L.; Mergel, J.; Stolten, D. A Comprehensive Review on PEM Water Electrolysis. *Int. J. Hydrog. Energy* 2013, *38*, 4901–4934.

(5) Trasatti, S. Electrocatalysis in the Anodic Evolution of Oxygen and Chlorine. *Electrochim. Acta* 1984, *29* (11), 1503–1512.

(6) Miles, M. H.; Thomason, M. A. Periodic Variations of Overvoltages for Water Electrolysis in Acid Solutions from Cyclic Voltammetric Studies. *J. Electrochem. Soc.* 1976, *123*, 1459–1461.

(7) Conway, B. E.; Mozota, J. Surface and Bulk Processes at Oxidized Iridium Electrodes-II. Conductivity-Switched Behaviour of Thick Oxide Films. *Electrochim. Acta* 1983, *28*, 9–16.

(8) Axnanda, S.; Crumlin, E. J.; Mao, B.; Rani, S.; Chang, R.; Karlsson, P. G.; Edwards, M. O. M.; Lundqvist, M.; Moberg, R.; Ross, P.; et al. Using "Tender" X-Ray Ambient Pressure X-Ray Photoelectron Spectroscopy as A Direct Probe of Solid-Liquid Interface. *Sci. Rep.* 2015, *5*, 9788.

(9) Itkis, D. M.; Velasco-Vélez, J. J.; Knop-Gericke, A.; Vyalikh, A.; Avdeev, M. V.; Yashina, L. V. Probing Operating Electrochemical Interfaces by Photons and Neutrons. *ChemElectroChem* 2015, *2*, 1427–1445.

(10) Knop-Gericke, A.; Pfeifer, V.; Velasco-Velez, J.-J.; Jones, T.; Arrigo, R.; Hävecker, M.; Schlögl, R. In Situ X-Ray Photoelectron Spectroscopy of Electrochemically Active Solid-Gas and Solid-Liquid Interfaces. *J. Electron Spectrosc. Relat. Phenom.* 2017, *221*, 10–17.

(11) Sanchez Casalongue, H. G.; Ng, M. L.; Kaya, S.; Friebel, D.; Ogasawara, H.; Nilsson, A. In Situ Observation of Surface Species on Iridium Oxide Nanoparticles during the Oxygen Evolution Reaction. *Angew. Chem., Int. Ed.* 2014, *53*, 7169–7172.

(12) Lettenmeier, P.; Majchel, J.; Wang, L.; Saveleva, V. A.; Zafeiratos, S.; Savinova, E. R.; Gallet, J.-J.; Bournel, F.; Gago, A. S.; Friedrich, K. A. Highly Active Nano-Sized Iridium Catalysts: Synthesis and Operando Spectroscopy in a Proton Exchange Membrane Electrolyzer. *Chemi.Sci.* 2018, *9*, 3570–3579.

(13) Pfeifer, V.; Jones, T. E.; Velasco Vélez, J. J.; Massué, C.; Arrigo, R.; Teschner, D.; Girgsdies, F.; Scherzer, M.; Greiner, M. T.; Allan, J.; et al. The Electronic Structure of Iridium and Its Oxides. *Surf. Interface Anal.* 2016, *48* (5), 261–273.

(14) Pfeifer, V.; Jones, T. E.; Wrabetz, S.; Massué, C.; Velasco Vélez, J. J.; Arrigo, R.; Scherzer, M.; Piccinin, S.; Hävecker, M.; Knop-Gericke, A.; et al. Reactive Oxygen Species in Iridium-Based OER Catalysts. *Chem. Sci.* 2016, *7*, 6791–6795.

(15) Velasco-Velez, J. J.; Pfeifer, V.; Hävecker, M.; Weatherup, R. S.; Arrigo, R.; Chuang, C.-H.; Stotz, E.; Weinberg, G.; Salmeron, M.; Schlögl, R.; et al. Photoelectron Spectroscopy at the Graphene-Liquid Interface Reveals the Electronic Structure of an Electrodeposited Cobalt/Graphene Electrocatalyst. *Angew. Chemie Int. Ed.* 2015, *54* (48), 14554–14558.

(16) Nappini, S.; Matruglio, A.; Naumenko, D.; Dal Zilio, S.; Bondino, F.; Lazzarino, M.; Magnano, E. Graphene Nanobubbles on TiO2 for In-Operando Electron Spectroscopy of Liquid-Phase Chemistry. *Nanoscale* 2017, *9*, 4456–4466.

(17) Guo, H.; Strelcov, E.; Yulaev, A.; Wang, J.; Appathurai, N.; Urquhart, S.; Vinson, J.; Sahu, S.; Zwolak, M.; Kolmakov, A. Enabling Photoemission Electron Microscopy in Liquids via Graphene-Capped Microchannel Arrays. *Nano Lett.* 2017, *17*, 1034–1041.

(18) Nilsson, A.; Nordlund, D.; Waluyo, I.; Huang, N.; Ogasawara, H.; Kaya, S.; Bergmann, U.; Näslund, L. Å.; Öström, H.; Wernet, P.; et al. X-Ray Absorption Spectroscopy and X-Ray Raman Scattering of Water and Ice; an Experimental View. *J. Electron Spectrosc. Relat. Phenom.* 2010, *177*, 99–129.

(19) Schreck, S.; Wernet, P. Isotope Effects in Liquid Water Probed by Transmission Mode X-Ray Absorption Spectroscopy at the Oxygen K-Edge. *J. Chem. Phys.* 2016, *145*, 104502.

(20) Cicero, G.; Grossman, J. C.; Schwegler, E.; Gygi, F.; Galli, G. Water Confined in Nanotubes and between Graphene Sheets: A First Principle Study. *J. Am. Chem. Soc.* 2008, *130*, 1871–1878.

(21) Buckley, D. N.; Burke, L. D. The Oxygen Electrode - Part 5. - Enhancement of Charge Capacity of an Iridium Surface in the Anodic Region. *J. Chem. Soc., Faraday Trans. 1* 1975, *71*, 1447–1459.

(22) Gottesfeld, S.; Srinivasan, S. Electrochemical and Optical Studies of Thick Oxide Layers on Iridium and Their Electrocatalytic Activities for the Oxygen Evolution Reaction. *J. Electroanal. Chem.* 1978, *86*, 89–104.

(23) Kötz, R.; Neff, H.; Stucki, S. Anodic Iridium Oxide Films - XPS-Studies of Oxidation State Changes and O2 Evolution. *J. Electrochem. Soc.* 1984, *131*, 72–77.

(24) Hüppauff, M.; Lengeler, B. Valency and Structure of Iridium in Anodic Iridium Oxide Films. *J. Electrochem. Chem.* 1993, *140*, 598–602.

(25) Hall, H. Y.; Sherwood, P. M. A. X-Ray Photoelectron Spectroscopic Studies of the Iridium Electrode System. *J. Chem. Soc., Faraday Trans. 1* 1984, *80*, 135–152.

(26) Glarum, S. H.; Marshall, J. H. The A-C Response of Iridium Oxide Films. *J. Electrochem. Soc.* 1980, *127*, 1467–1474.

(27) Weber, D.; Schoop, L. M.; Wurmbrand, D.; Nuss, J.; Seibel, E. M.; Tafti, F. F.; Ji, H.; Cava, R. J.; Dinnebier, R. E.; Lotsch, B. V. Trivalent Iridium Oxides: Layered Triangular Lattice Iridate K0.75 Na0.25 IrO2 and Oxyhydroxide IrOOH. *Chem. Mater.* 2017, *29*, 8338–8345.

(28) Kawasaki, J. K.; Uchida, M.; Paik, H.; Schlom, D. G.; Shen, K. M. Evolution of Electronic Correlations across the Rutile, Perovskite, and Ruddelsden-Popper Iridates with Octahedral Connectivity. *Phys. Rev. B* 2016, *94*, 121104(R).

(29) Ping, Y.; Galli, G.; Goddard, W. A. Electronic Structure of IrO2: The Role of the Metal d-Orbitals. *J. Phys. Chem. C* 2015, *119*, 11570–11577.

(30) Nong, H. N.; Reier, T.; Oh, H.-S.; Gliech, M.; Paciok, P.; Vu, T. H. T.; Teschner, D.; Heggen, M.; Petkov, V.; Schlögl, R.; et al. A Unique Oxygen Ligand Environment Facilitates Water Oxidation in Hole-Doped IrNiOx Core–Shell Electrocatalysts. *Nat. Catal.* 2018, *1* (11), 841–851.

(31) Velasco-Vélez, J. J.; Jones, T. E.; Streibel, V.; Hävecker, M.; Chuang, C.-H.; Frevel, L.; Plodinec, M.; Centeno, A.; Zurutuza, A.; Wang, R.; et al. Electrochemically Active Ir NPs on Graphene for OER in Acidic Aqueous Electrolyte Investigated by in Situ and Ex Situ Spectroscopies. *Surf. Sci.* 2019, *681*, 1–8.

(32) Rossmeisl, J.; Qu, Z.-W.; Zhu, H.; Kroes, G.-J.; Nørskov, J. K. Electrolysis of Water on Oxide

Surfaces. *J. Electroanal. Chem.* 2007, *607* (1–2), 83–89.

(33) Minguzzi, A.; Locatelli, C.; Lugaresi, O.; Achilli, E.; Cappelletti, G.; Scavini, M.; Coduri, M.; Masala, P.; Sacchi, B.; Vertova, A.; et al. Easy Accommodation of Different Oxidation States in Iridium Oxide Nanoparticles with Different Hydration Degree as Water Oxidation Electrocatalysts. *ACS Catal.* 2015, *5*, 5104–5115.

(34) Abbott, D. F.; Lebedev, D.; Waltar, K.; Povia, M.; Nachtegaal, M.; Fabbri, E.; Copéret, C.; Schmidt, T. J. Iridium Oxide for the Oxygen Evolution Reaction: Correlation between Particle Size, Morphology, and the Surface Hydroxo Layer from Operando XAS. *Chem. Mater.* 2016, *28*, 6591–6604.

(35) Pauporté, T.; Aberdam, D.; Hazemann, J.-L.; Faure, R.; Durand, R. X-Ray Absorption in Relation to Valency of Iridium in Sputtered Iridium Oxide Film. *J. Electroanal. Chem.* 1999, *465*, 88–95.

(36) Hillman, A. R.; Skopek, M. A.; Gurman, S. J. X-Ray Spectroscopy of Electrochemically Deposited Iridium Oxide Films: Detection of Multiple Sites through Structural Disorder. *Phys. Chem. Chem. Phys.* 2011, *13* (12), 5252–5263.

(37) Ping, Y.; Nielsen, R. J.; Goddard, W. A. The Reaction Mechanism with Free Energy Barriers at Constant Potentials for the Oxygen Evolution Reaction at the IrO 2 (110) Surface. *J. Am. Chem. Soc.* 2017, *139* (1), 149–155.

(38) Giannozzi, P.; Baroni, S.; Bonini, N.; Calandra, M.; Car, R.; Cavazzoni, C.; Ceresoli, D.; Chiarotti, G. L.; Cococcioni, M.; Dabo, I.; et al. QUANTUM ESPRESSO: A Modular and Open-Source Software Project for Quantum Simulations of Materials. *J. Phys. Condens. Matter* 2009, *21*, 395502.

(39) Perdew, J. P.; Burke, K.; Ernzerhof, M. Generalized Gradient Approximation Made Simple. *Phys. Rev. Lett.* 1996, *77*, 3865–3868.

(40) Vinson, J.; Rehr, J. J.; Kas, J. J.; Shirley, E. L. Bethe-Salpeter Equation Calculations of Core Excitation Spectra. *Phys. Rev. B* 2011, *83*, 115106.

(41) Bard, A. J.; Faulkner, L. R. *Electrochemical Methods - Fundamentals and Applications*, 2nd ed.; John Wiley & Sons, Inc.: New York, 2000.

(42) Siegbahn, H. Electron Spectroscopy for Chemical Analysis of Liquids and Solutions. *J. Phys. Chem.* 1985, *89*, 897–909.

(43) Yi, Y.; Weinberg, G.; Prenzel, M.; Greiner, M.; Heumann, S.; Becker, S.; Schlögl, R. Electrochemical Corrosion of a Glassy Carbon Electrode. *Catal. Today* 2017, *295*, 32–40.

(44) Berendsen, H. J. C.; Postma, J. P. M.; Van Gunsteren, W. F.; DiNola, A.; Haak, J. R. Molecular Dynamics with Coupling to an External Bath. *J. Chem. Phys.* 1984, *81*, 3684–3690.

(45) Soininen, J. A.; Shirley, E. L. Scheme to Calculate Core Hole–Electron Interactions in Solids. *Phys. Rev. B* 2001, *64* (16), 165112.

(46) Shirley, E. L. Ti 1s Pre-Edge Features in Rutile: A Bethe-Salpeter Calculation. *J. Electron. Spectrosc.* 2004, *136*, 77–83.

(47) Vinson, J.; Rehr, J. J. Ab Initio Bethe-Salpeter Calculations of the X-Ray Absorption Spectra of Transition Metals at the L-Shell Edges. *Phys. Rev. B.* 2012, *86*, 195135.

(48) Pehlke, E.; Scheffler, M. Evidence for Site-Sensitive Screening of Core Holes at the Si and Ge (001) Surface. *Phys. Rev. B.* 1993, *71*, 2338–2341.

(49) Gauthier, J. A.; Dickens, C. F.; Chen, L. D.; Doyle, A. D.; Nørskov, J. K. Solvation Effects for Oxygen

Evolution Reaction Catalysis on IrO2(110). *J. Phys. Chem. C* **2017**, *121*, 11455–11463.

4. On the active surface of iridium oxo-hydroxides under applied potential

4.1 Preliminary Remarks

In the previous and following chapter (3 and 5), various iridium (hydr-)oxides are investigated using in situ spectroscopy. The resulting spectra are interpreted with the help of calculated spectra using DFT calculations of IrO_2 (110) surfaces. Although this approach explains the observed phenomena well, the calculated and measured atomic structures are different and a "structure gap" is present. This gap is narrowed within this fourth chapter in which a detailed investigation of the layered IrOOH structure and the respective nanosheets is presented. With the same combination of in situ spectroscopy and DFT calculations on IrOOH nanosheets, it was possible to, first, observe the electronic structure of IrOOH in the oxidation state of Ir^{III} and Ir^{IV} (IrOO), and, second, record the active state of these nanosheets with both, ab initio and experimental techniques. These observations address Q1, Q2, and Q3. However, the small structure gap of these results does not significantly improve the qualitative correlations obtained from using the IrO_2 (110) surface to qualitatively explain the electrochemistry of iridium (hydr–)oxides. This chapter thereby validates the methodology used in chapter 3 and 5.

The layered IrOOH material was developed and synthesized by Sourav Laha and Daniel Weber and was characterized with UV-Vis spectroscopy by Filip Podjaski and Alberto Jiménez-Solano at the Max Planck Institute for Solid State Research (MPI-SSR) under the supervision of Bettina Lotsch. Structural characterization using XRD was done by Maxwell Terban under the supervision of Robert Dinnebier (MPI-SSR) and by Frank Girgsdies at the Fritz-Haber-Institute (FHI). The remaining experiments were also performed at the FHI, unless otherwise mentioned. TPR experiments using hydrogen and reactor-based CO titration were done with the help of Andrey Tarasov. Respective in situ X-ray spectroscopy under CO at the BelChem beamline was recorded together with Travis Jones and the help of Juan-Jesús Velasco-Vélez. Ex situ TEM experiments were performed together with Thomas Götsch, who also analyzed the electron diffraction patterns and micrographs. Woosun Jang performed the DFT calculations with help from Travis Jones. The project was planned and developed together with Travis Jones, who also played an important role in the revisions. Axel Knop-Gericke, Thomas Lunkenbein, and Robert Schlögl offered advice and guidance for the project. All scientists contributed to the text by comments or text sections. Artistic renderings in Figure 4.5, Figure 4.6, and Figure 4.36 were made by Fabian Schnippering.

4.2 Abstract

Mixed Ir^{III}/Ir^{IV} (hydr-)oxides have been found to be highly active catalysts in the oxygen evolution reaction. They surpass the activity of crystalline rutile-type $Ir^{IV}O_2$ and exhibit hydrated and amorphous structures. However, reasons for their higher activity are difficult to pinpoint because of their complex atomic structure. Structure function relationships of mixed Ir^{III}/Ir^{IV} (hydr-)oxides are therefore difficult to find. We contribute to this area of research with operando X-ray spectroscopy of crystalline and highly active IrOOH nanosheets. The strength of our study is that we can directly link thermodynamic properties of surface species to their potential-dependent appearance in operando experiments. Thermodynamic properties are obtained from density functional theory and the link to experiment is provided by X-ray absorption spectroscopy, which is calculated ab initio and recorded experimentally under wet conditions and applied potential. Using this strategy, we could observe the changes in the electronic structure over the transition from Ir^{III} to Ir^{IV} and we show that a ligand centered oxidation step produces the active site of the oxygen evolution reaction on IrOOH nanosheets; a trend that holds for various iridium (hydr-)oxides. Our findings demonstrate that the degree of surface protonation mediates the electronic structure and function of electrocatalysts for evolving oxygen.

4.3 Introduction

The levelized cost of electricity from solar and wind has dropped below conventional methods based on fossil resources. Even in Germany, a country with relatively low solar irradiation, the power from large photovoltaic installations was cheaper than from conventional power plants in a particularly sunny year 2018.[1] Propelled by this trend, the use of green hydrogen as an energy carrier looks more promising than ever and worldwide initiatives to promote the use of hydrogen thrive.[2,3] A key technology to produce hydrogen using renewable energy sources (green hydrogen), is the proton exchange membrane (PEM) electrolyzer, which operates in acidic conditions. It is more compact than its alkaline counterpart, produces extremely pure hydrogen at high pressures and can be operated dynamically.[4–6] These benefits promise a decentralized solution to produce green hydrogen using electrical power from renewable sources. One limitation to this technology is the corrosive environment on the side of the anodic oxygen evolution reaction (OER), because it reduces the catalyst choice to mostly scarce, noble metal oxides. The materials with the best balance of stability and activity are iridium oxides.[7] Although it has been discussed that iridium might be too rare to provide the catalyst material for PEM electrolyzers at a global scale,[8,9] the exceptional combination of high activity and stability make iridium oxides an interesting example for the development of new catalyst materials.

Among iridium oxides, especially the amorphous iridium (hydr-)oxides have been found to be particularly active catalysts of the OER.[10–13] These materials are usually hydrated,[14–17] they exhibit larger surface areas than crystalline counterparts,[10,18,19] and the average oxidation state of iridium is between Ir^{III} and Ir^{IV}.[11,12,20] Interestingly, their higher activity could not be fully explained by their larger surface area when compared to more crystalline counterparts. Instead, amorphous materials are intrinsically

more active.[10,11,18,19] The latter result suggests that the distribution of surface species or the mixed oxidation state are reasons for the higher activity. Knowing the distribution of surface species and the oxidation state of the metal centers is then of paramount importance to understand electrocatalytic processes on iridium (hydr-)oxides.

There are two main obstacles to further investigate the role of surface species and their oxidation states on the catalytic activity of iridium (hydr-)oxides as electrocatalysts: First, measuring the electronic structure of the catalysts surface under operating conditions and, second, the complexity of amorphous structures and of the information obtained from measuring them. The first challenge has been addressed by X-ray spectroscopy. X-ray spectroscopy is a tool well suited to study the electronic structure of iridium (hydr-)oxides.[14,20,21] In particular, photoelectrons excited with soft X-rays can capture the electronic structure of the catalysts surface, due to the small escape depth of photoelectrons (a few nanometer for X-ray absorption using all primary and secondary electrons, and below one nanometer for photo- and Auger-electrons). In an effort to utilize this measurement technique under wet conditions, a variety of in situ cells have been developed and used.[22,23] For the case of iridium, in situ studies have been undertaken in water vapor probing iridium dioxide [24,25] or activated iridium metal [25,26] and under wet conditions as activated iridium nanoparticles.[27,28] By comparing to ab initio calculations of various surfaces of rutile-type IrO_2, the studies were able to identify electron-deficient oxygen species under reaction conditions.[25–28] These electron-holes on oxygen form when iridium (hydr-)oxides are oxidized far enough to enter a negative charge-transfer regime.[27,29] With the help of potentiodynamic X-ray absorption, it was even possible to distinguish between different surface oxygen species that can become electron deficient by correlating their formation with electrochemical oxidation events.[28]

Building on these studies, we aim to narrow the structure gap between what is measured operando and what is calculated ab initio. To that aim, we use 2D nanosheets of the iridium (hydr-)oxide IrOOH, which have been presented earlier.[30] We will show that the electronic structure of IrOOH is similar to other mixed Ir^{III}/Ir^{IV} (hydr-)oxides, while being a particularly active OER catalyst. Furthermore, we show for nanosheets of IrOOH that potential driven phase transitions transform the electronic structure of the electrocatalyst. Approaching potentials relevant to the OER, the nanosheets enter a negative charge transfer regime and oxygen is oxidized. Oxygen species at the edge of the sheets can be fully oxidized, forming oxyls. These radical oxygen species are likely to be the active sites of IrOOH nanosheets and other iridium (hydr-)oxides.

4.4 Results and Discussion

IrOOH is synthesized from a precursor material $K_{0.75}Na_{0.25}IrO_2$ by exchanging the cations for protons in 1 M HCl. The synthesis follows the procedure of a previous report [31] but the temperature treatment of the precursor was altered in order to avoid a hollandite side phase in the final product (see

Experimental section and Supporting Information for a more detailed description of the synthesis). IrOOH are dark crystallites with a tinge of pink.

4.4.1 Crystal structure

The powder X-ray diffraction (PXRD) pattern shown in Figure 4.1A exhibits pronounced peak broadening anisotropy, with sharp hk0 reflections demonstrating well-ordered brucite type sheets, and significant broadening of the 00l series indicating lower crystallinity, i.e. smaller domain size and/or some degree of stacking disorder, along the *c* axis. Within the limits of the method, we could not detect any hollandite byphase, confirming the effectiveness of the temperature treatment in the synthesis.

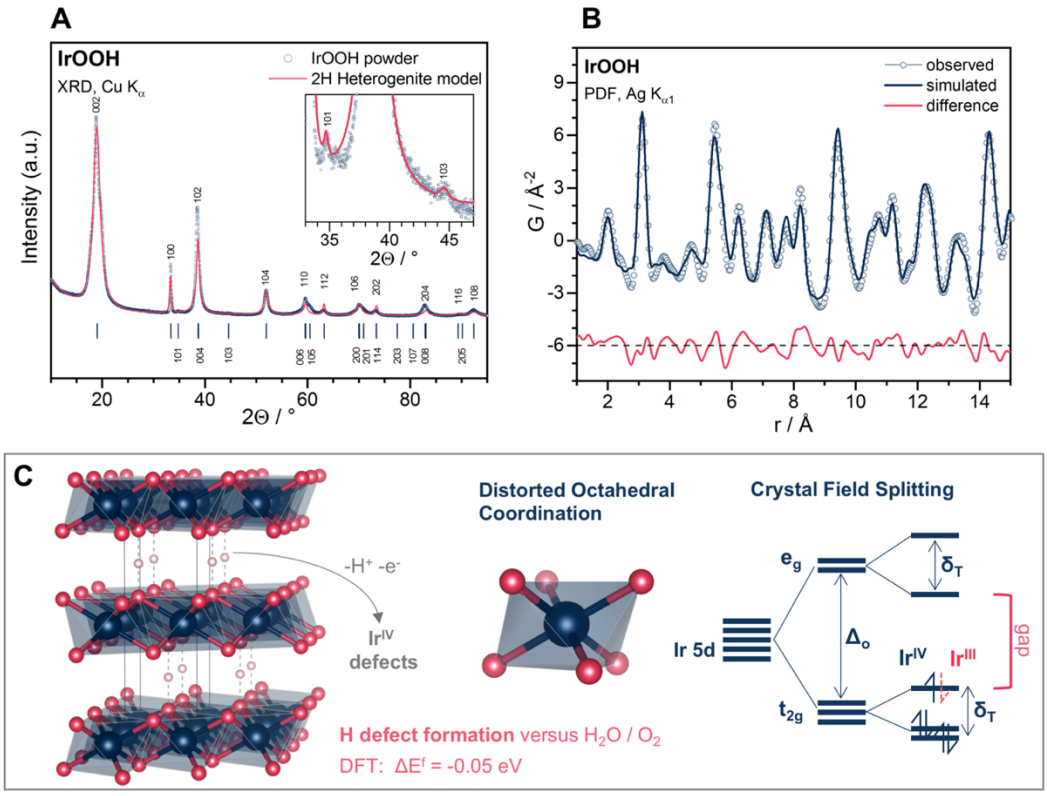

Figure 4.1: Characterization of IrOOH; A) Diffractogram and Rietveld simulation of heterogenite-2H, Laue indices of intense reflections are given above the curve; the inset shows the two superstructure reflections at 35° and 45°; B) the simulated and observed pair distribution function obtained from a heterogenite-2H model and IrOOH X-ray scattering; C) representation of the heterogenite-2H crystal structure and a scheme of the expected crystal field splitting for the valence states of iridium.

In contrast to the original publication,[31] which proposed a brucite-1*T* type structure (space group *P*-3*m*1) for IrOOH, we observe weak superstructure reflections at ~35° and ~45° 2θ, as shown in the inset of Figure 4.1A. These additional reflections can be indexed successfully by doubling the *c* axis, which indicates that the crystal structure of IrOOH is more appropriately described assuming a heterogenite-2*H* type model (space group $P6_3/cmm$) with an AB stacking of layers, in analogy to the structure reported for the precursor $K_{0.75}Na_{0.25}IrO_2$.[31] It should be pointed out here that corresponding brucite-1*T* and heterogenite-2*H* models, besides the aforementioned superstructure reflections, yield

almost identical Rietveld simulations (see Figure 4.9A and B, respectively). In contrast, a heterogenite-3*R* type (ABC) stacking would result in a distinctively different diffraction pattern and can thus be excluded (Figure 4.9C). Further support for the heterogenite-2*H* structure comes from density functional theory (DFT) calculations, which predict the formation energy of heterogenite-2*H* and brucite IrOOH to differ by 0.26 eV (see Table 4.4). Finally, it should be mentioned that the 002 reflection exhibits an unexplained fine structure, with a relatively sharp tip in the center and clearly visible shoulders of different heights on the left and right flanks, looking like a superposition of (at least) three peaks (Figure 4.10). This indicates that either the actual crystal structure of IrOOH, or the phase composition of the sample, is more complex than we are currently able to describe.

The heterogenite-2*H* structure was used as a starting point to analyze the pair distribution function (PDF) of IrOOH (Figure 4.1B). The observed and simulated oscillations of the PDF match well in the local structure range up to 15 Å, indicating good short- to medium-range order (see Supporting Information for more detail). The average Ir-O distance was found to be 2.01 Å and the closest Ir-Ir distance 3.11 Å. These distances are close to what was observed by PXRD, namely 2.05 Å and 3.10 Å, respectively. DFT calculations of fully relaxed heterogenite-2*H* structures were found to be 2.10 Å for the average Ir-O bond length and 3.23 Å for the closest Ir-Ir distance.

We can conclude that the long-, medium-, and short-range order in the experiments fits well to the heterogenite 2*H* structure, but its stacking order seems to be slightly disturbed. Heterogenite 2*H* also has a lower ground state energy than brucite-type or 3*R* stacking.

4.4.2 Hydrogen defects

A possible source of the stacking disorder could be the position and quantity of hydrogen between the layers, which is unknown from the techniques above. Enrichment with hydrogen is not expected because it would reduce Ir^{III} in the $[Xe]6s^0 5d^6$ configuration to Ir^{II} in a $5d^7$ configuration. Considering the expected crystal field splitting, such an electron configuration leads to a partial occupation of antibonding e_g-like states of the octahedrally coordinated iridium atoms, which comes at a high energy cost (see Figure 4.1C). More likely is the formation of hydrogen defects, which create Ir^{IV} defects with a $[Xe]6s^0 5d^5$ electron configuration. The driving force is possibly spin orbit splitting, which has been found to destabilize Ir^{III} oxides.[32] We estimated the formation energy of a hydrogen defect in a heterogenite-2*H* structure by DFT. When one out of eight hydrogen atoms are removed (Figure 4.20), the formation energy is -0.64 eV against a reservoir of water and oxygen (Table 4.5), which indicates that hydrogen defects can be formed spontaneously in air at room temperature, as it is indicated in Figure 4.1C. Removing one hydrogen further from the structure, is with about -1.29 eV as favorable. These defects affect the crystal structure, as our ab initio calculations show: removing one out of four hydrogen atoms increases the inter-layer spacing by ~0.1 Å while the basal plane contracts by the same magnitude. Distortion of the octahedra is more scattered for defected structures (see Figure 4.21). Hydrogen defects could therefore partly explain the lattice distortion observed in X-ray diffraction.

Accounting for a possibly undefined hydrogen content, we introduce the general stoichiometry $IrO_{2-2x}(OH)_{2x}$. The variable x and thereby the oxidation of iridium is determined using temperature programmed reduction (TPR) in hydrogen. The initial weight and the amount of hydrogen consumed in the reduction were used to calculate the stoichiometry (more detailed information is given in the Supporting Information). The resulting sample stoichiometry $IrO_{1.5}(OH)_{0.5}$ indicates that, depending on the level of exposure to air, every second hydrogen could be missing in IrOOH. Such a high defect density also leads to weak absorption of visible light expected for the gapped Ir^{III} in a $[Xe]6s^05d^6$ electron configuration (see Figure 4.28).

4.4.3 Electronic structure

Iridium(III) compounds have an electron configuration of $[Xe]6s^05d^6$. Thus, the t_{2g}-like states of the octahedrally coordinated Ir^{III} ions are completely occupied. The octahedral distortion in the case of IrOOH is expected to only have a small effect on t_{2g} degeneracy and will therefore not close the gap (see Figure 4.1C). A more detailed picture of the electronic structure is obtained from ab initio calculations.

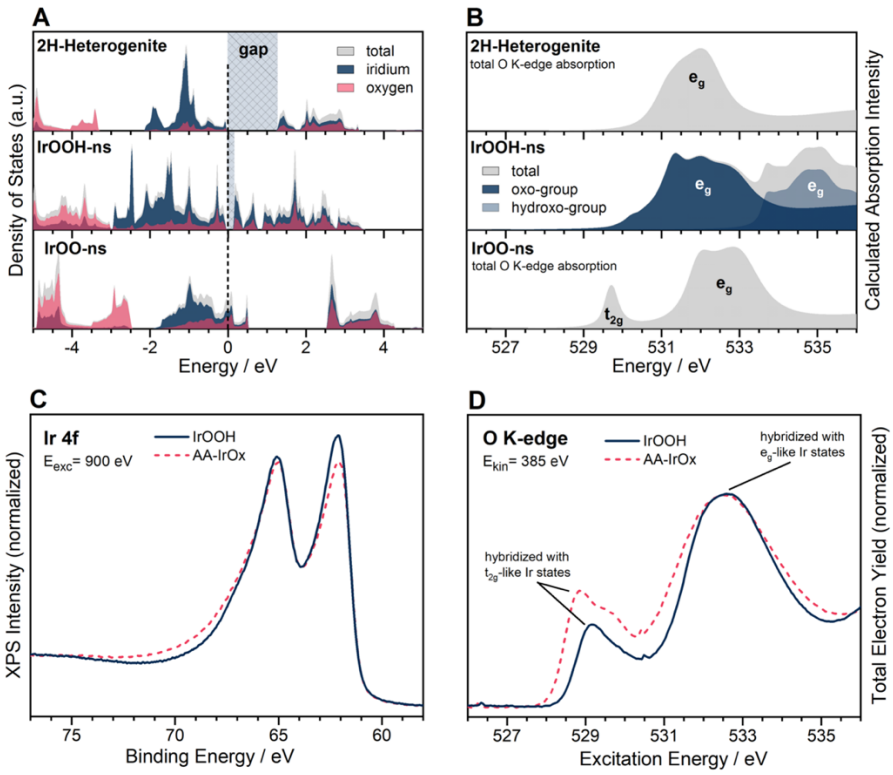

Figure 4.2: A) Total and partial DOS relative to the Fermi-energy of heterogenite-2H IrOOH, single sheets of IrOOH, and single sheets without hydrogen (IrOO); B) O K-edge spectra calculated by DFT coupled with the solution of the Bethe-Salpeter equation; C) experimental Ir 4f XP spectra and D) O K-edge absorption of IrOOH and AA-IrOx.

Figure 4.2A shows the calculated density of states (DOS) of heterogenite-2*H* with an occupied t_{2g} and an unoccupied e_g contribution. They are clearly separated by a gap of 1.3 eV. This is in fair agreement

with the 1.9 eV from a closer analysis of diffuse UV-Vis reflectance (Figure 4.30), as our DFT method underestimates the magnitude of the gap.[33] The creation of H-defects then leads to a partial occupation of t_{2g}-like states. At the extreme, the sheet is without any hydrogen. The DOS of one hydrogen-free sheet has a clear contribution at the Fermi energy (Figure 4.2A) and t_{2g}-like states are indeed partially occupied. In addition, the t_{2g}-e_g splitting is increased for the case of IrOO compared to IrOOH in the heterogenite-2*H* structure.

A good measure of the unoccupied projected DOS (PDOS) is X-ray absorption spectroscopy of core electrons. In this method, the X-rays excite core electrons into unoccupied states and it has been shown that the integrated intensity of the first possible transition (white line) scales with the empty PDOS of the probed element.[34] This means, the white line intensity is a measure of the hole character or oxidation state of the probed element. In the case of IrOOH, oxygen and iridium both contribute to the density of states above (and below) the Fermi energy because they are strongly hybridized (see Figure 4.2A). The projected DOS of oxygen, therefore, contains information about the metal center and vice versa. In the following, we will use O K-edge absorption, because it has a detailed fine structure and the white line position of surface oxygen species are well separated for iridium oxides.[26,28] The calculated O K-edges are shown next to their respective density of states in Figure 4.2B. The heterogenite-2*H* structure with its t_{2g}-like states fully filled has an absorption feature at 532 eV, which originate from hybridization with e_g-like states of iridium. In IrOOH nanosheets (IrOOH-ns), hydrogen cannot be shared between neighboring layers, so that oxygen species are not equivalent anymore. The white line of oxo-groups centers at 530.6 eV and the white line of hydroxo-groups is split into two peaks at 533.8 eV and 534.6 eV. The hydrogen-free sheet (IrOO-ns) has two absorption features at 529.6 eV and 532.7 eV, which originate from excitations into empty t_{2g}- and e_g-like states, respectively. The experimental results are shown in Figure 4.2C-D: IrOOH (as prepared) has two absorption white lines; one of which appears slightly above 529 eV and a second resonance appears at ~532.5 eV (Figure 4.2D), which would agree well with a t_{2g}-like and e_g-like contribution of a mixed Ir^{III}/Ir^{IV} oxidation state. In an effort to quantify the ratio of Ir^{III} to Ir^{IV} in heterogenite-2*H* powder, we integrated the absorption intensities, which are related to electron hole density on oxygen, and found a ratio of 1:2 (discussion of Figure 4.31). This is in fair agreement with the results from TPR (1:1), but a large error for the integration of the O K-edges is expected for the integrated intensity due to the unknown position and shape of the background. Also, the exposure to air was not controlled and might be different in the powders used for the TPR and spectroscopic measurement.

An experimental comparison to an active industrial catalyst AA-IrOx, which has been discussed in detail elsewhere,[12,20,35,36] is strikingly similar. AA-IrOx is also a mixed Ir^{III}/Ir^{IV} (hydr-)oxide resonances slightly below 529 eV and at 532.5 eV (see Figure 4.2D), suggesting a similar electronic structure in the two materials. Also X-ray photoelectron spectroscopy (XPS) of the Ir 4f level is very similar in shape and the binding energy (BE) of the main line (Ir 4f 7/2) is about 62 eV in both materials (see Figure 4.2C). The broadening to higher binding energies can be attributed to shake-up satellites [20,37] or small losses from excitations close to the Fermi edge characteristic for metallic samples.

Despite these similarities, it is not yet clear if they are caused by a similarity in the Ir-O bonding. This is, because final state effects in iridium compounds influence their spectroscopy. The Ir 4f binding energy, for example, reversely shifts with oxidation state, due to final state effects,[20] and the resonant excitation energy of the O K-edge absorption white line could shift in the presence of a band gap, as the e_g contributions in Figure 4.2B show.

4.4.4 (Electro-)Chemistry of IrOOH

The first chemical test is CO oxidation at room temperature. AA-IrOx is known to oxidize CO at room temperature and the reactive species has been identified to be an electron-deficient oxygen species absorbing at 529 eV.[35] We tested reactivity with CO in a flow-through reactor with 250 ppm of CO in Ar at standard pressure and room temperature. With this method the complete surface of the material is in contact with the gas phase, providing good sensitivity. In a complementary experiment at the same partial pressure of CO (0.25 mbar), we also measured the spectroscopic changes on the surface of the same powders in situ using a near-ambient pressure XPS (NAP-XPS) setup. Changes in the gas phase during in situ experiments were recorded by mass spectrometry (Figure 4.32).

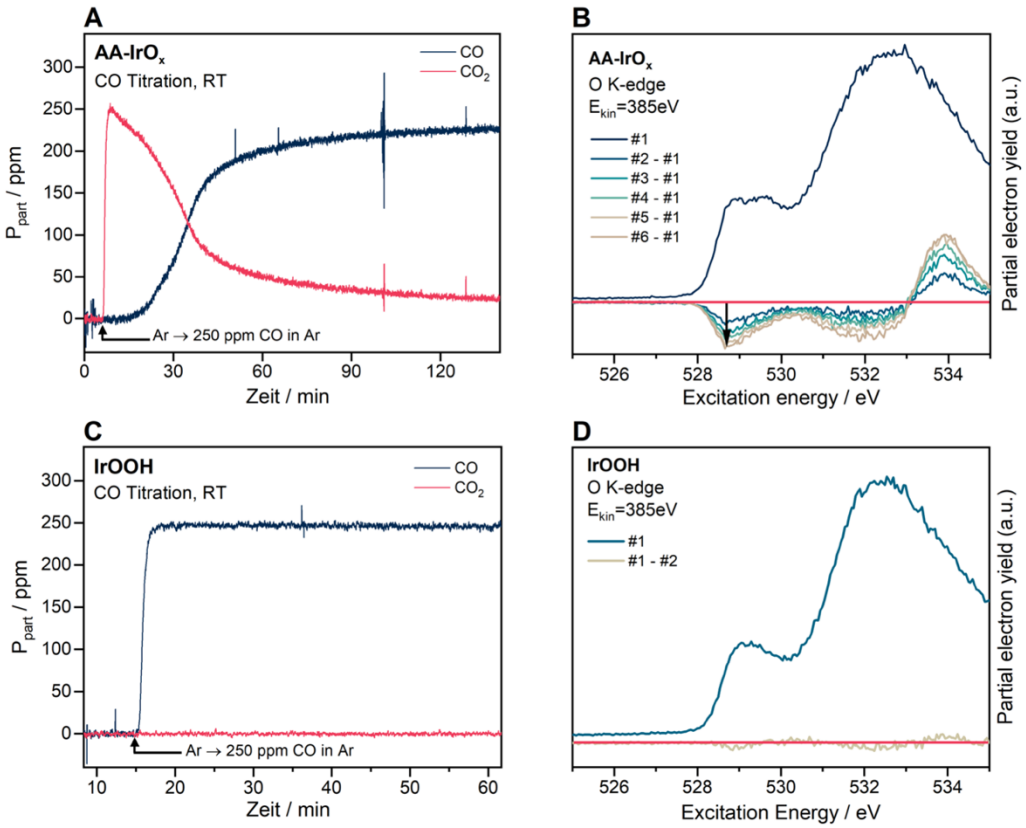

Figure 4.3: A)-B) AA-IrOx and C)-D) IrOOH powder in a flow-through reactor tube and NAP-XPS setup in an atmosphere of 250 ppm CO in Ar and 0.25 mbar CO, respectively; CO and CO2 gas concentrations are provided in A) and C); O K-edge absorption and consecutive differences to the first are given in B) and D).

Results of the reactor experiment using 25.2 mg of AA-IrOx are given in Figure 4.3A. Initially, 250 ppm of CO in Ar at ambient pressure are fully converted to CO_2 by the AA-IrOx catalyst. The conversion

drops to 0.5 within about 30 minutes. In situ O K-edge absorption at the same partial pressure of CO (0.25 mbar) is given in Figure 4.3B. While CO is converted to CO_2 (see Figure 4.32 for in situ mass spectrometry), a t_{2g} absorption feature slightly below 529 eV and a corresponding e_g feature at 532 eV are diminished (Figure 4.3B). This spectroscopic signature has been assigned to an electron-deficient oxygen species.[35] The loss of the electron deficient oxygen species seems to be connected to a loss of a broad feature at about 2 eV above the main lines in the Ir 4f XP spectra (Figure 4.33B). At the expense of this broad feature, a sharp doublet at 61.5 eV and 63.5 eV grows. Iridium bound to electron deficient oxygen species are reduced to metallic iridium.

Results for IrOOH are shown in Figure 4.3C. No conversion of CO was detected at room temperature for 25.3 mg of IrOOH powder. In order to assure that this result is not an effect of surface area, we accounted for the BET surface areas of the powders. IrOOH has a BET surface area of 0.56 m^2g^{-1}, which is 65 times smaller than AA-IrOx (see Supporting Information). However, the amount of CO_2 evolving from IrOOH in the first 60 minutes on stream was only $1.1 \cdot 10^{-8}$ mol, which is 490 times smaller than the $5.4 \cdot 10^{-6}$ mol CO_2 from AA-IrOx in the same time period. Hence, the surface area alone cannot explain the different behavior in CO oxidation. In situ spectroscopy (see Figure 4.3D and Figure 4.33) barely changes with the introduction of CO, as it has been found for untreated IrO_2 at room temperature (Figure 4.33).

From this first chemical test, it consistently results that the oxygen species of AA-IrOx and IrOOH absorbing at 529 eV are chemically different. AA-IrOx contains an electron-deficient oxygen species absorbing slightly below 529 eV, which is able to oxidize CO at room temperature. The oxygen species in IrOOH absorbs slightly above 529 eV. With the help of calculated O K-edge spectra in Figure 4.2B, we can assign this oxygen species in IrOOH to trivalent oxygens of the basal plane, which are bound to Ir^{IV} sites. These sites are probably caused by the formation of hydrogen defects in IrOOH but are not active in CO oxidation. The difference between the absorption of IrOOH and AA-IrOx are similar to the oxygen species which is titrated by CO in AA-IrOx (Figure 4.34) which means that the oxygen species active in CO oxidation is missing in IrOOH powders when compared to AA-IrOx.

Another chemical characterization of AA-IrOx and IrOOH is their electrochemical behavior. Cyclic voltammetry (Figure 4.4A) of both materials show four oxidation events, but they appear broader for AA-IrOx and are centered at different potentials when compared to IrOOH. These oxidation features are likely to originate from proton-electron transfers,[28,38] which we will refer to as (de-)protonations. The centers of these features appear at different potentials in IrOOH and AA-IrOx, pointing towards chemical differences in the Ir-O-H bonding strength. In an amorphous material like AA-IrOx the assignment of these features is difficult and can be broadly assigned to (de-)protonation events from classes of oxonium- and hydroxo-groups with varying O-H bonding strength. The classification can be made by the number of bonds from oxygen to iridium - oxygen with one, two, or three bonds to iridium will be denoted as μ_1-O, μ_2-O, and μ_3-O, respectively. The degree of hydrogenation is denoted as μ_x-OH_2 and μ_x-OH for oxonium- and hydroxo-groups, respectively. Oxonium groups exist for μ_1-O, while hydroxo-groups can exist for μ_x-O for x=1, 2, 3. Four deprotonation events are thus expected, which

matches the four main features in the CVs of Figure 4.4A. The weakly interacting sulfate counter ion in the experiment is not considered. The bonding strength and thereby the (de-)protonation potential depends on the oxygen valency and the oxidation state of oxygen and adjacent iridium atoms, while smaller oxygen valencies and larger oxidation states lead to stronger O-H bonds and higher (de-)protonation potentials.

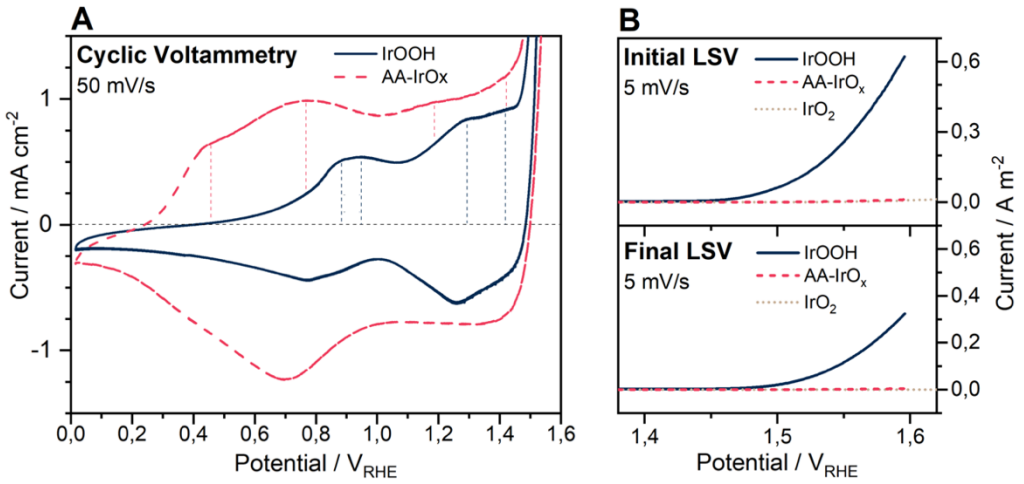

Figure 4.4: A) Cyclic voltammetry of AA-IrOx and IrOOH and B) their respective linear sweep voltammetry in comparison to rutile type IrO_2 on a rotating glassy carbon disk electrode in Ar-saturated 0.1 M H_2SO_4.

The electrocatalytical activity of the two materials in the OER was tested with linear sweep voltammetry before and after an electrochemical degradation test of several hours (see Experimental section). The currents were normalized to the BET surface area of the powders (see Supporting Information), so that the intrinsic activity of the surfaces can be compared. The resulting OER currents are compared in Figure 4.4B. Before and after a degradation test IrOOH appears more active than AA-IrOx in catalyzing the oxygen evolution. Normalizing the currents by capacitance leads to the same qualitative result (see Figure 4.35). While the two materials are similarly active on the basis of mass and geometrical surface area, IrOOH appears to have an intrinsically more active surface structure in the catalysis of the OER.

4.4.5 From bulk IrOOH to in situ spectroscopy of IrOOH nanosheets

By studying the bulk, we have learned that the in-plane crystal structure of IrOOH is well-defined and that hydrogen defects are formed in the presence of oxygen and water. These defects created Ir^{IV} sites, which lead to a mixed Ir^{III}/Ir^{IV} material. In other words, IrOOH should easily adapt a state of Ir^{III} or Ir^{IV} by means of (de-)protonation. An ideal driving force for this transition is the electrochemical potential because it can be controlled precisely, (de-)protonation reactions are rapid, and charge transport can be directly measured by currents. In defining the chemical potential of the electrons, the electrochemical potential can control the state of a material at different thermodynamic equilibria. A precondition to that ability is that the given reaction is not kinetically hindered. To satisfy that condition, we turned to nanosheets of IrOOH. For single sheets with a good contact to the electrode, deprotonation or electron transfer is not limited by bulk diffusion and thermodynamic equilibrium can be reached rapidly.

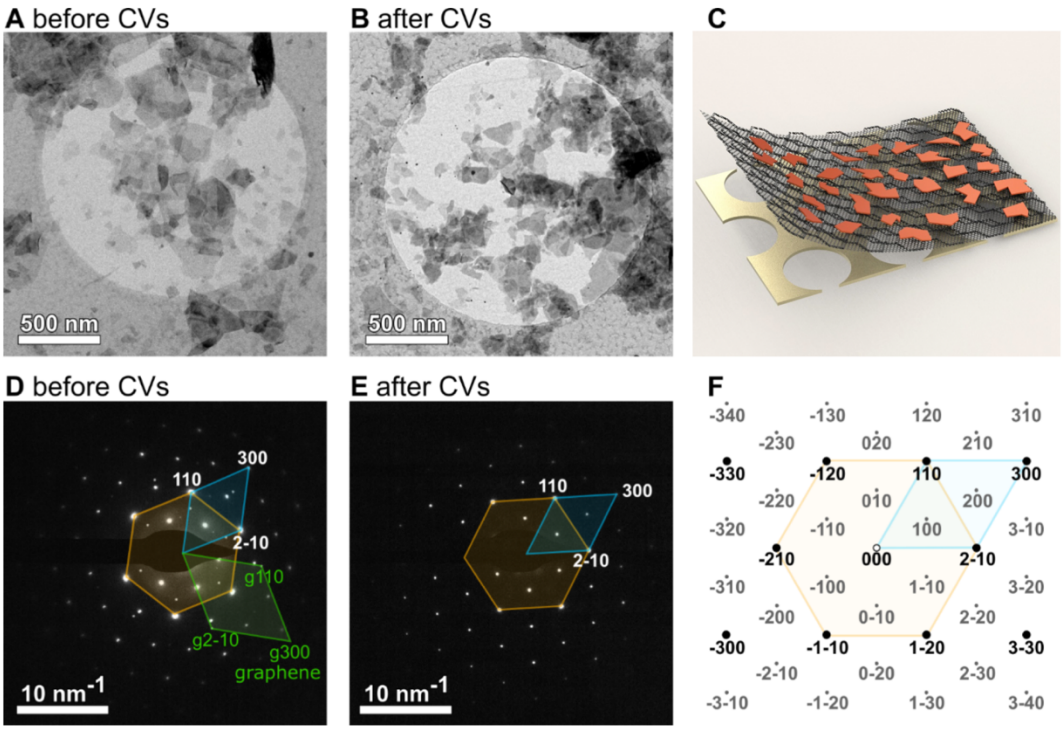

Figure 4.5: A)-B) Bright field micrographs and D)-E) electron diffractograms from a transmission electron microscope before and after an electrochemical treatment of Au/SLG/IrOOH-ns; For easier comparison, polygons were drawn into the diffraction patterns (experimental and calculated) to represent the conventional (orange) and primitive (blue) reciprocal unit cells of IrOOH nanosheets or graphene (green); C) schematic of the sample preparation using graphene and IrOOH nanosheets for ex situ TEM; F) map of indices for diffractograms.

The process of exfoliation and deposition is described in previous work,[30] but instead of using Ti disks, we used graphene on copper grown in a chemical vapor deposition process. The copper foil was subsequently removed by the etching solution ammonium peroxodisulfate and transferred onto a substrate in clean water (more details are given in the Experimental section and the Supporting Information). In order to check if this procedure has an influence on the structure of the nanosheets, we transferred nanosheets on a single layer of graphene (SLG) onto a Quantifoil gold grid covered with a holey carbon film. The obtained nanosheets on free-standing SLG were inspected in a transmission electron microscope (see Figure 4.5). The crystallites were partly stacked and overlapping but the single sheets on free-standing graphene can still be seen clearly (Figure 4.5A). Selected area electron diffraction (SAED, Figure 4.5D) of the nanosheets as deposited shows that the crystal structure of the separate sheets is preserved in the wet chemical transfer method. The SAEDs, recorded from a single nanosheet, show a single-crystalline pattern both before (Figure 4.5D) and after 50 CVs between 0.35 and 1.65 V_{RHE} (Figure 4.5E). The recorded diffractograms agree well with the calculated [001] zone axis pattern displayed in Figure 4.5F, both with respect to the lattice spacings (see Table 4.8) as well as in the relative intensities of the spots. These findings suggest that the crystal structure is largely unchanged after exfoliation, deposition onto graphene, transfer onto the carbon grid, and electrochemical treatment.

For in situ and operando spectroscopy, which combine electrochemical control and surface sensitive X-ray spectroscopy, we transferred the graphene-nanosheet electrodes onto disks of the proton and anion exchange membrane FAD by Fumatech. The resulting architecture can be written as FAD/IrOOH-ns/SLG. During in situ experiments, this sample architecture is wetted from the backside with liquid electrolyte (see Figure 4.6) and contacted by a cover lid with a circular cutout and a boron-doped diamond (BDD) coating, resulting in (0.1 M H_2SO_4)/FAD/IrOOH-ns/SLG/BDD. A platinum wire and an Ag/AgCl electrode are immersed in the liquid electrolyte behind the polymer membrane and serve as a counter and reference electrode, respectively. The graphene blanket contributes essential benefits to that approach: it serves as a current collector and an evaporation barrier, leading to a thin layer of confined electrolyte (see chapter 2). At the same time, it is transparent to soft X-rays and photoelectrons, allowing surface sensitive X-ray spectroscopy of electrocatalysts under wet conditions at pressures below 1 mbar.[28,39]

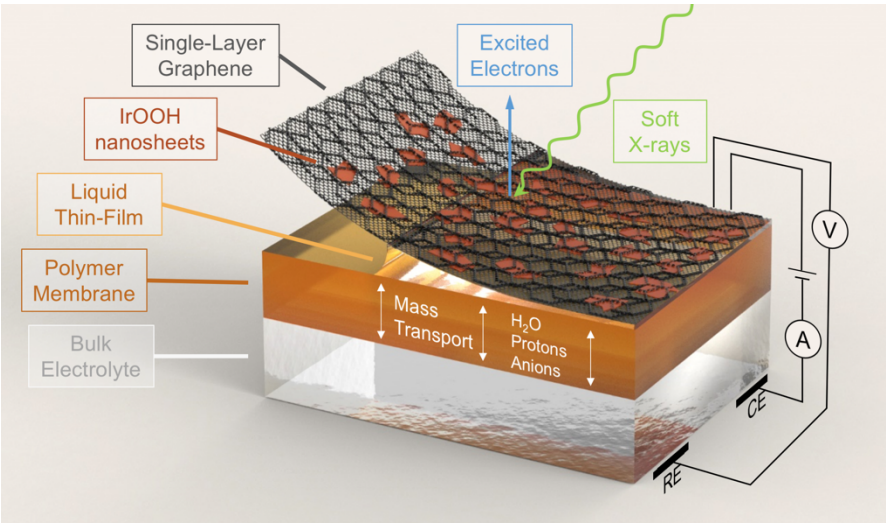

Figure 4.6: Schematic rendering of the operando X-ray spectroscopy setup; nanosheets of IrOOH are immersed in a liquid thin film between a polymer electrolyte membrane and a graphene cover; a reference electrode (RE) and counter electrode (CE) are immersed in bulk electrolyte; soft X-rays excite electrons into vacuum (top), where they are detected.

In addition to the microscopic analysis, we verified the chemical similarity of both IrOOH nanosheets and bulk powder by their electrochemical response in the in situ cell. Their cyclic voltammetry (CV) is given in Figure 4.37. Both CVs show oxidation features at 0.7 V_{RHE}, 1.0 V_{RHE}, and at 1.3 V_{RHE} and differ mostly in how strongly the features are expressed. We can conclude that the electrochemical behavior and therefore chemical nature of the bulk is conserved in the nanosheets.

4.4.6 The redox transition from Ir^{III} to Ir^{IV}

Oxidation features at ~1 V_{RHE} are typical for iridium oxides and are widely believed to be connected to the redox transition from Ir^{III} to Ir^{IV}.[14,40–42] In the case of IrOOH, ab initio calculations showed that deprotonation of the basal μ_3-OH and μ_3-OH_2 at the edges of IrOOH nanosheets lead to a formal oxidation of Ir^{III} to Ir^{IV} (see Table 4.1). Two potentials appear sensible to measure the electronic structure of IrOO(H) in the state of Ir^{III} and Ir^{IV}: 0.5 V_{RHE} and 1.1 V_{RHE}, respectively (see Figure 4.4A).

Table 4.1: Oxygen species at an IrOOH edge and their absorption features; formal oxidation states of iridium are given for different degrees of protonation; hydrogen occupations and formal oxidation states falling in the negative charge transfer regime are indicated in red; the respective structures used for the calculations are indicated by superscript letters and given in Figure 4.24.

IrOOH nanosheets

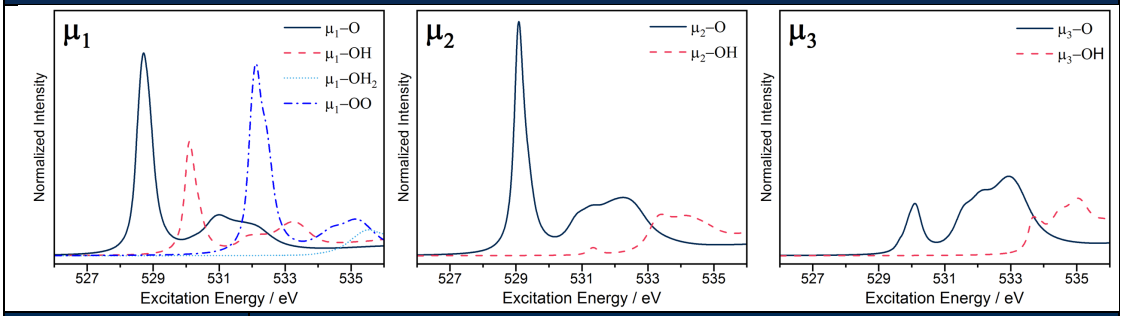

Oxygen species	μ_1-O	μ_1-OH	μ_1-OH_2	μ_2-O	μ_2-OH	μ_3-O	μ_3-OH	
Absorption white line position / eV	528.7[f]	530.1[e]	535.5[a]	529.1[e]	531.3[d]	530.1[e]	533.7[a]	
Relative intensity	3.5[f]	1.8[e]	e_g	3.4[e]	0.2[d]	1.0[e]	e_g	
Löwdin charge	-0.15[f]	-0.87[e]	-1.12[a]	-0.28[f]	-0.84[d]	-0.28[f]	-0.39[a]	
Iridium species	**#O coordinated to Ir**							**Ir formal ox. state**
Basal plane Ir	-	-		-	-	3	3	+3
Basal plane Ir	-	-		-	-	6	-	+4
Edge Ir	-	-	1	-	2	2	1	+3
Edge Ir	-	1		-	2	3	-	+4
Edge Ir	-	1		2	-	3	-	+5
Edge Ir	1	-		2	-	3	-	+6

[a-f] values taken from respective structure in Figure 4.24

At 0.5 V_{RHE} the CV in Figure 4.4A (and, in situ, in Figure 4.37) appears tapered, indicating a less conductive or gapped material,[43,44] which is expected for Ir^{III} (hydr-)oxides in the $5d^6$ configuration. Figure 4.7B-C show the spectroscopic measurements at 0.5 V_{RHE} in a well-equilibrated state, or, in other words, with negligible currents (Figure 4.38). The Ir 4f spectrum shows two symmetric peaks with a spin doublet separation of 3.0 eV, the expected intensity ratio of 4:3, and the Ir 4f 7/2 peak position is 62.0 eV (see Table 4.2). The symmetric line shape is a good indication of a gapped material. The t_{2g}-like states are fully filled and XPS satellites are of the charge transfer type rather than the asymmetric broadening in metals caused by small excitations around the Fermi energy. Also noticeable is the reverse core level shift in comparison with rutile-type IrO_2 appearing at 61.8 eV.[20,21] Since the initial state shift is mostly determined by the oxidation state and the offsite potential, $Ir^{III}OOH$ is expected to be shifted to lower binding energies compared to $Ir^{IV}OO$. Final state screening is, however, less effective in the case of Ir^{III}, since it requires an electron to be transferred from the ligand shell to the metal center. The O K-edge at 0.5 V_{RHE} shows a single contribution at 531.5 eV, which originates from an excitation from the core level into unoccupied e_g-like states (Figure 4.7B). The white line at 529 eV,

which was present in the powder, does not appear. The red-shift of the e_g absorption feature when compared to the powder is presumably caused by a reduced t_{2g}-e_g splitting in the Ir^{III} state (see Figure 4.2A-B). The reduced octahedral splitting is expected, due to an expansion of the lattice with protonation (see DFT prediction in Figure 4.23).

Table 4.2: Ir 4f fit parameters of IrOOH-ns in 0.1 M H_2SO_4 at 0.5 V_{RHE} and 1.1 V_{RHE}; Line shapes are given in reference to the CasaXPS software,[45] an equal-sign indicates a condition for the fit.

	A Ir 4f 7/2	B Ir 4f 5/2		
Line shape	SGL(35)	SGL(35)		
Center / eV	62.0	A + 3.0		
FWHM / eV	1.26	= A		
Area	58%	42%		
$Ir^{IV}OO$ @ 1.1 V_{RHE}	**A'** Ir 4f 7/2	**B'** Ir 4f 5/2	**C & D** Sat 1	**E & F** Sat 2
Line shape	DS(0.05, 200) SGL(35)	DS(0.05, 200) SGL(35)	SGL(35)	SGL(35)
Center / eV	61.7	A' + 3.0	D = C + 3.0 (A' or B') + 1.0	E = F + 3.0 (A' or B') + 2.2
FWHM / eV	1.26	= A'	C = D 1.62	E = F 1.2
Area	38%	A'/ B' = 4/3 28%	C/D = 4/3 15%+11%	E/F = 4/3 4%+3%

[a] Gaussian/Lorentzian Sum Form SGL(p) with
SGL(x, F, E, m) = (1-m) exp (-4 ln2 $(x-E)^2F^{-2}$) + m/(1+4 $(x-E)^2$ F^{-2}) and m=p/100
[b] Doniach-Ŝunjić line shape [46] DS(a,n) with asymmetry parameter a and convolution width n

At 1.1 V_{RHE} the first main oxidation features have passed, and the CV appears widened at these potentials. The currents took less than 2 mins to equilibrate (see Figure 4.38) and after 5 mins, spectroscopy was recorded. The line shape of the Ir 4f spectrum has changed to a clearly asymmetric line shape with contributions at higher binding energies (Figure 4.7E). Similar to previous work,[20] we used an asymmetric Doniach-Ŝunjić line shape [46] with two shake-up satellites. The Ir 4f 7/2 BE is 61.7 eV and the spin doublet separation is 3.0 eV (Table 4.2). The first satellite (sat1) is caused by an excitation from states at the Fermi energy into a sharp feature in the unoccupied DOS (Figure 4.7F). The most probable energy loss for that transition is ~1 eV, as it appears in the fit (Table 4.2). The second satellite (sat2) is clearly expressed in the spectrum shown in Figure 4.7E and the doublet is essential to the fit. The position appears ~2 eV above the main lines, which would correspond to an excitation from a large density of states at -2 eV into states right above the Fermi energy (Figure 4.7F). The O K-edge also agrees with what is expected from the calculated absorption spectra of IrOO (see Figure 4.2B). A clear absorption white line is present slightly above 529 eV next to a second feature at 532.5 eV (Figure 4.7D). As described above, these features are excitations into unoccupied states hybridized with t_{2g}- and e_g-like states of Ir^{IV} (Figure 4.7F).

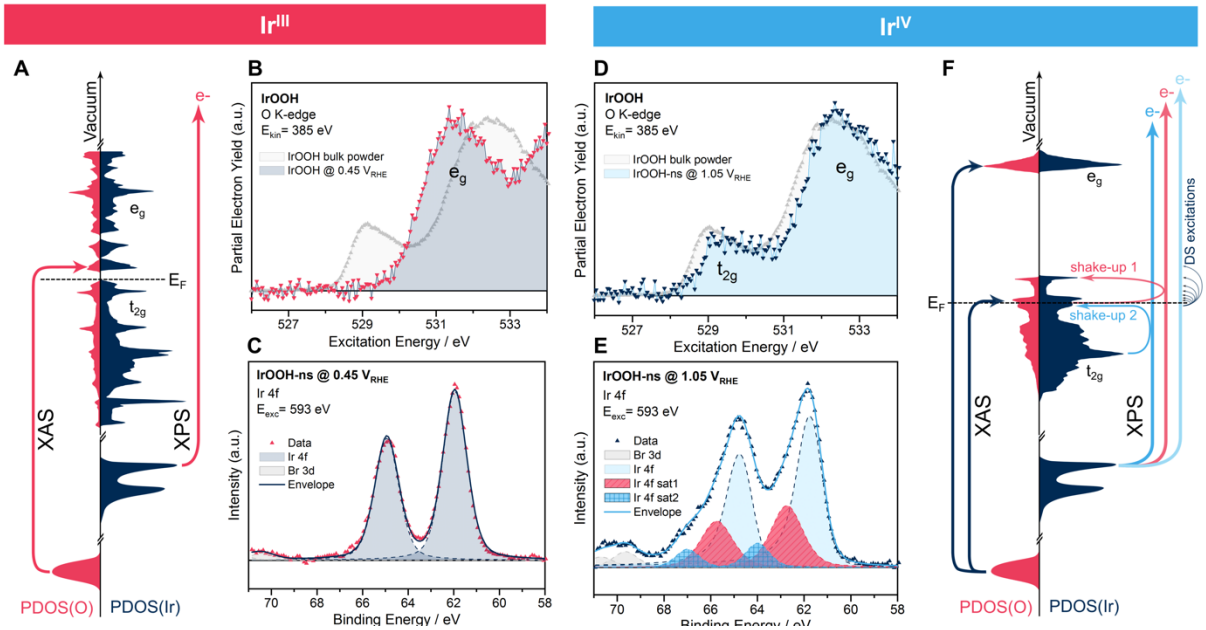

Figure 4.7: Operando B) D) O K-edge absorption and C) E) Ir 4f XP spectra of (0.05 M H_2SO_4)/FAD/IrOOH-ns/SLG at a potential of B)-C) 0.5 V_{RHE} and D)-E) 1.1 V_{RHE} and schematics for X-ray spectroscopy on single sheets of A) $Ir^{III}OOH$ and F) $Ir^{IV}OO$, in which schematic projected density of states are shown for iridium (dark blue) and oxygen (red); the bands around the Fermi energy (E_F) split by an octahedral crystal field are indicated as t_{2g}- and e_g-like bands; sample excitations of core electrons are depicted for X-ray absorption (XAS) and X-ray photoelectron spectroscopy (XPS); the XPS excitations in F) are accompanied by shake-up processes or Doniach- Ŝunjić excitations close to the E_F, explaining the satellites and asymmetric line shape in E); a Shirley-type background was subtracted from the Ir 4f XP spectrum.

In the same fashion, we analyzed the Ir^{III}/Ir^{IV} transition in two more materials: first, the thermochemical iridium (hydr-)oxide AA-IrOx introduced above (see Figure 4.39) and, secondly, activated Ir^0 nanoparticles, which were first presented in reference [28] (Figure 4.40). The latter serves as an example for an electrochemically prepared iridium (hydr-)oxide. Despite structural differences, all three iridium (hydr-)oxides have a similar electronic structure under a fixed potential. The Ir 4f XP spectrum appears symmetric in all samples at low potentials and a shake-up satellite structure similar to the one observed for IrOO(H) appears when the materials are oxidized to potentials of about 1.2 V_{RHE}. The O K-edge absorption shows one feature at around 533 eV in the state of Ir^{III} and a white line at 529 eV appears when the materials are oxidized to Ir^{IV}. We can thereby conclude that, independent from the initial state of the material and the relative distribution of μ_x-oxygen (x=1,2,3) species, the surface of (hydr-)oxides are fully protonated in liquid electrolyte at low potentials and iridium is expected to be in an average oxidation state of +3. At 1.2 V_{RHE} the iridium (hydr-)oxide surface oxidizes to Ir^{IV} by means of deprotonation. This process is reversible.

4.4.7 Beyond Ir^{IV} and the oxygen evolution reaction on mixed Ir^{III}/Ir^{IV} (hydr-)oxides

The IrOO(H) nanosheets have reached the state of Ir^{IV} at 1.1 V_{RHE} and the basal planes are deprotonated. The question remains what the active surface of the nanosheets is. Two oxidation features are observed in cyclic voltammetry of IrOOH-ns, one of them broad, the other narrow. They

are centered at 1.2 V_{RHE} and 1.4 V_{RHE}, respectively. The total charge of the nanosheets is doubled in these oxidation features (see Figure 4.8B). The resulting formal oxidation states of iridium are provided in Table 4.1 for an IrOO(H) nanosheet with edge sites. The deprotonation of the bridging μ_2-O sites leads to a formal oxidation state of Ir^{V} and additional deprotonation of μ_1-O leads to formally Ir^{VI}. However, it has been shown that compounds with iridium and oxygen enter the negative charge transfer regime at oxidation states higher than +4. Additional holes are then not centered on the metal site only, but become oxygen centered.[27,29] This effect is visible in the Löwdin charges on μ_2-O and μ_1-O (Table 4.1). This additional hole density leads to an increase of the O K-edge white line intensity, while the excitation energy decreases. The center of the white line is expected at 529.1 eV in the case of μ_2-O and 528.8 eV in the case of μ_1-O (Table 4.1). These low onsets of the white line and the increasing intensity of these features will aid in the detection of these edge sites.

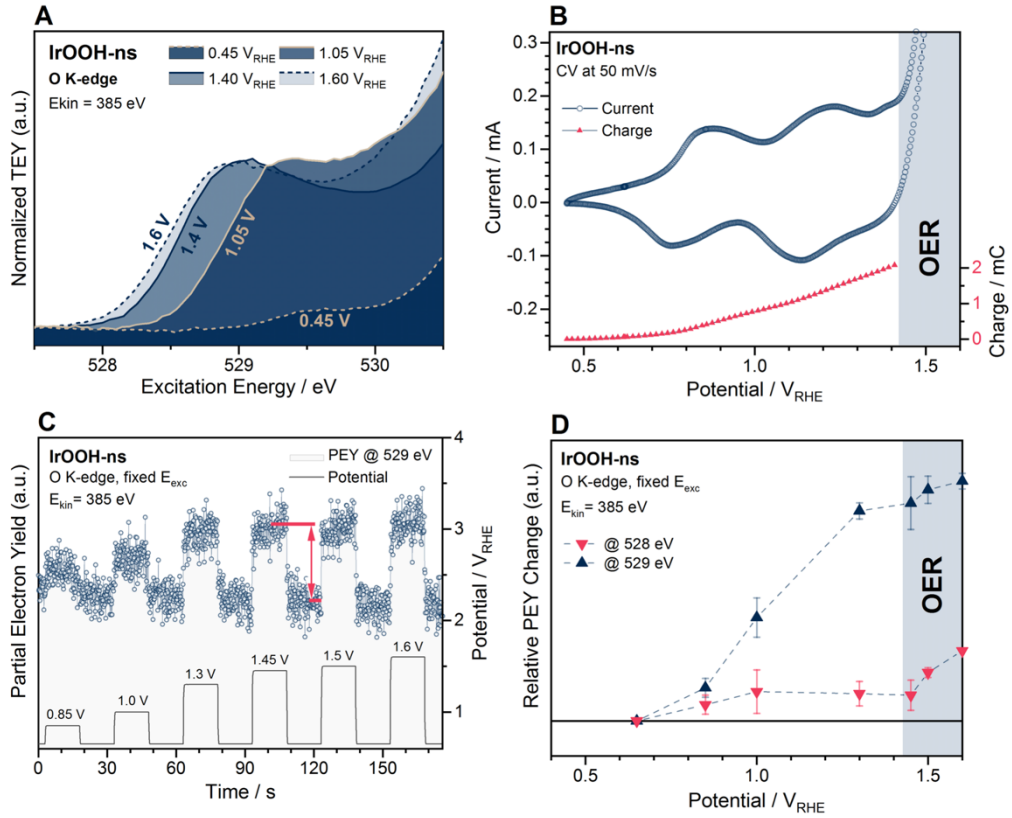

Figure 4.8: Electrochemical operando spectroscopy of (0.05 M H_2SO_4)/FAD/IrOOH-ns/SLG; A) O K-edge absorption spectra normalized to the peak intensity of the pre-edge; B) cyclic voltammogram and the integrated charge up to the OER; C) exemplary potentiodynamic X-ray absorption showing the applied potential and the signal response of the partial electron yield at E_{exc}=529 eV; D) signal difference relative to the signal intensity at 0.65 V_{RHE}, as indicated in red in part C); data for D) was recorded at several positions and the signal at 528 eV and 529 eV.

Experimental O K-edge spectra of nanosheets at the onset (1.45 V_{RHE}) and under operation conditions (1.55 V_{RHE} and 1.65 V_{RHE}) are shown in Figure 4.8A. The trend is clear and appears as predicted. At the onset of the OER, at 1.45 V_{RHE}, the main intensity of the white line is now slightly below 529 eV, due to new contributions between 528 eV and 529 eV. The electron deficient oxygen species associated with these absorption features are being formed towards the onset of the OER, but the deprotonation is

not complete. The additional broadening to the Ir 4f is in good agreement with further oxidation (see Figure 4.42). Beyond the onset of OER, i.e. 1.65 V_{RHE}, slight broadening towards lower excitation energies is observed, which points towards further deprotonation of μ_1-OH. These changes are qualitative, because the spectra were recorded at different measurement positions to avoid beam damage (see experimental section and supporting information) and normalized to their pre-edge intensity. Quantification was obtained by an experiment with short potential steps using potentiodynamic X-ray absorption (Figure 4.8C), where the pre-edge intensity was used to track the contribution of electron deficient oxygen species to the O K-edge at a given potential. The statistical result from four measurements is shown in Figure 4.8D. The signal intensity at 529 eV, which will be influenced by contributions of μ_2-O and μ_1-O, increase with the first oxidation wave up to 1.1 V_{RHE} and further increase with potential before it saturates approaching OER. The signal at 528 eV, which only captures the onset of the resonance characteristic for μ_1-O (see Table 4.1), shows no saturation and increases only with the onset of the OER, suggesting an active role in the oxidation of water.

A similar development of the electronic structure towards potentials relevant to the OER is observed for AA-IrOx powder, anodic (hydr-)oxide on metallic iridium nanoparticles, and bulk IrOOH powder (Figure 4.42).

These similarities in the electronic structure at a given potential imply that the oxidation behavior of mixed iridium (hydr-)oxides is mostly independent of the connectivity. The distribution of μ_x-oxygen species (x = 1, 2, 3) and their degree of protonation, however, is likely to differ at the same potential, because a different connectivity will lead to a different degree of deprotonation at the same average oxidation state. Thus, the electronic structure of iridium (hydr-)oxides is qualitatively the same at a given potential, but the distribution of surface species is probably different.

Quantitatively, the distribution of μ_x-oxygen (x = 1, 2, 3) or local geometry around active sites matter. As it was discussed for Figure 4.4B, IrOOH is by far more active than the commercial catalyst AA-IrOx when accounted for its low surface area. This means that intrinsic properties of IrOOHs surface are responsible for the higher activity. A similar phenomenon has been observed in a previous studies showing that a different degree of crystallization can lead to intrinsically higher surface acitivity.[10,11,18,19] On IrOOH, the distribution of μ_2-O:μ_1-O at the edge is 1:1. While μ_1-O is expected to be the active site, due to its electron deficiency, the equal ratio and possibly local geometry in IrOO appears to be highly efficient in catalyzing the OER.

4.5 Conclusion

We used the layered material IrOOH and nanosheets of the same as a model system for the oxidation behavior of iridium (hydr-)oxides . The crystal structure of the sheets is well-defined, which opened the possibility to compare experimental results to DFT studies on the same material. In this way, we were able to assign oxygen species to features in their X-ray absorption and to develop fitting models for Ir 4f XPS. We further used that knowledge to look at other mixed Ir^{III}/Ir^{IV} (hydr-)oxides and found that

the qualitative oxidation behavior is the same for all investigated materials. Their surfaces oxidize from Ir^{III} to Ir^{IV} in the first main oxidation events and are in the state of Ir^{IV} at ~1.1 V_{RHE}. Further oxidation to the onset of the OER at about 1.45 V_{RHE} falls into the regime of negative charge transfer and the electron holes are increasingly shared with oxygen. During OER, the availability of highly active and electron-deficient μ_1-O increases. Our study suggests that the major role of electrochemical potentials is to define the oxidation state of surfaces. This leads to a qualitatively similar electronic structure at a given potential. However, the resulting distribution of oxygen sites will influence the activity of Ir^{III}/Ir^{IV} (hydr-)oxides in their function as catalysts of the OER. This means, that not the initial oxidation state, but the morphology and potential-dependent oxidation of the active surface are the main influences on the activity of iridium (hydr-)oxides in the OER.

4.6 Experimental section

IrOOH powder was obtained from the precursor $K_{0.75}Na_{0.25}IrO_2$ by exchanging alkali cations in 1 M HCl for 5 days.[31] The precursor was synthesized from one equivalent iridium powder, 2.6 equivalent K_2CO_3, and 0.4 equivalent Na_2CO_3, which were heated in air at 850 °C for 120 h. Exfoliable material was obtained from a precursor synthesized with a different heating procedure, namely 900 °C for 15 h. Exfoliation was done using tetrabutyl ammonium hydroxide (TBAOH), ultrasonication, and separation by centrifuging the suspensions. In situ samples were produced in a chemical transfer method using FAD membranes by Fumatech (Bietigheim-Bissingen), bilayer- or single-layer graphene from Graphenea (San Sebastian), and (dropcasted) catalyst material.

XRD measurements were performed in Bragg-Brentano geometry on a Bruker AXS D8 Advance II theta/theta diffractometer, using Ni filtered Cu $K\alpha_{1+2}$ radiation. Total scattering measurements were collected using a Stoe Stadi-P diffractometer with AgKα1 radiation, a Ge(111) Johann monochromator, and a DECTRIS Mythen 1K detector in Debye-Scherrer geometry. Their PDF was fitted with simulated PDFs from a structure model based on XRD results using the PDFgui software.

All ab initio density-functional theory (DFT) calculations performed in this work are done with the Quantum EPSRESSO package.[47,48] The generalized gradient approximation is used in form of Perdew-Burke-Ernzerhof (GGA-PBE) type functionals from the Standard Solid State Pseudopotential (SSSP) library [49–52] to treat the exchange and correlation energy. Cutoffs for kinetic energy and charge density are set to 60 Ry and 480 Ry respectively and the Marzari-Vanderbilt type cold smearing was set to a width of 0.01 Ry. A gamma-centered reciprocal grid with an equivalent distance of 0.2 $Å^{-1}$ between adjacent k-points was used throughout the work in order to achieve the k-grid consistency of various structures. The convergence threshold for electronic self-consistency was set to 10^{-8} Ry. Atomic geometries and lattice constants (in-plane lattice constants only in 2D structures) were fully relaxed until the total energy and forces converged within the threshold of 10^{-6} and 10^{-4} atomic units, respectively. In the case of 2D and edge structures, a spacing of at least 18 Å was ensured in the non-periodic directions.

A homebuilt setup was used for flow-through TPR experiments using quartz reactor tubes inside a tube furnace. Gas analysis was done by a thermal conductivity detector, which was calibrated using reference gas mixtures. Electrochemical measurements (excluding in situ studies) have been done with a rotating disk made of glassy carbon and a thin catalyst coating (40 µg catalyst and ~8 ng Nafion per cm^2).

TEM measurements were conducted using a ThermoFisher Scientific Talos F200X, operated at 200 kV. Special care was taken to minimize beam damage, which was evident from ring-like patterns in the SAEDs after damage.

Ex situ spectroscopy and in situ measurements in CO were both recorded at the BelChem beamline at the BESSY II synchrotron facility. Electrochemical in situ and operando experiments have been done at the ISISS beamline, also at BESSY II. XAS spectra have been processed with a self-written Python script and XP spectra were fitted using the CasaXPS software.[45] The energy calibration method for O K-edge absorption has an error below ±0.1 eV; the calibration error of XP spectra is below ±0.15 eV and below ±0.1 eV in the case of in situ Ir 4f spectra of IrOOH nanosheets.

For further information on experimental procedures and methods, please visit the Supporting Information.

4.7 Supporting Information

4.7.1 Synthesis of IrOOH and exfoliation

$K_{0.75}Na_{0.25}IrO_2$ was prepared following a similar procedure as in the previous report.[31] One equivalent of iridium powder was mixed with a flux containing 2.6 equivalent of K_2CO_3 and 0.4 equivalent of Na_2CO_3 and heated in a corundum crucible in air at 850 °C for 120 h. The product was quenched to room temperature and quickly transferred to an argon filled glovebox to obtain a grey product containing a mixture of $K_{0.75}Na_{0.25}IrO_2$ crystallites and remaining flux.

The product was treated with 1 M HCl (1 mL mg^{-1}) for 5 days to remove the excess flux and exchange the alkali cations with protons. The acid was exchanged every day. The remaining residue was washed with deionized water and dried at room temperature for overnight to obtain IrOOH crystallites with a tinge of pink. We used powder X-ray diffraction (PXRD), scanning electron microscopy (SEM) and energy dispersive X-ray spectroscopy (EDX) to characterize the quality of the products.

The IrOOH sample obtained following from the above procedure does not exfoliate. To prepare exfoliable IrOOH, the synthesis condition of the precursor had to $K_{0.75}Na_{0.25}IrO_2$ be modified.[30] The mixture of iridium powder, K_2CO_3 and Na_2CO_3 (in the molar ratio of 1 : 2.6 : 0.4) was heated to 900 °C for 15 h in air and was quenched to room temperature. The resulting product was treated with 1 M HCl and washed with deionized water to obtain the exfoliable bulk IrOOH.

The exfoliable bulk IrOOH powder was dispersed in a 10 mM aqueous solution of tetrabutyl ammonium hydroxide (TBAOH) with a molar ratio of IrOOH : TBAOH = 1 : 2 and ultrasonicated for 30 min to result in a blue colored IrOOH nanosheet suspension. The unexfoliated residues were separated by centrifuging the suspension at 1000 rpm for 30 min. The supernatant suspension was further centrifuged at 15000 rpm for 30 min to make all the nanosheets precipitate at the bottom. The TBAOH solution was removed and the remaining nanosheets were redispersed in isopropanol and were drop casted onto single layer of graphene (SLG) on copper foil obtained from Graphenea (San Sebastian).

4.7.2 Powder X-ray diffraction

The powder X-ray diffraction (PXRD) measurements were performed in Bragg-Brentano geometry on a Bruker AXS D8 Advance II theta/theta diffractometer, using Ni filtered Cu $K\alpha_{1+2}$ radiation and a position sensitive energy dispersive LynxEye silicon strip detector. The sample powder was filled into the ca. 0.5 mm deep and 20 mm diameter recess of a zero-background silicon single crystal sample holder so that the smooth surface of the powder bed was at the same level as the sample holder surface. The XRD data were analyzed by whole powder pattern fitting according to the Rietveld method as implemented in the DIFFRAC.TOPAS software (version 5, Bruker AXS, 1999-2014).

In Figure 4.9 we compare three different stacking geometries of the same sheet structure. The brucite-like 1*T* structure (Figure 4.9A) has a simple AA stacking order. Within the limitations imposed by the

anisotropic nature of the peak broadening, all major reflections of the pattern are matched reasonably well. However, as the inset of Figure 4.9A shows, two additional minor reflections are not reproduced by this model. Using a heterogenite-2*H* type structure with AB stacking instead, both the main reflections and the minor superstructure reflections can be simulated (Figure 4.9B). Finally, in the case of the heterogenite 3*R* structure with an ABC stacking, the majority of the simulated reflections does not agree with the observed diffraction pattern, thus ruling out this possibility.

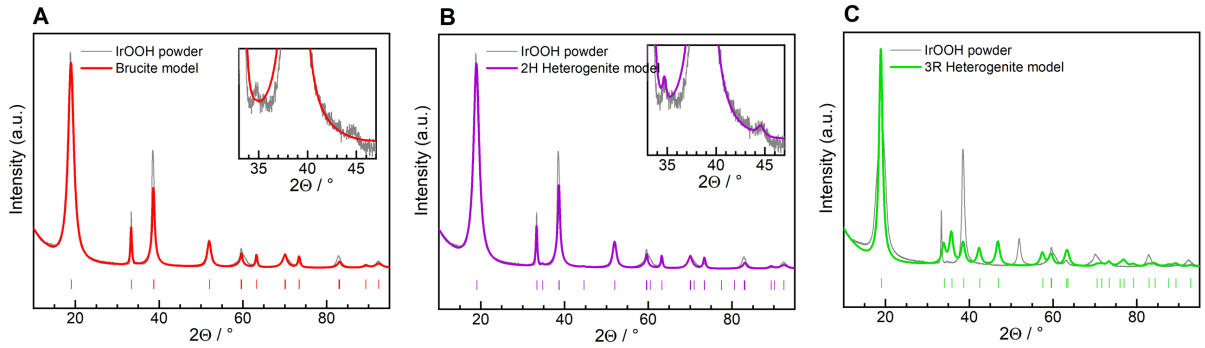

Figure 4.9: Powder X-ray diffraction of IrOOH (gray) compared with an A) brucite-1T- B) heterogenite-2H, and C) heterogenite 3R model.

Concerning the origins of the observed anisotropic peak broadening, several explanations are possible. Apart from a probably platelet-like aspect ratio of the crystalline domains or anisotropic micro-strain, some contribution by stacking disorder between the layers seems likely. The peak profile of the main reflection in the stacking direction of the IrOOH layers shows a complex structure, which seems to be composed of at least three components (Figure 4.10). However, simply superimposing two or three crystal structure models with slightly different layer distances did not yield an improvement of the fit, since the higher angle part of the observed pattern did not support this approach. Hence, at least part of the structural complexity of IrOOH currently remains unresolved.

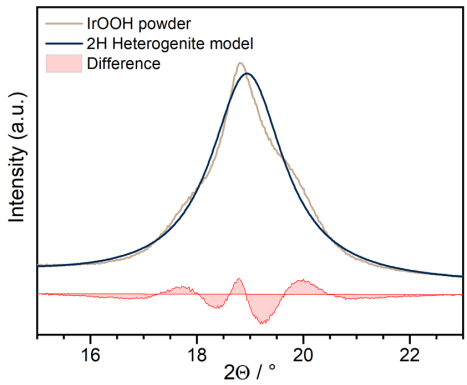

Figure 4.10: 002 reflection of IrOOH from powder X-ray diffraction (beige) and the difference (red) to a heterogenite-2H model (dark blue).

4.7.3 Pair distribution function (PDF) analysis

Total scattering measurements were collected using a Stoe Stadi-P diffractometer with AgKα1 radiation (λ = 0.55941 Å, 22.162 keV), a Ge(111) Johann monochromator, and a DECTRIS Mythen 1K detector in Debye-Scherrer geometry. Samples were loaded into 0.2 mm ID glass capillaries and measured at room temperature, over a range of 2θ = 2–127.73°, with 0.495° step size and 200 s counting time per step. Background scattering intensities from the capillary and air were measured and subtracted. Correction and normalization of the integrated total scattering patterns were carried out, using PDFgetX3 [53] within xPDFsuite,[54] to obtain the total scattering structure function, F(Q), and the pair distribution function (PDF), G(r). For elastic scattering, $Q = 4\pi sin\theta/\lambda$, where λ is the x-ray wavelength and 2θ is the scattering angle.

Analysis of the PDF provides a useful method for interpreting structure information from total scattering data, which treats both Bragg and diffuse scattering equally.[55] A diffraction measurement over a wide range of momentum transfer and with good statistics is required to obtain suitable PDFs for structure analysis. In order to obtain the pair distribution function, the measured powder diffraction intensities are first normalized by the average form factor squared to obtain the total scattering structure function $S(Q)$, defined as

$$S(Q) = \frac{I(Q) - \langle f(Q)^2 \rangle + \langle f(Q) \rangle^2}{\langle f(Q) \rangle^2}$$

The experimental PDF denoted $G(r)$, is the truncated Fourier transform of the reduced, total scattering structure function, $F(Q) = Q[S(Q) - 1]$, as

$$G(r) = \frac{2}{\pi} \int_{Q_{min}}^{Q_{max}} F(Q) sin(Qr) dQ,$$

where $G(r)$ is the magnitude of the scattering momentum transfer. In practice, values of Q_{min} and Q_{max} are determined by the experimental setup, and Q_{max} is often reduced below the experimental maximum to reduce the effects of low signal-to-noise in the high-Q region on the Fourier transformation. To aid in qualitative assessment of the long-distance structural correlations, a modification function can be applied to $F(Q)$ prior to Fourier transformation by,

$$G(r) = \frac{2}{\pi} \int_{Q_{min}}^{Q_{max}} M(Q) F(Q) sin(Qr) dQ$$

and,

$$M(Q) = \frac{sin(Qr_{ij})}{Qr_{ij}}.$$

$M(Q)$ is called a modification function, in this case a Lorch function,[56,57] which damps the intensity of $F(Q)$ to 0 at Q_{max}. This reduces the effects of termination and noise on the Fourier transform, which suppresses non-structural high frequency oscillations in the PDF. A Lorch function with a Q_{max} of 20.25 Å^{-1} was used for all data.

The PDF gives the scaled probability of finding two atoms in a material a distance r apart and is relative to the density of atom pairs in the material. For a macroscopic scatterer, $G(r)$ is calculated from a known structure model according to

$$G(r) = 4\pi r[\rho(r) - \rho_0],$$

$$\rho(r) = \frac{1}{4\pi r^2 N}\sum_i \sum_{j \neq i} \frac{f_i f_j}{\langle f \rangle^2} \delta(r - r_{ij}).$$

Here, ρ_0 is the average number density of the material and ρ(r) is the local atomic pair density, which is the mean weighted density of neighbor atoms at distance r from an atom at the origin. The sums in $\rho(r)$ run over all atoms in the sample, f_i is the scattering factor of atom i, $\langle f \rangle$ is the average scattering factor and r_{ij} is the distance between atoms i and j. In this study, Eqs. 4 and 5 were used to fit the PDF generated from a structure model to the experimental PDFs in using the program PDFgui.[58] The delta functions in Eq. 5 were Gaussian-broadened. PDF modeling was performed by adjusting the lattice parameters, atomic positions where allowed by symmetry, atomic displacement parameters (ADPs), correlated motion of neighboring atoms δ2, domain size (*sp-diameter*), a global scale factor, and phase-specific scale factors for multiphase fits. The refinements were run by minimizing R_w, calculated as

$$R_w = \sqrt{\frac{\sum_{i=1}^{n}[G_{obs}(r_i) - G_{calc}(r_i, P)]^2}{\sum_{i=1}^{n} G_{obs}(r_i)^2}},$$

which was used to quantify the goodness-of-fit for the model. Additional Rietveld refinements were performed using TOPAS v6.[59]

Results

Diffraction patterns measured by AgKα1 radiation were assessed prior to reduction and Fourier transformation to the pair distribution functions (PDFs). AA-IrOx shows sharp Bragg reflections indicating highly crystalline metallic iridium, which was confirmed by Rietveld refinement, Figure 4.11. A significant diffuse component indicates the amorphous AA-IrOx component which is highlighted by the background function in green. Rietveld refinement was also attempted on the IrO_2 sample for reference purposes in Figure 4.12. However, distortions in relative peak intensities and unindexed peaks indicate either a slightly different structure from pure Rutile-type IrO_2, or impurity phases in the sample. For IrOOH, Rietveld refinement could not be performed due to significant anisotropic peak broadening. A comparison of the simulated diffraction pattern and reflection positions for the IrOOH heterogenite-2*H* structure are shown in Figure 4.13. Also, reflections are indexed, which indicates that the structure is likely of the heterogenite-2*H*-type but with significant direction-dependent disorder. Triangular Warren-type line shape of the peaks,[60] and the layered nature of the heterogenite-2*H* structure suggest that the disorder may be related to disorder of the layer orientations.

Data reduction from the scattering intensities I(Q) to the reduced structure functions F(Q) and finally to the PDFs, G(r), are demonstrated in Figure 4.14. Single-phase structure refinements of Rutile-type IrO_2 to the PDF of IrO_2 and heterogenite-2*H* to the PDF of IrOOH were performed over a local structure

range of 1-15 Å. Despite the distortions indicated by the diffraction patterns, the fits to the local structure are fairly good for what can be expected for laboratory PDF data, Figure 4.15 and Figure 4.16. This indicates that the local structure of IrO_2 can be mostly described by the Rutile-type structuring, indicating that this is the predominant nature of local atomic packing in the sample. The agreement of heterogenite-2*H* structure to IrOOH also indicates that despite long range disorder, this material consists of heterogenite-2*H*-type layers. Finally, for the AA-IrOx sample, a multiphase refinement was performed consisting of metallic iridium, Hollandite-type, and Rutile-type IrO_2, Figure 4.17 and Figure 4.18. The fit is good, indicating that the amorphous component of AA-IrOx consists of a structure with characteristics of the local packing in both Hollandite and Rutile-type IrO_2, in agreement with the results of Willinger et al.[36] The refinement resulted in an amorphous structure with the characteristic of Hollandite to Rutile local structure in an atomic ratio of approximately 80:20. Average Ir-O and Ir-Ir atom-pair distances are given in Table 4.3.

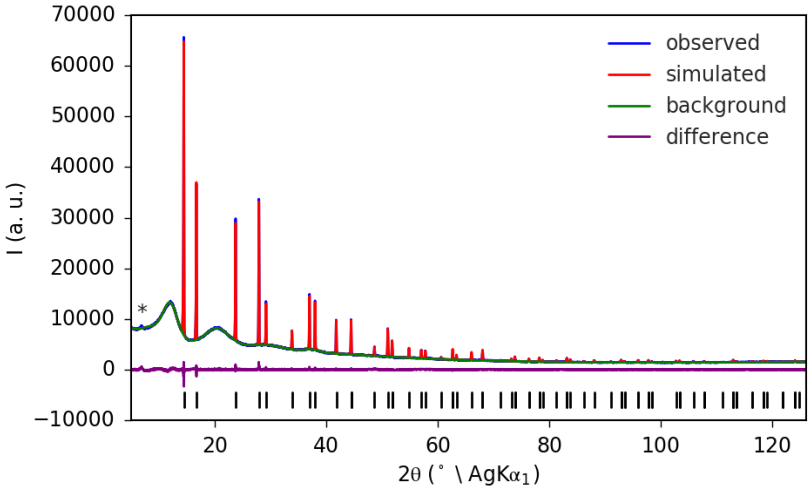

Figure 4.11: Fit (red) from Rietveld refinement of FCC metallic iridium structure (space group Fm-3m) and the XRPD pattern measured from the AA-IrOx sample (blue) are shown. The difference is shown offset below (purple), and the reflection positions are indicated below by vertical black lines. A significant amount of scattered intensities are concentrated in the diffuse scattering component, highlighted by the background function (green), which represents the amorphous AA-IrOx component. A small peak unindexed by FCC iridium is also marked (*) at approximately 6.9°.

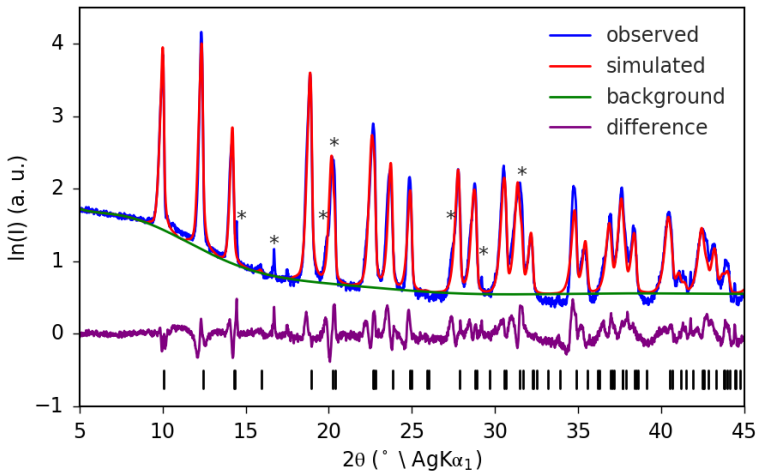

Figure 4.12: Fit (red) from Rietveld refinement of Rutile-type IrO_2 structure (space group $P4_2/mnm$) and the XRPD pattern measured from the IrO_2 sample (blue) are shown on a logarithmic scaling. The background function (green), difference (purple), and reflection positions (black vertical lines) are also shown. The fit is poor, primarily due to peaks not indexed by the structure (*), and some differences in relative peak intensity not described by the structure.

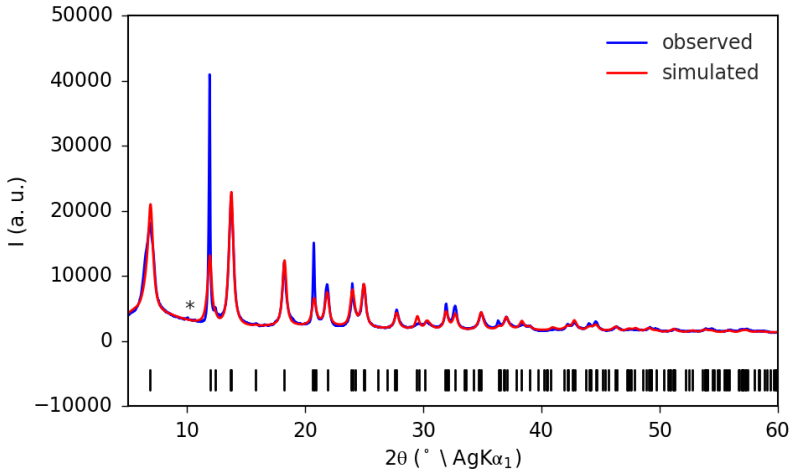

Figure 4.13: A simulation (red) from the heterogenite-2H IrOOH structure (space group $P6_3/mmc$) and the XRPD pattern measured from the IrOOH sample (blue) are shown, with reflection positions indicated by vertical black lines. Rietveld refinement could not be performed due to complicated anisotropic peak broadening, likely resulting from interlayer stacking disorder, which can be noted by the triangular Warren line shapes observed for the broadened reflections.

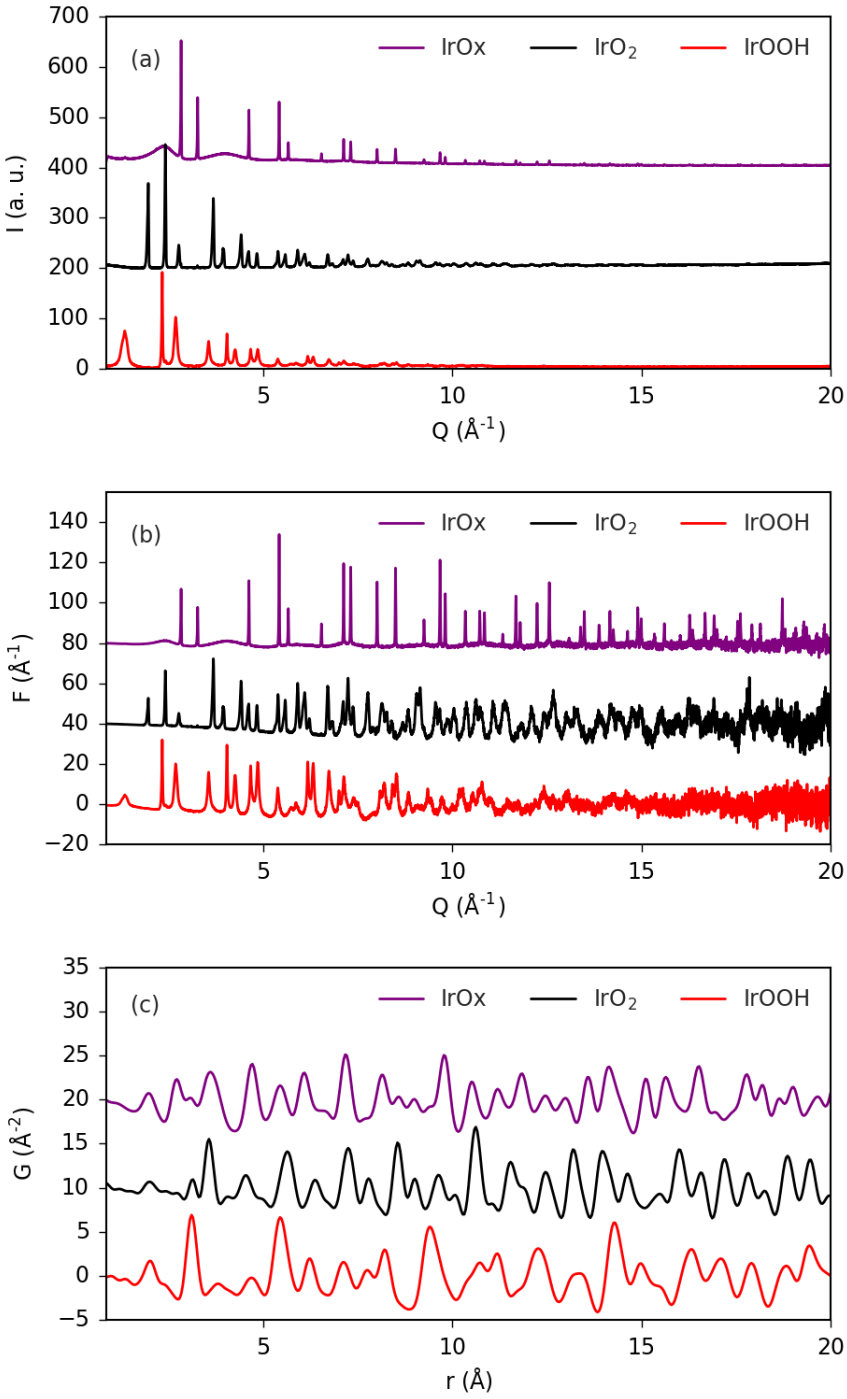

Figure 4.14: (a) Background subtracted total scattering intensities, (b) reduced total scattering structure functions, and (c) PDFs for the three samples are shown.

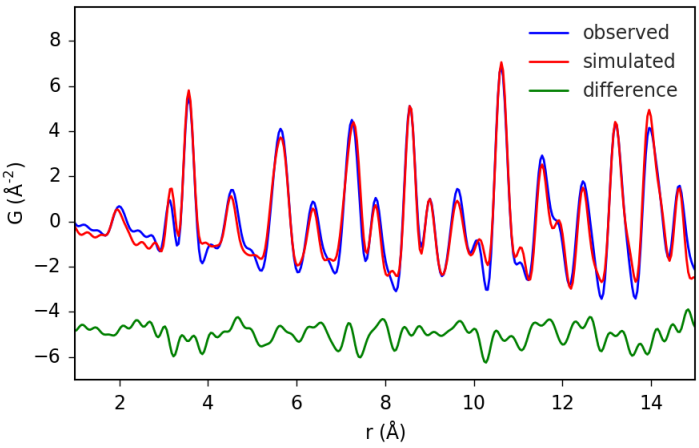

Figure 4.15: Fit (red) from real-space refinement of Rutile-type IrO_2 structure (space group $P4_2/mnm$) and the PDF measured from the IrO_2 sample (blue) are shown, R_w = 0.212.

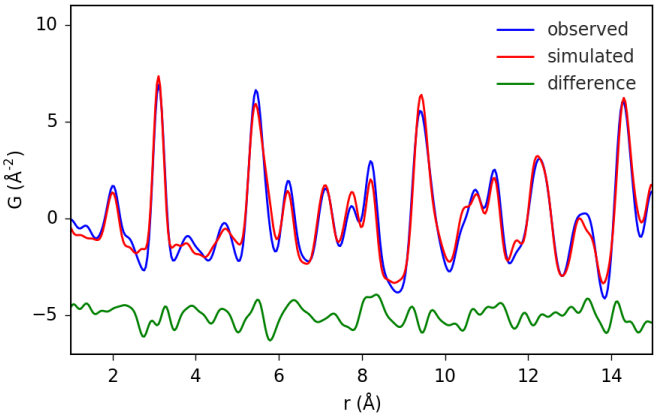

Figure 4.16: Fit (red) from real-space refinement of heterogenite-2H IrOOH structure (space group $P6_3/mmc$) and the PDF measured from the IrOOH sample (blue) are shown, R_w = 0.213.

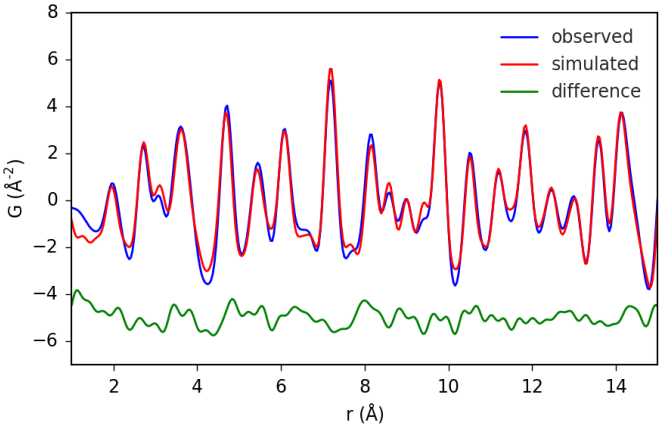

Figure 4.17: Fit (red) from multiphase real-space refinement of metallic iridium, Hollandite and Rutile-type IrO_2, and the PDF measured from the AA-IrOx sample (blue) are shown, R_w = 0.200.

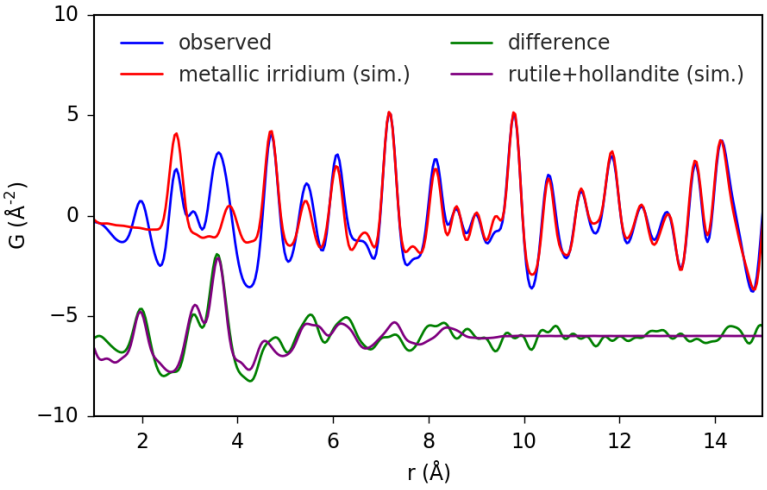

Figure 4.18: Contribution from metallic iridium (red) is compared to the measured PDF for AA-IrOx (blue). The difference (green) indicates the local structuring of the amorphous component and is compared to the separated Hollandite + Rutile-type phase (purple), both resulting from the multiphase refinement shown in Figure 4.17.

Table 4.3: Approximate atom-pair distances for Ir-O and Ir-Ir pairs extracted by fitting a Gaussian to the peak positions.

	IrOOH	IrO_2	IrOx (amorphous)	IrOx (metallic Ir)
Ir-O / Å	2.009	1.992	1.988	-
Ir-Ir / Å	3.110	3.133, 3.569	3.096, 3.613	2.697

4.7.4 Ab initio calculations

Bulk IrOOH was compared in two structures, the heterogenite-2*H* and the brucite-1*T* structure (see Figure 4.19). IrO_2 in a rutile structure was used for reference purposes. The lattice parameters, the cohesive energy, and the formation energy of all bulk structures are given in Table 4.4. The calculated lattice parameters a_0 and c_0 of rutile-type IrO_2 at 0 K are 0.68 % and 0.75 % larger than the experimental values at 300 K.[61]

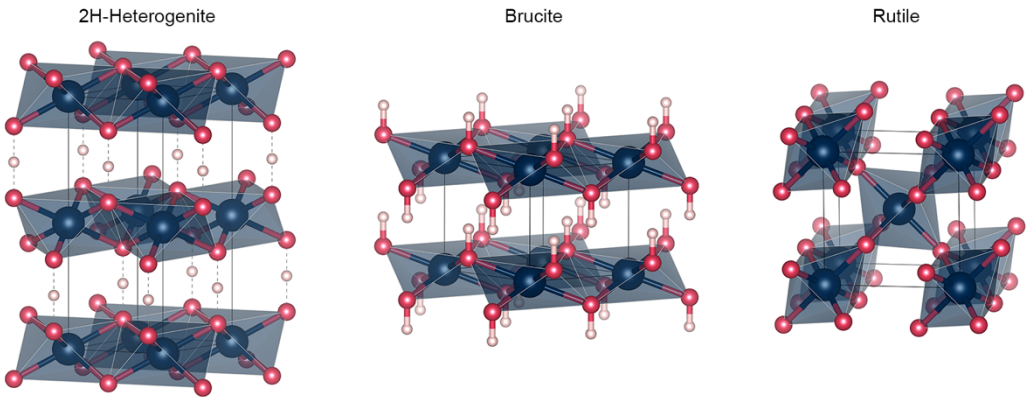

Figure 4.19: Bulk atomic structure of different iridium oxides: heterogenite-2H, brucite, and Rutile. Dark blue, red, and light pink spheres denote Ir, O, and H atoms, respectively.

Table 4.4: DFT-calculated lattice parameters (a_0, c_0), cohesive energy (E^{coh}), and formation energy (E^{form}) of bulk iridium oxides.

Structure	a_0 (Å)	c_0 (Å)	E^{coh} (eV / atom)	E^{form} (eV / atom)
Heterogenite-2*H*	3.234	8.509	-4.580	-0.920
Brucite	3.537	3.762	-4.047	-0.665
Rutile	4.529	3.178	-5.292	-1.170

Bulk IrOOH was determined to adopt the heterogenite-2*H* structure by XRD (see above). The quantity and position of hydrogen in heterogenite-2*H* is, however, unknown from XRD. We tried to evaluate if hydrogen vacancies (V_H) could thermodynamically form in air by a computational experiment. Four structures were picked: the heterogenite-2*H* structure with no vacancy, one vacancy (V_H), and two vacancies (2 V_H), while the latter has been calculated in two variants with vacancies in the same plane and in different planes (see Figure 4.20). The formation energies of the vacancies with respect to the parent heterogenite-2*H* structure are given in Table 4.5. As it appears in the table, the formation of hydrogen defect is thermodynamically favorable against a reservoir of water and oxygen, so that heterogenite-2*H* is likely to have hydrogen defects when stored on air. Removal of the first and second hydrogen are equally exothermic.

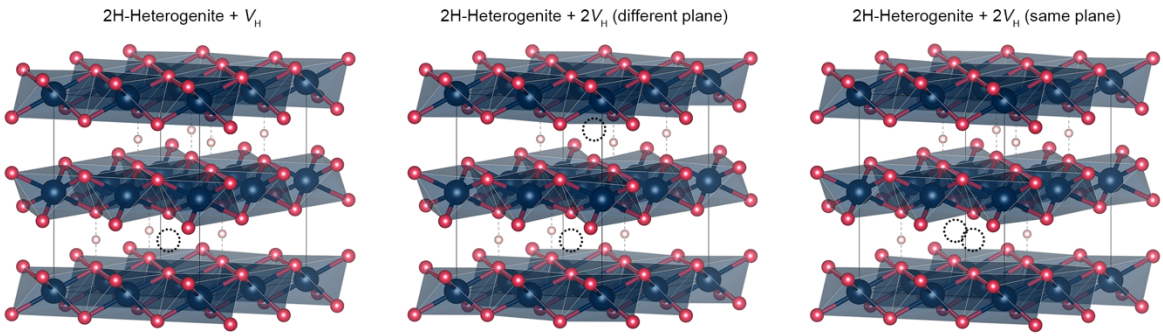

Figure 4.20: Side view of heterogenite-2H structures with hydrogen vacancies (V_H). Dark blue, red, and light pink spheres denote Ir, O, and H atoms, respectively. The dotted circle is also drawn to show the position of hydrogen vacancies present in the unit cell.

Table 4.5: Hydrogen defect (V_H) formation energy in different defected heterogenite-2H structures.

Structure	$E^f(\mu_H = \frac{1}{2}E_{H_2})$ (eV / atom)	$E^f(\mu_H = \frac{1}{2}(E_{H_2O} - \frac{1}{2}E_{O_2}))$ (eV / atom)
Heterogenite-2*H* + V_H	0.900	-0.635
Heterogenite-2*H* + $2V_H$ (different plane)	1.763	-1.307
Heterogenite-2*H* + $2V_H$ (same plane)	1.788	-1.282

It was also measured by means of polyhedral distortion indices if hydrogen defects could be responsible for structural lattice distortions. We chose the quadratic elongation (<λ>) and bond angle variance (σ^2) as distortion indices and define them by

$$<\lambda> = \frac{1}{n}\sum_{i=1}^{n}\left(\frac{l_i}{l_0}\right)^2$$

$$\sigma^2 = \frac{1}{m-1}\sum_{i=1}^{m}(\phi_i - \phi_0)^2$$

, where n is the coordination number of the polyhedral center (n = 6 in our work where Ir is in the octahedral environment); l_i is the distance between polyhedral center and i^{th} vertex atom; l_0 is the counterpart of l_i measuring the center-to-vertex distance of an ideal polyhedron having the same volume to target polyhedron; m, ϕ_i , and ϕ_0 denotes the number of bond angles in target polyhedron, i^{th} bond angle, and the ideal bond angle of the regular polyhedron. The results are presented in Figure 4.21. The lattice constants change by about 0.1 Å (see Figure 4.21a) when removing every fourth hydrogen atom from the layers, while the in-plane constant as well as the octahedral volume (see Figure 4.21b) contract, and the distance between the layers increases, while a larger scattering in the distortion of the octahera is observed (Figure 4.21c-d).

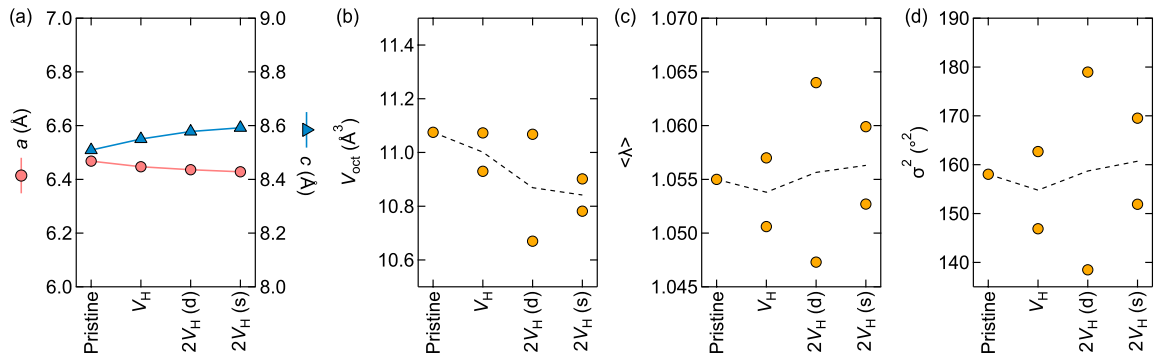

Figure 4.21: (a) DFT-calculated lattice parameter a and c, (b) volume of Ir-O_6 octahedra, (c) quadratic elongation, and (d) bond angle variance of pristine and defected heterogenite-2H structures. Dotted lines in b-d is to show the averaged value.

We define three different 2D IrOOH nanosheet structures, namely the $IrOOH_{asym}$, *d*-$IrOOH_{sym}$, and *p*-$IrOOH_{sym}$ (see Figure 4.22). $IrOOH_{asym}$ has asymmetrically adsorbed H atoms on one side of the 2D IrOO nanosheet, while the $IrOOH_{sym}$ structures have symmetrically adsorbed H atoms on both sides. The prefix *d*- (diagonal) and *p*- (parallel) in front of the $IrOOH_{sym}$ label denote the configuration of H atoms seen in the top view (see bottom of Figure 4.22). The lattice parameter *a*, the cohesive energy, and the formation energy of the structures are provided in Table 4.6. How the degree of protonation affects the atomic structure is measured with the octahedral distortion, as done above. A significant contraction of the octahedra (Table 4.6 and Figure 4.23a) accompanied by a reduced distortion (Figure 4.23b-c) is observed with an oxidation from IrOHOH over IrOOH to IrOO. At the same average oxidation state, i.e. +3 in IrOOH, the hydrogen distribution influences the volume of the octahedra strongly, while the distortion does not change much. The distortion of the rather unstable IrOHOH structure (Table 4.6) is, however, much more distorted in a similar octahedral volume, when compared to the IrOOH structures.

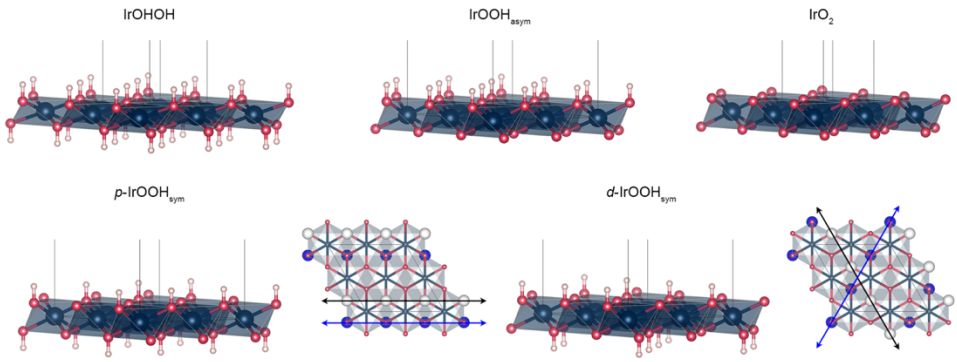

Figure 4.22: Atomic structure of 2D iridium oxide nanosheet structures. Dark blue, red, and light pink spheres denote Ir, O, and H atoms, respectively. Black and blue arrows plotted on the top view of p-$IrOOH_{sym}$ and d-$IrOOH_{sym}$ show the difference in the position of hydrogen atoms.

Table 4.6: DFT-calculated lattice parameter (a_0), cohesive energy (E^{coh}), and formation energy (E^{form}) of 2D iridium oxide nanosheets.

Structure	a (Å)	E^{coh} (eV / atom)	E^{form} (eV / atom)
p-$IrOOH_{sym}$	6.509	-4.412	-0.752
d-$IrOOH_{sym}$	6.493	-4.452	-0.792
$IrOOH_{asym}$	6.529	-4.382	-0.723
IrOHOH	7.144	-3.844	-0.462
IrOO	6.276	-5.048	-0.926

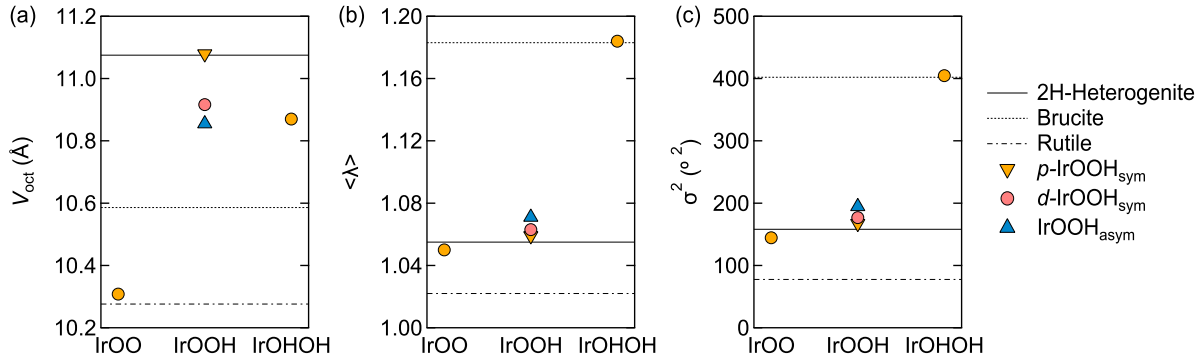

Figure 4.23: (a) DFT-calculated volume of Ir-O_6 octahedra, (b) quadratic elongation, and (c) bond angle variance of bulk and 2D nanosheets grouped by the average oxidation state of iridium. Different types of IrOOH are displayed in different markers to guide the eye (p-$IrOOH_{sym}$: orange inverted triangle, d-$IrOOH_{sym}$: red circle, $IrOOH_{asym}$: blue triangle).

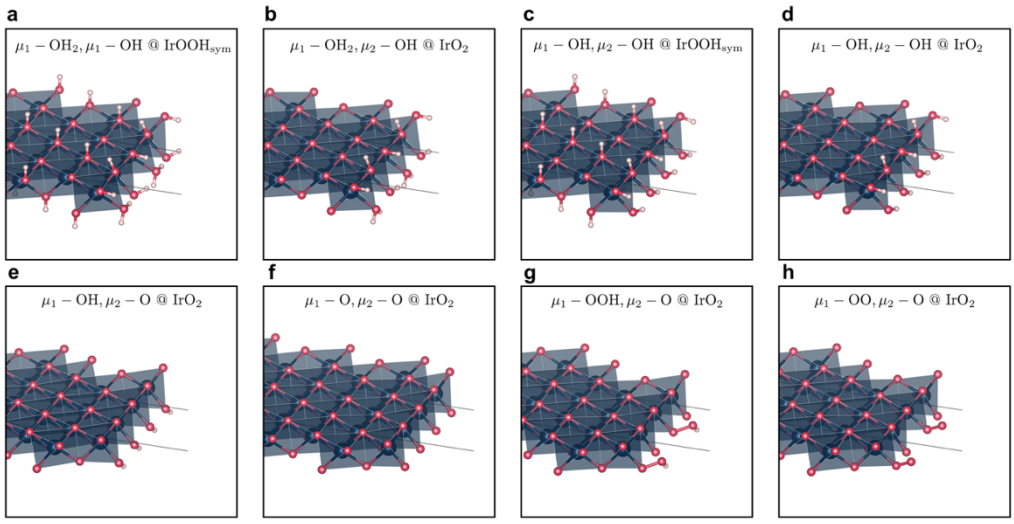

Figure 4.24: Atomic structure of 2D iridium oxide nanosheet structures with its edge exposed. Dark blue, red, and light pink spheres denote Ir, O, and H atoms, respectively.

With the aim to include all sites possibly contributing to the activity, we used edge terminated nanosheets (see Figure 4.24). Structures with an average iridium oxidation state of +2 were excluded because they are thermodynamically unfavorable (see the example of IrOHOH in Table 4.6). From the edge structures, we obtained the information provided in Table 4.1.

Table 4.7: DFT-calculated cohesive energy (E^{coh}), and formation energy (E^{form}) of iridium oxide edge structures.

Structure	E^{coh} (eV / atom)	E^{form} (eV / atom)
a	-4.229	-0.799
b	-4.630	-0.952
c	-4.264	-0.799
d	-4.681	-0.951
e	-4.802	-0.956
f	-4.887	-0.904
g	-4.749	-0.893
h	-4.800	-0.878

4.7.5 Temperature programmed reduction (TPR)

A homebuilt setup was used for TPR experiments using quartz reactor tubes inside a tube furnace and gas dosing valves with a low dead volume. The sample powder was weighed on a high-precision scale (target of 45 mg), filled in a flow-through reactor tube made of quartz glass, and held in place by quartz wool. Prior to experiments, the samples were dried in a flow of pure Ar at room temperature for at least one hour. Chemical reduction of the powdered materials was done in a constant flow (100 mL/min) of 4.95 % H_2 in Ar. For the reduction itself, we used a flow of 100 mL/min, which results in a contact time of 65 s at room temperature. The switch between reactive and inert gas atmosphere was realized with valves optimized for a low dead-volume. Hydrogen consumption was measured by an X-Stream thermal conductivity detector by Emerson. The temperature program consisted of a heating ramp (6 K/min) to 450 °C, a dwelling step of 10 mins at the highest temperature, and a cool-down. Oxidation states were referenced to the total hydrogen consumption during the reduction of CuO with the same molar loading (~17 mg of CuO). The maximum temperature for the reduction of CuO was 700 °C.

The oxidation state in IrOOH was calculated based on the amount of hydrogen that was consumed in the reduction process. The amount of hydrogen was obtained by the integration of the absolute difference between the hydrogen concentration measured with the fresh sample and the same sample after reduction. In this way, we also capture reductive processes at room temperature (see Figure 4.25), which was especially relevant for the material AA-IrOx. The total amount of hydrogen consumed was then used for the calculation of the equivalent oxygen weight. Since the latter depends on the speciation, i.e. oxo- or hydroxo-groups, the result was calculated for a range of possible stoichiometries. In the case of IrOOH, we used the general formula $IrO_{2-2x}(OH)_{2x}$ to calculate the weight loss for a range of x-values in steps of $\Delta x = 0.05$. Substracting the weight loss from the initial weight (45.2 mg of powder) then allows the determination of the amount of iridium reduced by hydrogen and, hence, the average oxidation state of the metal site for each stoichiometry. These experimental oxidation state for different values of x were compared to the formal oxidation state of the

stoichiometry in Figure 4.26. In the point where the formal and experimental oxidation state intersect, the observed oxidation state agrees with the model. The intersection is at x = 0.23 (linear interpolation), which is close to the stoichiometry $IrO_{1.5}(OH)_{0.5}$. This means that, depending on the level of exposure to air, every second hydrogen could be missing in IrOOH. The obtained value might underestimate the oxidation state of iridium because crystal water was not accounted for.

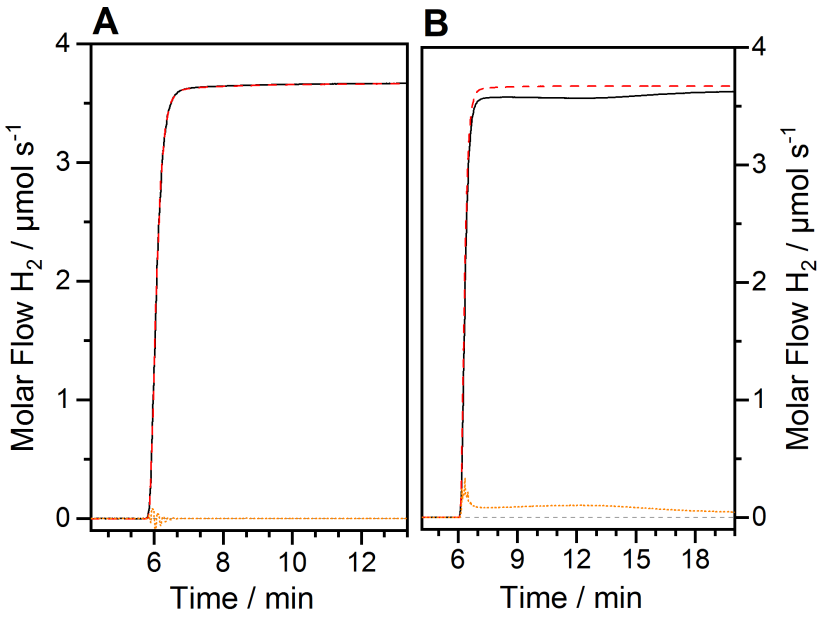

Figure 4.25: Introduction of 4.95 % H_2 in Ar to the reactor before (solid line) and after (dashed line) complete reduction and their difference (dotted line) for a) IrOOH and b) AA-IrOx.

It is worth noting that the reduction process of AA-IrOx occurs at lower temperatures compared to IrOOH and it is exothermic (Figure 4.27).

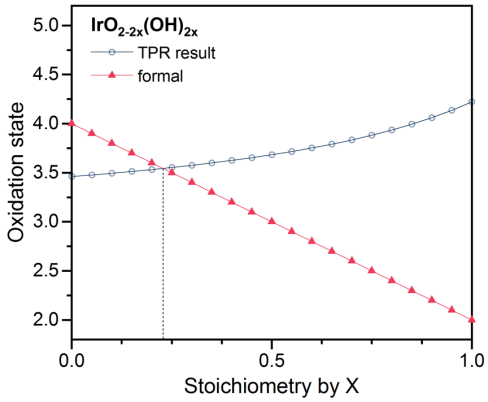

Figure 4.26: Chemical oxidation state of $IrO_{2-2x}(OH)_{2x}$, formally and calculated by means of the weight loss from hydrogen reduction in the TPR experiment.

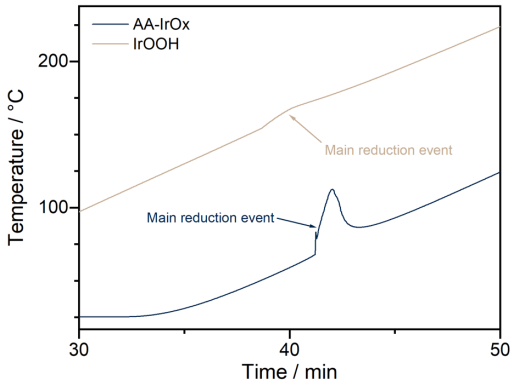

Figure 4.27: Temperature reading close to powder fill for IrOOH and AA-IrOx; the time-scale is relative with arbitrary zero.

4.7.6 UV-Vis spectroscopy

The UV-Vis absorptance of IrOOH powder was measured in a FLS 980 photoluminescence spectrometer by Edinborough Instruments equipped with a Xe lamp as source. The IrOOH powder was dispersed in water and exfoliated IrOOH nanosheets were dispersed in ethanol. Absorptance was measured in a synchronous scan and a monochromator allowed selective detection of the incident wavelength, excluding photoluminescence. The result is given in Figure 4.28. The absorptance spectrum does not show the characteristic drop expected for gapped materials. Instead, only a dip centered at ~2.5 eV is detected.

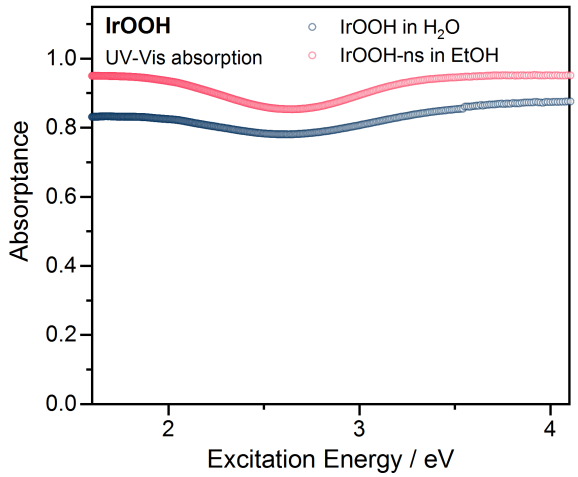

Figure 4.28: Absorptance of IrOOH powder or IrOOH-ns dispersed in water or ethanol, respectively; excluding photoluminescence.

Diffuse reflectance was recorded on a Cary 5000 spectrometer from Agilent using an in situ gas phase holder and a Praying Mantis cell. The materials $BaSO_4$ and Spectralon were used as white standards (see Figure 4.29). A flat surface of powdered sample was used to obtain the reflectance of the samples relative to the white standard. We used the Kubelka Munk function F(R) to calculate the absorption coefficient. The band gap was estimated by the root of a linear fit, as suggested by Tauc et al. for a direct and allowed bandgap.[62] For both white standards we found a bandgap of 1.9 eV (Figure 4.30).

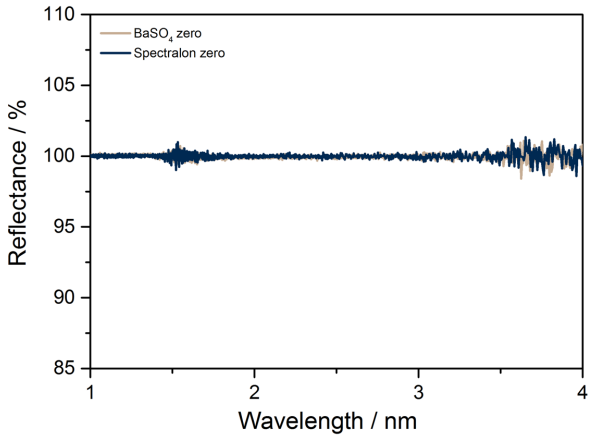

Figure 4.29: Reflectance of reference materials relative to reference measurement.

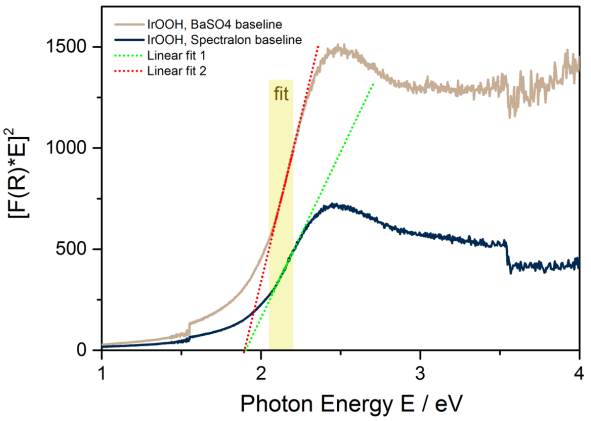

Figure 4.30: Tauc-plot for a direct allowed bandgap transition (squared product of the absorbance and the excitation energy) for IrOOH normalized by two different white standards; fitting of linear functions (dotted lines) in the yellow region.

4.7.7 Data processing of X-ray spectroscopy

X-ray spectroscopy was recorded at the BESSY II synchrotron facility in Berlin at either the ISISS or the UE56-2 PGM1 beamline. Data acquisition was performed with a differentially pumped analyzer by SPECS (Berlin) using the Prodigy recording software, also by SPECS. Absorption spectroscopy was processed with a homemade Python script. The script calibrates the excitation energy by using gas phase signals, i.e. water or CO, or features in the mirror current. In the case of water vapor, the 3p Rydberg state was set to 537.25 eV following the recommendation in reference [63]; in the case of CO, the 2p π* signal was set to 534.1 eV following reference [64]. The script furthermore corrects the recorded intensity for synchrotron ring current and beamline flux. For the latter we used flux curves on an oxygen-free gold foil at elevated temperature. The flux curves for the operando measurements were recorded in the respective water vapor pressure, i.e. 0.25 mbar. Constant values were used for background subtraction. X-ray photoelectron spectroscopy (XPS) was processed and fitted using the CasaXPS software. The excitation energy was calibrated with tables created in the same week using a gold reference or, in the case of thin samples such as IrOOH-ns, with the difference in binding energy (BE) between XP spectra excited with first and second order contributions of the bending magnet of

the ISISS beamline. The error of the energy calibration is smaller than 0.15 eV for the tables and smaller than 0.1 eV for the second order alignment. XP spectra were used as recorded, normalized from 0 to 1, or fitted using a Shirley-type background. The information about the background is provided in each case. Differences between two spectra were calculated by linear extrapolation of one dataset to the binding-energy scale of the other.

4.7.8 O K-edge integration

Oxygen states in iridates are hybridized with the metal center and therefore show a t_{2g}-like and e_g-like contribution. Assuming that the hybridization is similar for different oxidation states, the integrated absorption signal of the O K-edge can give insight into the occupation of metal-centered orbitals. However, because of the stated assumption and the unknown shape of the background below the O K-edge signal, this method needs verification. We therefore integrated the O K-edge absorption signal (partial electron yield) of rutile type IrO_2 from the pre-edge to the first minimum at about 531 eV and to the second minimum at about 536 eV (see Figure 4.31). Since we would expect 4 electron holes contributing to the intensity of the e_g-like orbitals, a quarter of the difference between the two integrations is the intensity representative of one electron hole in the e_g. The analysis gives 5.8 for a quarter of the difference, which is the intensity of one electron hole. The t_{2g}-contribution itself amounts to 5.8 as well, indicating one electron hole in t_{2g}-like orbitals. Since expectation and testing agree, we applied this method to IrOOH. With the same analysis, we obtain 5.14 for the quarter-difference and 3.6 for the white line intensity. This would mean that 70% have a hole in t_{2g}-like states, which is in fair agreement with the value obtained from TPR.

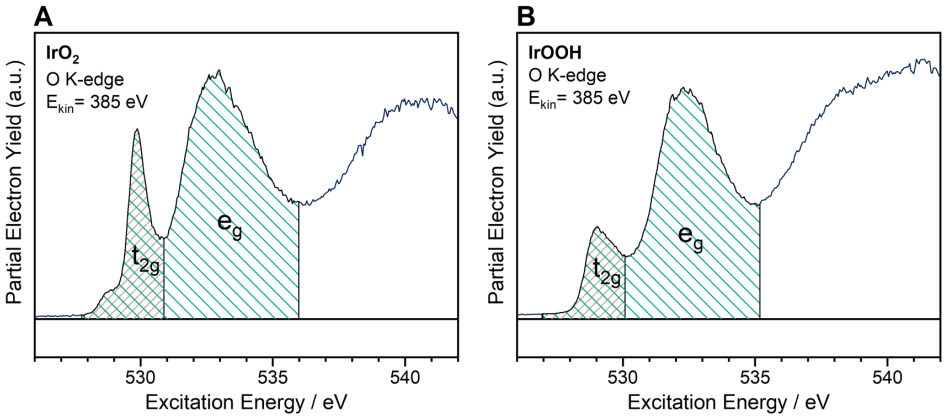

Figure 4.31: O K-edge integration for IrO_2 and IrOOH.

4.7.9 BET surface area

The BET surface area of the powders was determined using an Autosorb-6-B setup by Quantachrome. The samples were dried at 423 K in vacuum and the volumetric physisorption of Kr was performed at 77 K for 11 pressures, ranging from p/p_0 = 0.05-0.3. The measurements were reproduced at least once. We determined the BET surface area of both powders. We obtained 0.56 m^2g^{-1} for IrOOH and 36.5 m^2g^{-1} for AA-IrOx.

4.7.10 CO oxidation in flow-through reactor

CO oxidation was carried in the same reactor as the TPR (see above). The samples were dried in pure Ar for about two hours before 250 ppm CO in Ar were introduced. We recorded concentrations of CO and CO_2 with non-dispersive infrared technique using an Advance Optima setup with an Uras 14 module from ABB.

4.7.11 In situ X-ray spectroscopy during CO oxidation at room temperature

About 20 mg of sample powder were pressed into pellets and mounted on a sapphire holder using steel plates. A thermocouple was mounted between the holey front-plate and the powder pellet for temperature monitoring. Spectroscopy was recorded at the UE56-2 PGM1 beamline at the BESSY II synchrotron Berlin in a near ambient pressure X-ray photoelectron spectroscopy (NAP-XPS) setup. The powder pellet samples were initially kept at high vacuum. CO oxidation was carried out at a backpressure of 0.25 mbar, which is the same partial pressure as in the reactor experiment. For introducing the reactive gas mixture to the measurement chamber, the sample was kept at high vacuum in a separate compartment with a smaller volume. As soon as the pressure in the main chamber stabilized, the sample was re-introduced, causing only a small change in pressure. The gas was continuously analyzed with a Prisma quadrupole mass spectrometer by Pfeiffer Vacuum GmbH (Asslar, Germany), which was connected to the main experiment chamber via a leak valve. The mass spectrometer was operated at ~$5 \cdot 10^{-7}$ mbar (Figure 4.32). The result is qualitatively the same as in the reactor experiment: AA-IrOx is active in CO oxidation at room temperature, IrOOH is not. Ten minutes after introducing AA-IrOx, it was retracted back into the load-lock, in which it regenerated. After a few minutes, it was re-introduced, which lead to increased production of CO_2 (bottom of Figure 4.32A).

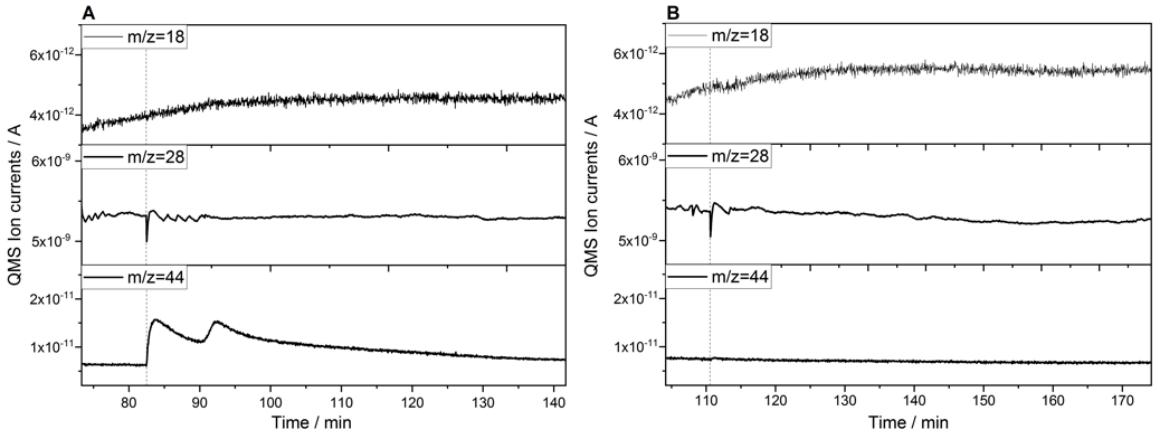

Figure 4.32: Online mass spectrometry of A) AA-IrOx in 0.25 mbar CO; dotted line indicates introduction of the sample to the measurement chamber.

In situ spectra in 0.25 mbar CO at room temperature are provided in Figure 4.33. The first spectrum in the CO atmosphere was subtracted from the consecutive spectra to show the changes more clearly. In situ X-ray absorption on the O K-edge of AA-IrOx (Figure 4.33A) indicate a strong loss of absorption at ~528.7 eV and 532 eV, which agrees well with the previous findings.[35] The loss of the electron

deficient oxygen species seems to be connected to a loss of a broad feature at about 2 eV above the main lines in the Ir 4f XP spectra (Figure 4.33B). At the expense of this broad feature, a sharp doublet at 61.5 eV and 63.5 eV grows. Iridium bound to electron deficient oxygen species are reduced to metallic iridium. The same type of plot is shown for the O 1s XPS signal (Figure 4.33C). Signal intensity at 530 eV and 529 eV is reduced in CO atmosphere, while a new feature at ~533.5 eV develops. The latter is a contribution from adsorbed CO.

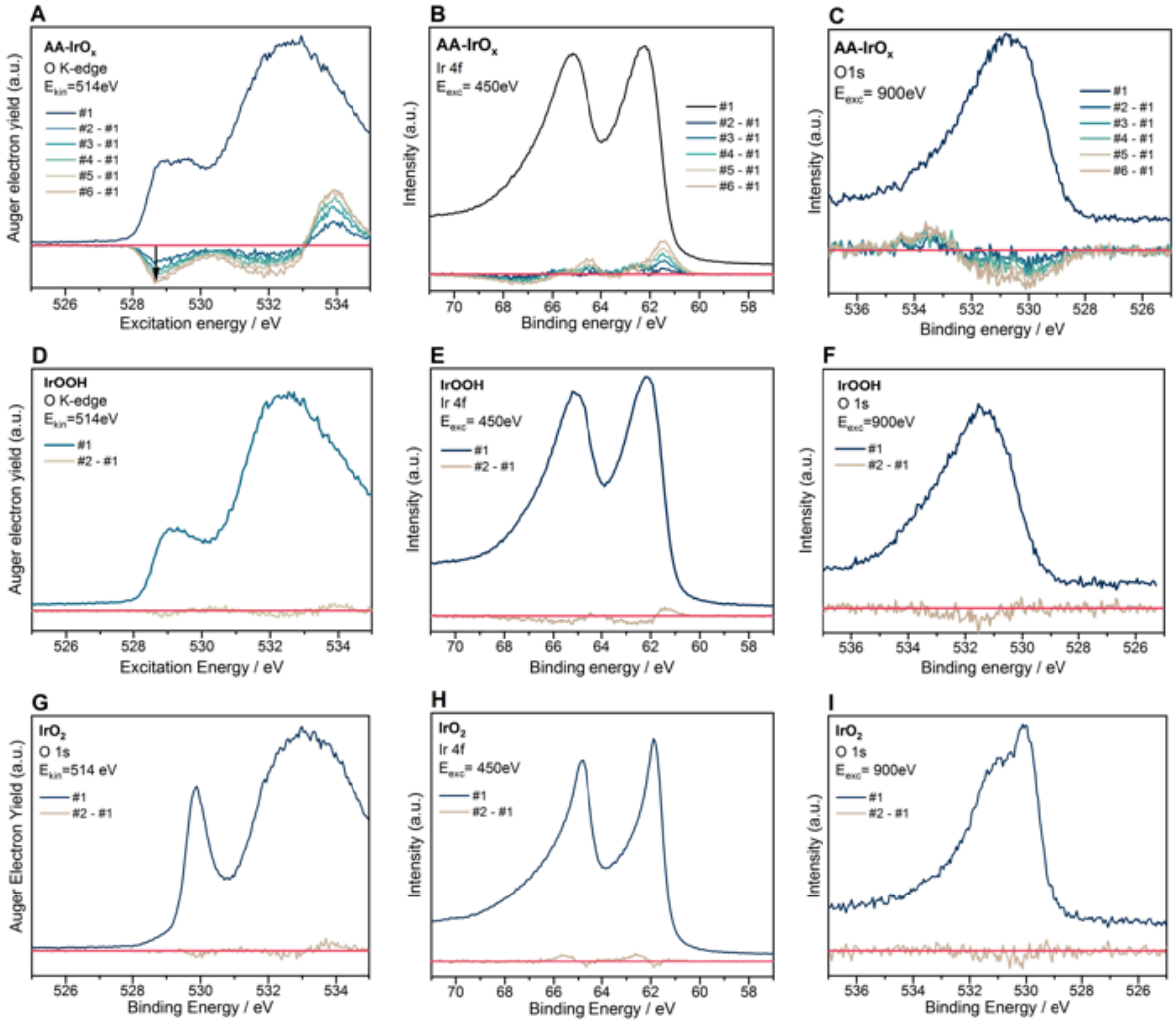

Figure 4.33: In situ A) D) G) O K-edge absorption, B) E) H) Ir 4f XP spectra, and C) F) I) O 1s XP spectra of A)-C) AA-IrOx, D)-F) IrOOH, and G)-I) rutile-type IrO_2 in 0.25 mbar CO at room temperature; the first spectrum in CO and the respective differences to the first are shown; spectra of the same type were recorded 8 minutes apart.

The same set of Ir 4f & O 1s spectra are provided for IrOOH in Figure 4.33D-F and for IrO_2 in Figure 4.33G-I, respectively. Almost no difference between the first and the second spectrum was detected. Although the changes were small, the trends for the XP spectra of IrOOH can be summarized as growing doublets at 61.5 eV and 64.5 eV at the expense of broad features at 63 eV and 66 eV, while features in the O 1s at 531.5 eV are slightly reduced. The O K-edge absorption shows losses at 529 eV and 532.5 eV, but they are weaker than for AA-IrOx. A slight surface reduction of the oxide to metallic iridium is the most likely explanation. In the case of IrO_2, a loss of a doublet at 61.8 eV and 64.8 eV is

accompanied by an increasing, broader doublet at 62.5 eV and 65.5 eV. A possible explanation is the loss of the well-screened main-line, due to a reduction to an Ir^{III} species with less efficient screening. The O K-edge absorption loses some intensity characteristic for oxide features (530 eV and 532 eV), which is corroborated by the O 1s XP spectrum diminishing at 530 eV.

We can conclude from this chemical test that AA-IrOx contains an oxygen species absorbing slightly below 529 eV, which is able to oxidize CO at room temperature. This oxygen species is electron-deficient and can be assigned to bridging oxygens.[35] The oxygen species in IrOOH, while also appearing near 529 eV in the O K-edge, is of different chemical nature and is unable to oxidize CO at room temperature. That these oxygen species are indeed a difference between IrOOH and AA-IrOx is demonstrated in Figure 4.34. The difference in the normalized O K-edge absorption and Ir 4f spectrum of the two powders under vacuum (Figure 4.34A-B) have a pre-edge feature slightly below 529 eV (Figure 4.34A) and a high BE feature in the Ir 4f spectrum (Figure 4.34B). The same characteristics can be found in the CO titration experiment of AA-IrOx (Figure 4.34C-D) when normalized in the same way. These similarities indicate that the oxygen species titrated by CO at room temperature is missing in the IrOOH powder when compared to AA-IrOx.

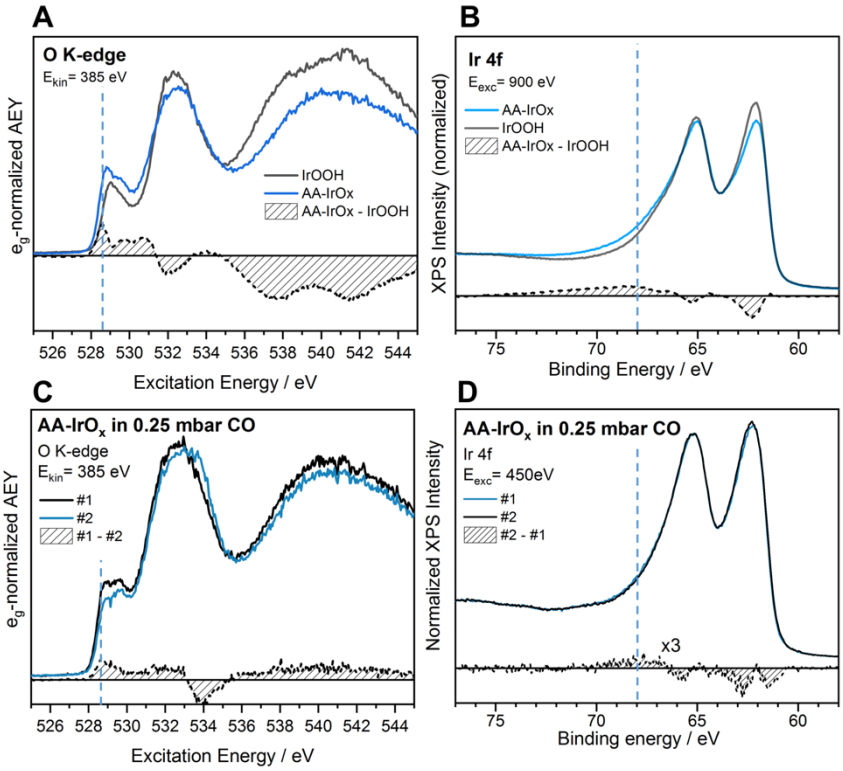

Figure 4.34: A) C) O K-edge absorption and B) D) Ir 4f XP spectra of A)-B) IrOOH and AA-IrOx powder in high vacuum and C)-D) of AA-IrOx in 0.25 mbar CO (consecutive spectra); O K-edge spectra are normalized to the integrated eg-intensity between 530.1 eV and 535.1 eV; Ir 4f XP spectra are normalized to the background binding energy at 77 eV and 58 eV.

4.7.12 Electrochemical characterization

The electrochemical characterization was performed in clean glassware filled with Ar-saturated 0.1 M H_2SO_4 using a flamed Pt wire as counter electrode and a saturated $Hg/HgSO_4$ reference electrode.

Catalyst inks were prepared using 5 mg ground catalyst powder in 490 µL H_2O, 490 µL EtOH, and 20 µL of a Nafion solution by Sigma Aldrich (5% Nafion in alcohols and water). Catalyst inks were sonicated for 15 mins and shortly before use. Inks older than one day were disposed. The rotating glassy carbon disk (5 mm in diameter) was polished subsequently with a 1 µm and 0.5 µm alumina suspension and cleaned before dropcasting 2 µL of the ink. The ink dried under rotation in air.

Electrochemical characterization was performed with a Biologic potentiostat before and after a stress test. The characterization consisted of impedance spectroscopy to determine the overall resistance of the system, cyclovoltammetry (CV) between 0.02 V_{RHE} and 1.45 V_{RHE} at 50 mV/s, CV-series in potential windows of 0.05 V_{RHE} width centered around 0.2 V_{RHE} and 1.0 V_{RHE} at 1, 2, 5, 10, 20, 50, 100, 200, and 500 mV/s, and linear sweep voltammetry (LSV) between 1.0 V_{RHE} and 1.6 V_{RHE} at 5 mV/s. The degradation consisted of cycles starting with chrono-potentiometry at a potential at which the current density reached 2-3 mA/cm^2 in the LSV experiment followed by CVs between 0.3 V_{RHE} and 1.6 V_{RHE}. These cycles were repeated for about 3-5 hours before the final characterization was made.

The capacitance was evaluated from the CV-series (see previous paragraph) using a self-written script averaging the difference in oxidative and reductive current for repetitions of CVs at a given speed (usually two repetitions). The catalyst mass was obtained from the volume that was dropcasted assuming homogeneous weight distribution in the ink. LSV measurements were then normalized by mass, geometric surface area, capacitance, or BET surface area (see Figure 4.35). All potentials are pH and iR corrected and are converted to the reversible hydrogen electrode (RHE).

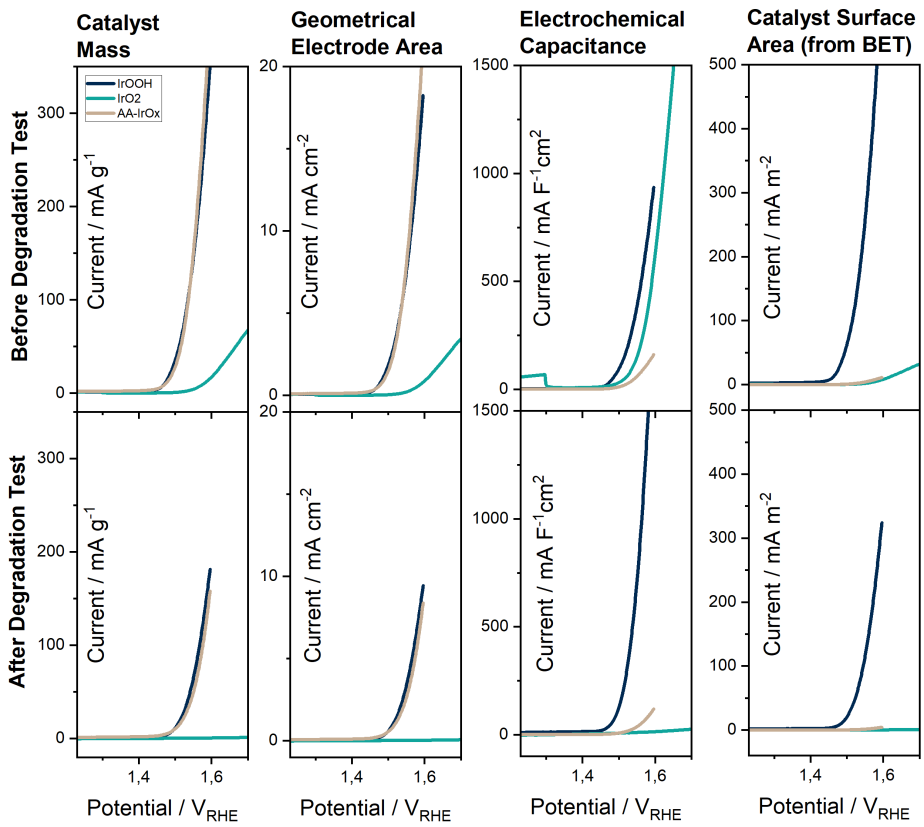

Figure 4.35: Linear sweep voltammetry before (top) and after (bottom) stress test, normalized to catalyst mass, geometrical surface area, capacitance, and BET surface area.

4.7.13 Sample preparation for ex situ TEM and operando X-ray spectroscopy

The in situ samples were prepared from the proton exchange membrane FAD by Fumatech (Bietigheim-Bissingen). Circular disks (11 mm in diameter) were soaked for several days in 0.5 M Na_2SO_4 before transfer of graphene. Single and bilayers of graphene (SLG and BLG) were received from Graphenea (San Sebastian) on copper foil. Copper was etched in aqueous solution of $(NH_4)_2S_2O_8$ (40 g/L) overnight. After exchange of the etching solution to pure water, the swimming layer of graphene was transferred onto the substrate of choice (see Figure 4.36). Two substrates were used: gold grids from Plano (Marburg) with circular holes of 1000 µm (Quantifoil grids R1.2/1.3 Au 200) and FAD membrane disks. IrOOH nanosheets (see above for exfoliation procedure) were deposited on SLG@Cu before etching of Cu and transfer onto the substrate. Powder samples, by contrast, were deposited directly onto FAD in form of a catalyst ink consisting of pure water and dispersed powder. In a consecutive step BLG was transferred on top of the catalyst layer.

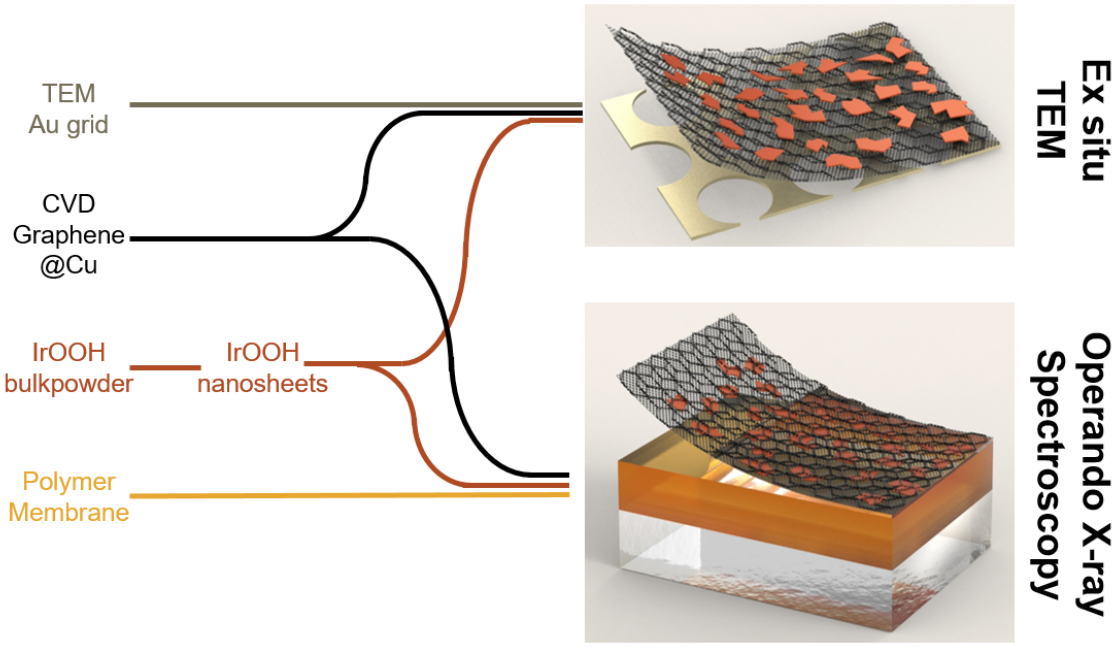

Figure 4.36: Schematic of the sample preparation using graphene and IrOOH nanosheets for ex situ TEM and operando X-ray spectroscopy under wet conditions.

4.7.14 Ex situ TEM

Transmission electron microscopy (TEM) measurements were conducted using a ThermoFisher Scientific Talos F200X, operated at 200 kV. The instrument was equipped with a ThermoFisher Scientific Ceta 16M camera and a Schottky source.

The [001] zone axis pattern displayed in Figure 4.5F in the main text was computed within the kinematic theory for the heterogenite-2*H* structure, space group no 196, $P6_3/mmc$ using CrysTBox.[65] The match of relative intensities between the calculated axis pattern and the measured SAEDs can be explained by the thin nature of these nanosheets, rendering dynamic scattering events negligible. Additional lattice stemming from graphene was used as an internal standard for the calibration of the diffraction pattern. The extracted lattice spacings are given in Table 4.8, which agree with literature values down to about 1%. From the {100} spots in the pattern, the unit cell size *a* (corresponding to the in-plane Ir–Ir distance) can be determined to be 0.315 nm, which is very close to the obtained XRD values. Due to the fact that the crystal is viewed in a [001] zone axis, no information about distances along this axis is obtained and, thus, it is impossible to determine *c* or, subsequently, the Ir–O and out-of-plane Ir–Ir distances.

Table 4.8: Measured lattice spacings from selected area electron diffraction patterns compared to calculated ones obtained from the crystallographic data.

(a) Before EC (Figure 4.5D)

d_{exp} / nm	d_{ref} / nm	Phase	hkl
0.273	0.2681 *	IrOOH	100
0.214	0.2134 [66]	Graphene	100
0.158	0.1548 *	IrOOH	110 | 2-10
0.136	0.1341 *	IrOOH	200
0.123	0.1232 [66]	Graphene	110 | 2-10
0.091	0.0894 *	IrOOH	300

* based on the XRD results obtained in the present work

(b) After EC (Figure 4.5E)

dexp / nm	dref / nm	Phase	hkl
0.267	0.2681 *	IrOOH	100
0.213	0.2134 [66]	Graphene	100
0.156	0.1548 *	IrOOH	110 | 2-10
0.134	0.1341 *	IrOOH	200
0.123	0.1232 [66]	Graphene	110 | 2-10

* based on the XRD results obtained in the present work

4.7.15 Operando X-ray spectroscopy and electrochemistry

The in situ electrochemistry cell using polymer membranes in an electrochemical NAP-XPS module has been presented earlier.[22,23] We used these cells with a boron-doped diamond coated Nb lid contacting the sample from the top, while the backside of the membrane was in contact with a steady flow of 0.05 M H_2SO_4. A platinum wire and a Ag/AgCl reference electrode (DRIREF-2SH stored in saturated KCl solution) were immersed in the liquid electrolyte and used as counter and reference electrode, respectively. The samples were activated with 2 CVs between 0.5 V_{RHE} and 1.45 V_{RHE}. Exemplary CVs for IrOOH powder and nanosheets are provided in Figure 4.37.

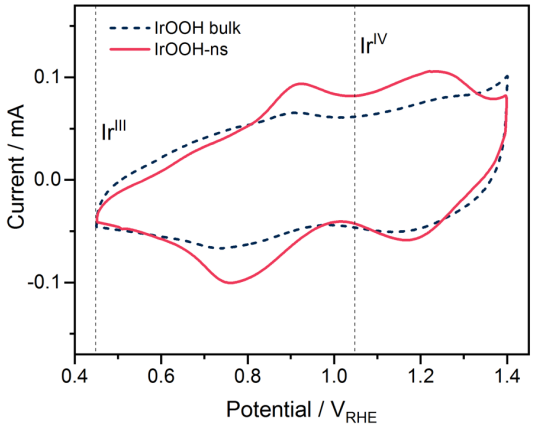

Figure 4.37: Cyclic voltammetry of (0.05 M H_2SO_4)/FAD/IrOOH/BLG and (0.05 M H_2SO_4)/FAD/IrOOH-ns/SLG before operando spectroscopy.

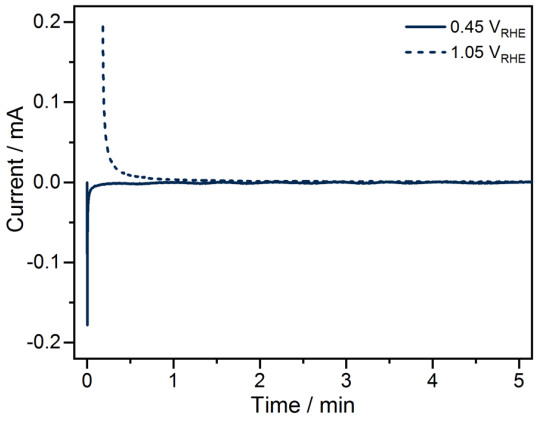

Figure 4.38: Chronoamperometry of (0.05 M H_2SO_4)/FAD/IrOOH-ns/SLG at 0.45 V_{RHE} and 1.05 V_{RHE}.

Operando X-ray spectroscopy was recorded at the ISISS beamline at the BESSY II synchrotron facility during low-alpha conditions with a decaying ring current of < 100 mA. The low alpha mode was chosen in order to reduce beam induced damage and to avoid the impact of top-up injections in the storage ring onto potentiodynamic X-ray absorption. Spectra were recorded after stabilization of currents at a given potential (examples are given in Figure 4.38). Beam damage of the polymer membrane was minimized by moving to a new measurement position after each potential step. It was assured that the samples were homogeneous enough in the measured region to provide consistent data sets. Measurements recorded after more than 5 min on the same spot were not used for detailed analysis. The pressure in the main chamber was regulated by additional water dosing and a PID-controlled pressure valve by Pfeiffer Vacuum GmbH (Asslar, Germany). The target water pressure of 0.25 mbar was sustained throughout operando spectroscopy, except for the samples containing Ir NPs, for which the pressure ranged between 0.05 and 0.15 mbar.

For comparison to Figure 4.7 in the main text, Ir 4f and O K-edge absorption of AA-IrOx (Figure 4.39), Ir nanoparticles (NPs) (Figure 4.40), and bulk IrOOH (Figure 4.41) are provided in the state of Ir^{III} and Ir^{IV}. Fitting restrictions are provided in Table 4.2; with the exception of Ir NPs, for which metallic iridium

was fitted in addition, with the Ir 4f 7/2 contribution appearing at 60.9 eV, a doublet splitting of 3.0 eV, and a Doniach-Ŝunjić line shape. The trends in the O K-edge absorption is the same for all samples. One main feature is observed for the e_g-contribution between 532 eV and 533 eV, which appears in all spectra, while a t_{2g}-feature appears at about 529 eV in the state of Ir^{IV}, or at ~1.2 V_{RHE}. An exception are contributions which are difficult to reduce, such as the rutile structure and possibly the hollandite motifs found in AA-IrOx (see above), which absorb at 530 eV. The Ir 4f doublets at low potentials can be fitted with two summed Gaussian-Lorentzian contributions. The Ir 4f 7/2 contribution is centered at a BE of about 62 eV. The full width half maximum (FWHM) of the contribution varies between 1.2 eV and 1.8 eV. The Ir 4f fit of AA-IrOx at 0.45 V_{RHE} (Figure 4.39B) lacks some high-BE broadening, which is again caused by irreducible Ir^{IV} oxide contributions. In the oxidized form, all three samples can be fitted with three doublets, one doublet with the Doniach-Ŝunjić line shape and two satellite features with a summed Gaussian-Lorentzian as their line shape. The distance to the main peak varies from 0.6 eV to 1.0 eV for the first satellite and the second satellite has a distance of 1.9 eV to 2.1 eV from the main line. The FWHM varies between 1.0 eV and 1.8 eV. This means that the more complex bulk with partly amorphous structures presented here are not precisely described by the fit but the electronic structure appears similar.

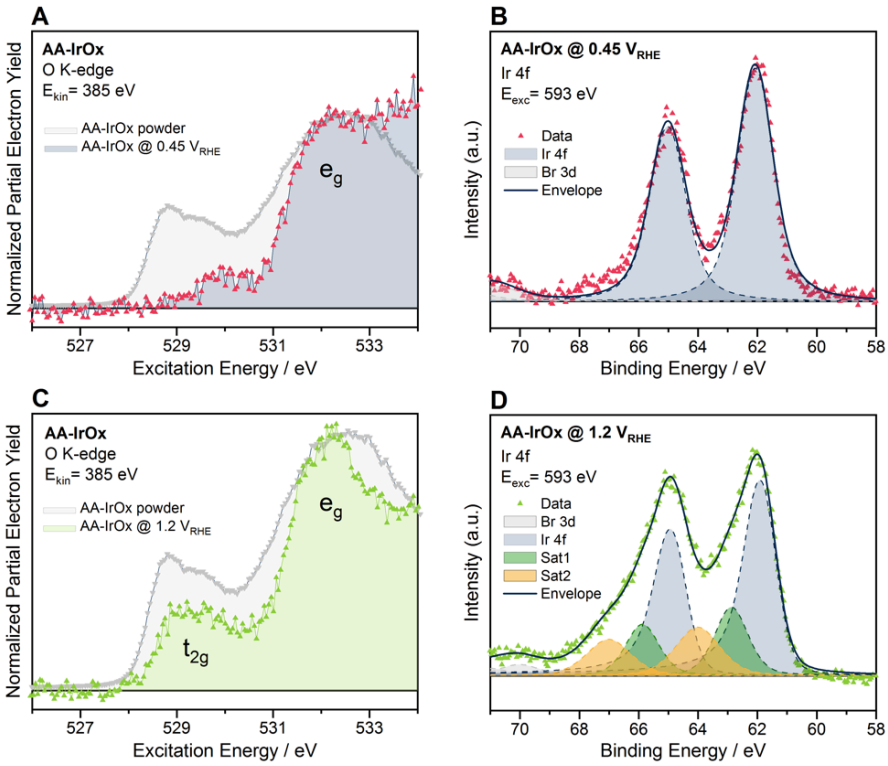

Figure 4.39: A) C) O K-edge and B) D) Ir 4f XP spectra of (0.05 M H_2SO_4)/FAD/AA-IrOx/BLG at A) B) 0.45 V_{RHE} and C) D) 1.2 V_{RHE}; a Shirley-type background was subtracted from the Ir 4f XP spectrum.

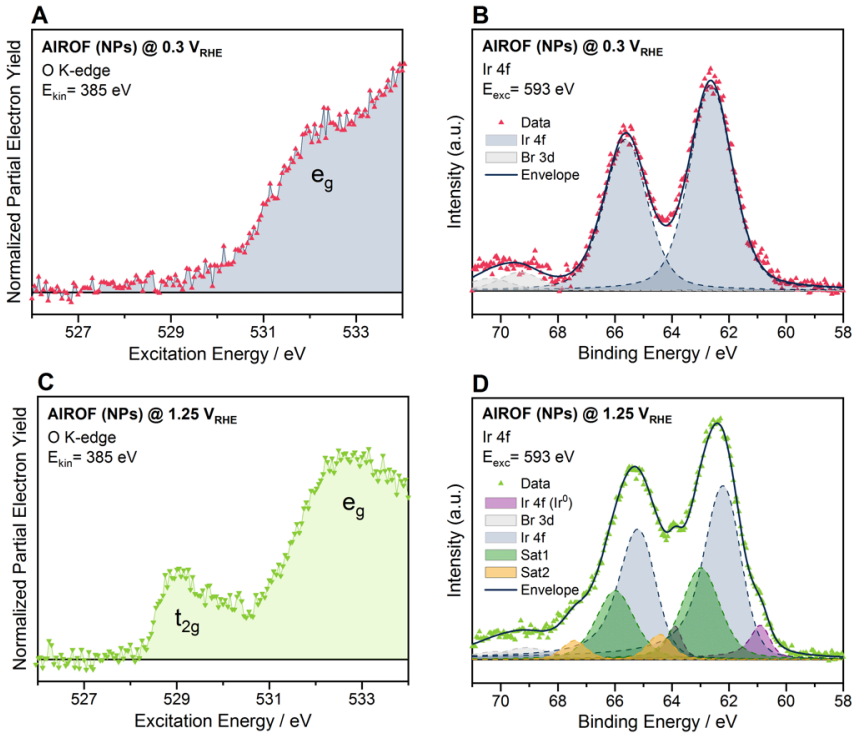

Figure 4.40: A) C) O K-edge and B) D) Ir 4f XP spectra of (0.1 M H_2SO_4)/FAD/Ir NPs/SLG at A) B) 0.3 V_{RHE} and C) D) 1.25 V_{RHE}; a Shirley-type background was subtracted from the Ir 4f XP spectrum.

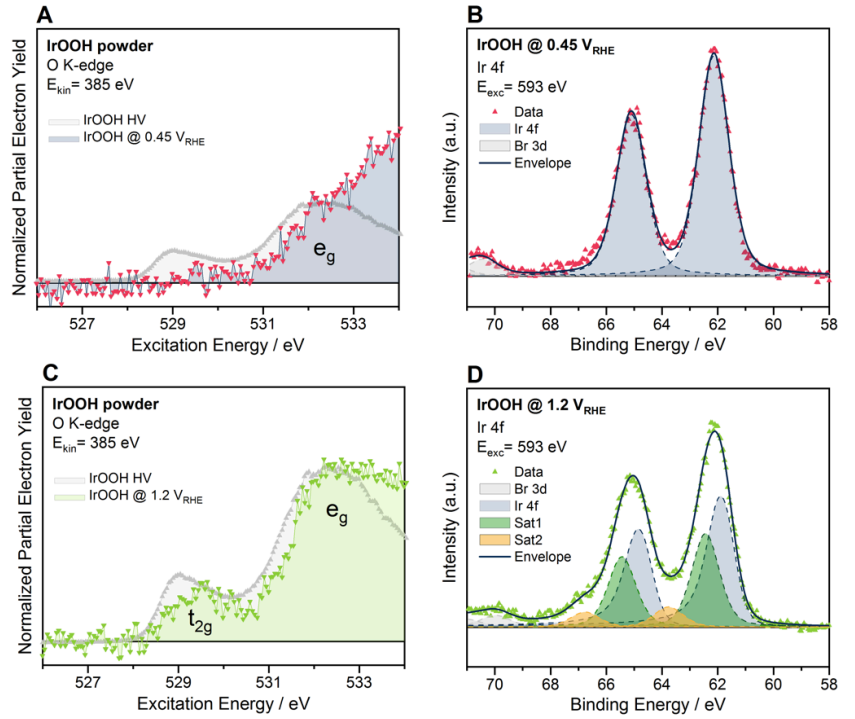

Figure 4.41: A) C) O K-edge and B) D) Ir 4f XP spectra of (0.05 M H_2SO_4)/FAD/IrOOH/BLG at A) B) 0.45 V_{RHE} and C) D) 1.2 V_{RHE}; a Shirley-type background was subtracted from the Ir 4f XP spectrum.

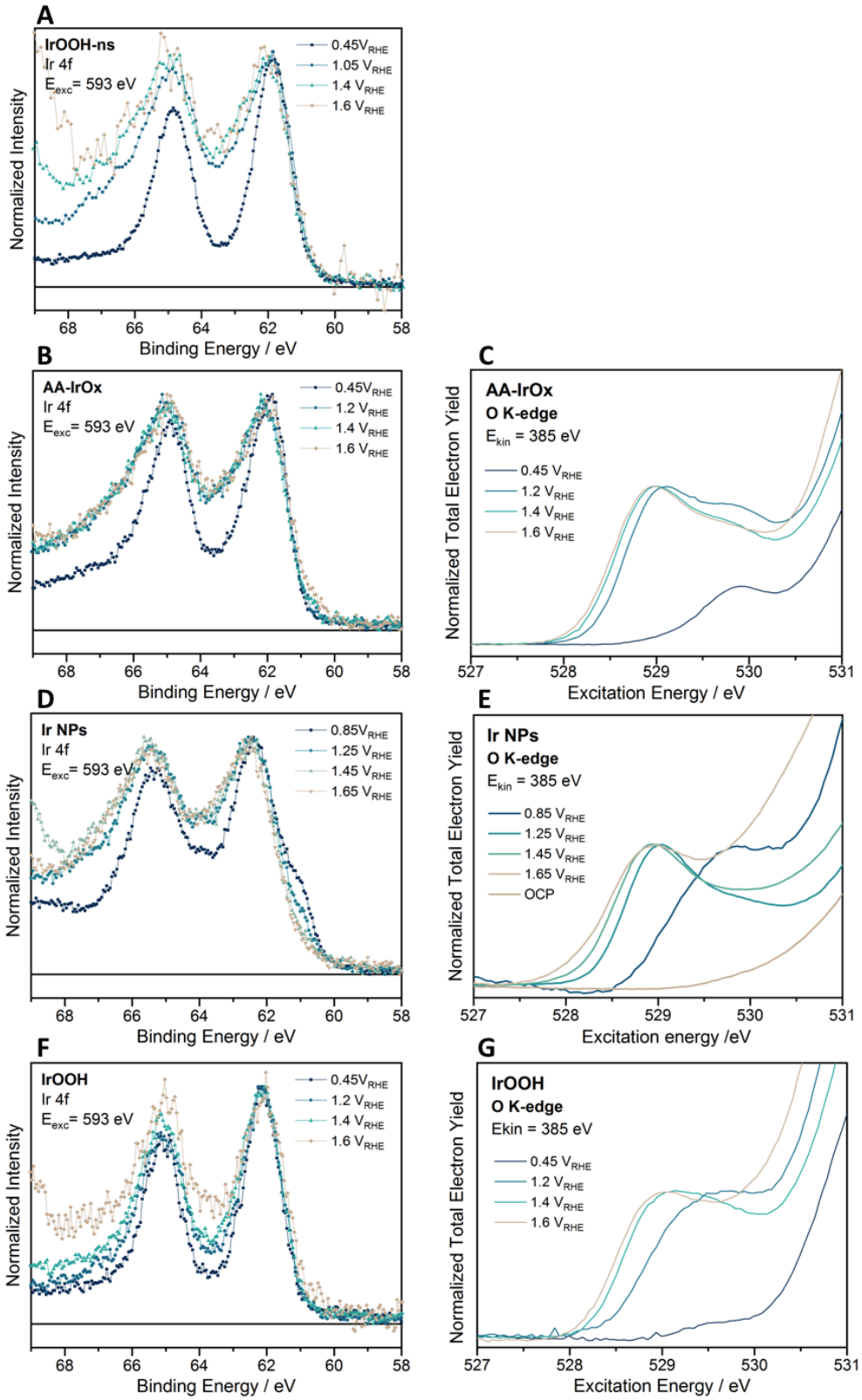

*Figure 4.42: In situ and operando Ir 4f XP spectra (left) and O K-edge absorption spectra (right) of a) (0.05 M H_2SO_4)/FAD/IrOOH-ns/SLG and b)-g) (0.05 M H_2SO_4)/FAD/*Ir catalyst*/BLG; XP spectra were normalized to the Ir 4f 7/2 peak intensity and absorption spectra were normalized to the peak intensity of the pre-edge; in the case of IrNPs the electrolyte was 0.1 M H_2SO_4.*

In Figure 4.42 the Ir 4f XP spectra and the O K-edge absorption as well as their development towards OER relevant potentials are compared for IrOOH-ns, AA-IrOx, Ir NPs, and IrOOH. The Ir 4f spectra in all samples develop a more asymmetric line shape with higher potentials. The change in the line shape is most pronounced in the oxidation from low potentials to ~1.2 V_{RHE}, but further asymmetric broadening is observed in potentials relevant to OER. However, a minor additional broadening is observed in AA-IrOx and Ir NPs, while IrOOH-ns and IrOOH powder continue to change beyond the potential of 1.4 V_{RHE}. The corresponding trend in the O K-edge absorption is a shift of the white line towards lower excitation energies. The largest change occurs, again, in the oxidation up to ~1.2 V_{RHE}, in which an absorption feature between 529 eV and 530 eV appears. A second absorption feature slightly below 529 eV is present at 1.2 V_{RHE} in AA-IrOx and at ~1.4V_{RHE} in Ir NPs and IrOOH. At potentials relevant to the OER, further broadening to lower excitation energies is consistently observed in all samples of the set. It can be summarized that the Ir 4f XP and the O K-edge absorption spectra follow the same trends but vary in the details of energy position and intensity distribution, pointing towards a different electronic and chemical structure, i.e. a variation in the distribution of oxygen species (μ_1-O, μ_2-O, or μ_3-O).

4.8 Bibliography

(1) Kost, C.; Shammugam, S.; Jülch, V.; Huyen-Tran, N.; Schlegl, T. *Fraunhofer ISE: Levelized Cost of Electricity - Renewable Energy Technologies, March 2018*; 2018.

(2) International Partnership for Hydrogen and Fuel Cells in the Economy https://www.iphe.net/ (accessed Jan 23, 2020).

(3) IEA. *The Future of Hydrogen for G20*; 2019.

(4) Holladay, J. D.; Hu, J.; King, D. L.; Wang, Y. An Overview of Hydrogen Production Technologies. *Catal. Today* 2009, *139* (4), 244–260.

(5) Carmo, M.; Fritz, D. L.; Mergel, J.; Stolten, D. A Comprehensive Review on PEM Water Electrolysis. *Int. J. Hydrog. Energy* 2013, *38*, 4901–4934.

(6) Buttler, A.; Spliethoff, H. Current Status of Water Electrolysis for Energy Storage, Grid Balancing and Sector Coupling via Power-to-Gas and Power-to-Liquids: A Review. *Renew. Sustain. Energy Rev.* 2018, *82*, 2440–2454.

(7) Spanos, I.; Auer, A. A.; Neugebauer, S.; Deng, X.; Tüysüz, H.; Schlögl, R. Standardized Benchmarking of Water Splitting Catalysts in a Combined Electrochemical Flow Cell/Inductively Coupled Plasma–Optical Emission Spectrometry (ICP-OES) Setup. *ACS Catal.* 2017, *7* (6), 3768–3778.

(8) Bernt, M.; Siebel, A.; Gasteiger, H. A. Analysis of Voltage Losses in PEM Water Electrolyzers with Low Platinum Group Metal Loadings. *J. Electrochem. Soc.* 2018, *165* (5), F305–F314.

(9) Vesborg, P. C. K.; Jaramillo, T. F. Addressing the Terawatt Challenge: Scalability in the Supply of Chemical Elements for Renewable Energy. *RSC Adv.* 2012, *2* (21), 7933–7947.

(10) Reier, T.; Teschner, D.; Lunkenbein, T.; Bergmann, A.; Selve, S.; Kraehnert, R.; Schl, R.; Strasser, P. Electrocatalytic Oxygen Evolution on Iridium Oxide : Uncovering Catalyst-Substrate Interactions and Active Iridium Oxide Species. *J. Electrochem. Soc.* 2014, *161* (9), 876–882.

(11) Abbott, D. F.; Lebedev, D.; Waltar, K.; Povia, M.; Nachtegaal, M.; Fabbri, E.; Copéret, C.; Schmidt, T. J. Iridium Oxide for the Oxygen Evolution Reaction: Correlation between Particle Size, Morphology, and the Surface Hydroxo Layer from Operando XAS. *Chem. Mater.* 2016, *28*, 6591–6604.

(12) Massue, C.; Pfeifer, V.; Huang, X.; Noack, J.; Tarasov, A.; Cap, S.; Schlögl, R. High-Performance Supported Ir-Oxohydroxide Water Oxidation Electrocatalysts. *ChemSusChem* 2017, 1–16.

(13) Spöri, C.; Briois, P.; Nong, H. N.; Reier, T.; Billard, A.; Kühl, S.; Teschner, D.; Strasser, P. Experimental Activity Descriptors for Iridium-Based Catalysts for the Electrochemical Oxygen Evolution Reaction (OER). *ACS Catal.* 2019, *9* (8), 6653–6663.

(14) Kötz, R.; Neff, H.; Stucki, S. Anodic Iridium Oxide Films - XPS-Studies of Oxidation State Changes and O2 Evolution. *J. Electrochem. Soc.* 1984, *131*, 72–77.

(15) Hall, H. Y.; Sherwood, P. M. A. X-Ray Photoelectron Spectroscopic Studies of the Iridium Electrode System. *J. Chem. Soc., Faraday Trans. 1* 1984, *80*, 135–152.

(16) Smith, R. D. L.; Sporinova, B.; Fagan, R. D.; Trudel, S.; Berlinguette, C. P. Facile Photochemical Preparation of Amorphous Iridium Oxide Films for Water Oxidation Catalysis. *Chem. Mater.* 2014, *26*, 1654–1659.

(17) Li, T.; Kasian, O.; Cherevko, S.; Zhang, S.; Geiger, S.; Scheu, C.; Felfer, P.; Raabe, D.; Gault, B.; Mayrhofer, K. J. J. Atomic-Scale Insights into Surface Species of Electrocatalysts in Three Dimensions. *Nat. Catal.* 2018, *1* (4), 300–305.

(18) Trasatti, S. Electrocatalysis in the Anodic Evolution of Oxygen and Chlorine. *Electrochim. Acta* 1984, *29* (11), 1503–1512.

(19) Bernicke, M.; Ortel, E.; Reier, T.; Bergmann, A.; Ferreira De Araujo, J.; Strasser, P.; Kraehnert, R. Iridium Oxide Coatings with Templated Porosity as Highly Active Oxygen Evolution Catalysts: Structure-Activity Relationships. *ChemSusChem* 2015, *8* (11), 1908–1915.

(20) Pfeifer, V.; Jones, T. E.; Velasco Vélez, J. J.; Massué, C.; Arrigo, R.; Teschner, D.; Girgsdies, F.; Scherzer, M.; Greiner, M. T.; Allan, J.; et al. The Electronic Structure of Iridium and Its Oxides. *Surf. Interface Anal.* 2016, *48* (5), 261–273.

(21) Freakley, S. J.; Ruiz-Esquius, J.; Morgan, D. J. The X-Ray Photoelectron Spectra of Ir, IrO2 and IrCl3 Revisited. *Surf. Interface Anal.* 2017, *49* (8), 794–799.

(22) Knop-Gericke, A.; Pfeifer, V.; Velasco-Velez, J.-J.; Jones, T.; Arrigo, R.; Hävecker, M.; Schlögl, R. In Situ X-Ray Photoelectron Spectroscopy of Electrochemically Active Solid-Gas and Solid-Liquid Interfaces. *J. Electron Spectrosc. Relat. Phenom.* 2017, *221*, 10–17.

(23) Carbonio, E. A.; Velasco-Velez, J.-J.; Schlögl, R.; Knop-Gericke, A. Perspective—Outlook on Operando Photoelectron and Absorption Spectroscopy to Probe Catalysts at the Solid-Liquid Electrochemical Interface. *J. Electrochem. Soc.* 2020, *167* (5), 054509.

(24) Sanchez Casalongue, H. G.; Ng, M. L.; Kaya, S.; Friebel, D.; Ogasawara, H.; Nilsson, A. In Situ Observation of Surface Species on Iridium Oxide Nanoparticles during the Oxygen Evolution Reaction. *Angew. Chem., Int. Ed.* 2014, *53*, 7169–7172.

(25) Saveleva, V. A.; Wang, L.; Teschner, D.; Jones, T.; Gago, A. S.; Friedrich, K. A.; Zafeiratos, S.; Schlögl, R.; Savinova, E. R. Operando Evidence for a Universal Oxygen Evolution Mechanism on Thermal and Electrochemical Iridium Oxides. *J. Phys. Chem. Lett.* 2018, *9* (11), 3154–3160.

(26) Pfeifer, V.; Jones, T. E.; Velasco Vélez, J. J.; Arrigo, R.; Piccinin, S.; Hävecker, M.; Knop-Gericke, A.; Schlögl, R. In Situ Observation of Reactive Oxygen Species Forming on Oxygen-Evolving Iridium Surfaces. *Chem. Sci.* 2017, *8*, 2143–2149.

(27) Velasco-Vélez, J. J.; Jones, T. E.; Streibel, V.; Hävecker, M.; Chuang, C.-H.; Frevel, L.; Plodinec, M.; Centeno, A.; Zurutuza, A.; Wang, R.; et al. Electrochemically Active Ir NPs on Graphene for OER in Acidic Aqueous Electrolyte Investigated by in Situ and Ex Situ Spectroscopies. *Surf. Sci.* 2019, *681*, 1–8.

(28) Frevel, L. J.; Mom, R.; Velasco-Vélez, J.-J.; Plodinec, M.; Knop-Gericke, A.; Schlögl, R.; Jones, T. E. In Situ X-Ray Spectroscopy of the Electrochemical Development of Iridium Nanoparticles in Confined Electrolyte. *J. Phys. Chem. C* 2019, *123* (14), 9146–9152.

(29) Nong, H. N.; Reier, T.; Oh, H.-S.; Gliech, M.; Paciok, P.; Vu, T. H. T.; Teschner, D.; Heggen, M.; Petkov, V.; Schlögl, R.; et al. A Unique Oxygen Ligand Environment Facilitates Water Oxidation in Hole-Doped IrNiOx Core–Shell Electrocatalysts. *Nat. Catal.* 2018, *1* (11), 841–851.

(30) Weber, D.; Schoop, L. M.; Wurmbrand, D.; Laha, S.; Podjaski, F.; Duppel, V.; Müller, K.; Starke, U.; Lotsch, B. V. IrOOH Nanosheets as Acid Stable Electrocatalysts for the Oxygen Evolution Reaction. *J. Mater. Chem. A* 2018, *6* (43), 21558–21566.

(31) Weber, D.; Schoop, L. M.; Wurmbrand, D.; Nuss, J.; Seibel, E. M.; Tafti, F. F.; Ji, H.; Cava, R. J.; Dinnebier, R. E.; Lotsch, B. V. Trivalent Iridium Oxides: Layered Triangular Lattice Iridate K0.75

Na0.25 IrO2 and Oxyhydroxide IrOOH. *Chem. Mater.* 2017, *29*, 8338–8345.

(32) Miao, M.-S.; Seshadri, R. Rh2O3 versus IrO2: Relativistic Effects and the Stability of Ir4+. *J. Phys. Condens. Matter* 2012, *24* (21), 215503.

(33) Cohen, A. J.; Mori-Sánchez, P.; Yang, W. Insights into Current Limitations of Density Functional Theory. *Science* 2008, *321* (5890), 792–794.

(34) Stöhr, J.; König, H. Determination of Spin- and Orbital-Moment Anisotropies in Transition Metals by Angle-Dependent X-Ray Magnetic Circular Dichroism. *Phys. Rev. Lett.* 1995, *75* (20), 3748–3751.

(35) Pfeifer, V.; Jones, T. E.; Wrabetz, S.; Massué, C.; Velasco Vélez, J. J.; Arrigo, R.; Scherzer, M.; Piccinin, S.; Hävecker, M.; Knop-Gericke, A.; et al. Reactive Oxygen Species in Iridium-Based OER Catalysts. *Chem. Sci.* 2016, *7*, 6791–6795.

(36) Willinger, E.; Massué, C.; Schlögl, R.; Willinger, M. G. Identifying Key Structural Features of IrOx Water Splitting Catalysts. *J. Am. Chem. Soc.* 2017, *139* (34), 12093–12101.

(37) Riga, J.; Tenret-Noël, C.; Pireaux, J. J.; Caudano, R.; Verbist, J. J.; Gobillon, Y. Electronic Structure of Rutile Oxides TiO2, RuO2 and IrO2 Studied by X-Ray Photoelectron Spectroscopy. *Phys. Scr.* 1977, *16*, 351–354.

(38) Lezna, R. O.; Kunimatsu, K.; Ohtsuka, T.; Sato, N. In Situ Infrared Spectroscopy of Iridium Oxide. *J. Electrochem. Soc.* 1987, *134* (12), 3090–3094.

(39) Mom, R.; Frevel, L.; Velasco-Vélez, J.-J.; Plodinec, M.; Knop-Gericke, A.; Schlögl, R. The Oxidation of Platinum under Wet Conditions Observed by Electrochemical X-Ray Photoelectron Spectroscopy. *J. Am. Chem. Soc.* 2019, *141* (16), 6537–6544.

(40) Mcintyre, J. D. E.; Peck, W. F.; Nakahara, S. Oxidation-State Changes and Structure of Electrochromic Iridium Oxide-Films. *J. Electrochem. Soc.* 1980, *127* (6), 1264–1268.

(41) Hüppauff, M.; Lengeler, B. Valency and Structure of Iridium in Anodic Iridium Oxide Films. *J. Electrochem. Chem.* 1993, *140*, 598–602.

(42) Pauporté, T.; Aberdam, D.; Hazemann, J.-L.; Faure, R.; Durand, R. X-Ray Absorption in Relation to Valency of Iridium in Sputtered Iridium Oxide Film. *J. Electroanal. Chem.* 1999, *465*, 88–95.

(43) Conway, B. E.; Mozota, J. Surface and Bulk Processes at Oxidized Iridium Electrodes-II. Conductivity-Switched Behaviour of Thick Oxide Films. *Electrochim. Acta* 1983, *28*, 9–16.

(44) Costentin, C.; Porter, T. R.; Save, J. Conduction and Reactivity in Heterogeneous-Molecular Catalysis: New Insights in Water Oxidation Catalysis by Phosphate Cobalt Oxide Films. 2016.

(45) Fairley, N.; Carrick, A. CasaXPS. 2017.

(46) Doniach, S.; Sunjic, M. Many-Electron Singularity in X-Ray Photoemission and X-Ray Line Spectra from Metals. *J. Phys. C Solid State Phys.* 1970, *3* (2), 285–291.

(47) Giannozzi, P.; Baroni, S.; Bonini, N.; Calandra, M.; Car, R.; Cavazzoni, C.; Ceresoli, D.; Chiarotti, G. L.; Cococcioni, M.; Dabo, I.; et al. QUANTUM ESPRESSO: A Modular and Open-Source Software Project for Quantum Simulations of Materials. *J. Phys. Condens. Matter* 2009, *21*, 395502.

(48) Giannozzi, P.; Andreussi, O.; Brumme, T.; Bunau, O.; Buongiorno Nardelli, M.; Calandra, M.; Car, R.; Cavazzoni, C.; Ceresoli, D.; Cococcioni, M.; et al. Advanced Capabilities for Materials Modelling with Quantum ESPRESSO. *J. Phys. Condens. Matter* 2017, *29* (46), 465901.

(49) Prandini, G.; Marrazzo, A.; Castelli, I. E.; Mounet, N.; Marzari, N. Precision and Efficiency in Solid-State Pseudopotential Calculations. *npj Comput. Mater.* 2018, *4* (1), 72.

(50) Lejaeghere, K.; Bihlmayer, G.; Bjorkman, T.; Blaha, P.; Blugel, S.; Blum, V.; Caliste, D.; Castelli, I. E.; Clark, S. J.; Dal Corso, A.; et al. Reproducibility in Density Functional Theory Calculations of Solids. *Science* 2016, *351* (6280), aad3000.

(51) Garrity, K. F.; Bennett, J. W.; Rabe, K. M.; Vanderbilt, D. Pseudopotentials for High-Throughput DFT Calculations. *Comput. Mater. Sci.* 2014, *81*, 446–452.

(52) Dal Corso, A. Pseudopotentials Periodic Table: From H to Pu. *Comput. Mater. Sci.* 2014, *95*, 337–350.

(53) Juhás, P.; Davis, T.; Farrow, C. L.; Billinge, S. J. L. PDFgetX3 : A Rapid and Highly Automatable Program for Processing Powder Diffraction Data into Total Scattering Pair Distribution Functions. *J. Appl. Crystallogr.* 2013, *46* (2), 560–566.

(54) Yang, X.; Juhas, P.; Farrow, C. L.; Billinge, S. J. L. XPDFsuite: An End-to-End Software Solution for High Throughput Pair Distribution Function Transformation, Visualization and Analysis. *J. Appl. Crystallogr.* 2014.

(55) Egami, T.; Billinge, S. *Underneath the Bragg Peaks, Volume 16*, 2nd Editio.; Elsevier Ltd: Oxford, Amsterdam, San Diego, 2012.

(56) Lorch, E. Neutron Diffraction by Germania, Silica and Radiation-Damaged Silica Glasses. *J. Phys. C Solid State Phys.* 1969, *2* (2), 305.

(57) Soper, A. K.; Barney, E. R. On the Use of Modification Functions When Fourier Transforming Total Scattering Data. *J. Appl. Crystallogr.* 2012, *45* (6), 1314–1317.

(58) Farrow, C. L.; Juhas, P.; Liu, J. W.; Bryndin, D.; Božin, E. S.; Bloch, J.; Proffen, T.; Billinge, S. J. L. PDFfit2 and PDFgui: Computer Programs for Studying Nanostructure in Crystals. *J. Phys. Condens. Matter* 2007, *19* (33), 335219.

(59) Coelho, A. A. TOPAS and TOPAS-Academic : An Optimization Program Integrating Computer Algebra and Crystallographic Objects Written in C++. *J. Appl. Crystallogr.* 2018, *51* (1), 210–218.

(60) Warren, B. E. X-Ray Diffraction in Random Layer Lattices. *Phys. Rev.* 1941, *59* (9), 693–698.

(61) McDaniel, C. L.; Schneider, S. J. Phase Relations in the Systems TiO2-IrO2 and SnO2-IrO2 in Air. *J. Res. Natl. Bur. Stand. Sect. A Phys. Chem.* 1967, *71A* (2), 119.

(62) Tauc, J.; Grigorovici, R.; Vancu, A. Optical Properties and Electronic Structure of Amorphous Germanium. *Phys. Status Solidi* 1966, *15* (2), 627–637.

(63) Nilsson, A.; Nordlund, D.; Waluyo, I.; Huang, N.; Ogasawara, H.; Kaya, S.; Bergmann, U.; Näslund, L. Å.; Öström, H.; Wernet, P.; et al. X-Ray Absorption Spectroscopy and X-Ray Raman Scattering of Water and Ice; an Experimental View. *J. Electron Spectrosc. Relat. Phenom.* 2010, *177*, 99–129.

(64) Hitchcock, A. P.; Brion, C. E. K-Shell Excitation Spectra of CO, N2 and O2. *J. Electron Spectros. Relat. Phenomena* 1980, *18* (1), 1–21.

(65) Klinger, M.; Jäger, A. Crystallographic Tool Box (CrysTBox): Automated Tools for Transmission Electron Microscopists and Crystallographers. *J. Appl. Crystallogr.* 2015, *48* (6), 2012–2018.

(66) Trucano, P.; Chen, R. Structure of Graphite by Neutron Diffraction. *Nature* 1975, *258* (5531), 136–137.

5. The roles of chemistry and bias in electrocatalytic oxygen evolution

5.1 Preliminary Remarks

The work presented in this chapter is concerned with how the surface coverage of electron-deficient oxygen influences the rate of the OER (Q4. This is done by utilizing and extending concepts of previous chapters. Potentiodynamic X-ray absorption, for example, was combined with pulse voltammetry. This combination allows the simultaneous determination of oxidation charge, relative hole coverage, and OER current at a given potential in the same experiment. In addition to O K-edge absorption, the experiment was done using bulk-sensitive Ir L-edge absorption in order to track iridium's average oxidation state. At the center of the publication, however, is the ab initio analysis of how the hole coverage on the surface impacts the rate of the OER. The analysis artificially separates the chemical and electrochemical contribution to the barrier of the rate determining step. The calculated results compare favorably to the potential-dependent rate of experimental electrochemistry.

The idea to combine pulse voltammetry with potentiodynamic X-ray absorption at O K-edges, the execution of it, and the strategy for data analysis was developed together with Detre Teschner. Hong Nhan Nong and Camillo Spöri helped carrying out the experiments. A similar concept was applied to Ir L-edges by Arno Bergmann, Janis Timoshenko, Detre Teschner, and Hong Nhan Nong. The electrochemical measurements (i.e. pulse voltammetry were done by Hong Nhan Nong with the help of Malte Klingenhof, Hoang Phi Tran, and Camillo Spöri. Guido Zichittella prepared chlorine treated samples under the supervision of Javier Pérez-Ramírez. Travis Jones performed DFT calculations with the help of Simone Piccinin. Detre Teschner and Travis Jones designed the study, evaluated the data, and wrote the text. Javier Pérez-Ramírez, Beatriz Roldan Cuenya, Robert Schlögl, and Peter Strasser offered guidance for the project. All scientists named above, as well as Rik Mom and Axel Knop-Gericke commented on the manuscript. I am grateful that I was actively involved in the discussion and development of this project by Travis Jones and Detre Teschner.

Material from: Nong, H. N.; Falling, L. J.; Bergmann, A.; Klingenhof, M.; Tran, H.-P.; Spöri, C.; Mom, R.; Timoshenko, J.; Zichittella, G.; Knop-Gericke, A.; Piccinin, S.; Pérez-Ramírez, J.; Roldan Cuenya, B.; Schlögl, R.; Strasser, P.; Teschner, D.; Jones, T. E.; Key role of chemistry versus bias in electrocatalytic oxygen evolution. Nature **2020**, *587*, 408-413"; DOI: 10.1038/s41586-020-2908-2.

5.2 Abstract

Electrocatalysts [1] facilitate two fundamental processes in chemistry—electron transfer [2] and chemical bond formation/rupture[3]—to convert renewable electrical energy into chemical fuels. These fuels require the protons and electrons supplied by the electrocatalytic oxygen evolution reaction (OER).[4–6] The set of reaction steps constituting the overall OER are thought to result in an electrochemical mechanism qualitatively distinct from the chemical ones familiar in thermal catalysis.[1] Chief among these differences is that the OER rate depends on the electrochemical bias—often exponentially, consistent with the empirical relationship know as Tafel's law.[7–12] The frequent validity of Tafel's equation has inspired efforts to extract mechanistic information from the Tafel slopes [8,10,11] under the assumption that the bias acts directly on the reaction coordinate of the rate determining step. However, there is no fundamental justification for this for an electro*catalytic* reaction.[12] Here we use a range of materials to demonstrate the overpotential mediates the OER though charge accumulation rather than acting directly on the reaction coordinate. We found the OER rate is controlled by chemical bond making/breaking, which leads to a linear dependence of the activation free energy on the amount of oxidative charge stored in the electrocatalyst. We show how this relationship underlies electrocatalytic performance and how it can be probed by experiment. By demonstrating potential dependent protonation and oxidation states account for electrocatalytic performance, we anticipate these results will aid in the design of new electrocatalytic materials.

5.3 Introduction

During electrocatalytic water oxidation di-oxygen is generated through the oxygen evolution reaction (OER). The reaction involves the transfer of four electrons across the anode, the rupture of O-H bonds, and the formation of an O-O bond. The resultant electrochemical kinetics are complex and have proven challenging to decipher. In the limit of fast mass transport and sufficiently high overpotential η, the measured OER current I typically depends exponentially on overpotential,[4,5,13,14] thereby allowing the electrocatalytic OER rates to be fit by the empirical two parameter Tafel equation, $\eta = a + b \log I$. For outer-sphere redox reactions this type of Tafel's law behavior emerges naturally because the overpotential acts directly on the reaction coordinate.[2] This makes Butler-Volmer kinetic theory hold and allows mechanistic information to be gained from the Tafel slope b.[12] For the inner-sphere reactions involved in the OER, however, the mechanistic role of η is unclear and Tafel's law becomes phenomenological.[12] Despite this challenge, numerous studies have aimed to assess the electrocatalytic OER mechanism from Tafel slopes under the assumption the rate-determining step (rds) is described by Butler-Volmer kinetic theory. Studies based on this assumption often lead to the conclusion that the rds varies with bias[4,5,13,14]. However, oxidative charges stored in OER electrocatalysts can react in the absence of an applied bias,[15,16] and this purely chemical reaction may mediate the OER rate and would not be expected to obey Butler-Volmer kinetic theory.[15–17] We sought to investigate these roles of chemistry and bias by studying one the most successful class of OER anode, iridium-based materials.[5,13,14] We employed a combination of *operando* potentiodynamic X-ray

absorption spectroscopy (XAS) at the Ir and O edges [18] with pulse voltammetry and DFT calculations to disentangle the roles of bond making/breaking and electron transfer kinetics on the OER and offer mechanistic details into how bias and charge mediate the electrocatalytic reaction.

5.4 Results and Discussion

5.4.1 Influence of charge on OER activity

To explore the role of chemical bond making/breaking steps in the OER we begin by comparing the potential dependent charge accumulation on an amorphous IrO_x electrocatalyst (calcined at 250°C) with its OER performance. Pulse voltammetry was used to quantify charge accumulation. The experiment consists of increasing anodic voltage pulses (from 1.42 to 1.80 V non-iR corrected potential vs. RHE in 20 mV/step) separated from one another by resting at a cathodic bias below the OER onset, 1.35 V vs. RHE (Figure 5.6a). A section of this experiment is shown in Figure 5.1a to highlight the oxidative/reductive current pulses emerging upon anodic/cathodic voltage steps. Integration of this current response yields the total oxidative charge stored in the electrocatalyst at a given potential, see SI for details. Doing so allows us to plot not only the potential (iR corrected, unless otherwise noted) against log OER current, but also the relationship of each against stored charge (total charge, unless otherwise noted), see Figure 5.1b-d.

Inspection of the Tafel plot (Figure 5.1b) shows the expected behavior. Up to 1.54 V the Tafel slope is 39 mV/dec, in line with the 40 mV/dec observed for highly active Ir electrocatalysts.[17] Anodic of 1.54 V the Tafel slope increases to ~64 mV/dec, behavior ascribed to a qualitative change of the rds.[8] Like the log OER current, the charge (Figure 5.1c) is bi-linear in external bias with a slope change at 1.54 V. Here, the slope change indicates a change in capacitance from ~22.1 mF below 1.54 V to ~15.9 mF above 1.54 V. This measured capacitance (Table 5.1 and Table 5.2) is significantly larger than the order 10 $\mu F/cm^2$ double layer capacitance of conducting planar electrodes; areal capacitance measurements reveal our measured values are 1-2 of orders of magnitude larger than those of an ideal electrode (Table 5.2). This large discrepancy suggests additional means of *pseudocapacitive* charge storage are active,[19] as previously discussed for Ir (and Ru) based materials.[20]

This *pseudocapacitive* charge storage appears to be connected to the OER kinetics. The total charge vs. log current profile (Figure 5.1d) remains linear throughout the entire potential range; there is no significant change of slope when crossing the critical potential where the Tafel slope bends. While our example is a thermally activated oxide, other materials spanning a range of activities and properties provide identical trends (Figure 5.7-12), as does the analysis of the transient current response (see Figure 5.6-13 and Supplementary Text), suggesting the observed behavior is general. This uniform linear dependence of log current on the total charge suggests the OER rate may respond directly to *pseudocapacitive* charge storage. In order to test this hypothesis, we must identify how such charge is accumulated.

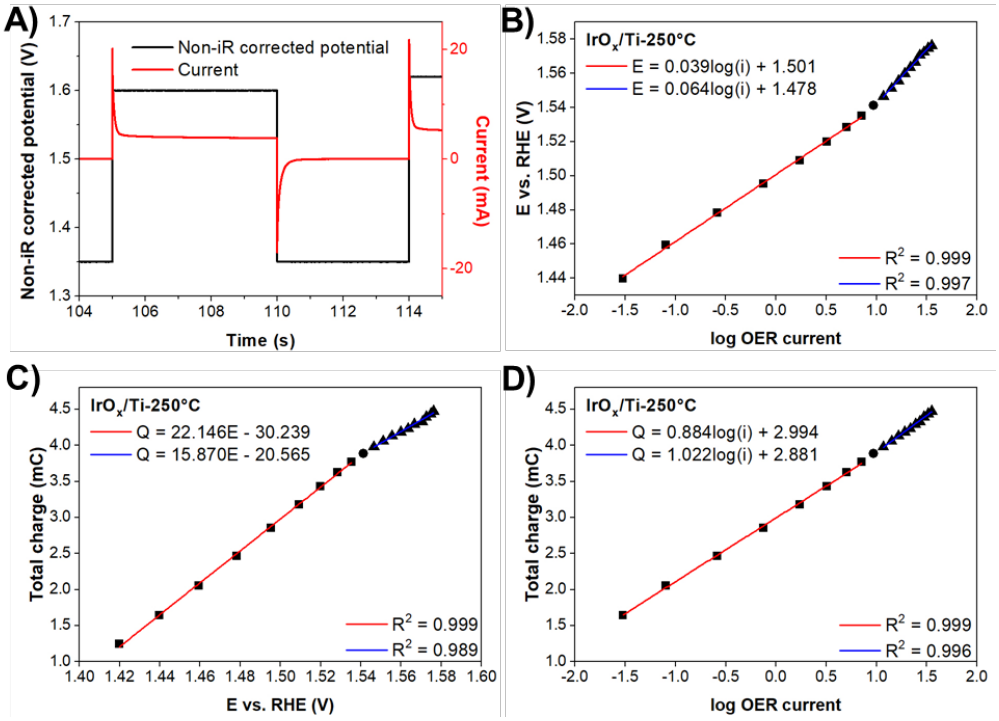

Figure 5.1: (A) A section of the pulse voltammetry protocol: cathodic potential at constant 1.35 V vs. RHE and increasing anodic potential steps (from 1.42 up to 1.80 V vs. RHE in 20 mV pro steps). The overlaid current signal shows its response to the potential steps. (B) iR corrected potential vs. log OER current (OER current in mA), or Tafel plot, derived from the pulse voltammetry measurement. (C) Total charge (integral cathodic charge) vs. iR corrected potential derived from the pulse voltammetry measurement. (D) Total charge (integral cathodic charge) vs. log OER current derived from the pulse voltammetry measurement. Sample: IrOx/Ti-250°C. For other samples see Figure 5.7-12.

5.4.2 Charge storage mechanism

To understand the mechanism of charge storage it is useful to consider cyclic voltammetry (CV). When performed under acidic conditions using Ir oxides with little or no crystallinity, such experiments suggest redox processes occur around 0.8–1.0 V and near the OER onset. These processes are assigned to Ir redox couples of Ir(III)/Ir(IV) and Ir(IV)/Ir(V), respectively.[21] All of these redox features are, however, broad and thus the capacitive behavior originating from them is rather smooth with potential (Figure 5.14b). To see how this smooth capacitive behavior is manifested in the mechanism of charge storage, we investigate the evolution of the total charge vs. potential for the amorphous IrO_x in a potential window of ~0.8-1.6 V vs. RHE, shown in Figure 5.15a. The total capacitance (~20 mF for IrO_x/Ti-250°C) is relatively independent of potential, allowing us to conclude the capacitance is similar over the range of 0.8–1.6 V vs. RHE. A similar situation has been found with other samples (see Table 5.1 and Figure 5.15b-e). When viewed with respect to the number of atoms the magnitude of these number becomes particularly apparent. For the highly-crystalline (AA-D), for instance, we can use the measured BET surface area in Table 5.3 to derive a surface hole coverage (h^+) of ~0.8 ML at ~1.6 V vs. RHE. Similarly, for amorphous Alpha Aesar IrO_x where bulk charging is expected, we find the charge in the above potential window approaches the equivalent of 8 ML, or about 1 h^+ per total Ir atom.

We can now turn to the atomic mechanism of charge storage by way of *operando* steady-state and potentiodynamic XAS at the Ir $L_{2,3}$- and O K-edges under electrocatalytic conditions, experimental details in SI.

We begin with the Ir $L_{2,3}$-edges of IrO_x/Ti-250°C. The integral intensity of the white line (IWL) of these spectra offers a measure of the number of empty 5d states on Ir, hence Ir oxidation state.[14,22] Following the IWL then allows us to observe the charge accumulated on Ir centers as a function of electrochemical bias (see Figure 5.16). Figure 5.2a shows the IWL of IrO_x/Ti-250°C as a function of bias over a broad potential range; the IWLs of reference IrO_2 and the dry catalyst are also indicated. The IrO_x/Ti-250°C oxidation state can be seen to increase linearly with bias from 0.5 V to ~1.6 V. The WL intensity at 11221.5 eV can also be seen to track the IWL in Figure 5.2a, enabling potentiodynamic XAS at this energy.

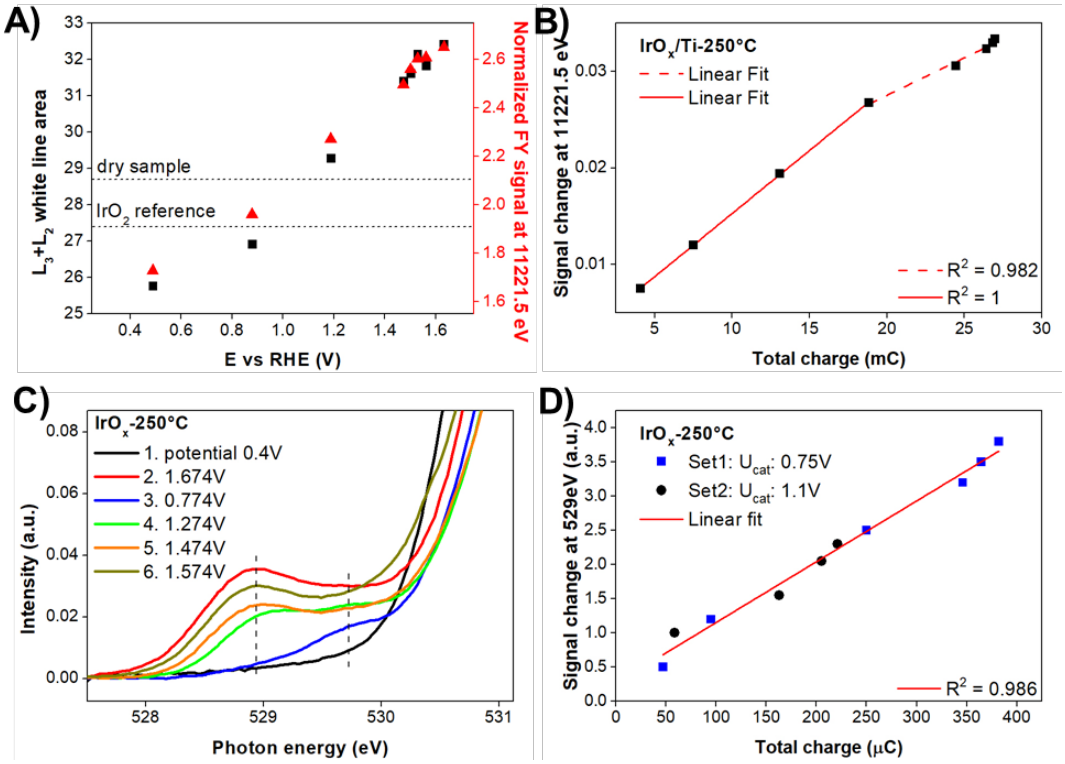

Figure 5.2: (A) The L_2 + L_3 IWL (left) and the normalized fluorescence yield signal at 11221.5 eV (right) of steady-state operando Ir L-edge XAS of IrOx/Ti-250°C at selected potentials (vs. RHE) together with the dry sample and reference IrO_2 show Ir oxidation state increases with potential, for details see Figure 5.16. (B) Correlation of the signal change of the Ir L_3-edge at 11221.5 eV vs. the total charge derived from pulse voltammetry in a broad potential window. Sample: IrOx/Ti-250°C (C) Steady-state operando O K-edge XAS of IrOx/Graphene-250°C at selected (non-iR corrected) potentials in the order indicated. Dashed lines indicate the peak position of μ_2-O (at 528.9 eV) and μ_1-OH (at ca. 529.7 eV). (D) Signal change of the resonance at 529 eV shows the correlation of O^{I-} content vs. the total charge derived from pulse voltammetry in a broad potential window demonstrating O 2p holes store oxidative charge. Sample: IrOx/Graphene-250°C; two experiments with different cathodic potentials are shown. For another sample see Figure 5.17.

To probe the dynamic response of the iridium oxidation state we performed electrochemical pulse experiments using *operando* potentiodynamic XAS (Figure 5.2b) by monitoring the WL intensity at 11221.5 eV during potential pulses up to 1.78 V vs. non-iR corrected RHE (Figure 5.16d). These results show the iridium oxidation state in IrO_x/Ti-250°C increases linearly with cathodic charge up to ~20 mC, at which point the increase is less pronounced. Above ~20 mC Ir oxidation cannot fully account for the transferred charge, and additional pseudocapacitive charge storage is activated. This finding can be explained by the observation that iridium oxides enter a negative charge transfer regime when the Ir oxidation state exceeds IV, resulting in the formation of ground state O 2p holes, or O^{I-}.[14,23]

Such O 2p holes can be measured with *operando* O K-edge XAS.[18] This measurement reproduces the aforementioned bias vs. charge trends (Figure 5.18a), though the magnitude of charge is lower due to reduced catalyst loading. The sample was measured at potentials from 0.4 to 1.674 V (non-iR corrected); the resulting steady-state *operando* O K-edge XAS are provided in Figure 5.2c. At 0.4 V no features are visible in the 528-530 eV energy range where surface O appears.[18,23] A feature at ~529 eV (the electrophilic 2-fold coordinated O, μ_2-O)[18,23] develops upon raising the potential to 1.674 V. Decreasing the potential to 0.774 V leads to the disappearance of μ_2-O, while restoring the bias to 1.274 V, and higher, repopulates the species. Besides this reversible formation of μ_2-O, a crucial piece of information is the relatively small amount of μ_1-O oxyl appearing at ~528.3 eV (Figure 5.18b)[18,23] and the presence of μ_1-OH at ~529.7 eV [18,23] under OER conditions.

The reversible and continual increase in intensity at 528-529 eV suggests O 2p holes store oxidative charges into the OER. To see the amount of charge storage we performed pulse experiments while monitoring the O K-edge intensity at 529 eV. These experiments used a potential window of 0.95–1.70 V vs. RHE (non-iR corrected) with a resting cathodic potential at 0.75 V vs. RHE. The resulting linear correlation between accumulated charge and the signal change of μ_2-O (Figure 5.2d) suggests oxidative charge is accumulated by deprotonation of surface oxygen (which is coupled to electron transfer). We find this relationship is general (Figure 5.17).

5.5 OER mechanism on Ir-based materials

Our results suggest deprotonation stores pseudocapacitive charge into the OER and that this oxidative hole coverage (Θ_{h+}) correlates with the observed catalytic rate. To understand how, we turned to DFT calculations at the PBE level using a (110) surface of rutile-type IrO_2 (see SI for details). We began by equilibrating surfaces with varying hydrogen coverage in water by way of *ab initio* molecular dynamics (MD). MD snapshots were used to compute a surface phase diagram, Figure 5.3. From this we find explicit solvent interactions introduce a coverage dependence to the adsorption energy of hydrogen (Figure 5.19). This, so-called, Frumkin behavior [7] broadens the μ_2-OH deprotonation window over a potential range of ~0.8-1.5 V and extends μ_1-OH deprotonation to ~2.0 V, Figure 5.3, in agreement with experiment.

Using the computed phase diagram to estimate the surface coverage of oxidative holes we went on to study the kinetics of the OER. We began with Θ_{h^+}=3/4 ML and a 1:1 ratio of μ_1-O:μ_1-OH, which is representative of the catalyst at ~1.5 V, Figure 5.3. The initial structure was taken from an MD snapshot, retaining two water bilayers to recover surface solvation effects.[24] Minimum energy paths for various elementary steps were then computed in two ways: i) with a fixed electrochemical bias [25,26] and ii) using a fixed number of electrons.[27] The former is the experimental condition; the latter is an artificial constraint used to probe the degree to which an elementary step is purely chemical.

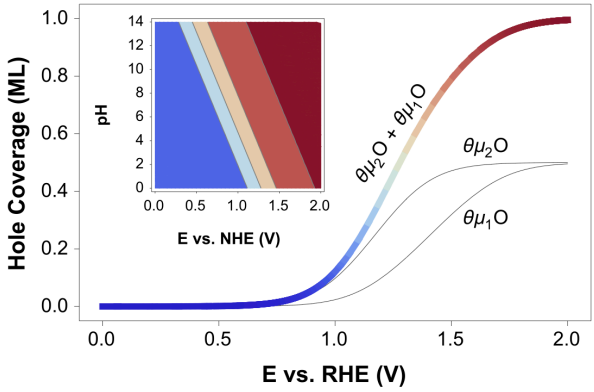

Figure 5.3: Phase diagram plotted as oxidative charge on the surface vs. applied bias (vs. RHE). A IrO_2 (110) surface was used, which fixes the ratio of μ_2:μ_1 sites at 1:1. The inset shows pH vs. V (vs. NHE) behavior for Θ_{h^+}= 0, 1/4, 1/2, 3/4, and 1 ML, where the low and high coverage regimes are shaded blue and red, respectively. See SI and Figure 5.19 and Figure 5.20 for more details.

Our choice of elementary steps was guided by a general mechanism of the OER, which, under acidic conditions can be viewed as four proton-coupled electron transfer steps in a first approximation:[27,28]

1) $* + H_2O \rightarrow OH_{ads} + H^+ + e^-$
2) $OH_{ads} \rightarrow O_{ads} + H^+ + e^-$
3) $O_{ads} + H_2O \rightarrow OOH_{ads} + H^+ + e^-$
4) $OOH_{ads} \rightarrow OO_{ads} + H^+ + e^-$,

where * denotes an empty site and all intermediates are adsorbed.

A Tafel analysis suggests the second step is rate-limiting,[10] though the third step has also been suggested to be the rds.[27,28] The remaining proton-coupled electron transfers are thought to be barrierless.[27] Thus, we focused on steps 2 and 3. Step 2 is the formation of the μ_1-O oxyl through μ_1-OH deprotonation and electron transfer, a prerequisite for O-O bond formation.[14,18,27] Step 3 is the nucleophilic attack of the μ_1-O oxyl by water to form the O-O bond. Formation of μ_1-O was not found to be rate limiting and will not be discussed further, see SI.

5.5.1 External bias and rate

To see how the activation energy for oxyl–water coupling through water nucleophilic attack is affected by the bias, E_a was computed using a fixed electrochemical potential. For simplicity, we began with the potential of zero charge (pzc) for the Θ_{h^+}=3/4 ML surface (1:0 μ_2-O: μ_2-OH and 1:1 μ_1-O:μ_1-OH)

corresponding to ~1.5 V vs. RHE, see Figure 5.3. Figure 5.4a shows O-O coupling occurs on this surface with the concerted transfer of hydrogen to a μ_2-O site. The corresponding E_a is 0.63 eV with a heat of reaction (ΔH_{rxn}) near zero; it is denoted by a green triangle in Figure 5.4b and is similar to previous observations.[27] The two additional green triangles at ΔH_{rxn}~0 eV in Figure 5.4b show that increasing the electrochemical bias by an additional 0.1 to 0.5 V to capacitively charge the surface while constraining Θ_{h+} to 3/4 ML has minimal impact on the activation energy. The effect of this capacitive charging is indicated by a solid arrow and the label Q_c in the figure.

If the average surface oxidation state is not artificially constrained when the bias is increased, the fully oxidized limit of Θ_{h+}=1 ML is reached at ~2.0 V vs. RHE, the pzc for this surface. The effect of including this oxidation is indicated by Q_T in Figure 5.4b; the corresponding arrow shows the change from the Θ_{h+}=3/4 ML to Θ_{h+}=1 ML surface. Inspection of the figure reveals that including oxidative charging reduces ΔH_{rxn} to ~-0.2 eV. Furthermore, unlike the purely capacitive charging of Θ_{h+}=3/4 ML denoted by Q_c, oxidation to Θ_{h+}=1 ML results in a corresponding drop in E_a (from ~0.60 eV to 0.23 eV). There is no change in mechanism associated with this drop in E_a.

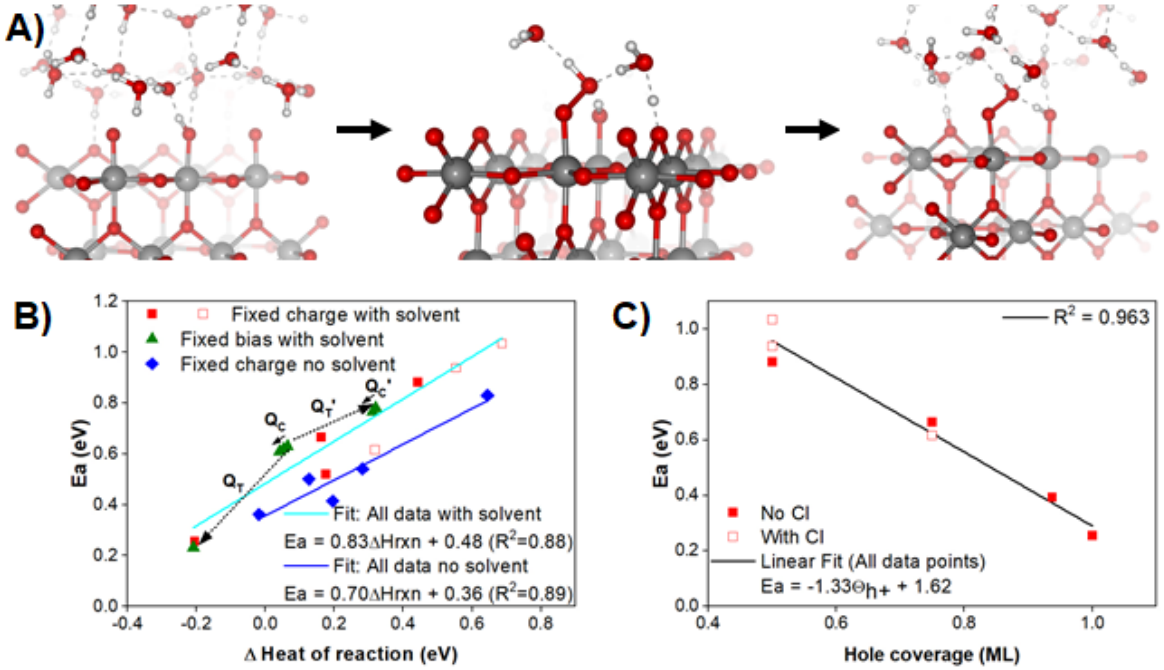

Figure 5.4: (A) Water-oxyl coupling on the (110) surface of rutile-type IrO_2 with μ_2-O and 1:1 μ_1-OH:μ_1-O. In the initial state, a water molecule near the oxyl (left panel) forms an O-O bond with the μ_1-O at the transition state (middle panel)—for clarity only the solvent directly involved are shown—with the simultaneous transfer of hydrogen to a surface μ_2-O through the formation of Zundel-like species. In the final state (right panel) the μ_1-O has been transformed into a μ_1-OOH. (B) Computed activation energies for O-O coupling plotted as a function of ΔH_{rxn}, where ΔH_{rxn} becomes more negative as Θ_{h+} increases. Green triangles show E_a computed at the pzc for surfaces with Θ_{h+}=1/2, 3/4, and 1 ML (in order of increasing exothermicity) under constant potential conditions. For Θ_{h+}=1/2 and 3/4 ML green triangles include results with purely capacitive charging from 0.1 to 0.5 V, e. g. charging the interface while artificially constraining the average surface oxidation state. This capacitive charging is donated by Q_c (Q_c') for the Θ_{h+}=3/4 (1/2) ML surface with the small arrow indicating E_a marginally drops with capacitive charging. The arrow labeled Q_T shows the effect of the corresponding total

charge for the Θ_{h+}=3/4 ML surface, while Q_T' shows the effect of reducing the surface to Θ_{h+}=1/2 ML. Red squares show E_a as a function of ΔH_{rxn} under a constant charge condition. The unfilled red squares show surfaces with adsorbed Cl. Chlorine was used to investigate charge storage using a non-reducible ligand, and a full discussion including the corresponding experiments can be found in the SI. Blue diamonds show the corresponding energies in the absence of solvent. (C) Activation energies for O-O coupling as a function of oxidative hole coverage.

Similarly, reducing the Θ_{h+}=3/4 ML surface to yield Θ_{h+}=1/2 ML (1:1 μ_2-O:μ_2-OH and 1:1 μ_1-O:μ_1-OH) increases E_a to 0.78 eV at this surface's pzc, the change is denoted by Q_T' in Figure 5.4b and corresponds to a cathodic bias of ~0.3 V. On the chemically reduced surface, E_a is nearly insensitive to an anodic bias (0.3 V) when the oxidation state is fixed, denoted by Q_C'. This effect can be seen by examining the green triangles at ΔH_{rxn}~0.3 eV in Figure 5.4b. Together these results demonstrate E_a for O-O coupling obeys the Brønsted–Evans–Polanyi relationship familiar from traditional catalysis. As a result, E_a is linearly dependent on ΔH_{rxn}, changes in which are dominated by surface oxidation rather than capacitive charge. This type of behavior is expected from classical theory, as the kinetics of inner-sphere reactions should be rather insensitive to building a double-layer.[12]

5.5.2 Oxidative charge and rate

While the previous examples suggest the activation energy of the rds is dominated by the bond formation/rupture chemistry [3] familiar in traditional catalysis, they contain the electrode potential. To see to what degree oxidative charge alone mediates the relationship between E_a and ΔH_{rxn} we performed minimum energy path calculations using a fixed number of electrons to decouple the elementary step from the electrode.

Fixing the number of electrons does not change the oxyl–water coupling mechanism or break the linear relationship between E_a and ΔH_{rxn}, red squares in Figure 5.4b. That is, $E_a = E_0 + \alpha \Delta H_{rxn}$ in the absence of electron transfer. Moreover, the Brønsted–Evans–Polanyi slope, $0 \leq \alpha \leq 1$ is insensitive to the chemical nature of the ligands introducing the oxidative charges. The open red squares in Figure 5.4b, for instance, show the same trend when spectator O(H) is replaced by Cl (see SI for a full discussion with experimental verification and Figure 5.21 for Bader charges on the active oxygen). Figure 5.4b shows the activation energy's dependence on oxidative charge is consistent with inner-sphere chemistry; removing the solvation layers results in only a small change to the Brønsted–Evans–Polanyi relationship, in line with the expectation of the minor role of the double layer on the kinetics of inner-sphere reactions. Thus, as the surface becomes more reduced E_a increases; as the surface becomes more oxidized E_a decreases. Both changes occur in a purely chemical fashion to reveal a linear Brønsted–Evans–Polanyi relationship underlying the rds.

Because ΔH_{rxn} is controlled by surface oxidation, there is a linear dependence of the log OER current on oxidative charge. This allows us to recast the Brønsted–Evans–Polanyi relationship as $E_a = \zeta \Theta_{h+} + \kappa$, where ζ weights the effectiveness of oxidative charge on E_a—the coverage of which is denoted by Θ_{h+}—and κ is the barrier in the limit of zero charge.

Using the parameters found for the (110) surface we are then in a position to compute the electrocatalytic response of IrO_2. To do so we introduce the coverage dependence to the rate constant for the electrode reaction though an Eyring-like equation:

$$\text{OER current} = F\frac{k_B T}{h}\theta_{\mu 1}\exp\left(-\frac{\zeta\theta_{h+}+\kappa}{k_B T}\right) \qquad \text{(Eq. 1)},$$

where the constants in Eq. 1 take on their usual meaning,[7] $\theta_{\mu 1}$ accounts for the oxyl coverage, and the exponential captures the charge dependence of the rate.

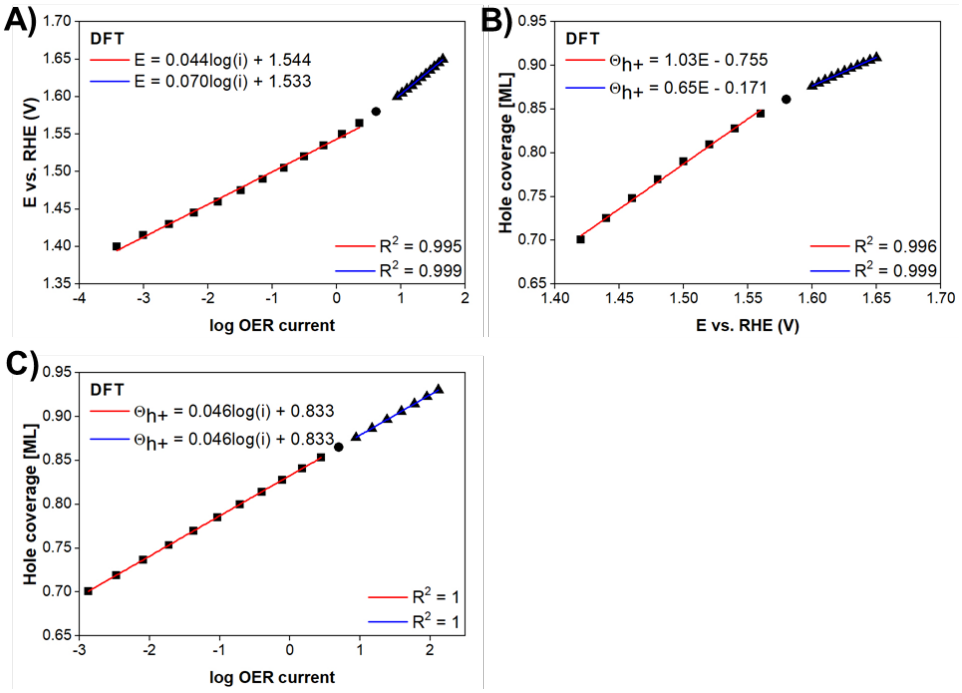

Figure 5.5: (A) Tafel plot computed with DFT data from the (110) surface of rutile-type IrO_2 using Eq. (1). (B) Computed hole coverage as a function of bias corresponding to (A). (C) Computed hole coverage vs. log OER current corresponding to (A).

The Tafel plots and charge vs. log OER current computed using Eq. (1) are in good agreement with experiment, Figure 5.5. A Tafel slope of 44 mV/dec is found up to 1.58 V, increasing to 70 mV/dec at higher bias. By way of comparison, crystalline IrO_2 calcined at 450°C has Tafel slopes of 43-47 mV/dec and 71-76 mV/dec over the same potential windows (Figure 5.7 and Figure 5.8). From the calculations the bend in the Tafel slope can now, however, be ascribed to a change in the Θ_{h+} response to bias, Figure 5.5b, rather than the qualitative change in mechanism suggested by a formal Tafel slope analysis. The log OER current is predicted to be linear in Θ_{h+}, Figure 5.5c, consistent with our experimental results.

We anticipate this linear dependence of log current on charge is common. This is because bond rupture or formation is slow compared to electron transfer and Brønsted–Evans–Polanyi behavior is expected when bond making/breaking is the principal contributor to the reaction coordinate.[3] In

support of this assertion, we find all the Ir-based catalysts show a linear relationship between log OER current and total charge, Figure 5.7-13. Moreover, NiFe layered double hydroxides in alkaline electrolyte provide the same type of dependence, Figure 5.22. While such behavior can emerge trivially on an electrode with constant capacitance, we argue it is rooted in the catalysis of the OER, as we have shown explicitly for Ir based materials.

5.5.3 Activation free energies

An important consequence of these findings is that the linear activation free energy relationships underlying electrocatalytic OER can be probed experimentally. In these cases, the rds is decoupled from the bias, resulting in a simple form for ζ and κ whereby plotting ln I(OER) against oxidative charge yields a slope of $-\zeta/k_BT$. Assuming the measured pseudocapacitive charge is entirely due to surface deprotonation, and using the BET surface areas from Table 5.3 with the integrated charge, we find $\zeta \sim$ -1.2 and -1.3 eV/ML for the AA-D and AA-450°C catalysts, respectively. These values compare favorably with the computed $\zeta \sim$ -1.3 eV/ML, Figure 5.4c. κ can be defined similarly as the activation free energy at zero oxidative charge, for which we find 1.4-1.7 eV experimentally and ~1.6 eV from DFT.

5.6 Conclusions and Outlook

We used a combination of experimental and computational techniques to show how the activation energy of the rds of the electrocatalytic OER depends on oxidative charge. Our results show the surface of the catalyst is not static under OER conditions but responds to the applied bias through changing its oxidation and protonation states. These changes affect the activation energy of the rds in a purely chemical manner to give rise to a linear activation free energy relationship familiar from traditional catalysis. We have shown these relationships can be both computed and measured to offer new means of understanding and improving electrocatalytic performance.

5.7 Supplementary Information on Methodology

5.7.1 Synthesis of $IrNi_x$ bimetallic precursor alloy nanoparticles

Synthesis of $IrNi_x$ bimetallic precursor alloy nanoparticles was performed according to previously reported polyol methods.[14,29] In brief, 0.122 g of Ni (II) acetate tetrahydrate (99.999%, Alfa Aesar), 0.156 g of 1,2-tetradecanediol (90%, Sigma Aldrich), 0.45 ml oleylamine (70%, Sigma Aldrich) and 0.45 ml oleic acid (99%, Alfa Aesar) were added to 30 ml dibenzyl ether (≥ 98%, Sigma Aldrich) in a three-neck flask. The mixture was then heated to 80 °C and maintained at this temperature for 30 minutes under stirring and nitrogen flow to remove trace water. The temperature was then increased to reaction temperature 240 °C, and 0.060 g of $Ir(CH_3COO)_3$ (≥ 48% wt. Ir, Chempur) was added to the reaction flask. After 1 hour, the reaction was allowed to cool down to room temperature.

5.7.2 Preparation of $IrNi_x$ nanoparticles on Ti and glassy carbon cylinders

Ti cylinders (10 mm diameter) were ground and polished to a mirror-like surface finish according to the protocol in Ref. 30. In brief, the cylinders were first ground with SiC paper (Buehler), followed by grinding using ultra pad with diamond suspension (9 µm, Buehler), and lastly polished using micro cloth with silica suspension (0.02 µm, Bueler). The polished Ti cylinders were treated in 23% vol. HNO_3 at 80 °C for 2 hours to remove impurities. Before use as catalyst substrates, the Ti cylinders were cleaned with ultrapure water and absolute ethanol.

3.335 mL of the $IrNi_x$ nanoparticles suspension after the synthesis was transferred into a 15 mL centrifuge tube. The nanoparticles were washed with absolute ethanol several times and collected by centrifuge at 6000 rpm for 6 minutes. After the cleaning step, the collected nanoparticles were re-dispersed in 1 mL of absolute ethanol by sonification of 10 minutes. 10 µL of the nanoparticle suspension were drop-casted on a pre-polished and cleaned Ti and glassy carbon cylinders (10 mm diameter), dried in air at room temperature. Both sample types were then annealed in 4% vol. H_2/Ar at 400 °C for 1 hour. The samples were denoted as IrNi/Ti and IrNi/GC. For quantification, 400 µL of the nanoparticle suspension were transferred in a quartz tube. The nanoparticles were dried and subsequently dissolved with a mixture of aqua regia and $NaClO_3$ (Alfa Aesar) using a microwave in order to determine the Ir content using ICP-OES. The Ir loading on the substrate cylinders was 9.7 μg_{Ir}.

5.7.3 Preparation of IrO_x films on Ti cylinders

Thin Ir precursor films were applied onto the polished cleaned Ti cylinders by spin coating (WS-650MZ-23NPP, Laurell). 40 µL of the coating solution (80 g L^{-1} Ir(III) acetate, 99.95%, Chempur in absolute ethanol) was applied on the spinning cylinder at 200 revolution per minute (rpm) ensuring full coverage. The rotation velocity was then increased to 2000 rpm with 200 revolution s^{-2} and dwelled for 45 s. The coated cylinders were annealed in a preheated muffle furnace (Carbolite) at 250 °C for 15 minutes. The samples were denoted as IrO_x/Ti-250°C. A similar spin coating procedure but using 40 g L^{-1} Ir(III) acetate solution and followed by annealing at 450 °C was applied. The obtained samples were denoted as IrO_2/Ti-450°C.

To determine the Ir loading on the cylinders, uncalcined films were dissolved in 10 mL of water and the Ir concentrations in the solutions were measured by ICP-OES. The Ir loadings in IrO_x/Ti-250°C and IrO_2/Ti-450°C samples were 64.2 μg_{Ir} and 31.1 μg_{Ir}, respectively.

5.7.4 Preparation of electrodes for IrO_x Alfa Aesar-based samples

IrO_x powder (CAS: 12030-49-8) was sourced from Alfa-Aesar (Premion™, 99.99%, metals basis). To prepare the working electrodes, 5 mg of catalyst was suspended in 3.980 mL of ultrapure water (Millipore, 18 MΩ), 1.000 mL of isopropanol and 20 µL of 5 wt% Nafion solution with horn sonication for 20 minutes to form a uniform ink. 10 µL of the ink was pipetted onto a pre-polished and cleaned glassy carbon rotating disk electrode (RDE, 5 mm diameter, Pine Instrument) and dried at 60 °C for 9 minutes in air, resulting in a thin catalyst film. The amount of catalysts on the GC electrode was 10 μg_{IrOx}.

5.7.5 Preparation of NiFe layered double hydroxide (LDH) powder

NiFe-LDH was prepared via a microwave assisted autoclave synthesis. For the preparation 1200 µL (0.6 M) $Ni(OAc)_2$*$4H_2O$ (Sigma Aldrich, 99.99 % purity) and 240 µL (0.6 M) $Fe(NO_3)_3$*$9H_2O$ (Alfa Aesar, 98 % purity) were mixed. 6 mL dimethylformamid (DMF, Carlo Erba Reagents) were added to the precursor solution and the reaction mixture was stirred for 2 h. 4 mL DMF and 8 mL ultrapure water (18.2 MΩ) were additionally added before a two-step (60 min at 120 °C and 30 min at 160 °C) microwave treatment was conducted. The resulting product was collected via centrifugation, washed with ethanol and ultrapure water followed by lyophilization.

5.7.6 Preparation of electrodes for NiFe-LDH samples

To prepare the working electrodes, 4 mg NiFe-LDH was suspended in 768 µL ultrapure water (18.2 MΩ), 200 µL i-PrOH and 32 µL Nafion (5 wt %) using horn sonication for 15 min. 10 µL of the resulting ink was pipetted on a pre-cleaned, -polished glassy carbon RDE (5 mm diameter, Pine Instruments) and dried at 55 °C for 10 min. The amount of catalyst on the GC was 40 $\mu g_{NiFe\text{-}LDH}$.

5.7.7 Electrochemical setup

Electrochemical experiments were performed in a three-compartment glass H cell with a rotating disk electrode (Pine Instrument) and a potentiostat (Biologic) at room temperature. A Pt-mesh and a Hg/Hg_2SO_4 (MMS) electrode (in saturated K_2SO_4) were used as counter electrode and reference electrode, respectively. The MMS electrode was calibrated against the reversible hydrogen electrode (RHE) before electrochemical measurements in H_2-saturated 0.05M H_2SO_4. All electrochemical measurements were carried out in N_2-saturated 0.05M H_2SO_4 and repeated on two to three electrodes for each catalyst. All potentials reported in this paper were normalized with respect to the RHE (V_{RHE}) unless stated otherwise.

5.7.8 Electrochemical protocol

The electrocatalytic OER activities of investigated catalysts were recorded by sweeping the potential from +1.0 to +1.8 V_{RHE} and back with a scan rate of 5 mV s^{-1} under electrode rotation of 1600 rpm. PEIS (Potentiostatic Electrochemical Impedance Spectroscopy) was carried out before each OER

measurement for iR correction. The Ir-mass based OER activity was evaluated taking the current normalized to the IrO_2 mass on the electrode with iR-corrected potential.

Before the OER scan, an activation step including 1 cyclic voltammetry between 1.0 and 1.8 V_{RHE} and 50 cycles between 0.05 and 1.5 V_{RHE} was applied for the IrNi samples to leach out Ni and oxidize Ir, creating a highly defective Ir(Ni)O_x catalyst.[14] For other samples, this activation step was skipped.

After the OER scan, three cyclic voltammetry (CV) between 0.4 and 1.4 V_{RHE} was performed, followed by a series of CVs between 0.93 and 1.03 V_{RHE} (for IrO_x/Ti-250°C and IrO_2/Ti-450°C) or between 1.1 and 1.2 V_{RHE} (for IrNi/Ti) with different scan rates (2, 5, 10, 25, 50, 75, 100, 125, 150, 175, 200, 250, and 300 mV s^{-1}) for the determination of outer and total charge.[31] All CVs were measured without electrode rotation whereas all other techniques were measured with a rotation velocity of 1600 revolutions per minute (rpm).

Subsequently, pulse measurements (also with 1600 rpm) were performed, in which the current was followed over time. In pulse measurements, the potential was kept at a low potential for 4 seconds, then switched to a higher potential E_h, kept at E_h potential for 5 seconds, and switched back to the low potential. The low potential is kept constant at 1.35 V_{RHE}, while the E_h was stepped upwards from 1.42 V_{RHE} to 1.8 V_{RHE} by 20 mV/step. The potential switching between 1.35 V_{RHE} and E_h was repeated until the E_h reached 1.8 V_{RHE}, then the pulse measurement was finished with the last 4 seconds at 1.35 V_{RHE}. The current was sampled at every 0.0002 (and 0.001) s for the cathodic (anodic) potential sections. The OER current was read at the end of the 5 s anodic potential segment. Another pulse voltammetry protocol applied a much broader potential window, with the cathodic low potential at 0.748 V_{RHE}, anodic steps in the potential window of 0.948-1.698 V_{RHE}, a holding time of 15 sec for each potential and a coarser current sampling at every 0.002 s. For the above experiments including the pulse measurements, a relatively high surface area counter electrode was placed in the same compartment as the working electrode to avoid the current being limited by the counter electrode. Rotation speed dependent pulse measurements were carried out using IrO_x/Ti-250°C; the results indicate the independence of both the Tafel plot (Q vs. E) and Q vs. log I to rotation speeds between 800 rpm and 2000 rpm (Figure 5.23).

The charge related to the potential step was calculated by integrating the current pulse over time taking into account that the background current signal is not necessarily zero.

Pulse experiment with NiFe-LDH was performed in the same fashion as detailed above, with the exception that the electrolyte was 0.1M KOH (Sigma-Aldrich, 99.99%) and the cathodic potential was 1.5 V_{RHE} to avoid crossing a strong catalyst redox at the OER onset with each potential step.

5.7.9 Impedance analysis

Following the above protocol, a series of potentio electrochemical impedance spectroscopy (PEIS) measurements was carried out at different electrode potentials below the OER onset, ranging from 0.4 to 1.4 V_{RHE}.

An equivalent circuit consisted of L1R1(Q2R2)(Q3R3) was used to fit the PEIS spectra, where L1, R1, R2, and R3 symbolize the inductance, the ohmic resistance of the electrolyte, the charge transfer resistance, and the catalyst film resistance, respectively.[32,33] The Q2 and Q3 are so-called Constant Phase Elements (CPE), whose impedance is described by the formula:[33]

$$Z_{CPE} = \frac{1}{B(i\omega)^{\alpha}} \quad \text{(Eq. 2)}$$

where B is a frequency independent term with units of (F $s^{\alpha-1}$), ω is the angular velocity and $i=(-1)^{1/2}$. The (Q2R2) parallel combination represents the charge transfer resistance of a faradaic process occurring at the catalyst/electrolyte interface, whereas the (Q3R3) combination represents the diffusion/adsorption of reaction intermediates[33,34]. Here the Q2 includes both the double layer capacitance and the pseudocapacitance. The corresponding effective capacitance $C_{eff,2}$ can be calculated according to the equation[32,35]

$$C_{eff,2} = Q_2^{\frac{1}{\alpha_2}}\left(\frac{1}{R_1} + \frac{1}{R_2+R_3}\right)^{\frac{\alpha_2-1}{\alpha_2}} \quad \text{(Eq. 3)}$$

The effective capacitance ($C_{eff,2}$) values at different electrode potentials and examples of experimental Nyquist plots and corresponding fits are presented in Figure 5.24.

5.7.10 Outer and total capacitance evaluation (Figure 5.25)

According to Trasatti et al.,[31,36] total charge (q^*_T) which is proportional to the whole active surface and outer charge (q^*_O), which is related to the "outer" surface of metal oxides and directly accessible to proton exchange, can be evaluated based on voltammetric charge at different scan rates.

The relationship between q^*_T and scan rate ν has been found to be:[31,36]

$$\frac{1}{q^*(\nu)} = \frac{1}{q_T^*} + k_1\nu^{1/2} \quad \text{(Eq. 4)}$$

By plotting the reciprocal of q* against the square root of the scan rate and extrapolating the linear fit toward ν = 0 mV/s, the intercept can be considered as the reciprocal of q^*_T.

The relationship between q^*_O and scan rate has been found to be:[31,36]

$$q^*(\nu) = q_O^* + k_2\nu^{-1/2} \quad \text{(Eq. 5)}$$

By plotting q* against the reciprocal of the square root of the scan rate and extrapolating the linear fit toward ν = ∞, the intercept can be considered as the q^*_O.

Instead of using voltammetric charge, whose values depend on the potential range, interfacial capacitance can be used.[32] The interfacial capacitance *(C)* can be evaluated according to the following equation:

$$C = \frac{\int_{E1}^{E2} i_a dE + \int_{E2}^{E1} |i_c| dE}{2\nu\,(E_2 - E_1)} \quad \text{(Eq. 6)}$$

Where i_a and i_c are the instantaneous anodic and cathodic current, respectively, E_1 and E_2 are the cutoff potentials in CVs.

By definition, the relationship between interfacial capacitance and the voltammetric charge is:

$$C(v) = \frac{q^*(v)}{E_2 - E_1} \quad \text{(Eq. 7)}$$

Therefore, in analogue to q^*_T and q^*_O, total capacitance C_T and outer capacitance C_O can be determined based on the following equations:

$$\frac{1}{C(v)} = \frac{1}{C_T} + k'_1 v^{1/2} \quad \text{(Eq. 8)}$$

$$C(v) = C_O^* + k'_2 v^{-1/2} \quad \text{(Eq. 9)}$$

5.7.11 Operando Ir L-edge XAS experiments

Operando X-ray absorption spectra were recorded in fluorescence mode at beamline P64 of Petra III using a Si(111) double crystal monochromator and a PIPS detector. The beamline energy was calibrated using IrO_2 reference material. The fluorescence radiation was detected through the backside of the 10µm Ti foil substrate with the sample normal oriented 45° with respect to the X-ray beam and detector. Ir L_3 and L_2 absorption spectra were recorded in one scan. 0.05M H_2SO_4 acted as electrolyte and a Pt mesh was applied as counter electrode and an Ag/AgCl (sat. KCl) reference electrode was used. Ohmic resistance was determined using the current interrupt method of the Biologic SP-200 potentiostat. The time-resolved X-ray absorption measurements were conducted with 1ms recording time at 11221.5 and 11150 eV during potential pulse experiments.

X-ray absorption spectra were background subtracted and normalized to the edge jump. The white line (WL) areas were determined following [22] in which numerical integration was applied after subtracting an arctangent function centered at the white line maximum with unit height and a width of 2 eV until the arctangent function crosses the spectrum and the differences turns negative. This approach benefits from being independent of the line shape or fit function. For details see also Figure 5.16c.

In a direct analogy to the electrochemical pulse experiments, we followed the charging dynamics using operando potentiodynamic XAS by first noting that the integral Ir L_3+L_2 white line intensity scales with the X-ray absorption of the L_3-edge at 11221.5 eV. As such, tracking the intensity at this energy with potentiodynamic XAS offers a means of (qualitatively) following Ir oxidation state. To do so, we monitored the fluorescence signal at 11221.5 eV (and the background signal below the Ir L_3-edge) during potential pulses between 0.84 V and up to 1.54 V (Figure 5.16). Around this X-ray energy (at the high photon energy side of the white line), the difference in fluorescence signal between charged and uncharged state is maximal under steady-state conditions. Furthermore, we verified that the fluorescence signal was equilibrated, completely assuring that charge transfer is not kinetically limited at the necessarily higher catalysts loadings by applying 15 s potential pulses.

5.7.12 Operando O K-edge XAS : Sample preparation

Nafion membranes in size of 11 mm disks (Nafion N117, The Chemours Company) were utilized as a proton exchange membrane supporting various Ir-based electrocatalysts. Graphenea (San Sebastian, Spain) supplied single layer graphene on copper. Pieces cut typically in size of 6x6 mm were placed on an etching solution with 10 g of $(NH_4)_2SO_4$ (Merck, Darmstadt, Germany) in 250mL MilliQ water for 12 hours. The swimming graphene sheets were then transferred onto the Nafion membrane by hand.

Nafion membranes used for IrNi deposition were sputtered with ca. 1.4 nm carbon. IrNi nanoparticles were deposited by electrophoretic deposition: 8 µL of the corresponding NP suspension was pipetted onto the membrane. 2V of potential was applied to the membrane (as working electrode) for 75 minutes. Afterwards, the membranes were shortly rinsed with absolute ethanol to remove excess NP suspension and washed further with water. Graphene sheets after Cu etching were transferred onto the thus prepared membranes.

IrO_x thin film on graphene/Cu was prepared by spin coating and calcination. 60 µL precursor solution of 5 gL^{-1} Ir (III) acetate was pipetted to the graphene/Cu foil (size ~ 12x12 mm) substrate at 200 rpm. The rotation velocity was then increased to 6000 rpm with 200 revolution s^{-2} and dwelled at this velocity for 45 s. The samples were annealed at 250 °C in air for 15 minutes. The thus prepared IrO_x/graphene/Cu foil was cut to ~ 6x6 mm in size and underwent similar 12 h Cu etching in $(NH_4)_2SO_4$ solution. Then, the swimming IrO_x/graphene sheets were transferred onto the Nafion membrane by hand.

5.7.13 Operando O K-edge XAS: Setup and spectroscopy

Operando O K-edge measurements presented were performed at the ISISS beamline (BESSY II) with the attached NAP-XPS end station and a module dedicated to electrochemistry. The in situ cell design is described in.[23] The equilibrium pressure in the chamber was a balance between the evaporation from the in-situ cell and the pumping speed via the 1 mm nozzle to the analyzer of the NAP-XPS endstation and ranged from 5.0×10^{-2} mbar to 1.5×10^{-1} mbar. For the pulse experiments, extra water vapor was dosed into the chamber to keep the water pressure constant at 2.5×10^{-1} mbar. This constant pressure condition was used to facilitate constant absorption signal over time. Operando O K-edge absorption spectra were recorded via two channels, the total (TEY) and partial electron yield (PEY). The first uses a bias voltage of 90 V on the nozzle against the analyzer and working electrode to collect as many electrons from the sample as possible. This signal was utilized to record high quality steady state O K-edge spectra (step size 0.05 eV and dwell time 0.2 s). The photon energy axis of the spectra was aligned by setting the 3p-Rydberg state of gas phase water to the reference value of 537.2 eV. O K-edge spectra of the samples after removing the dominating gas phased signal were normalized to the maximum intensity at ~538 eV. As for the partial Auger electron yield channel, electrons only with a kinetic energy of 385 eV were selected; the pass energy was 100 eV. This choice efficiently eliminates contributions from oxygen-containing species in the gas phase, removes any source of ambiguity as for background signals contributing in the pulse measurements, with the penalty of low quality and noisy signal. For the pulse experiments, the excitation energy of 529 eV was selected and

the PEY signal was followed over time while a pulse voltammetry protocol (cathodic low potential at 0.75 (or 1.1) V_{RHE}, anodic steps in the potential window of 0.95-1.7 V_{RHE}, and a holding time of 15 sec for each potential) was applied.

World Precision Instruments (Sarasota, USA) provided the Ag/AgCl reference electrodes of the type DRIREF-2SH, which was stored in saturated KCl solution, and a platinum wire was used as a counter electrode. The membrane was pressed onto the cell body with a boron-doped diamond lid. 0.05M sulfuric acid was used as electrolyte with a flow of 0.5 mL per minute maintaining a constant supply of electrolyte to the rear of the membrane during all experiments.

The counter, reference, and working electrode were connected to the SP-300 potentiostat (Biologic, Seyssinet-Pariset, France). The working electrode was grounded to the electron analyzer of the end station. The channels of the potentiostat were operated in floating mode. The Ag/AgCl reference electrode was calibrated against the reversible hydrogen electrode (RHE) after the electrochemical measurements in H_2-saturated 0.05M H_2SO_4.

Since both the Nafion membrane as well as the Ir-electrocatalysts are beam sensitive, caution was exercised to record every steady state O K-edge spectrum on a previously non-beam-exposed sample spot. As for the *operando* pulse voltammetry experiments, acquisition of the PEY signal requires 3 minutes (6 anodic and accordingly 6 cathodic voltage pulses, with holding time of 15 sec for each potential).

5.7.14 Halogen treatment

The halogen-based treatments conducted on Alfa-Aesar iridium oxide samples, which are summarized in Table 5.3, were performed at ambient pressure in a continuous-flow fixed-bed reactor setup described elsewhere.[37] Briefly, the gases: HCl (Air Liquide, purity 2.8, anhydrous), O_2 (PanGas, purity 5.0), Cl_2 (Pan Gas, purity 2.8), and He (PanGas, purity 5.0; carrier gas) were fed using digital mass-flow controllers (Bronkhorst®) to the mixing unit equipped with a pressure indicator. A quartz reactor (internal diameter, d_i = 8 mm) was loaded with the sample (weight, W_{samp} = 0.25 g), and placed in a homemade electrical oven. Prior to testing, the bed was heated in a He flow to the desired temperature (T = 298-723 K) and allowed to stabilize for at least 30 min before the gaseous mixture was fed at the desired space velocity (F_T:W_{samp} = 40 L STP h^{-1} g_{samp}^{-1}) and feed composition (Table 5.3). All treatments were conducted with a holding time ( ) of 1.5 h, unless specified otherwise. Prior to any chlorination treatment, excluding the Deacon one, all iridium oxide samples were pre-calcined in static air at 723 K for 1 h and with a heating ramp of 5 K min^{-1}. After the treatments, the reactor was quenched to room temperature in He flow and the sample was retrieved for *ex situ* characterization and for OER assessment.

Quantification of Cl_2 at the reactor outlet after the Deacon reaction (HCl + O_2) was performed by its absorption in an impinging bottle filled with 0.1 M KI solution ($Cl_2 + 3I^- \rightarrow I_3^- + 2Cl^-$) followed by

iodometric titration (Mettler Toledo G20 Compact Titrator) of the formed triiodide ($I_3^- + 2S_2O_3^{2-} \rightarrow 3I^- + S_4O_6^{2-}$) with 0.01 M sodium thiosulfate solution (Aldrich, 99.99%). The activity data collected during the Deacon treatment are summarized in Table 5.5.

5.7.15 Additional characterization of halogen-treated samples

The surface area of the catalysts was determined using a volumetric physisorption apparatus (Autosorb-6-B, Quantachrome). The catalysts were treated in a dynamic vacuum at 423 K for 2.4 h prior to adsorption of Kr at 77 K. The specific surface area was calculated according to the BET method in the pressure range p/p0 = 0.05–0.3 using 11 data points.

X-ray diffraction (XRD) measurements were performed in Bragg–Brentano geometry on a Bruker AXS D8 Advance II theta/theta diffractometer, using Ni filtered Cu Kα radiation and a position sensitive LynxEye silicon strip detector and on a STOE STADI P transmission diffractometer equipped with a primary focusing germanium monochromator (Cu Kalpha_1 radiation) and DECTRIS MYTHEN 1K position sensitive solid-state detector.

Samples related to the chlorination series were analyzed by X-ray photoelectron spectroscopy. In particular, the Cl 2p region and the Cl/Ir ratio was examined. To afford high resolution and surface sensitive Cl 2p spectra, the powder samples (after pressing them into pellets) were analyzed by synchrotron XPS using the BElChem beamline of BESSY II. Photon energy to excite Ir 4f and Cl 2p core levels was 415 eV. Quantification for all samples was based on theoretical cross sections with asymmetry parameter correction from Yeh and Lindau,[38] but it was assumed that the difference in the inelastic mean free path and the transmission function of the spectrometer for the different photoelectrons (~352 eV for Ir 4f and ~215 eV for Cl 2p) approximately cancel out each other. Nevertheless, any error should necessarily be systematic, and thus the ordering of the samples with respect to the chlorination degree should not be affected.

An electrode sample, based on catalysts films (AA-D) on GC disks prior and after OER tests was analyzed by laboratory XPS (with a non-monochromatized Al Kα (1486.6 eV) excitation and a hemispherical analyzer (Phoibos 150, SPECS)) to understand whether or not the chlorination degree of the sample changes upon the harsh OER conditions. Although the resolution of laboratory XPS is significantly worse than in the synchrotron experiment, the shape of the Cl 2p spectrum remained approximately the same and only a mild 10% loss of the Cl2p/Ir4f area ratio was observed.

5.7.16 Computational details

Spin polarized density functional theory calculations were performed with the Quantum ESPRESSO package version 6.4.1 using the PBE exchange and correlation potential.[39] Pseudopotentials were taken from the standard solid-state pseudopotentials database version 1.1.[40] For all calculations a kinetic energy (charge density) cutoff of 60 Ry (540 Ry) was employed. For surface phase diagrams we used symmetric 4 layer (1×2) (110) rutile-type IrO_2 slabs separated by 18 water molecules and considered five distinct surface terminations: i) μ_2-OH/μ_2-OH and μ_1-OH/μ_1-OH; ii) μ_2-O/μ_2-OH and μ_1-OH/μ_1-OH; iii) μ_2-O/μ_2-O and μ_1-OH/μ_1-OH; iv) μ_2-O/μ_2-O and μ_1-O/μ_1-OH; v) μ_2-O/μ_2-O and μ_1-O/μ_1-O,

see Figure 5.20. Each surface was allowed to equilibrate with the solvent for ca. 4 ps using a 1 fs timestep at 350 K; the elevated temperature was used due to the well-known over structuring of water induced by PBE. A Berendsen thermostat was used to control the ionic temperature with dt/τ of 1/50. A 2×2 **k**-point mesh was used with Marzari-Vanderbilt cold smearing using a smearing parameter of 0.02 Ry.[41] Surface phase diagrams were generated using the computational hydrogen electrode [42] by taking random snapshots from the last ps of the MD simulations. A total of 8-32 MD snapshots were used for each coverage, where the number of snapshots was chosen to ensure energy convergence to better than 0.1 eV. Zero-point energy corrections were considered for μ_1-OH and μ_2-OH and were taken from separate calculations on the surfaces relaxed in vacuum. Snapshot energies were computed with a 4×4 **k**-point mesh. This snapshot approach allows a reduction in the error associated with the slowly converging energy of the water.[43] Following Ref. 44 we can remove the bulk water contribution to the interface energy as follows:

$$\left\langle E_{\text{int}} \right\rangle = \frac{1}{N}\left(\sum_{i=1}^{N} E_{tot} - \sum_{i=1}^{N} E_{H_2O} - \sum_{i=1}^{N} E_{surf} \right) \quad \text{(Eq.10)}$$

where N is the number of snapshots, E_{tot} is the total energy of the solvated surface, E_{H2O}, is the total energy of the water alone, and E_{surf} is the total energy of the surface. The average interface energy $\left\langle E_{\text{int}} \right\rangle$ then corresponds to the average solvated surface energy without the bulk water contribution. The phase diagram shown in Figure 5.3 was generated by interpolating between the computed hydrogen coverages using a quadratic function to capture the Frumkin behavior, see Figure 5.19. That is, the adsorption energy of hydrogen was allowed to vary with coverage.

Minimum energy paths were computed by starting with an MD snapshot of the μ_2-O/μ_2-O and μ_1-O/μ_1-OH, but retaining only 2 water bilayers on one surface and introducing ca. 15 Å of vacuum to separate periodic images. The μ_1-OH was then removed from the non-solvated side of the slab and the coordinates of the bottom two layers were fixed to their bulk values. Fixed charge calculations were computed with zero net charge in the simulation cell. Fixed bias calculations were performed using the effective screening medium method.[25,26] Transition states were identified by the climbing image nudged elastic band method by first allowing the initial states to relax to their 0 K structures. This process was repeated for all surface terminations using a 4×4 **k**-point mesh with Marzari-Vanderbilt cold smearing and a smearing parameter of 0.02 Ry. The paths were considered converged when the force on each image was below 0.05 eV/Å. Constant bias simulations were performed at a surface's potential of zero charge and from 0.1 V to 0.5 V anodic of this potential, depending on the surface. Constant bias simulations were performed for the following surface terminations: μ_2-OH/μ_2-O and μ_1-O/μ_1-OH; μ_2-O/μ_2-O and μ_1-O/μ_1-OH; μ_2-O/μ_2-O and μ_1-O/μ_1-O. In addition to these surfaces, constant charge simulations were performed for: μ_2-Cl/μ_2-O and μ_1-O/μ_1-OH; μ_2-Cl/μ_2-O and μ_1-O/μ_1-O; μ_2-Cl/μ_2-O and μ_1-Cl/μ_1-O; μ_2-OH/μ_2-O and μ_1-O/μ_1-Cl to investigate alternative ligands for charge storage. Solvent free calculations were also performed for the μ_2-OH/μ_2-O and μ_1-O/μ_1-OH; μ_2-O/μ_2-O and μ_1-O/μ_1-OH; μ_2-O/μ_2-O and μ_1-O/μ_1-O; μ_2-Cl/μ_2-O and μ_1-O/μ_1-OH; μ_2-Cl/μ_2-O and μ_1-O/μ_1-O. A 4 layer

(2×4) cell was also used to simulate surfaces with 2/8 μ_1-OH coverage under the solvated constant charge condition using a 2×2 **k**-point mesh.

5.8 Supplementary Text

5.8.1 Details of charge integration

The charge integration scheme applied in the main text was developed to deal with the complication that the anodic current is a convolution of capacitive charge, catalyst oxidation and OER currents. To do so we note the cathodic current pulse can be related to the number of electrons injected into the oxidized catalyst to reduce it back to its state before the OER. Below the OER onset, the cathodic charge equals the anodic charge (Table 5.4and Figure 5.6b), and the line shape of the current decay is essentially identical for both oxidation and reduction. We assume that charge conservation also holds once the OER sets in; thus, the integrals of the cathodic current pulses can be used to probe the amount of oxidative charge that was stored in the electrocatalyst at the applied anodic potential. That is, the anodic catalyst charge equals the inverse cathodic charge and the difference of the anodic and cathodic charge is the OER charge. The perfect correlation of OER current and thus derived OER charge, with a slope of 5 (i.e. 5 seconds time on OER in the anodic voltage steps) demonstrates the validity of our assumption of charge conservation (Figure 5.6c).

5.8.2 Analysis of the transient current response to voltage pulses

In addition to the steady state data shown in Figure 5.1, we analyzed the transient current response to the voltage steps using the Dupont and Donne model,[45] see Figure 5.6-14. As described below, this approach offers a largely semantic distinction between what is termed *double layer* (C_{dl}) and *diffusion limited pseudocapacitance* (C_{diff}). Some caution is, however, needed with this distinction. It arises from the shape of the temporal decay profile. C_{dl} is defined to account for the exponential current decay, while C_{diff} accounts for the slow power-law decay portion of the current profile. We stress that such a distinction is largely semantic, but we retain it to make connections with existing literature more transparent. In the following we use C_{dl}-type and C_{diff}-type to distinguish temporal profiles.

In summary, we find the catalyst's total pseudocapacitance is one to two orders of magnitude larger than the double layer capacitance of conductive planar electrodes. The time-dependence of the charging/discharging current of the Ir oxide materials upon voltage steps is, however, still of C_{dl}-type. The cathodic C_{dl}-type pseudocapacitive charge (pseudocapacitance times potential step) extracted from the fit (Figure 5.2f) follows the total charge profiles as a function of potential (Figure 5.2b). At potentials where significant OER rates are observed, the capacitance values for the anodic current profiles are lower than the capacitance from the cathodic potential steps. As probed in the potential-step transients, the difference of the cathodic and anodic pseudocapacitive charge of C_{dl}-type as a function of the log OER current again shows a linear dependence (Figure 5.7g) when the lifetime of the charge is small and the OER rate is high. Further details of this analysis are given below.

Dupont and Donne [45] analyzed the (pseudo)capacitive behavior of common electrochemical capacitors using step potential electrochemical spectroscopy, which is similar to the pulse voltammetry technique applied here. The decaying current profile can be fit to known theoretical current-time profiles related to different types of charge storage mechanism. The current profile for a double layer capacitor in series with a resistor upon the application of a potential step can be described by:

$$\mathbf{i_{dl}} = \frac{\mathbf{E}}{\mathbf{R_s}} \exp\left(-\frac{\mathbf{t}}{\mathbf{R_s C_{dl}}}\right) \quad \text{(Eq.11)}$$

where the $\mathbf{R_s}$ is the series resistance (Ω) related to the resistance of the electrolyte, the electrode and the materials in the cell, $\mathbf{C_{dl}}$ is the double layer capacitance *(F)* of C_{dl}-type, and $\mathbf{t}$ is the time (s) after the potential ($\mathbf{E}$, in V) step.

Double layer charging, however, may not be the only charge storage mechanism. Slower, diffusion limited processes can also occur. In their simplest form these processes are described by the Cottrell equation for semi-infinite planar diffusion:[7]

$$\mathbf{i_d} = \frac{\mathbf{Constant}}{\sqrt{t}} \quad \text{(Eq. 12)}$$

giving rise to C_{diff}-type diffusion limited pseudocapacitance. In general, pseudocapacitive redox charge storage is often associated with such a diffusion limited process. However, we show that the main part of charge storage of the Ir materials is of C_{dl}-type.

To help demonstrate the above finding, Figure 5.6d shows the first 0.1s of the intensity normalized temporal current profile of five Ir samples upon a cathodic voltage pulse from 1.42 V to 1.35 V vs. RHE. The time constant of the current response varies essentially two orders of magnitude; the current of the commercial Alfa-Aesar IrO_x sample after treatment in the Deacon reaction ($4HCl + O_2 \rightleftharpoons 2Cl_2 + 2H_2O$) is roughly two orders of magnitude faster to decay than that of an amorphous IrO_x prepared by low-T (250°C) calcination. Due to the faster exponential dependence of C_{dl}-type charge storage (as opposed to the inverse square root dependence for C_{diff}-type charge storage), most of the difference in the initial time dependence translates to differences in the C_{dl}-type capacitance of the samples. Table 5.1 and Table 5.2 compile the capacitance values of a number of samples based on different evaluation methods, including integration of the current profile (total capacitance), fit of the temporal profile to extract C_{dl}-type capacitance, scan rate variation of cyclic voltammetry (total capacitance and outer capacitance) and impedance spectroscopy (double layer capacitance). As the values in the table indicate, every method finds the same ordering of the sample capacitance. Furthermore, though the capacitance values vary, there is reasonable agreement between the total capacitance values based on charge integration and scan rate variation. Outer and C_{dl}-type capacitance values are, as a rule, lower than total capacitance. It is clear that C_{dl}-type charging is the dominant contribution to the total charge. We note here that the double layer capacitance of conducting planar electrodes is typically a

few tens of μF/cm^2, one to two orders of magnitude lower than the capacitance values of the iridium samples (with known BET surface areas) observed in this work. Therefore, we probe *pseudocapacitance*.

In our simple fit model to describe the voltage steps, we used the C_{dl}-type and C_{diff}-type types of current terms (Eq. 11 and 12 with an additional constant, time independent term, due to the fact that the current normally does not decay exactly to zero). Figure 5.6f depicts a fit example and shows the quality of the fit with the standard deviation, suggesting that the quality of the fit is good enough to extract trends as a function of potential. The series resistance in our electrochemical cell (evaluated by impedance spectroscopy at various potentials) is normally in the range of 10-15 Ω (±5 Ω) which was reproduced by the fit reasonably well, within a few Ohms accuracy. Our focus is however on the evolution of the C_{dl}-type capacitance, which, for IrO_x/Ti-250°C, is shown in Figure 5.13e; the results of the other samples are compiled in Figure 5.7-12. The cathodic C_{dl}-type capacitance extracted from the cathodic current profiles is a weak function of the potential, changing between 16 and 19 mF up to ~1.53 V, above which it is slowly decreasing to 17.2 mF. These numbers are a few (1-3) mF lower than the estimates for the total capacitance based on the linear fits in Figure 5.13b. Now when the capacitance values are multiplied by the voltage step size (or $\mathbf{i_{dl}}$ is integrated over time), we get the C_{dl}-type charge as plotted in Figure 5.13f. The profile of cathodic C_{dl}-type charge (based on fitting the decaying current profile) follows the integral total charge profile very well; the only difference is that the C_{dl}-type charge is ~90% of the total charge. Since the C_{dl}-type contribution to the total charge is practically independent of the potential (Figure 5.14a), the C_{dl}-type charge also perfectly correlates with the log OER current (cf. Figure 5.13d). Therefore, a tempting explanation for the correlation of log OER current and total charge would be through the C_{dl}-type charge. To show that this is not the case, we consider the case of amorphous Alfa-Aesar IrO_x sample (Figure 5.11). Here the C_{dl}-type charge bends down at high potentials because charge storage in the bulk of the nanoparticles in form of bulk (C_{diff}-type) redox will trigger apparent loss of the C_{dl}-type capacitance and thus deviation from the observed linear dependence of the log OER current and C_{dl}-type charge. Bulk redox necessarily involves O uptake and release, which is in line with the observed participation of lattice O in the product O_2 when amorphous IrO_x are used as OER catalyst.[46]

Although fitting the anodic current profiles results in higher uncertainties due to overlap with OER—and especially due to potentially changing OER reaction rates over the course of the 5 s sampling time—we could nevertheless successfully extract $\mathbf{C_{dl}}$ from the anodic potential steps. The starting C_{dl}-type capacitance (as expected from Figure 5.6b is very similar to that of $\mathbf{C_{dl}}$ for the cathodic potential steps, but at some intermediate potentials the two curves start to deviate. Above 1.51 V the anodic $\mathbf{C_{dl}}$ decreases rapidly with potential. This is due to the much faster current decay in the anodic, as compared to the cathodic, voltage step when high anodic potentials are applied (Figure 5.6e). Consequently, the anodic C_{dl}-type charge (Figure 5.13f) drops significantly above 1.51 V. Although this observation may sound counterintuitive, the strong decrease of the anodic $\mathbf{C_{dl}}$ and anodic C_{dl}-type charge can be understood if we consider in detail what processes and states are probed in the anodic/cathodic voltage steps. In the cathodic step we probe the average resting state of the OER

reaction going back to the „frozen", unreactive state below OER. In the anodic step—when fast OER occurs, in the early part of the decay curve, which is sampled in $\mathbf{C_{dl}}$—a synchronized source and sink is triggered: oxidation via the potential and reduction via some OER elementary steps and oxygen evolution itself. Thus, on average, a lower apparent capacitance should be observed. At low OER potentials, when the lifetime of the charge (defined formally by dividing the total charge with the OER current; Figure 5.6g is high enough (much larger than the time constant of the decay curve), the effect will be very small. Therefore, the anodic and cathodic capacitance lines stay very close to each other, and here we probe probably only some early elementary steps of the reaction. Once, however, the reaction gets fast—thus the lifetime of the charge is low (on the order of the time constant of the current response)—the reduction of the capacitance will be large. The difference of the cathodic and anodic C_{dl}-type charge as probed in this synchronized short time transient as a function of the log OER current (Figure 5.13g) again shows a linear dependence once the lifetime of the charge is short and the OER rate is high. Thus, both the steady state data (Figure 5.6d) and transient results (Figure 5.13g) suggest that the log OER rate is a linear function of the oxidative charge accumulated on the catalyst.

5.8.3 Computational details: μ_1-OH deprotonation

On the μ_2-O/μ_2-O and μ_1-O/μ_1-OH surface the activation energy for μ_1-OH deprotonation with a constant charge is ca. 0.4 eV compared to the 0.67 eV for O-O coupling. Using a constant bias at the pzc leads to a reduction in both barriers to 0.3 eV and 0.63 eV, respectively. Thus, O-O formation appears to have higher activation energy than oxyl formation.

5.8.4 Computational details: Adsorbate interactions

The interactions between adsorbed hydrogen were explored in vacuum using both a (2×4) and (1×2) cell in an effort to test if Frumkin dehydrogenation behavior is induced by the solvent or adatom interactions. Figure 5.19 demonstrates there is no appreciable interaction between the hydrogen atoms adsorbed on different sites in vacuum, as the adsorption energy per hydrogen is independent of coverage. This implies Langmuir desorption behavior would be found in the absence of solvent. The quadratic behavior of the solvated hydrogen adsorption energy seen in Figure 5.19 shows that Frumkin behavior is present for the solvated surface. That is, the adsorption energy of hydrogen is coverage dependent. Thus, the chemical potential of adsorbed hydrogen, $\mu_{ads} = \partial E_{ads} / \partial \theta$, depends on coverage with a Frumkin parameter of ~1. This surface/solvent interaction then gives rise to the Frumkin deprotonation behavior, as seen in the computed phase diagram, Figure 5.20. This finding is in general agreement with our experimental observations.

5.8.5 Computational details: Surface chlorination

We used *ab initio* atomistic thermodynamics to explore the competition between O and Cl binding on rutile-type IrO_2, assuming Cl_2 and O_2 gas-phase sources. We found Cl tends to bind more strongly than O on the μ_1 site, see Figure 5.26. At any non-zero Cl_2 pressure μ_1-Cl is favored over μ_1-O at low temperatures. Conversely, bridging μ_2-O tends to be favored over bridging μ_2-Cl except in the case of relatively high Cl chemical potential. These results suggest pure μ_2 chlorination is unlikely to be achieved, though the μ_2 to μ_1 ratio can be controlled to a degree.

5.8.6 Computational details: OER current

At a sufficiently high overpotential the OER current can be described by its forward rate alone. As shown in the main text, this rate can be described by a Tafel-like equation by noting the rate constant for the electrode depends on the amount of charge stored in the material. In the case of a crystalline material like those investigate computationally this dependence is simply a dependence on surface coverage. The resulting Eq. 1 describes the general situation where a linear energy relationship mediates chemical bond making/breaking. Figure 5.5 was under the assumption of 1 cm^2 surface area of Ir with the hole coverage dependence on potential taken from the computed phase diagram (Figure 5.3). The parameters ζ and κ were taken from a fit of E_a to O(H) covered (110) surface like in Figure 5.4c, though the activation energy with Cl was excluded from this fit as we compare to a Cl free sample. The resulting equation E_a / eV = 1.23 Θ_{h+} + 1.53 was used to generate the Tafel plot in Figure 5.5.

5.8.7 Computational details: Effect of Halogen Treatment on OER

In the main text we showed the number of stored charges dominate the linear energy relationship mediating catalysis on crystalline iridium oxides by comparing DFT calculations on pure oxyhydroxide surfaces with those where O(H) was replaced by Cl. This choice was made as Cl is a non-reducible ligand that will only store one oxidative charge over the entire potential window of the OER [47] and thereby offers a means of further testing the importance of charge transfer. To verify this mechanism, we turned to experiment to irreversibly block surface sites with Cl.

Our DFT studies suggest that chlorine can displace both μ_1-O and μ_2-O on rutile-type IrO_2 (Figure 5.26). Thus, we decided to treat an amorphous IrO_x powder in the Deacon reaction [47] and compared its OER activity before and after Deacon treatment. While the sample underwent massive deactivation upon the Deacon treatment (sample AA-D in Figure 5.14d), the reasons are not clear. Comparison of an electrode sample of AA-D before and after OER by laboratory XPS shows that most of the Cl2p intensity is conserved after OER, but detailed characterizations also indicate the Deacon treatment leads to crystallization (Figure 5.14c) and subsequent loss of BET surface area (36.46 to 22.84 m^2g^{-1}) in addition to surface chlorination (Figure 5.27a).

We then sought to disentangle the effects of surface chlorination from changes in surface area. To do so, the amorphous IrO_x sample was first calcined in 1 bar air at 450°C, the highest temperature of the Deacon treatment. This calcination gave rise to crystallization (Figure 5.14c) and a reduction of the BET surface area (to 22.4 m^2g^{-1}). This loss in surface area led to a reduction of the OER activity (Figure 5.14d), but the sample (AA-450°C) was still significantly more active than the Deacon treated sample. Thus, we concluded the most important reason for deactivation of the Deacon treated sample was surface chlorination.

The significant degree of surface chlorination from the Deacon treatment makes it challenging to link the activity loss to charge storage, as the active sites may also be blocked. In the hope of finding a correlation between the degree of surface chlorination and the OER activity, we treated the pre-calcined (AA-450°C) sample under various chlorination conditions (in RT Cl_2, in HCl at 270°C, and the HCl-270°C sample was also post-treated in O_2 at 300°C). These samples show varying degrees of

deactivation (Figure 5.14d) and surface chlorination (Table 5.6). We concluded that increasing chlorination leads to continuous deactivation through site blocking and a reduction in oxidative charge storage, in agreement with our DFT results shown in Figure 5.4.

5.9 Supplementary Figures and Tables

Starting on next page...

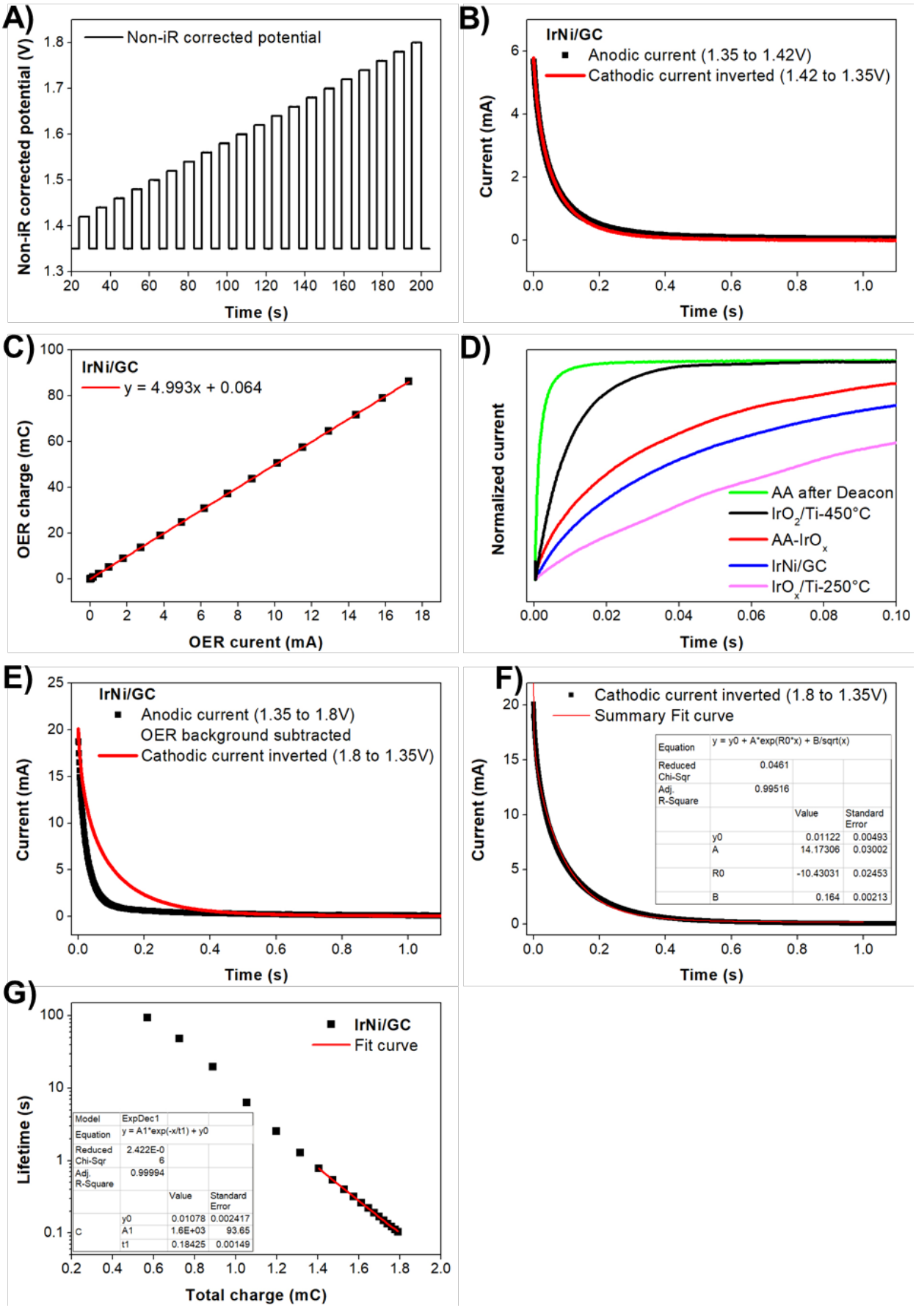
A)
Non-iR corrected potential
Non-iR corrected potential (V)
Time (s)
B)
IrNi/GC
Anodic current (1.35 to 1.42V)
Cathodic current inverted (1.42 to 1.35V)
Current (mA)
Time (s)
C)
IrNi/GC
y = 4.993x + 0.064
OER charge (mC)
OER curent (mA)
D)
Normalized current
AA after Deacon
IrO2/Ti-450°C
AA-IrOx
IrNi/GC
IrOx/Ti-250°C
Time (s)
E)
IrNi/GC
Anodic current (1.35 to 1.8V)
OER background subtracted
Cathodic current inverted (1.8 to 1.35V)
Current (mA)
Time (s)
F)
Cathodic current inverted (1.8 to 1.35V)
Summary Fit curve
Equation y = y0 + A*exp(R0*x) + B/sqrt(x)
Reduced Chi-Sqr 0.0461
Adj. R-Square 0.99516
Value Standard Error
y0 0.01122 0.00493
A 14.17306 0.03002
R0 -10.43031 0.02453
B 0.164 0.00213
Current (mA)
Time (s)
G)
IrNi/GC
Fit curve
Model ExpDec1
Equation y = A1*exp(-x/t1) + y0
Reduced Chi-Sqr 2.422E-06
Adj. R-Square 0.99994
Value Standard Error
C y0 0.01078 0.002417
A1 1.6E+03 93.65
t1 0.18425 0.00149
Lifetime (s)
Total charge (mC)

Figure 5.6: (A) Pulse voltammetry protocol between 1.35V cathodic and 1.42-1.8V vs. RHE anodic non-iR corrected potentials. (B) The first anodic and inverted cathodic current decay on the example of IrNi/GC. (C) The OER charge (total anodic charge integral – total cathodic charge integral) vs. the OER current. The slope is 5 because the duration of anodic pulse is 5 seconds. (D) Normalized current response upon a potential step (from 1.42 V to 1.35V vs. RHE) for selected samples. (E) Comparison of the anodic current decay after background subtraction (potential step from 1.35 to 1.8 V vs. RHE) with the inverted cathodic current signal upon the reverse (1.8 to 1.35 V vs. RHE). Note the much faster decaying signal of the anodic current. (F) An example of fitting the transient current decay with the 3-component fit model (see section Analysis of the transient current response to voltage pulses) (G) The life time of the charge (defined formally by dividing the total charge with the OER current; note the logarithmic scale) as a function of the total charge.

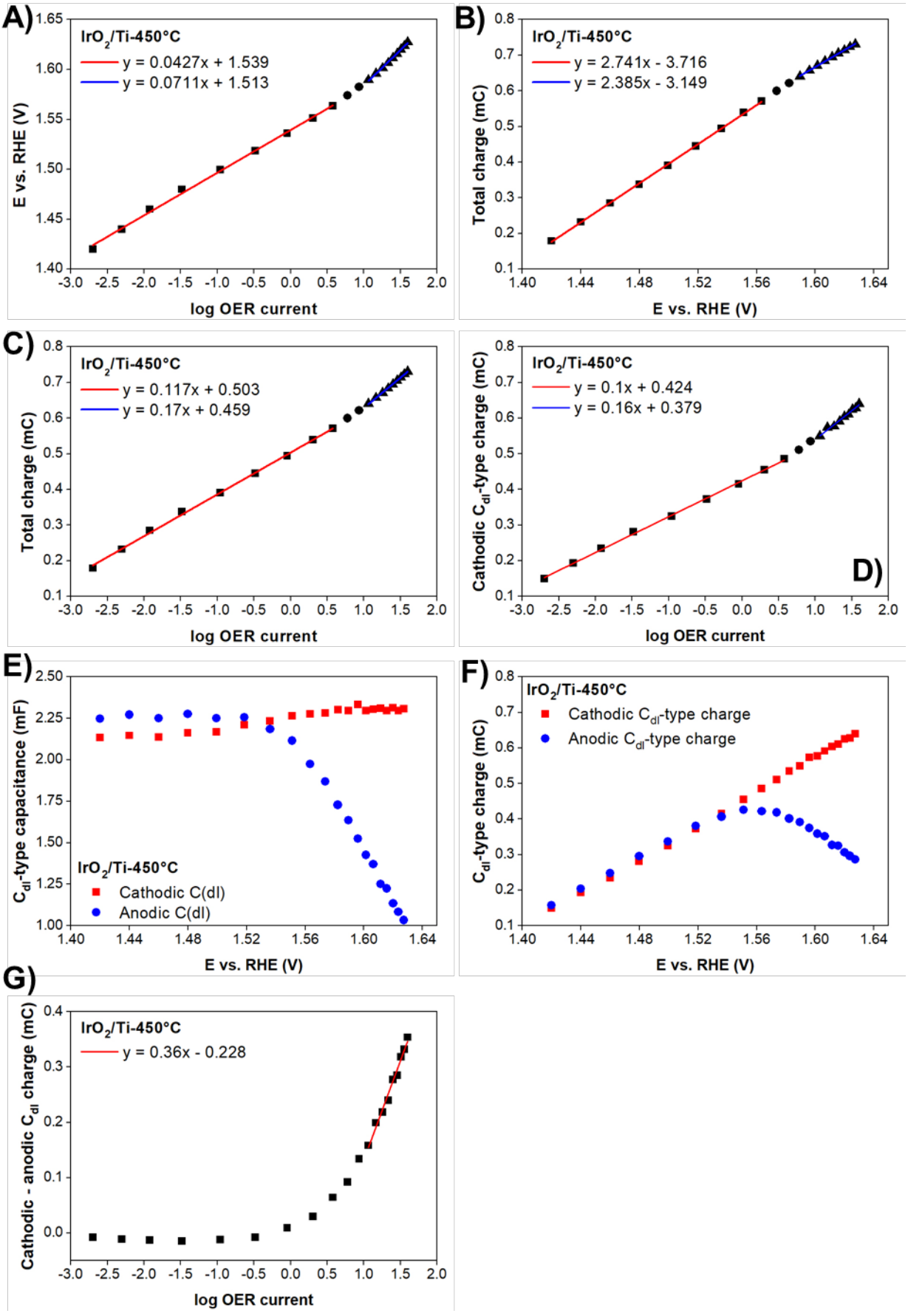
A)
IrO2/Ti-450°C
y = 0.0427x + 1.539
y = 0.0711x + 1.513
E vs. RHE (V)
log OER current
B)
IrO2/Ti-450°C
y = 2.741x - 3.716
y = 2.385x - 3.149
Total charge (mC)
E vs. RHE (V)
C)
IrO2/Ti-450°C
y = 0.117x + 0.503
y = 0.17x + 0.459
Total charge (mC)
log OER current
D)
IrO2/Ti-450°C
y = 0.1x + 0.424
y = 0.16x + 0.379
Cathodic Cdl-type charge (mC)
log OER current
E)
IrO2/Ti-450°C
Cathodic C(dl)
Anodic C(dl)
Cdl-type capacitance (mF)
E vs. RHE (V)
F)
IrO2/Ti-450°C
Cathodic Cdl-type charge
Anodic Cdl-type charge
Cdl-type charge (mC)
E vs. RHE (V)
G)
IrO2/Ti-450°C
y = 0.36x - 0.228
Cathodic - anodic Cdl charge (mC)
log OER current

Figure 5.7: (A) iR corrected potential vs. log OER current (OER current in mA), Tafel plot, derived from the pulse voltammetry measurement. (B) Total charge (integral cathodic charge) vs. iR corrected potential derived from the pulse voltammetry measurement. (C) Total charge (integral cathodic charge) vs. log OER current derived from the pulse voltammetry measurement. (D) Cathodic C_{dl}-type charge (time integral of the C_{dl}-type current; or C_{dl}-type capacitance times the applied potential step) vs. log OER current. (E) C_{dl}-type capacitance derived from fitting the current profiles of the pulse voltammetry measurement. Cathodic: fit of the cathodic current profiles upon the potential steps from anodic to cathodic. Anodic: fit of the anodic current profiles upon the potential steps from cathodic to anodic. (F) C_{dl}-type charge (time integral of the double layer current; or double layer capacitance times the applied potential step) vs. the iR corrected potential. (G) The difference between cathodic and anodic C_{dl}-type charge (from (F)) vs. log OER current. Sample: fresh IrO_2/Ti-450°C.

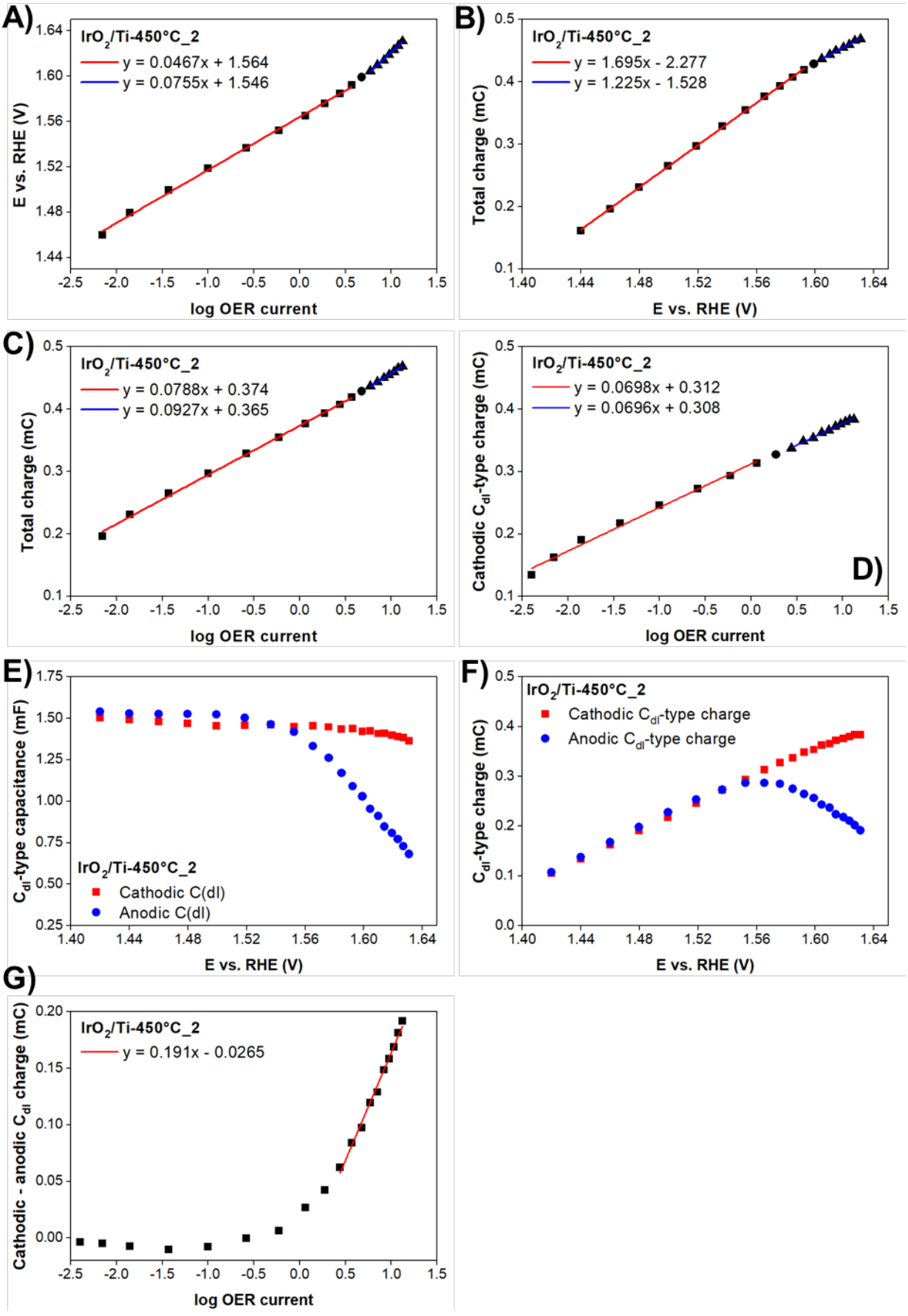
A)
IrO2/Ti-450°C_2
y = 0.0467x + 1.564
y = 0.0755x + 1.546
E vs. RHE (V)
log OER current
B)
IrO2/Ti-450°C_2
y = 1.695x - 2.277
y = 1.225x - 1.528
Total charge (mC)
E vs. RHE (V)
C)
IrO2/Ti-450°C_2
y = 0.0788x + 0.374
y = 0.0927x + 0.365
Total charge (mC)
log OER current
D)
IrO2/Ti-450°C_2
y = 0.0698x + 0.312
y = 0.0696x + 0.308
Cathodic Cdl-type charge (mC)
log OER current
E)
IrO2/Ti-450°C_2
Cathodic C(dl)
Anodic C(dl)
Cdl-type capacitance (mF)
E vs. RHE (V)
F)
IrO2/Ti-450°C_2
Cathodic Cdl-type charge
Anodic Cdl-type charge
Cdl-type charge (mC)
E vs. RHE (V)
G)
IrO2/Ti-450°C_2
y = 0.191x - 0.0265
Cathodic - anodic Cdl charge (mC)
log OER current

Figure 5.8: (A) iR corrected potential vs. log OER current (OER current in mA), Tafel plot, derived from the pulse voltammetry measurement. (B) Total charge (integral cathodic charge) vs. iR corrected potential derived from the pulse voltammetry measurement. (C) Total charge (integral cathodic charge) vs. log OER current derived from the pulse voltammetry measurement. (D) Cathodic C_{dl}-type charge (time integral of the C_{dl}-type current; or C_{dl}-type capacitance times the applied potential step) vs. log OER current. (E) C_{dl}-type capacitance derived from fitting the current profiles of the pulse voltammetry measurement. Cathodic: fit of the cathodic current profiles upon the potential steps from anodic to cathodic. Anodic: fit of the anodic current profiles upon the potential steps from cathodic to anodic. (F) C_{dl}-type charge (time integral of the C_{dl}-type current; or C_{dl}-type capacitance times the applied potential step) vs. the iR corrected potential. (G) The difference between cathodic and anodic C_{dl}-type charge (from (F)) vs. log OER current. Sample: extensively used and somewhat deactivated IrO_2/Ti-450°C.

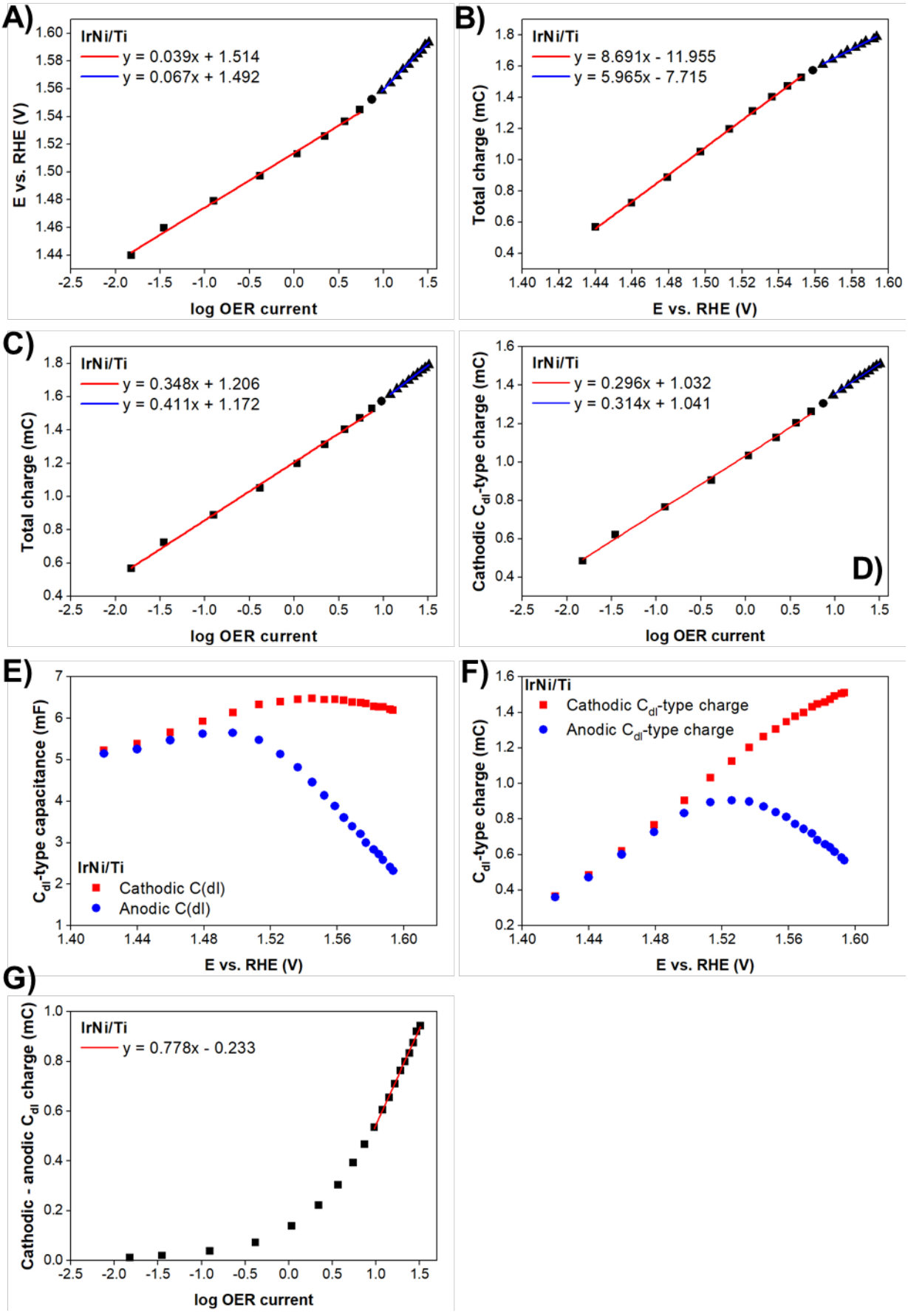
A)
IrNi/Ti
y = 0.039x + 1.514
y = 0.067x + 1.492
E vs. RHE (V)
log OER current
B)
IrNi/Ti
y = 8.691x - 11.955
y = 5.965x - 7.715
Total charge (mC)
E vs. RHE (V)
C)
IrNi/Ti
y = 0.348x + 1.206
y = 0.411x + 1.172
Total charge (mC)
log OER current
D)
IrNi/Ti
y = 0.296x + 1.032
y = 0.314x + 1.041
Cathodic Cdl-type charge (mC)
log OER current
E)
IrNi/Ti
Cathodic C(dl)
Anodic C(dl)
Cdl-type capacitance (mF)
E vs. RHE (V)
F)
IrNi/Ti
Cathodic Cdl-type charge
Anodic Cdl-type charge
Cdl-type charge (mC)
E vs. RHE (V)
G)
IrNi/Ti
y = 0.778x - 0.233
Cathodic - anodic Cdl charge (mC)
log OER current

Figure 5.9: (A) iR corrected potential vs. log OER current (OER current in mA), Tafel plot, derived from the pulse voltammetry measurement. (B) Total charge (integral cathodic charge) vs. iR corrected potential derived from the pulse voltammetry measurement. (C) Total charge (integral cathodic charge) vs. log OER current derived from the pulse voltammetry measurement. (D) C_{dl}-type charge (time integral of the C_{dl}-type current; or C_{dl}-type capacitance times the applied potential step) vs. log OER current. (E) C_{dl}-type capacitance derived from fitting the current profiles of the pulse voltammetry measurement. Cathodic: fit of the cathodic current profiles upon the potential steps from anodic to cathodic. Anodic: fit of the anodic current profiles upon the potential steps from cathodic to anodic. (F) C_{dl}-type charge (time integral of the C_{dl}-type current; or C_{dl}-type capacitance times the applied potential step) vs. the iR corrected potential. (G) The difference between cathodic and anodic C_{dl}-type charge (from (F)) vs. log OER current. Sample: IrNi/Ti.

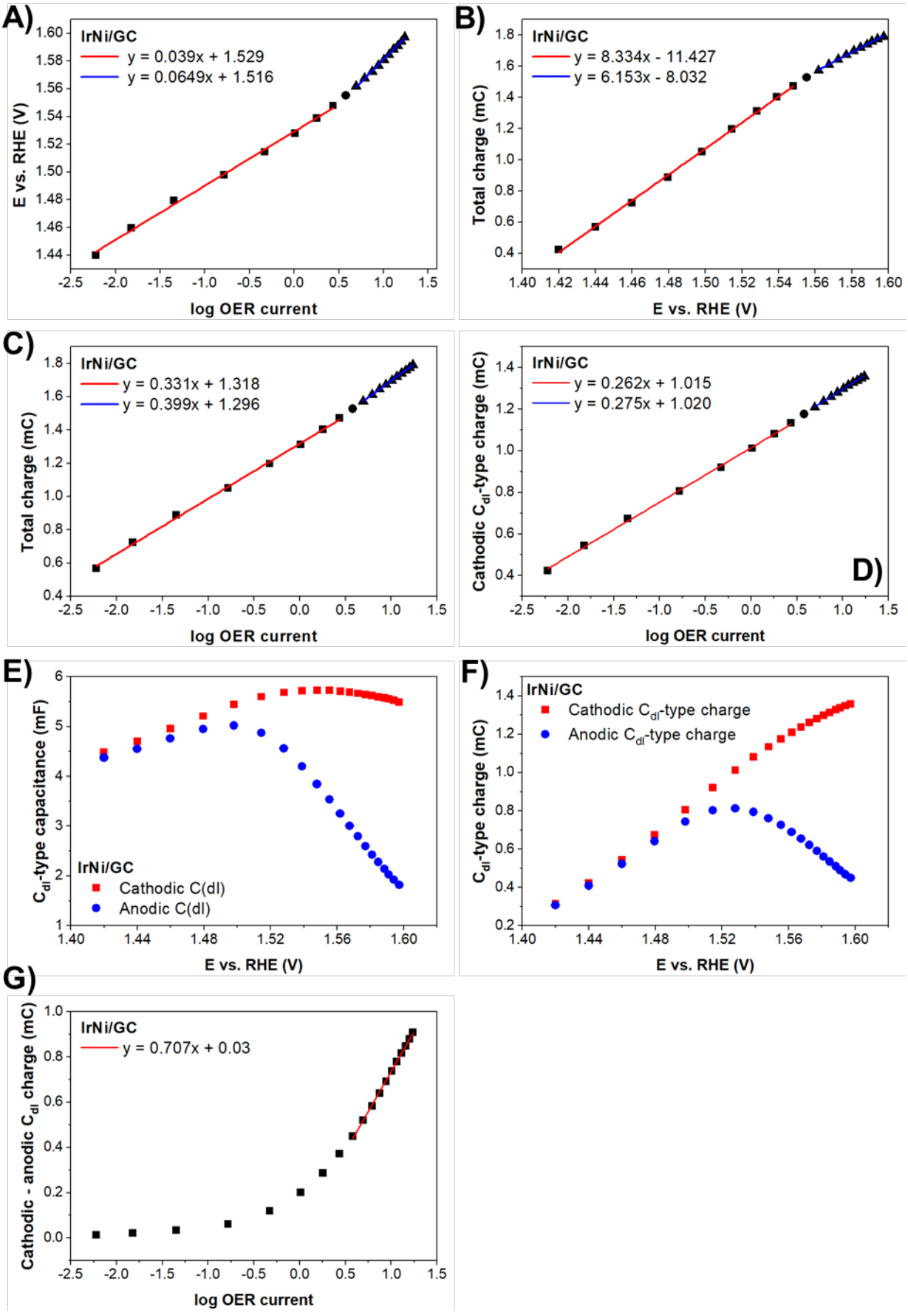
A)
IrNi/GC
y = 0.039x + 1.529
y = 0.0649x + 1.516
E vs. RHE (V)
log OER current
B)
IrNi/GC
y = 8.334x - 11.427
y = 6.153x - 8.032
Total charge (mC)
E vs. RHE (V)
C)
IrNi/GC
y = 0.331x + 1.318
y = 0.399x + 1.296
Total charge (mC)
log OER current
D)
IrNi/GC
y = 0.262x + 1.015
y = 0.275x + 1.020
Cathodic C_{dl}-type charge (mC)
log OER current
E)
IrNi/GC
Cathodic C(dl)
Anodic C(dl)
C_{dl}-type capacitance (mF)
E vs. RHE (V)
F)
IrNi/GC
Cathodic C_{dl}-type charge
Anodic C_{dl}-type charge
C_{dl}-type charge (mC)
E vs. RHE (V)
G)
IrNi/GC
y = 0.707x + 0.03
Cathodic - anodic C_{dl} charge (mC)
log OER current

Figure 5.10: (A) iR corrected potential vs. log OER current (OER current in mA), Tafel plot, derived from the pulse voltammetry measurement. (B) Total charge (integral cathodic charge) vs. iR corrected potential derived from the pulse voltammetry measurement. (C) Total charge (integral cathodic charge) vs. log OER current derived from the pulse voltammetry measurement. (D) Cathodic C_{dl}-type charge (time integral of the C_{dl}-type current; or C_{dl}-type capacitance times the applied potential step) vs. log OER current. (E) C_{dl}-type capacitance derived from fitting the current profiles of the pulse voltammetry measurement. Cathodic: fit of the cathodic current profiles upon the potential steps from anodic to cathodic. Anodic: fit of the anodic current profiles upon the potential steps from cathodic to anodic. (F) C_{dl}-type charge (time integral of the C_{dl}-type current; or C_{dl}-type capacitance times the applied potential step) vs. the iR corrected potential. (G) The difference between cathodic and anodic C_{dl}-type charge (from (F)) vs. log OER current. Sample: IrNi/GC (GC: glassy carbon).

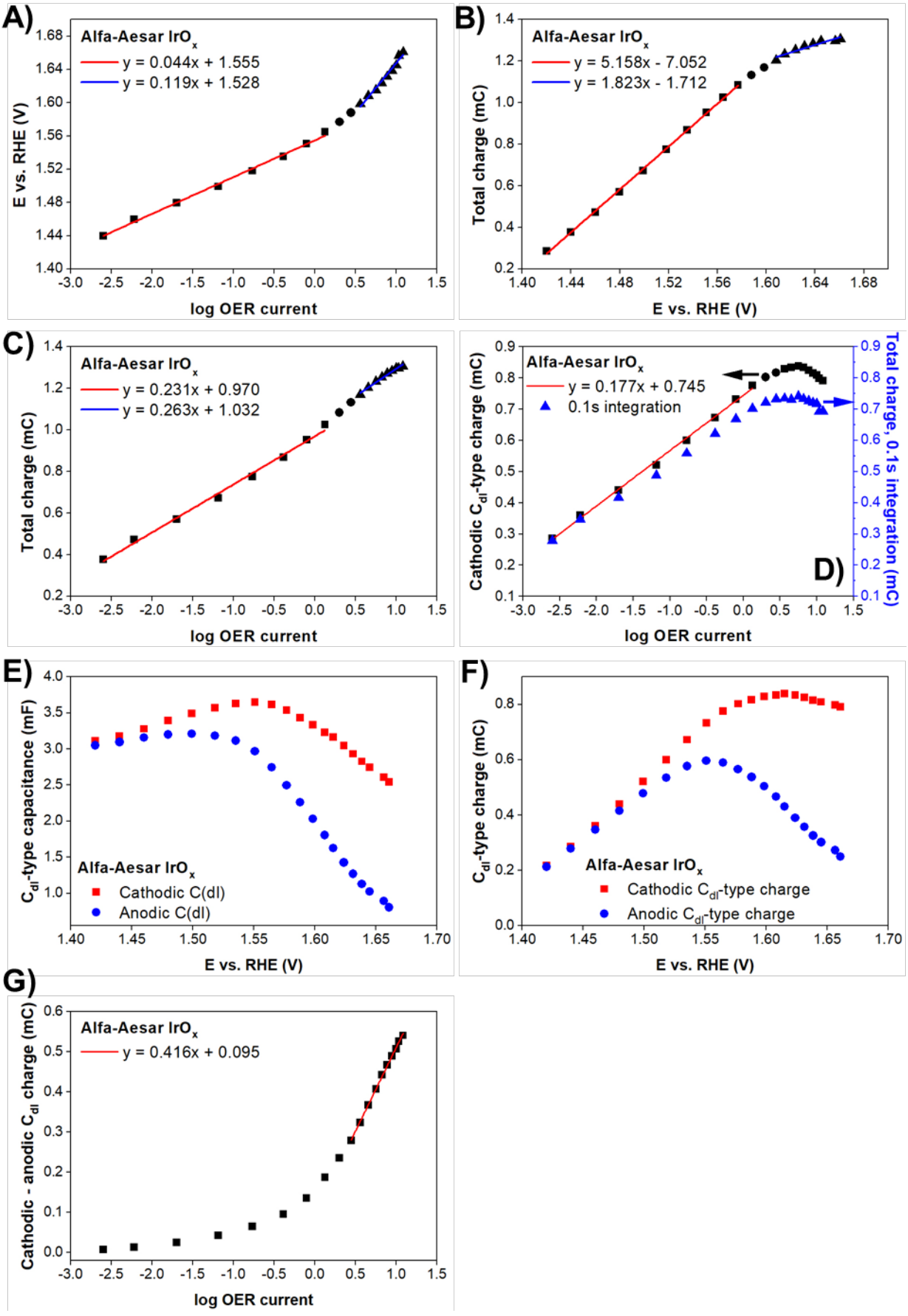
A)
Alfa-Aesar IrO$_x$
y = 0.044x + 1.555
y = 0.119x + 1.528
E vs. RHE (V)
log OER current
B)
Alfa-Aesar IrO$_x$
y = 5.158x - 7.052
y = 1.823x - 1.712
Total charge (mC)
E vs. RHE (V)
C)
Alfa-Aesar IrO$_x$
y = 0.231x + 0.970
y = 0.263x + 1.032
Total charge (mC)
log OER current
D)
Alfa-Aesar IrO$_x$
y = 0.177x + 0.745
0.1s integration
Cathodic C_{dl}-type charge (mC)
Total charge, 0.1s integration (mC)
log OER current
E)
Alfa-Aesar IrO$_x$
Cathodic C(dl)
Anodic C(dl)
C_{dl}-type capacitance (mF)
E vs. RHE (V)
F)
Alfa-Aesar IrO$_x$
Cathodic C_{dl}-type charge
Anodic C_{dl}-type charge
C_{dl}-type charge (mC)
E vs. RHE (V)
G)
Alfa-Aesar IrO$_x$
y = 0.416x + 0.095
Cathodic - anodic C_{dl} charge (mC)
log OER current

Figure 5.11: (A) iR corrected potential vs. log OER current (OER current in mA), Tafel plot, derived from the pulse voltammetry measurement. (B) Total charge (integral cathodic charge) vs. iR corrected potential derived from the pulse voltammetry measurement. (C) Total charge (integral cathodic charge) vs. log OER current derived from the pulse voltammetry measurement. (D) Cathodic C_{dl}-type charge (time integral of the C_{dl}-type current; or C_{dl}-type capacitance times the applied potential step) vs. log OER current. Here the total charge when integrating only 0.1 s time segments after the cathodic potential steps are overlaid. (E) C_{dl}-type capacitance derived from fitting the current profiles of the pulse voltammetry measurement. Cathodic: fit of the cathodic current profiles upon the potential steps from anodic to cathodic. Anodic: fit of the anodic current profiles upon the potential steps from cathodic to anodic. (F) C_{dl}-type charge (time integral of the C_{dl}-type current; or C_{dl}-type capacitance times the applied potential step) vs. the iR corrected potential. (G) The difference between cathodic and anodic C_{dl}-type charge (from (F)) vs. log OER current. Sample: commercial Alfa-Aesar IrO_x powder.

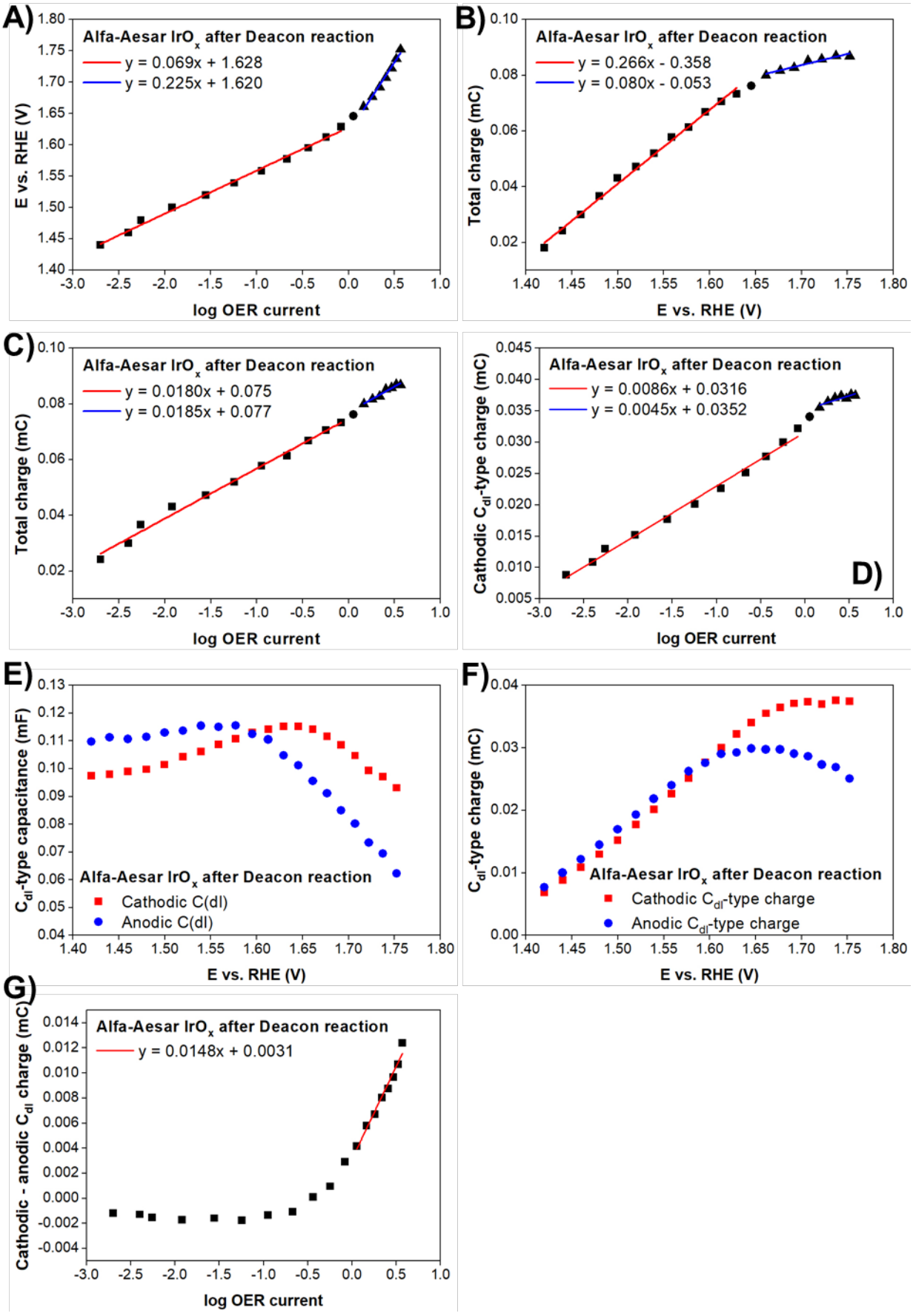
A)
Alfa-Aesar IrO$_x$ after Deacon reaction
y = 0.069x + 1.628
y = 0.225x + 1.620
E vs. RHE (V)
log OER current
B)
Alfa-Aesar IrO$_x$ after Deacon reaction
y = 0.266x - 0.358
y = 0.080x - 0.053
Total charge (mC)
E vs. RHE (V)
C)
Alfa-Aesar IrO$_x$ after Deacon reaction
y = 0.0180x + 0.075
y = 0.0185x + 0.077
Total charge (mC)
log OER current
D)
Alfa-Aesar IrO$_x$ after Deacon reaction
y = 0.0086x + 0.0316
y = 0.0045x + 0.0352
Cathodic C_{dl}-type charge (mC)
log OER current
E)
Alfa-Aesar IrO$_x$ after Deacon reaction
Cathodic C(dl)
Anodic C(dl)
C_{dl}-type capacitance (mF)
E vs. RHE (V)
F)
Alfa-Aesar IrO$_x$ after Deacon reaction
Cathodic C_{dl}-type charge
Anodic C_{dl}-type charge
C_{dl}-type charge (mC)
E vs. RHE (V)
G)
Alfa-Aesar IrO$_x$ after Deacon reaction
y = 0.0148x + 0.0031
Cathodic - anodic C_{dl} charge (mC)
log OER current

Figure 5.12: (A) iR corrected potential vs. log OER current (OER current in mA), Tafel plot, derived from the pulse voltammetry measurement. (B) Total charge (integral cathodic charge) vs. iR corrected potential derived from the pulse voltammetry measurement. (C) Total charge (integral cathodic charge) vs. log OER current derived from the pulse voltammetry measurement. (D) Cathodic C_{dl}-type charge (time integral of the C_{dl}-type current; or C_{dl}-type capacitance times the applied potential step) vs. log OER current. (E) C_{dl}-type capacitance derived from fitting the current profiles of the pulse voltammetry measurement. Cathodic: fit of the cathodic current profiles upon the potential steps from anodic to cathodic. Anodic: fit of the anodic current profiles upon the potential steps from cathodic to anodic. (F) C_{dl}-type charge (time integral of the C_{dl}-type current; or C_{dl}-type capacitance times the applied potential step) vs. the iR corrected potential. (G) The difference between cathodic and anodic C_{dl}-type charge (from (F)) vs. log OER current. Sample: commercial Alfa-Aesar IrO_x powder after treatment in the Deacon reaction.

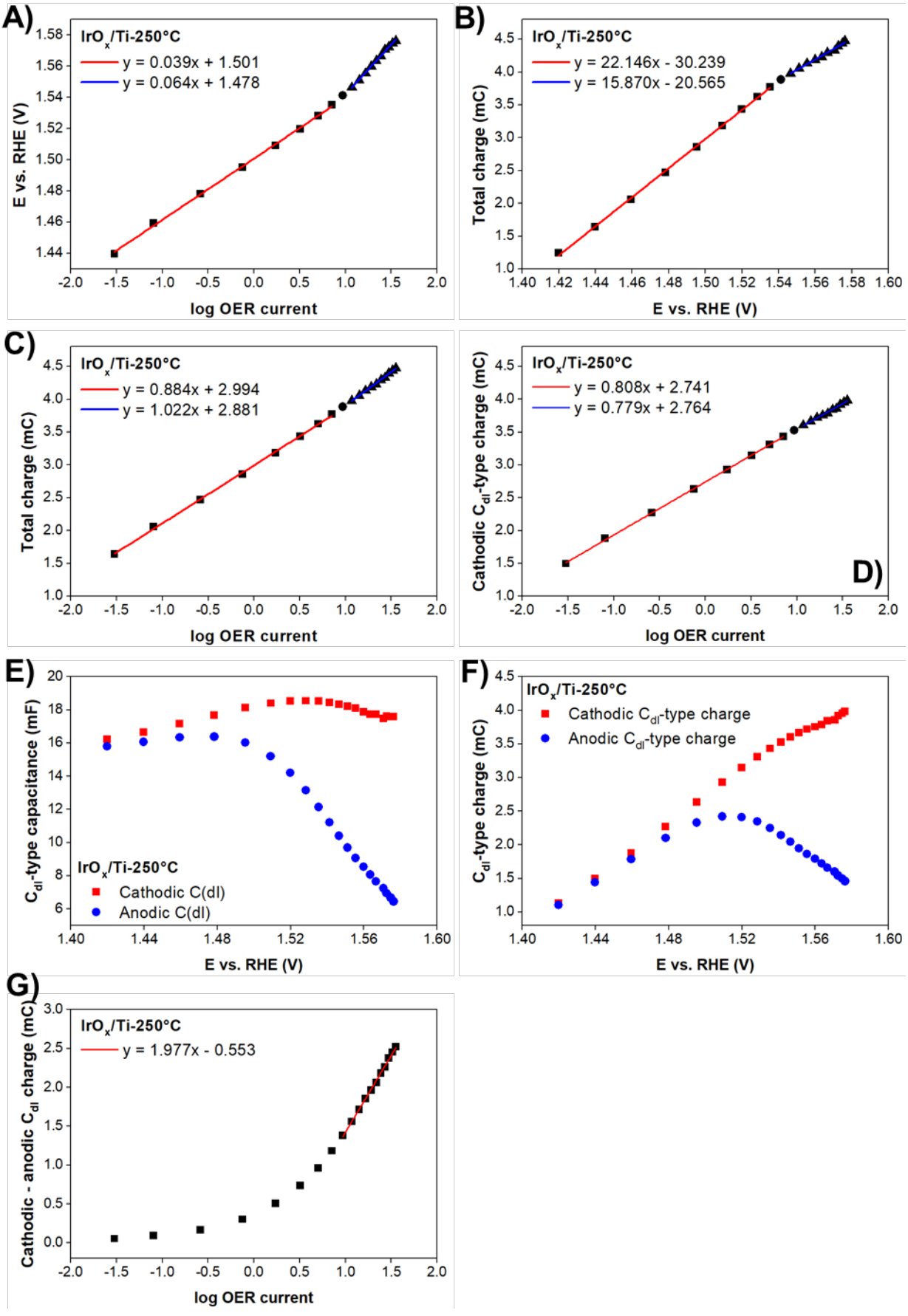
A)
IrO$_x$/Ti-250°C
y = 0.039x + 1.501
y = 0.064x + 1.478
E vs. RHE (V)
log OER current
B)
IrO$_x$/Ti-250°C
y = 22.146x - 30.239
y = 15.870x - 20.565
Total charge (mC)
E vs. RHE (V)
C)
IrO$_x$/Ti-250°C
y = 0.884x + 2.994
y = 1.022x + 2.881
Total charge (mC)
log OER current
D)
IrO$_x$/Ti-250°C
y = 0.808x + 2.741
y = 0.779x + 2.764
Cathodic C$_{dl}$-type charge (mC)
log OER current
E)
IrO$_x$/Ti-250°C
Cathodic C(dl)
Anodic C(dl)
C$_{dl}$-type capacitance (mF)
E vs. RHE (V)
F)
IrO$_x$/Ti-250°C
Cathodic C$_{dl}$-type charge
Anodic C$_{dl}$-type charge
C$_{dl}$-type charge (mC)
E vs. RHE (V)
G)
IrO$_x$/Ti-250°C
y = 1.977x - 0.553
Cathodic - anodic C$_{dl}$ charge (mC)
log OER current

Figure 5.13: (A) iR corrected potential vs. log OER current (OER current in mA), Tafel plot, derived from the pulse voltammetry measurement. (B) Total charge (integral cathodic charge) vs. iR corrected potential derived from the pulse voltammetry measurement. (C) Total charge (integral cathodic charge) vs. log OER current derived from the pulse voltammetry measurement. (D) Cathodic C_{dl}-type charge (time integral of the C_{dl}-type current; or C_{dl}-type capacitance times the applied potential step) vs. log OER current. (E) C_{dl}-type capacitance derived from fitting the current profiles of the pulse voltammetry measurement. Cathodic: fit of the cathodic current profiles upon the potential steps from anodic to cathodic. Anodic: fit of the anodic current profiles upon the potential steps from cathodic to anodic. (F) C_{dl}-type charge (time integral of the C_{dl}-type current; or C_{dl}-type capacitance times the applied potential step) vs. the iR corrected potential. (G) The difference between cathodic and anodic C_{dl}-type charge (from (F)) vs. log OER current. Sample: IrO_x/Ti-250°C.

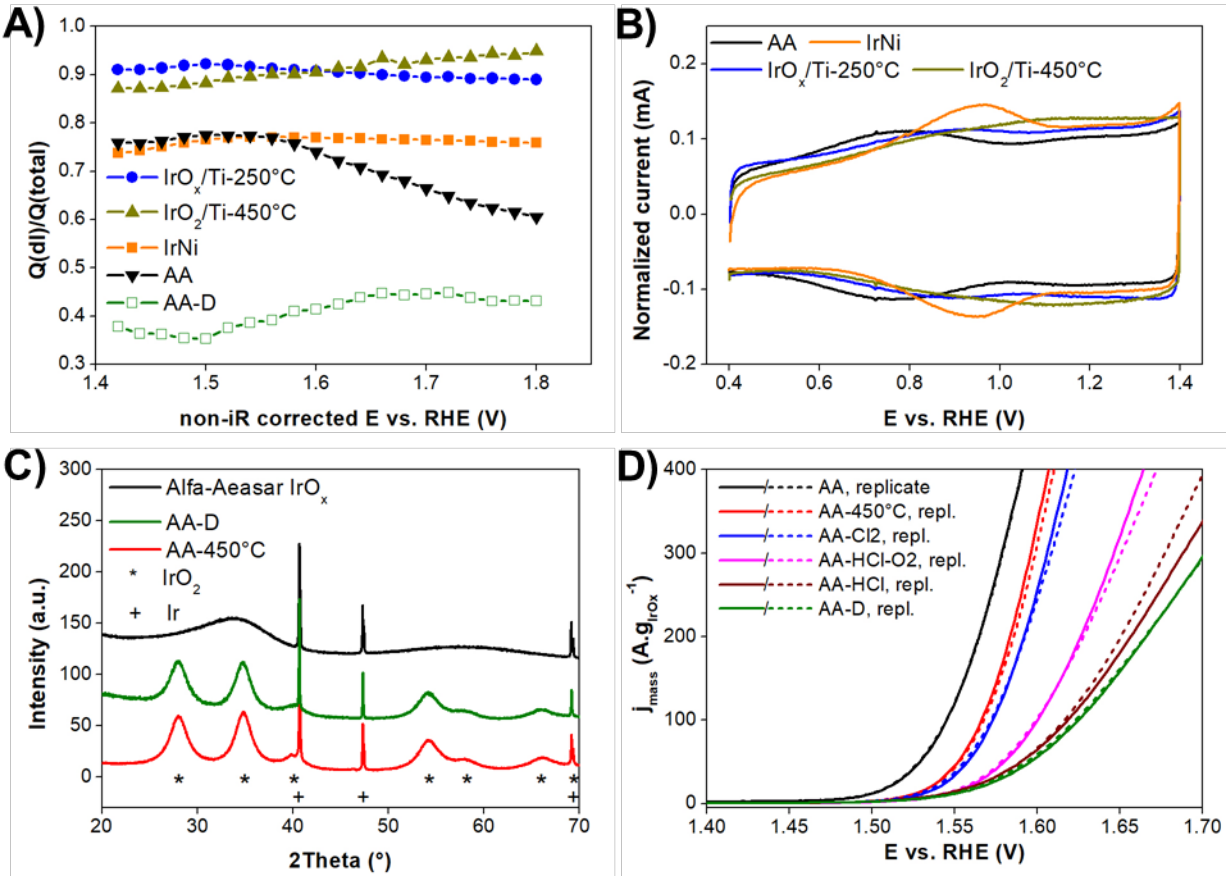

*Figure 5.14: (A) The ratio of C_{dl}-type charge (as determined from the current profile analysis) and the total charge (integral analysis) as a function of the non-iR corrected potential. (B) Cyclic voltammetry of selected sample between 0.4-1.4 V vs. RHE with 100 mV s^{-1} scan rate. (C) XRD patterns of the commercial Alfa-Aesar IrO_x and its derivatives after treatment in the Deacon reaction (AA-D) and calcination at 450°C in air (AA-450°C). The XRD patterns of IrO_2 and Ir are marked with * and +, respectively. (D) OER activity comparison of Alfa-Aesar IrO_x after various treatments. Samples: AA: pristine sample, AA-450°C: sample after calcination at 450°C, AA-Cl2: calcined sample after treatment in Cl_2 at RT. AA-HCl-O_2: calcined sample treated in HCl at 270 °C followed by treatment in O_2 at 300 °C. AA-HCl: calcined sample treated in HCl at 270 °C, AA-D: pristine sample treated in the Deacon reaction.*

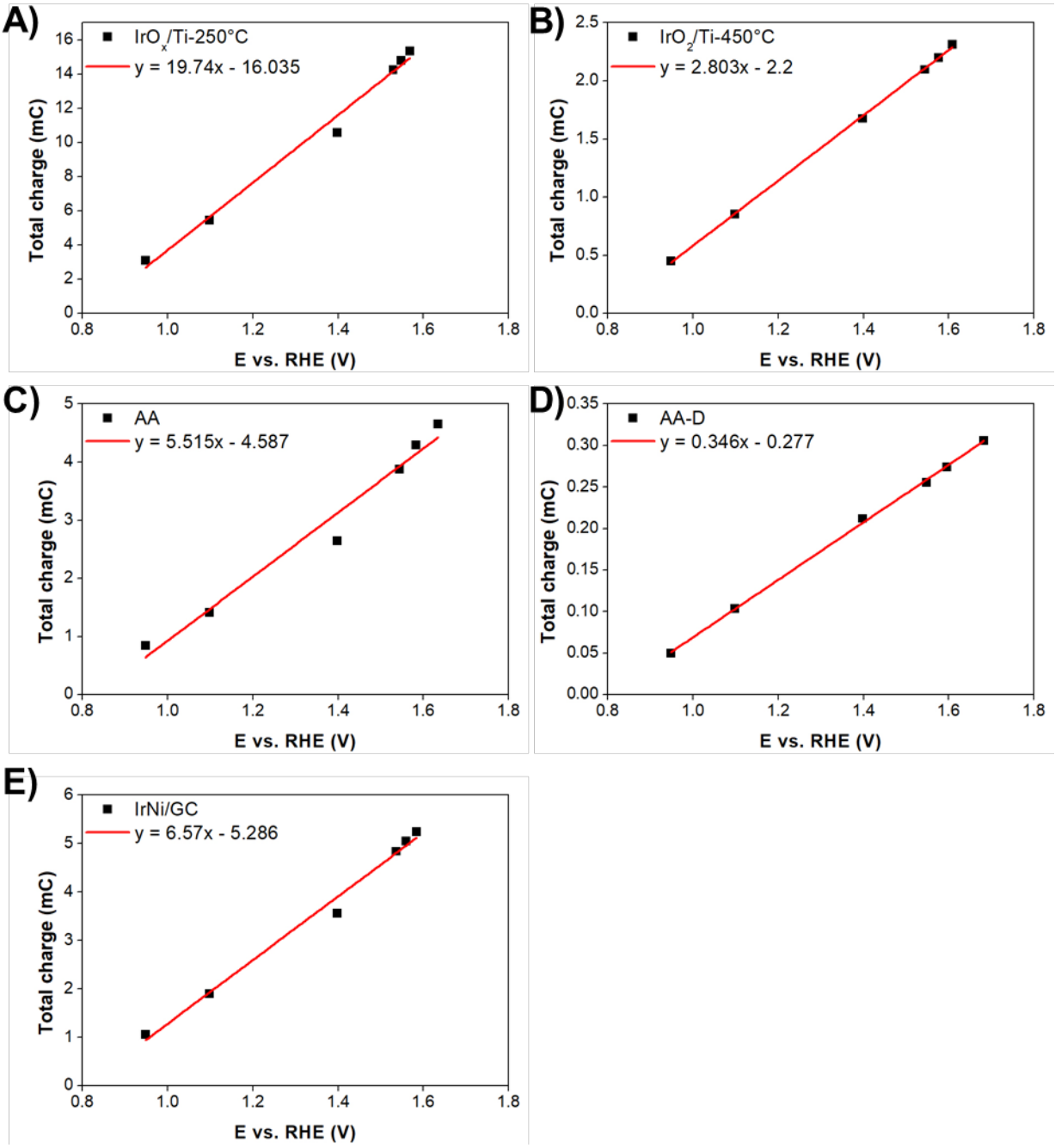

Figure 5.15: The total charge of selected samples as determined by integral pulse voltammetry analysis in the broad potential window. Protocol: cathodic potential: 0.75 V, anodic potentials: 0.95-1.7V non-iR corrected potentials. However, the figure plots the iR corrected potentials. Samples as marked.

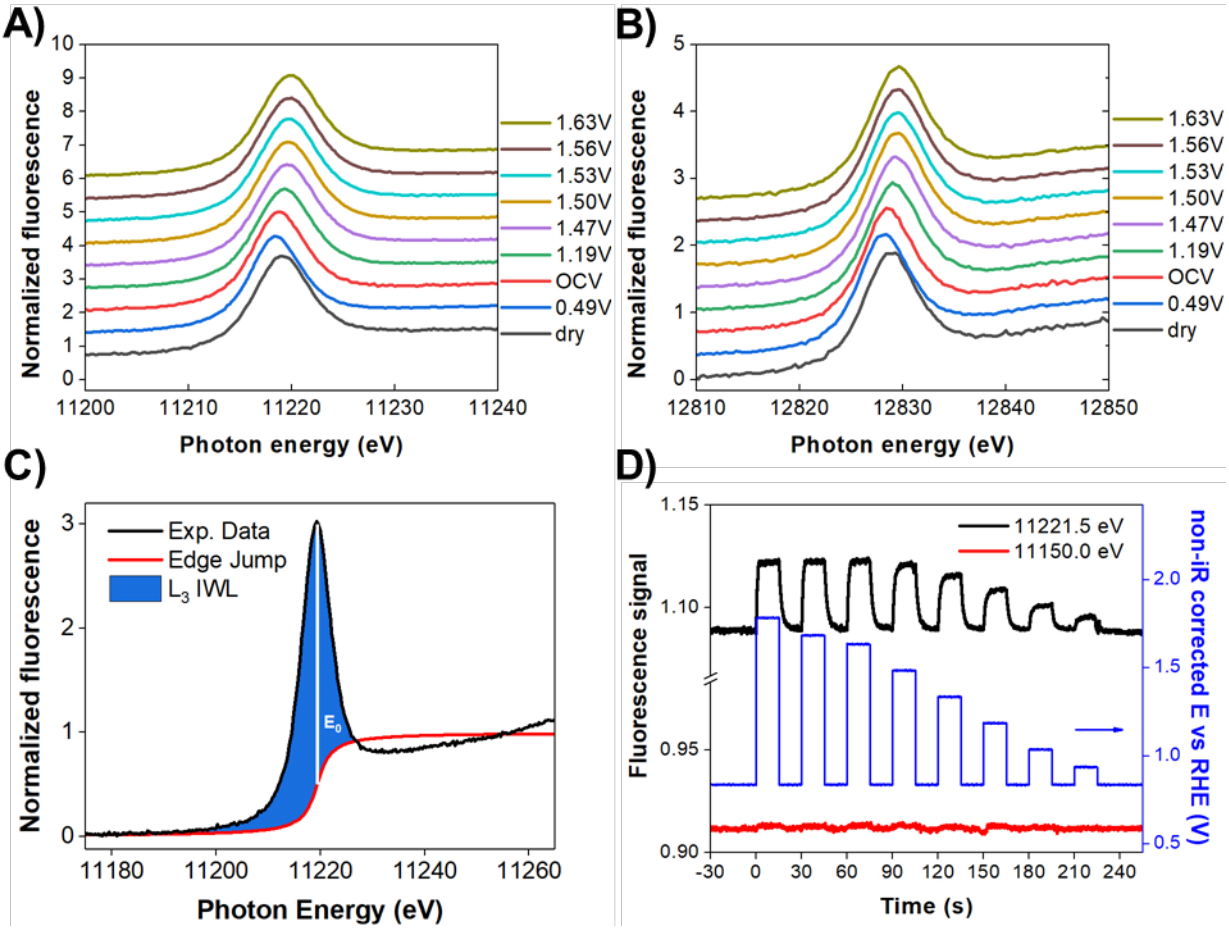

Figure 5.16: (A) and (B) Steady-state operando Ir L-edge X-ray absorption spectra of IrO_x/Ti-250°C at selected potentials at the L_3 and L_2 edge, respectively. (C) The schematics of white line (WL) area determination applied to the Ir L-edge XAS spectra. The WL area (blue area) was determined assuming an arctan edge jump (unit height, width 2 eV) to model the continuum step positioned at the WL maximum following.[22] (D) The protocol of operando potentiodynamic XAS experiment following the fluorescence signal evolution at two selected energies (11221.5 eV at the Ir L_3 white line and 11150 eV, below the Ir L_3 white line) The figure shows reversible positive signal evolution at the white line upon anodic polarization in line with catalyst's oxidation.

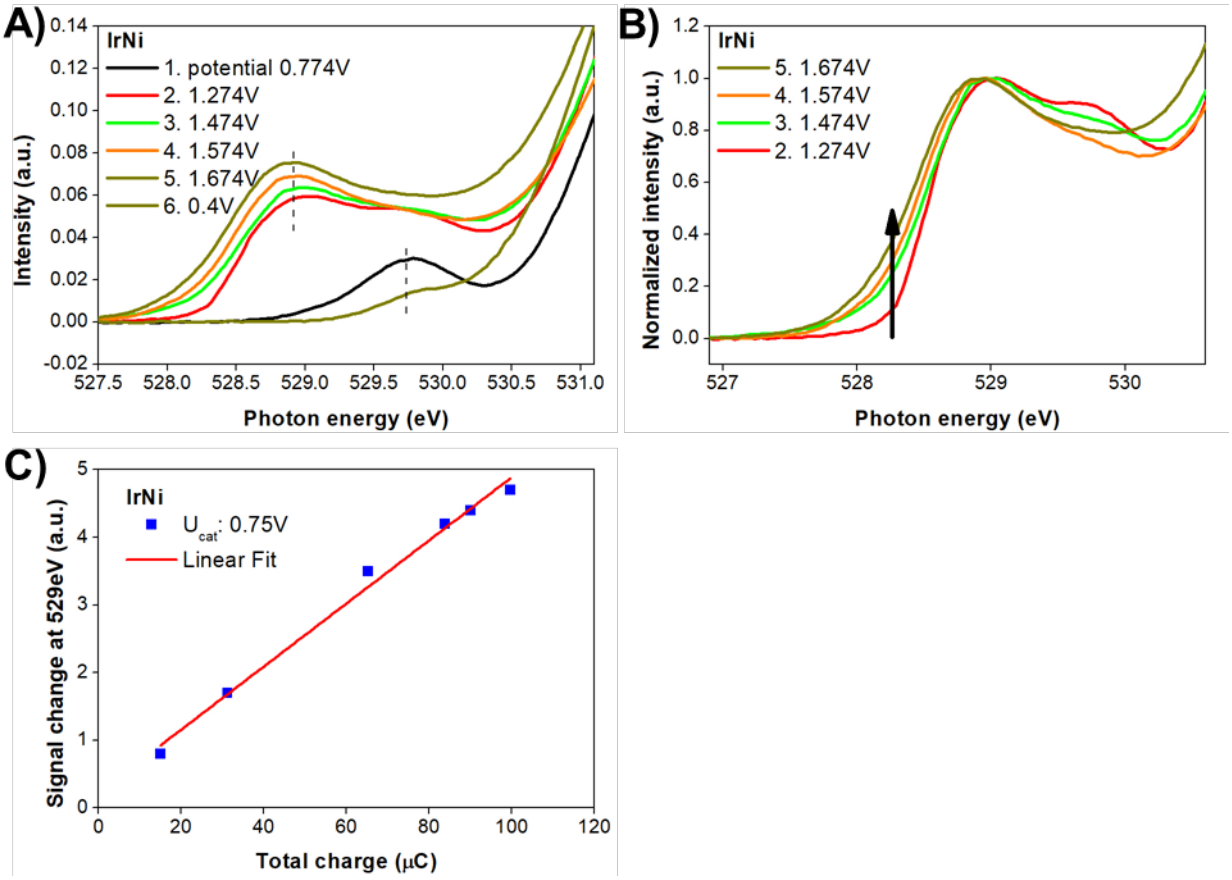

Figure 5.17: (A) Steady-state operando O K-edge X-ray absorption spectra of IrNi/Graphene at selected (non-iR corrected) potentials in the order indicated. (B) Steady-state operando O K-edge spectra of IrNi/Graphene at selected (non-iR corrected) potentials after scaling the spectra at 528.9 eV. (C) Correlation of the signal change of the O K-edge at 529 eV vs. the total charge derived from the pulse voltammetry experiment with broad potential window.

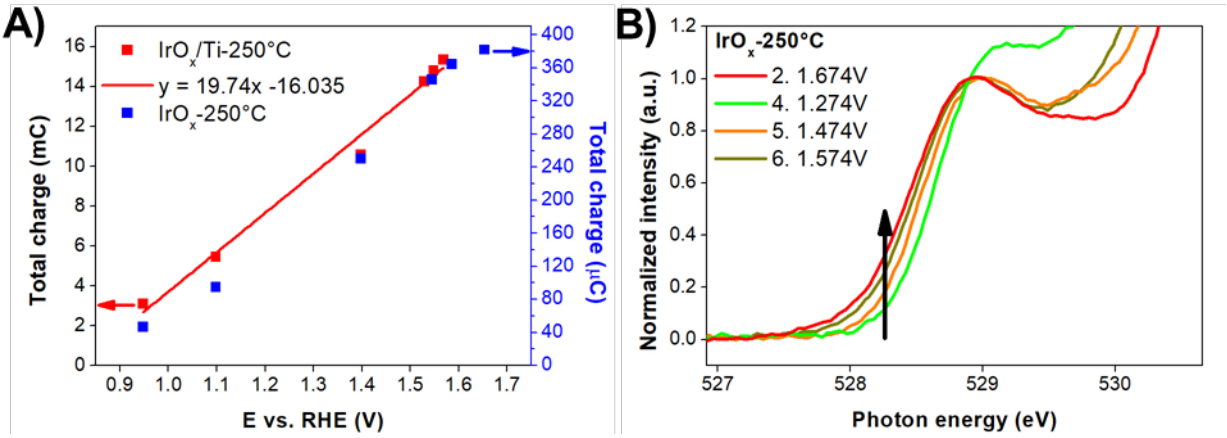

Figure 5.18: (A) Total charge (integral cathodic charge) vs. iR corrected potential derived from a pulse voltammetry experiment in a broad potential window. Constant cathodic potential: 0.748V vs. RHE. Two low temperature (250 °C) calcined IrO_x samples are overlaid: IrO_x/Ti-250°C measured in a standard 3-compartment electrochemical cell and IrO_x/Graphene-250°C in an operando O K-edge XAS experiment. (B) Steady-state operando O K-edge X-ray absorption spectra of IrO_x/Graphene-250°C at selected (non-iR corrected) potentials after scaling the spectra at 528.9 eV.

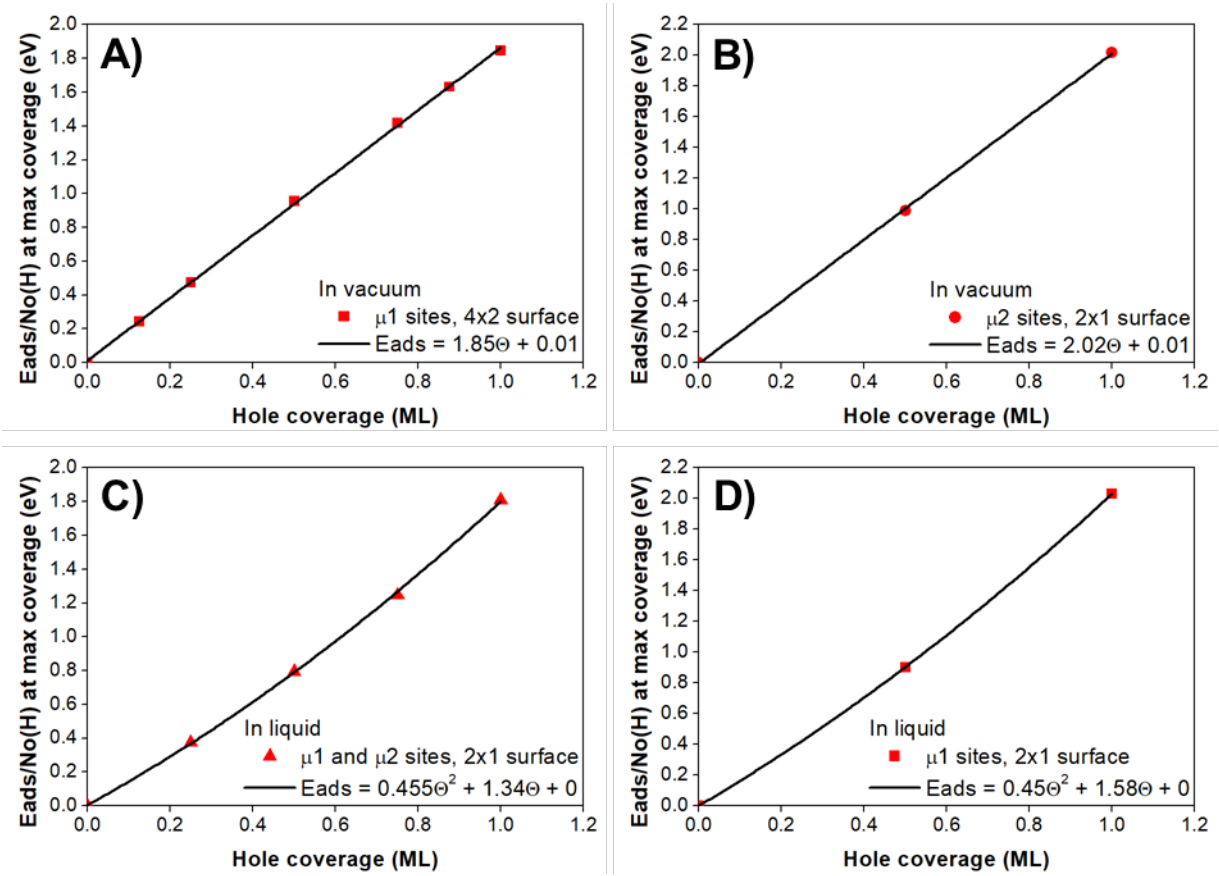

Figure 5.19: The total adsorption energy computed for H on oxygen terminated IrO_2 (110) plotted as a function of the hole coverage (note the energy is normalized by the number of H adsorption sites to make the data on different surfaces more easily comparable). (A) μ_1-O sites for a (4x2) cell in vacuum. (B) μ_2-O sites for a (2x1) cell in vacuum. (C) μ_1-O and μ_2-O sites for a (2x1) cell in liquid. (D) μ_1-O sites for a (2x1) cell in liquid.

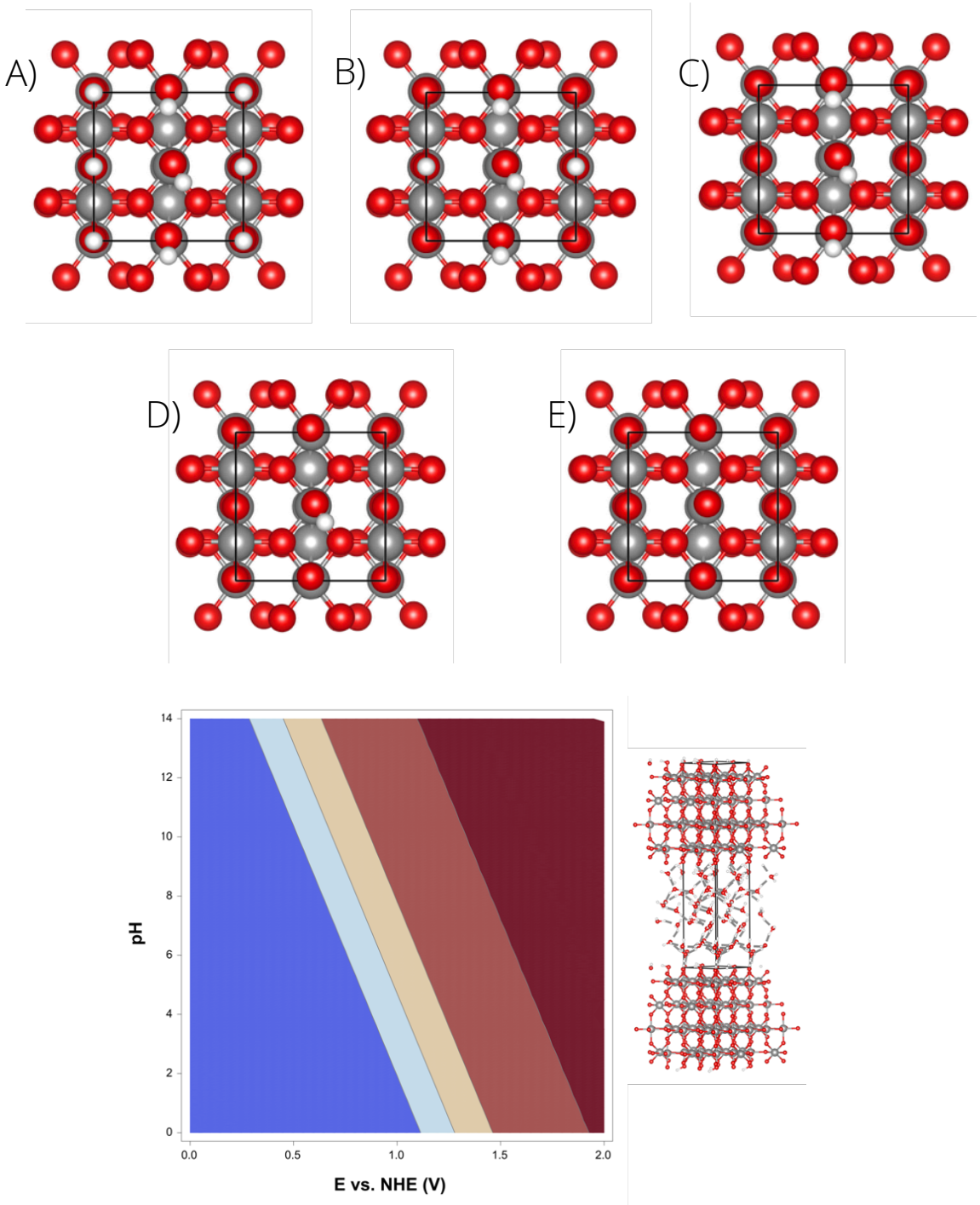

Figure 5.20: Top: The starting surface structures corresponding to various termination of the (110) surface of IrO_2. (A) μ_2-OH/μ_2-OH and μ_1-OH/μ_1-OH; (B) μ_2-O/μ_2-OH and μ_1-OH/μ_1-OH; (C) μ_2-O/μ_2-O and μ_1-OH/μ_1-OH; (D) μ_2-O/μ_2-O and μ_1-O/μ_1-OH; (E) μ_2-O/μ_2-O and μ_1-O/μ_1-O. Ir atoms are shown as grey, oxygen as red, and hydrogen as white. Bottom: Surface (pH, E) phase diagram computed using MD snapshots within an ab initio atomistic thermodynamics approach and an example of cell used to compute surface phase diagram. The coloring of the phases matched Figure 5.3, with blue showing the H covered surface (A) and red the O covered surface (E). Our computed phase diagram is similar to that found using ice-like solvent,[24] though with liquid water we see some evidence that the deprotonation events will be spread over a potential windows of a few tenths of a volt because of Frumkin behavior.

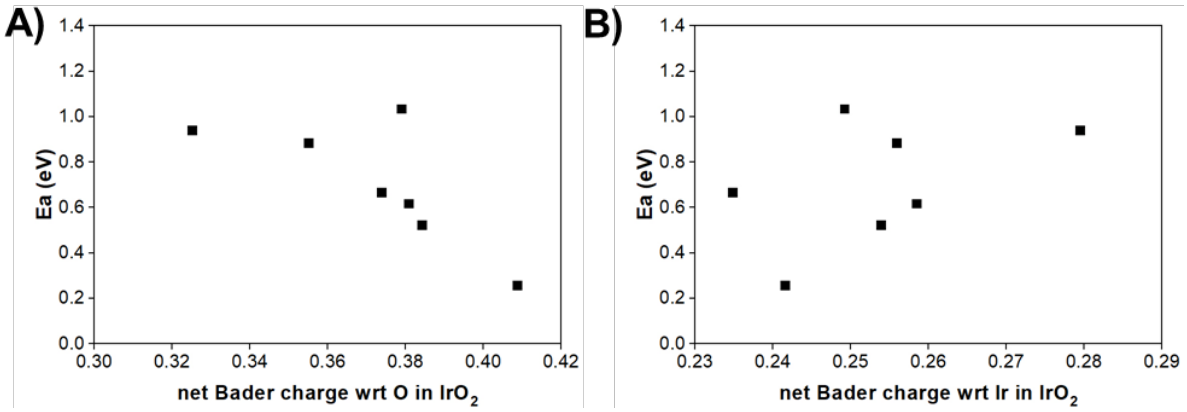

Figure 5.21: Bader charge: (A) The activation energy for O-O coupling computed under the constant charge condition plotted against the Bader charge on the μ_1-O involved in the reaction. (B) The same energy plotted against the Bader charge on the Ir bound to the active μ_1-O.

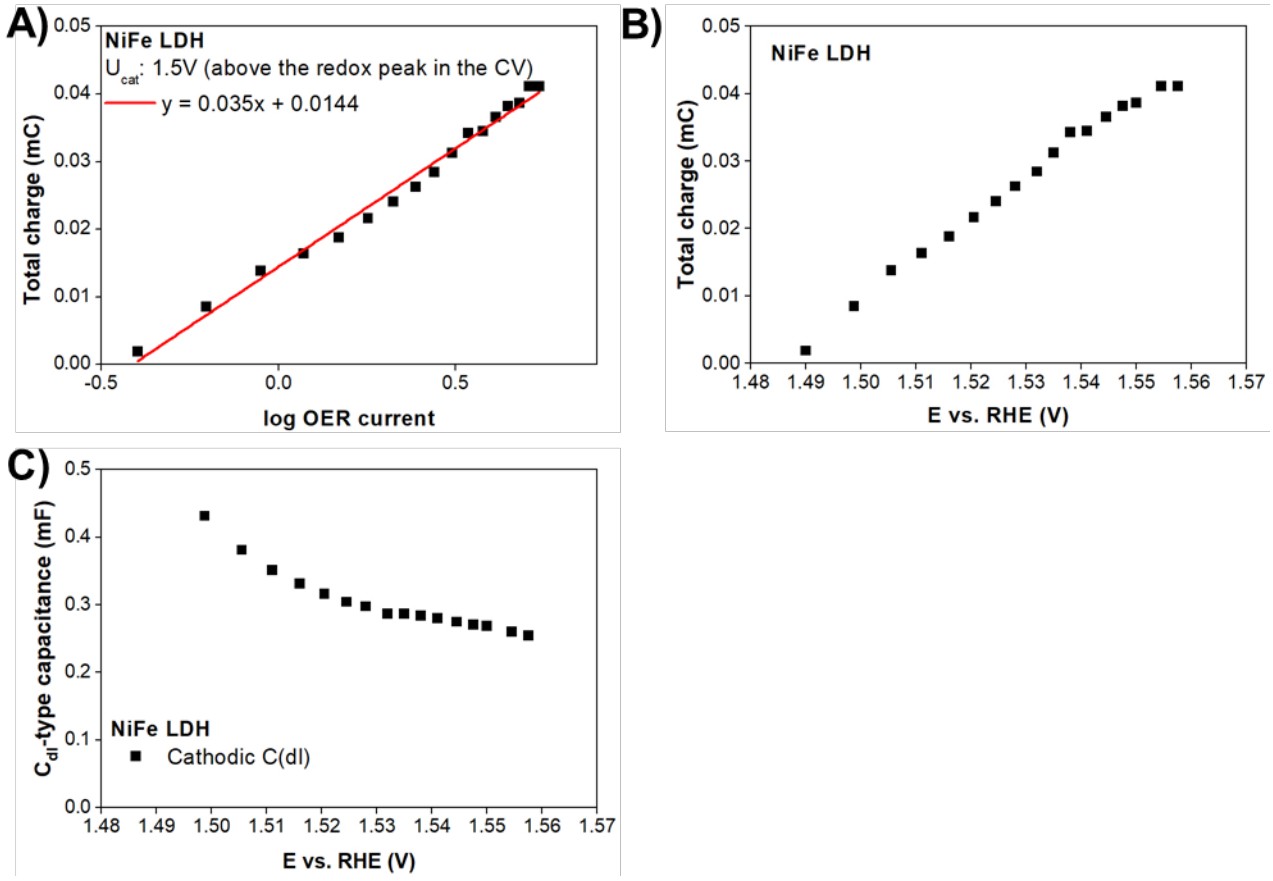

Figure 5.22: (A) Total charge (integral cathodic charge) vs. log OER current derived from the pulse voltammetry measurement. Sample: NiFe layered double hydroxide. The CV of the NiFe LDH contains a redox transition at the OER onset, and thus the constant cathodic potential was set to 1.5V, above the redox transition. (B) Total charge (integral cathodic charge) vs. iR corrected potential derived from the pulse voltammetry measurement. (C) C_{dl}-type capacitance derived from fitting the current profiles of the pulse voltammetry measurement.

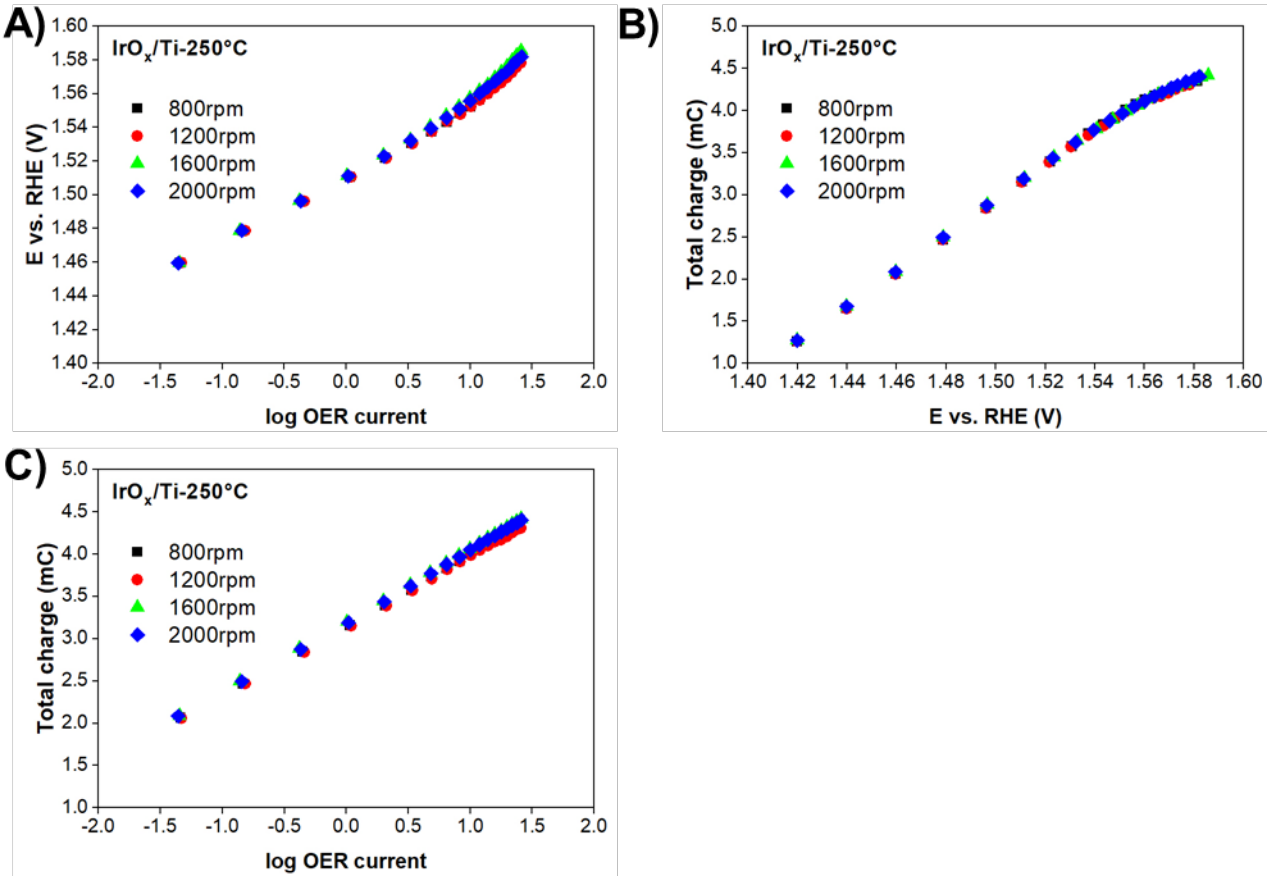

Figure 5.23: Rotation speed dependent pulse voltammetry measurement using IrO_x/Ti-250°C showing the independence of the (A) Tafel plot, (B) total charge (integral cathodic charge) vs. iR corrected potential and (C) total charge vs. log OER current to rotation speeds between 800 rpm and 2000 rpm. Data in the manuscript employs 1600 rpm.

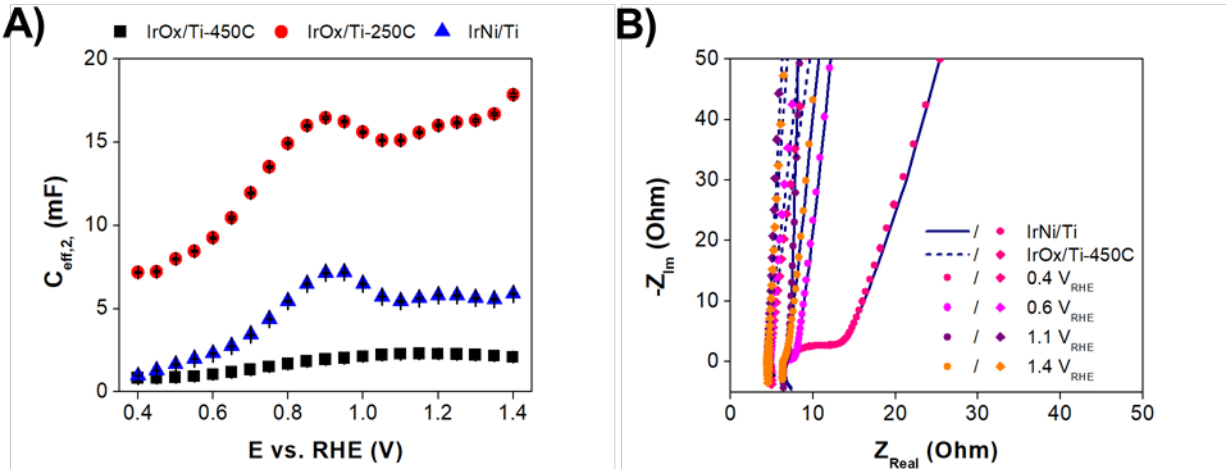

Figure 5.24: (A) Effective capacitance (derived from PEIS fitting) as a function of potential. (B) Example of selected impedance spectra (Nyquist plots) with the corresponding fits.

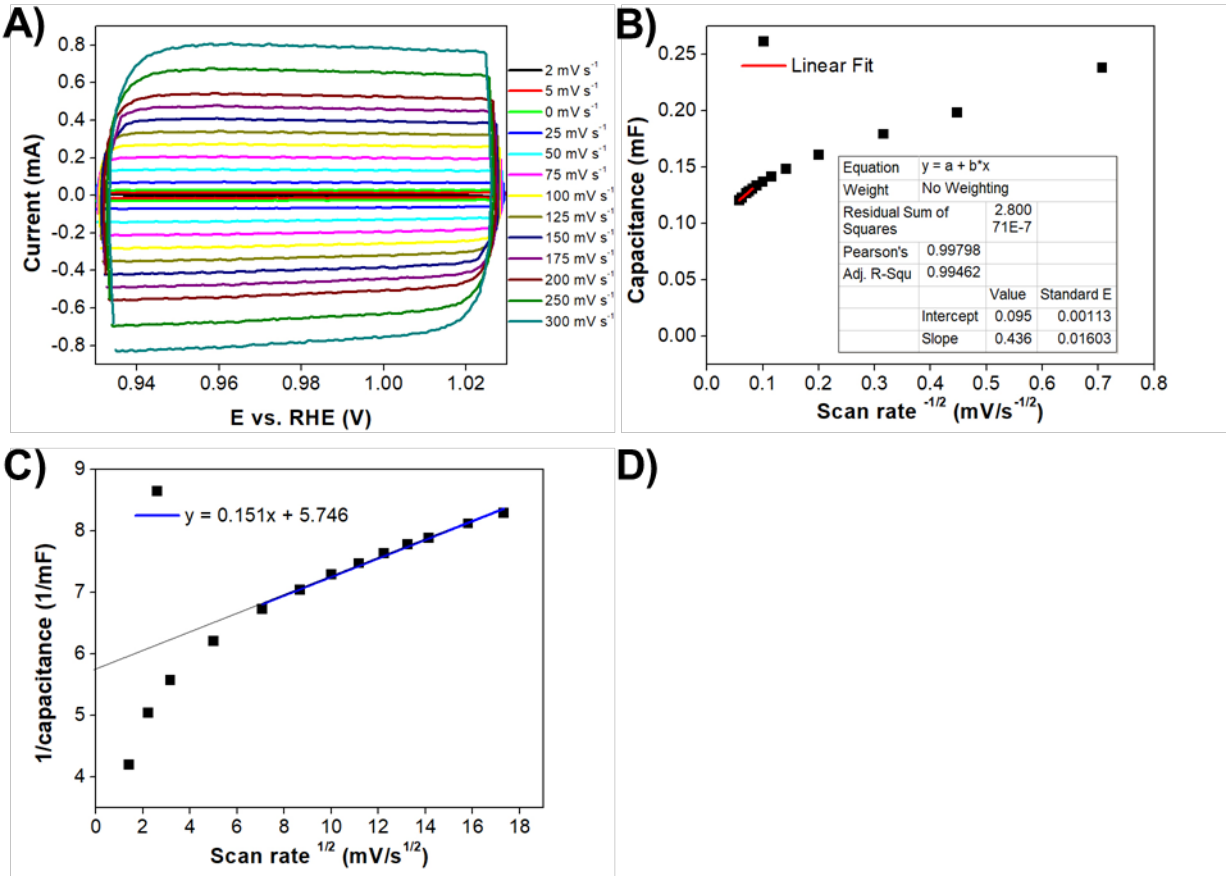

Figure 5.25: (A) iR-corrected cyclic voltammograms between 0.93 and 1.03 V_{RHE} with different scan rates. (B) and (C) evaluation of outer and total capacitance based on scan rate variation experiments.

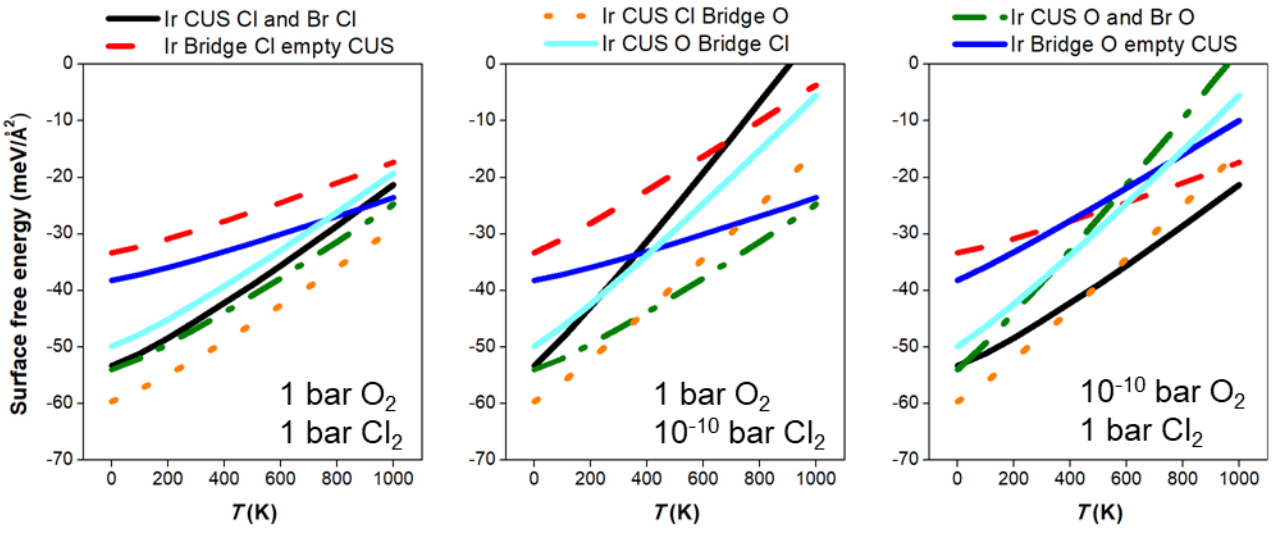

Figure 5.26: Surface free energies of various O/Cl surface terminations on the (110) surface of rutile-type IrO_2.

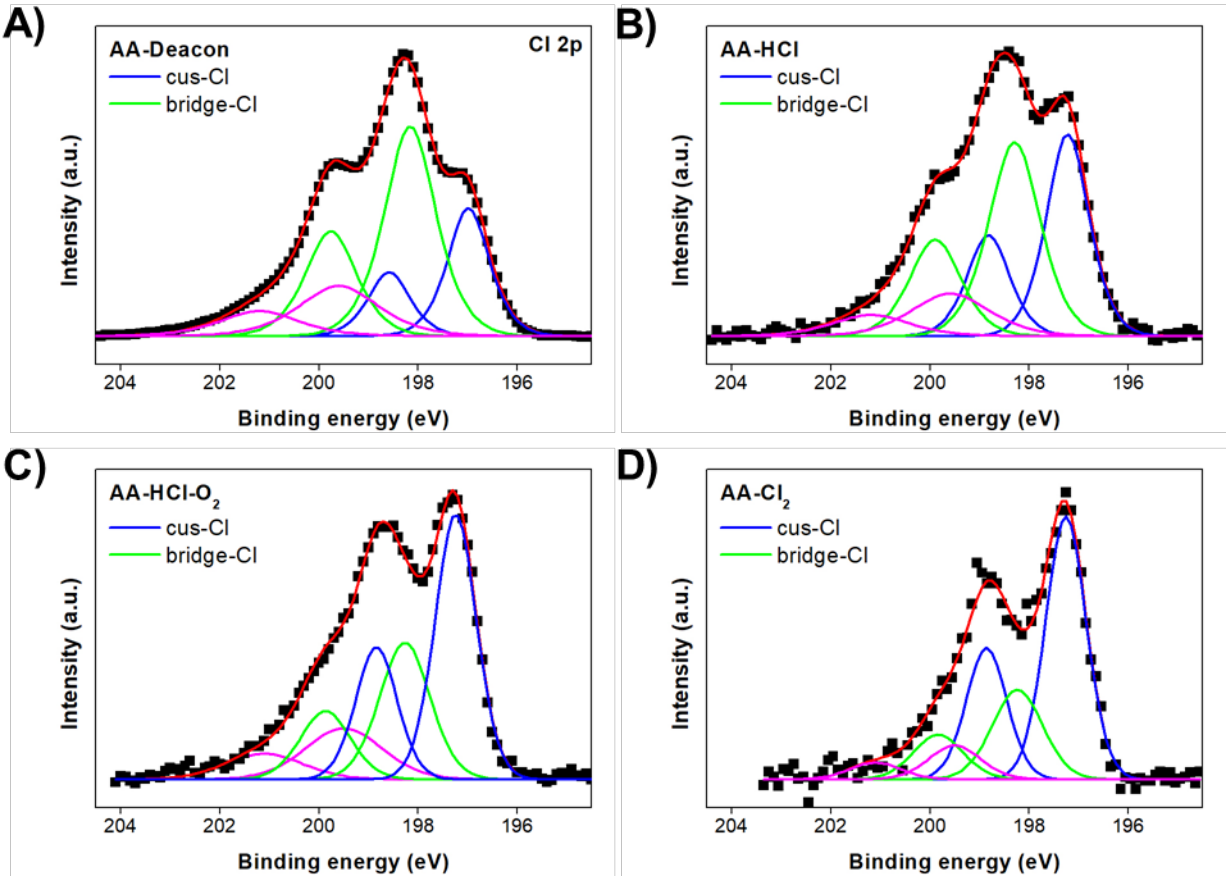

Figure 5.27: Cl 2p spectra of four chlorinated samples: (A) pristine Alfa-Aesar IrO_x sample treated in the Deacon reaction. (B) AA-HCl: calcined Alfa-Aesar IrO_x sample treated in HCl at 270 °C (C) AA-HCl-O_2: calcined Alfa-Aesar IrO_x sample treated in HCl at 270 °C followed by treatment in O_2 at 300 °C. (D) AA-Cl_2: calcined sample after treatment in Cl_2 at RT. Photon energy: 415 eV.

Table 5.1: Capacitance values (in mF) of selected Ir samples based on various evaluation methods.

Evaluation method	Type of capacitance	IrO_x/Ti-250°C	IrNi/Ti	AA-IrO_x	IrO_2/Ti-450°C	AA-D
Pulse voltammetry integration (U_{cat} = 0.75 V)	total	19.7	7.4	5.5	2.8	0.35
Pulse voltammetry integration (U_{cat} = 1.35 V)	total	22.1/15.9[a]	9.3/7.1[a]	5.2/1.8[a]	2.7/2.4[a]	0.27/0.08[a]
Fit cathodic line shape	double layer[b]	16-19	5.2-6.5	2.5-3.7	2.1-2.3	0.09-0.12
Scan rate variation	total	17.9	5.4	3.6	2.3	0.19
Scan rate variation	outer	6.5	3.53	1.7	1.9	0.12
Fit EIS spectra	double layer[b]	7.3-17.7[c]	5.5-7.2[c]	n.d.	1.1-2.5[c]	n.d.

[a] First and second numbers correspond to the slopes of the total charge vs. potential curves before and after the potential the Tafel slope bends.

[b] Due to the much larger capacitance values as compared to the double layer capacitance of planar metallic electrodes, in reality we probe here pseudocapacitance (C_{dl}-type).

[c] See Figure 5.24

Table 5.2: Areal capacitance values (in μF/cm^2) of Alfa-Aeasar IrO_x samples based on various evaluation methods.

Evaluation method	Type of capacitance	AA-IrO_x	AA-D
Pulse voltammetry integration (U_{cat} = 0.75 V)	total	1509	153
Pulse voltammetry integration (U_{cat} = 1.35 V)	total	1426/494[a]	118/35[a]
Fit cathodic line shape	double layer[b]	686-1015	39-53
Scan rate variation	total	987	83
Scan rate variation	outer	466	53

[a] First and second numbers correspond to the slopes of the total charge vs. potential curves before and after the potential the Tafel slope bends.

[b] Due to the much larger capacitance values as compared to the double layer capacitance of planar metallic electrodes, in reality we probe here *pseudocapacitance (*C_{dl}-type*)*.

Table 5.3: Samples and treatments used in the chlorination study.

Sample	Treatment / #	Feed composition / vol.%	Treatment temperature / K	BET / m^2g^{-1}
Alfa Aesar IrO_x	–	–	–	36.46
AA-D	Deacon[a]	HCl:O_2:He = 10:20:70	723-623	22.84
AA-450°C	Calcination	O_2:N_2 = 21:79	723	22.4
AA-HCl[b]	Chlorination 1	HCl:He = 10:90	543	19.64
AA-HCl-O_2[b]	Chlorination 2[c]	HCl:He = 10:90 O_2:He = 20:80	543 573	25.87
AA-Cl_2[b]	Chlorination 3	Cl_2:He = 10:90	298	22.02

[a] The sample was exposed for a total time of 3 h

[b] Chlorination treatments 1/2/3 were carried out after calcination at 723 K

[c] Each sub-treatment (a,b) was performed for 1.5 h

Table 5.4: Charge values (in mC) during pulse voltammetry in the broad potential window of 0.95–1.7 V (non iR-corrected). Cathodic potential: 0.75V vs. RHE. Two samples (IrNi/Ti and IrO_x/Ti-250°C) are selected to show that the cathodic and anodic charge is equal below the OER onset.

Non iR-corrected anodic potential / V	Charge (mC)			
	IrNi/Ti		IrO_x/Ti-250°C	
	anodic	cathodic	anodic	cathodic
1.7	282.1	-5.93	320	-15.35
1.6	103.2	-5.73	130.63	-14.8
1.55	38.4	-5.5	57.52	-14.25
1.4	4.23	-4.1	10.58	-10.56
1.1	2.2	-2.19	5.44	-5.44
0.95	1.25	-1.26	3.09	-3.09

Table 5.5: Yield of Cl_2 as a function of the reaction temperature in the Deacon reaction over Alfa Aesar IrO_x. The collected sample was denoted as AA-D.

Order / #	Temperature[a] / K	Yield of Cl_2 / %
1	723	70.7
2	673	30.7
3	623	3.1

[a] Other conditions: F_T: W_{samp} = 40 L STP h-1 g_{samp}-1, 10 vol.% HCl, O_2:HCl = 2, P = 1 bar, t = 3 h

Table 5.6: XPS results on surface chlorination.

Sample	Cl/Ir ratio	Bridge Cl %	Cl(Bridge)/Ir
AA-450°C	0	–	0
AA-Cl_2	0.076	26.7	0.02
AA-HCl-O_2	0.48	31.6	0.152
AA-HCl	0.61	45.4	0.277
AA-D	0.62	53.4	0.331

5.10 Bibliography

(1) Grubb, W. T. Catalysis, Electrocatalysis, and Hydrocarbon Fuel Cells. *Nature* **1963**, *198* (4883), 883–884.

(2) Marcus, R. A. Electron Transfer Reactions in Chemistry. Theory and Experiment. *Rev. Mod. Phys.* **1993**, *65* (3), 599–610.

(3) Marcus, R. A. Theoretical Relations among Rate Constants, Barriers, and Broensted Slopes of Chemical Reactions. *J. Phys. Chem.* **1968**, *72* (3), 891–899.

(4) Gür, T. M. Review of Electrical Energy Storage Technologies, Materials and Systems: Challenges and Prospects for Large-Scale Grid Storage. *Energy Environ. Sci.* **2018**, *11* (10), 2696–2767.

(5) Seh, Z. W.; Kibsgaard, J.; Dickens, C. F.; Chorkendorff, I.; Nørskov, J. K.; Jaramillo, T. F. Combining Theory and Experiment in Electrocatalysis: Insights into Materials Design. *Science* **2017**, *355* (6321), eaad4998.

(6) Hu, C.; Zhang, L.; Gong, J. Recent Progress Made in the Mechanism Comprehension and Design of Electrocatalysts for Alkaline Water Splitting. *Energy Environ. Sci.* **2019**, *12* (9), 2620–2645.

(7) Bard, A. J.; Faulkner, L. R. *Electrochemical Methods - Fundamentals and Applications*, 2nd ed.; John Wiley & Sons, Inc.: New York, 2000.

(8) Shinagawa, T.; Garcia-Esparza, A. T.; Takanabe, K. Insight on Tafel Slopes from a Microkinetic Analysis of Aqueous Electrocatalysis for Energy Conversion. *Sci. Rep.* **2015**, *5* (1), 13801.

(9) Fang, Y.-H.; Liu, Z.-P. Tafel Kinetics of Electrocatalytic Reactions: From Experiment to First-Principles. *ACS Catal.* **2014**, *4* (12), 4364–4376.

(10) De Faria, L. A.; Boodts, J. F. C.; Trasatti, S. Electrocatalytic Properties of Ternary Oxide Mixtures of Composition Ru0.3Ti(0.7-x)CexO2: Oxygen Evolution from Acidic Solution. *J. Appl. Electrochem.* **1996**, *26* (11), 1195–1199.

(11) Lyons, M. E. G.; Brandon, M. P. A Comparative Study of the Oxygen Evolution Reaction on Oxidised Nickel, Cobalt and Iron Electrodes in Base. *J. Electroanal. Chem.* **2010**, *641* (1–2), 119–130.

(12) Schmickler, W.; Santos, E. *Interfacial Electrochemistry*, 2nd ed.; Springer Berlin Heidelberg: Berlin, Heidelberg, 2010.

(13) Seitz, L. C.; Dickens, C. F.; Nishio, K.; Hikita, Y.; Montoya, J.; Doyle, A.; Kirk, C.; Vojvodic, A.; Hwang, H. Y.; Norskov, J. K.; et al. A Highly Active and Stable IrOx/SrIrO3 Catalyst for the Oxygen Evolution Reaction. *Science* **2016**, *353* (6303), 1011–1014.

(14) Nong, H. N.; Reier, T.; Oh, H.-S.; Gliech, M.; Paciok, P.; Vu, T. H. T.; Teschner, D.; Heggen, M.; Petkov, V.; Schlögl, R.; et al. A Unique Oxygen Ligand Environment Facilitates Water Oxidation in Hole-Doped IrNiOx Core–Shell Electrocatalysts. *Nat. Catal.* **2018**, *1* (11), 841–851.

(15) Corrigan, D. A. The Catalysis of the Oxygen Evolution Reaction by Iron Impurities in Thin Film Nickel Oxide Electrodes. *J. Electrochem. Soc.* **1987**, *134* (2), 377.

(16) Pearce, P. E.; Yang, C.; Iadecola, A.; Rodriguez-Carvajal, J.; Rousse, G.; Dedryvère, R.; Abakumov, A. M.; Giaume, D.; Deschamps, M.; Tarascon, J.-M.; et al. Revealing the Reactivity of the Iridium Trioxide Intermediate for the Oxygen Evolution Reaction in Acidic Media. *Chem. Mater.* **2019**, *31* (15), 5845–5855.

(17) Grimaud, A.; Demortière, A.; Saubanère, M.; Dachraoui, W.; Duchamp, M.; Doublet, M.-L.; Tarascon, J.-M. Activation of Surface Oxygen Sites on an Iridium-Based Model Catalyst for the Oxygen Evolution Reaction. *Nat. Energy* **2017**, *2* (1), 16189.

(18) Frevel, L. J.; Mom, R.; Velasco-Vélez, J.-J.; Plodinec, M.; Knop-Gericke, A.; Schlögl, R.; Jones, T. E. In Situ X-Ray Spectroscopy of the Electrochemical Development of Iridium Nanoparticles in Confined Electrolyte. *J. Phys. Chem. C* **2019**, *123* (14), 9146–9152.

(19) Augustyn, V.; Simon, P.; Dunn, B. Pseudocapacitive Oxide Materials for High-Rate Electrochemical Energy Storage. *Energy Environ. Sci.* **2014**, *7* (5), 1597–1614.

(20) Conway, B. E. Electrochemical Capacitors Based on Pseudocapacitance. In *Electrochemical Supercapacitors*; Conway, B. E., Ed.; Springer US: Boston, MA, MA, 1999; pp 221–257.

(21) Kuo, D. Y.; Kawasaki, J. K.; Nelson, J. N.; Kloppenburg, J.; Hautier, G.; Shen, K. M.; Schlom, D. G.; Suntivich, J. Influence of Surface Adsorption on the Oxygen Evolution Reaction on IrO 2 (110). *J. Am. Chem. Soc.* **2017**, *139* (9), 3473–3479.

(22) Clancy, J. P.; Chen, N.; Kim, C. Y.; Chen, W. F.; Plumb, K. W.; Jeon, B. C.; Noh, T. W.; Kim, Y. J. Spin-Orbit Coupling in Iridium-Based 5d Compounds Probed by x-Ray Absorption Spectroscopy. *Phys. Rev. B - Condens. Matter Mater. Phys.* **2012**, *86* (19), 1–8.

(23) Pfeifer, V.; Jones, T. E.; Velasco Vélez, J. J.; Arrigo, R.; Piccinin, S.; Hävecker, M.; Knop-Gericke, A.; Schlögl, R. In Situ Observation of Reactive Oxygen Species Forming on Oxygen-Evolving Iridium Surfaces. *Chem. Sci.* **2017**, *8*, 2143–2149.

(24) Gauthier, J. A.; Dickens, C. F.; Chen, L. D.; Doyle, A. D.; Nørskov, J. K. Solvation Effects for Oxygen Evolution Reaction Catalysis on IrO2(110). *J. Phys. Chem. C* **2017**, *121*, 11455–11463.

(25) Otani, M.; Sugino, O. First-Principles Calculations of Charged Surfaces and Interfaces: A Plane-Wave Nonrepeated Slab Approach. *Phys. Rev. B* **2006**, *73* (11), 115407.

(26) Bonnet, N.; Morishita, T.; Sugino, O.; Otani, M. First-Principles Molecular Dynamics at a Constant Electrode Potential. *Phys. Rev. Lett.* **2012**, *109* (26), 266101.

(27) Ping, Y.; Nielsen, R. J.; Goddard, W. A. The Reaction Mechanism with Free Energy Barriers at Constant Potentials for the Oxygen Evolution Reaction at the IrO 2 (110) Surface. *J. Am. Chem. Soc.* **2017**, *139* (1), 149–155.

(28) Rossmeisl, J.; Qu, Z.-W.; Zhu, H.; Kroes, G.-J.; Nørskov, J. K. Electrolysis of Water on Oxide Surfaces. *J. Electroanal. Chem.* **2007**, *607* (1–2), 83–89.

(29) Nong, H. N.; Gan, L.; Willinger, E.; Teschner, D.; Strasser, P. IrOx Core-Shell Nanocatalysts for Cost- and Energy-Efficient Electrochemical Water Splitting. *Chem. Sci.* **2014**, *5* (8), 2955–2963.

(30) Reier, T.; Teschner, D.; Lunkenbein, T.; Bergmann, A.; Selve, S.; Kraehnert, R.; Schl, R.; Strasser, P. Electrocatalytic Oxygen Evolution on Iridium Oxide : Uncovering Catalyst-Substrate Interactions and Active Iridium Oxide Species. *J. Electrochem. Soc.* **2014**, *161* (9), 876–882.

(31) Ardizzone, S.; Fregonara, G.; Trasatti, S. "Inner" and "Outer" Active Surface of RuO2 Electrodes. *Electrochim. Acta* **1990**, *35* (1), 263–267.

(32) Li, G.; Anderson, L.; Chen, Y.; Pan, M.; Abel Chuang, P.-Y. New Insights into Evaluating Catalyst Activity and Stability for Oxygen Evolution Reactions in Alkaline Media. *Sustain. Energy Fuels* **2018**, *2* (1), 237–251.

(33) Lassali, T. A. F.; Boodts, J. F. C.; Bulhões, L. O. S. Charging Processes and Electrocatalytic Properties of IrO2/TiO2/SnO2 Oxide Films Investigated by in Situ AC Impedance Measurements.

Electrochim. Acta 1999, *44* (24), 4203–4216.

(34) Rasten, E.; Hagen, G.; Tunold, R. Electrocatalysis in Water Electrolysis with Solid Polymer Electrolyte. *Electrochim. Acta* 2003, *48* (25–26), 3945–3952.

(35) Orazem, M. E.; Frateur, I.; Tribollet, B.; Vivier, V.; Marcelin, S.; Pébère, N.; Bunge, A. L.; White, E. A.; Riemer, D. P.; Musiani, M. Dielectric Properties of Materials Showing Constant-Phase-Element (CPE) Impedance Response. *J. Electrochem. Soc.* 2013, *160* (6), C215–C225.

(36) De Pauli, C. P.; Trasatti, S. Electrochemical Surface Characterization of IrO2 + SnO2 Mixed Oxide Electrocatalysts. *J. Electroanal. Chem.* 1995, *396* (1–2), 161–168.

(37) Zichittella, G.; Aellen, N.; Paunović, V.; Amrute, A. P.; Pérez-Ramírez, J. Olefins from Natural Gas by Oxychlorination. *Angew. Chemie Int. Ed.* 2017, *56* (44), 13670–13674.

(38) Yeh, J. J.; Lindau, I. Atomic Subshell Photoionization Cross Sections and Asymmetry Parameters: 1 < Z < 103. *At. Data Nucl. Data Tables* 1985, *32* (1), 1–155.

(39) Giannozzi, P.; Baroni, S.; Bonini, N.; Calandra, M.; Car, R.; Cavazzoni, C.; Ceresoli, D.; Chiarotti, G. L.; Cococcioni, M.; Dabo, I.; et al. QUANTUM ESPRESSO: A Modular and Open-Source Software Project for Quantum Simulations of Materials. *J. Phys. Condens. Matter* 2009, *21*, 395502.

(40) Gianluca Prandini, Antimo Marrazzo, Ivano E. Castelli, Nicolas Mounet, N. M. A Standard Solid State Pseudopotentials (SSSP) Library Optimized for Precision and Efficiency (Version 1.1, Data Download). *Mater. Cloud Arch.* 2018.

(41) Marzari, N.; Vanderbilt, D.; De Vita, A.; Payne, M. C. Thermal Contraction and Disordering of the Al(110) Surface. *Phys. Rev. Lett.* 1999, *82* (16), 3296–3299.

(42) Nørskov, J. K.; Rossmeisl, J.; Logadottir, A.; Lindqvist, L.; Kitchin, J. R.; Bligaard, T.; Jónsson, H. Origin of the Overpotential for Oxygen Reduction at a Fuel-Cell Cathode. *J. Phys. Chem. B* 2004, *108* (46), 17886–17892.

(43) Limmer, D. T.; Willard, A. P.; Madden, P.; Chandler, D. Hydration of Metal Surfaces Can Be Dynamically Heterogeneous and Hydrophobic. *Proc. Natl. Acad. Sci.* 2013, *110* (11), 4200–4205.

(44) Wang, D.; Sheng, T.; Chen, J.; Wang, H.-F.; Hu, P. Identifying the Key Obstacle in Photocatalytic Oxygen Evolution on Rutile TiO2. *Nat. Catal.* 2018, *1* (4), 291–299.

(45) Dupont, M. F.; Donne, S. W. Charge Storage Mechanisms in Electrochemical Capacitors: Effects of Electrode Properties on Performance. *J. Power Sources* 2016, *326*, 613–623.

(46) Fierro, S.; Nagel, T.; Baltruschat, H.; Comninellis, C. Investigation of the Oxygen Evolution Reaction on Ti/IrO2 Electrodes Using Isotope Labelling and on-Line Mass Spectrometry. *Electrochem. commun.* 2007, *9* (8), 1969–1974.

(47) Teschner, D.; Farra, R.; Yao, L.; Schlögl, R.; Soerijanto, H.; Schomäcker, R.; Schmidt, T.; Szentmiklósi, L.; Amrute, A. P.; Mondelli, C.; et al. An Integrated Approach to Deacon Chemistry on RuO 2 -Based Catalysts. *J. Catal.* 2012, *285* (1), 273–284.

6. Concluding remarks

The present work addresses the question of whether potential-driven surface phase transitions influence the activity of iridium (hydr-)oxides in catalyzing the oxygen evolution reaction (OER). Three milestones mark the progress in answering this scientific question.

The first milestone is a novel experimental technique. It uses a combination of permeable polymer membranes and graphene which sandwich an electrocatalyst. While the membrane supplies the electrocatalyst with water and ions, the graphene cover prevents evaporation of water. In this way, a liquid thin film similar to bulk electrolyte forms and covers the electrocatalyst. Surface sensitive X-ray spectroscopy using photoelectrons can be measured through the graphene cover. With this new experimental tool, it became possible to routinely probe the surface of electrocatalysts under wet conditions and applied potential. Equally as important as this novel experimental technique are density functional theory (DFT) calculations, since they provide insight into the thermodynamics of surface species and reaction intermediates on the atomic scale. The correlative overlap to experimental techniques was realized by calculated O K-edge absorption, by electrochemical potentials using a computational hydrogen electrode, and by reaction kinetics using calculated reaction barriers from the nudged elastic band method. This closely interlaced combination of ab initio techniques and operando spectroscopy is the basis of this work and thereby forms the first milestone.

The second milestone is the observation of potential-driven surface phase transitions. Three different classes of oxygen species populate surfaces of iridium (hydr-)oxides: oxygen bound to one (μ_1-O), two (μ_2-O), or three (μ_3-O) neighboring iridium atoms. Each class has a protonated (μ_x-OH) and a deprotonated (μ_x-O) form and the distribution of all oxygen species on the surface defines a surface phase. Which phase is most stable is dependent upon the potential. In this work, these surface oxygen species and their (de-)protonation behavior were observed directly. Characteristic spectroscopic features were predicted by DFT and tracked in a potential window employing potentio-dynamic X-ray absorption. The latter also allowed for a direct correlation of surface phase transitions and the majority of electrochemical currents. Two important conclusions could be drawn from the results: First, the width of any observed surface phase transition extends over several hundred millivolts, while at least one of them is not completed when the catalyst enters the potential regime relevant to the OER. Second, the electrochemical charge flowing into or from the electrode is related to surface oxidation and is thereby stored in surface atoms. DFT also predicted and experimental tests confirmed that these surface charges reside increasingly on oxygen at potentials relevant to the OER. The oxygen species with the largest tendency to localize charge is μ_1-O, which started to be formed at the onset of the OER.

The third milestone is the apparent influence of the phase transition and the surface charge on the rate of the OER. It is the milestone which is the most relevant to catalysis of the OER but which also required major contributions from colleagues and collaborators. We combined potentio-dynamic X-

ray absorption with pulse voltammetry and found that the surface charge, the OER currents, and the spectroscopic fingerprint of electron-deficient surface oxygen species are all correlated. In a subsequent theoretical model, it was possible to fully explain the complex OER current behavior of iridium (hydr-)oxides by using μ_1–O as an active site, which is involved in an ongoing surface phase transition. A key finding is that these surface phase transitions vary the oxidative charge and thereby affect the barrier of O-O bond formation. The latter is thought to be the rate determining step of the OER on iridium (hydr-)oxides.

I hope the scientific approach and its results will further the understanding of electrocatalysts in the future. The global transition to renewable energy sources is in urgent need of such knowledge.

Appendix- Overview of published content

Chapter 2

Falling, Lorenz J.; Mom, Rik V.; Sandoval Diaz, Luis E.; Nakhaie, Siamak; Stotz, Eugen; Ivanov, Danail; Hävecker, Michael; Lunkenbein, Thomas; Knop-Gericke, Axel; Schlögl, Robert; Velasco-Vélez, Juan Jesús. Graphene-Capped Liquid Thin Films for Electrochemical Operando X-Ray Spectroscopy and Scanning Electron Microscopy. *ACS Appl. Mater. Interfaces* **2020**, *12* (33), 37680–37692. https://doi.org/10.1021/acsami.0c08379.

Licence: *ACS Author Choice* via the Creative Commons CC-BY agreement

Version: Chapter 2 conforms with the published version

Chapter 3

Frevel, Lorenz J.; Mom, Rik; Velasco-Vélez, Juan-Jesús; Plodinec, Milivoj; Knop-Gericke, Axel; Schlögl, Robert; Jones, Travis E. In Situ X-Ray Spectroscopy of the Electrochemical Development of Iridium Nanoparticles in Confined Electrolyte. *J. Phys. Chem. C* **2019**, *123* (14), 9146–9152. https://doi.org/10.1021/acs.jpcc.9b00731.

Licence: *ACS Author Choice* via the Creative Commons CC-BY agreement

Version: Chapter 3 conforms with the published version, with correction

Chapter 4

Version: Chapter 4 is unpublished, submission forthcoming

Chapter 5

Nong, Hong Nhan; Falling, Lorenz J.; Bergmann, Arno; Klingenhof, Malte; Tran, Hoang Phi; Spöri, Camillo; Mom, Rik; Timoshenko, Janis; Zichittella, Guido; Knop-Gericke, Axel; Piccinin, Simone; Pérez-Ramírez, Javier; Cuenya, Beatriz Roldan; Schlögl, Robert; Strasser, Peter; Teschner, Detre; Jones, Travis E. Key Role of Chemistry versus Bias in Electrocatalytic Oxygen Evolution. *Nature* **2020**, *587* (7834), 408–413. https://doi.org/10.1038/s41586-020-2908-2.

Licence: Under exclusive licence to Springer Nature Limited

Version: Chapter 5 is the pre-print version of the publication